ANALYTICAL AND NUMERICAL SIMULATION OF NUCLEATION AND GROWTH OF CARBON NANOTUBES IN A COMPLEX PLASMA

THESIS SUBMITTED TO
DELHI TECHNOLOGICAL UNIVERSITY
FOR THE AWARD OF THE DEGREE OF

DOCTOR OF PHILOSOPHY

By

Ms. UMANG SHARMA
(2K16/PHD/AP/15)

Under the supervision of

PROF. (DR.) SURESH C. SHARMA

DEPARTMENT OF APPLIED PHYSICS
DELHI TECHNOLOGICAL UNIVERSITY
DELHI-110042 (INDIA)

JULY 2022

Dedicated to my loving family

DELHI TECHNOLOGICAL UNIVERSITY
(Govt. of National Capital Territory of Delhi)
Shahbad Daulatpur, Bawana Road, Delhi-110042

CERTIFICATE

This is to certify that the thesis entitled "***Analytical and numerical simulation of nucleation and growth of carbon nanotubes in a complex plasma***" submitted by ***Ms. Umang Sharma (2K16/PhD/AP/15)*** to Delhi Technological University (DTU), Delhi, India for the degree of Doctor of Philosophy, is a bonafide record of the research work carried out by her under my supervision and guidance. The work embodied in this thesis has been carried out in the Plasma & Nano-Simulation Lab, Department of Applied Physics, Delhi Technological University (DTU), Delhi, India. The work of this thesis is original and has not been submitted in parts or fully to any other Institute or University for the award of any other degree or diploma.

25.07.2022

Prof. (Dr.) Suresh C. Sharma
Supervisor
Dean (Acad-PG) &
Professor, Department of Applied Physics
Delhi Technological University, Delhi-110042, India

25th July 2022

Prof. (Dr.) Rinku Sharma
Head of the department &
Professor, Department of Applied Physics
Delhi Technological University, Delhi-110042, India

DELHI TECHNOLOGICAL UNIVERSITY
(Govt. of National Capital Territory of Delhi)
Shahbad Daulatpur, Bawana Road, Delhi-110042

DECLARATION

I, **Ms. Umang Sharma**, hereby certify that the thesis titled ***"Analytical and numerical simulation of nucleation and growth of carbon nanotubes in a complex plasma"*** submitted in the fulfilment of the requirements for the award of the degree of Doctor of Philosophy is an authentic record of my research work carried out under the supervision of ***Prof. (Dr.) Suresh C. Sharma***. This work in the same form or any other form has not been submitted by me or anyone else earlier for any purpose. Any material borrowed or referred to is duly acknowledged.

Umang
24/07/2022

Umang Sharma
(2K16/PhD/AP/15)
Department of Applied Physics
Delhi Technological University
Delhi-110042, India

ACKNOWLEDGEMENT

Above all, I express my genuine thanks to the Almighty and Shri Radhavallabh Lal Ji for giving me immense strength and patience to work hard all these years.

I express my heartfelt gratitude to my grandparents, **Late Mr. Rishi Kumar Shastri, Late Mrs. Jaidevi** and **Late Mrs. Ratan Prabha Sharma**. I believe that even from the heavenly abode, they showered me with their immense blessings and strength all these years. I know they would feel proud of their granddaughter.

I wholeheartedly want to thank my guide, **Prof. (Dr.) Suresh C. Sharma**, Professor, Department of Applied Physics & Dean (Acad-PG) Delhi Technological University (DTU), for his excellent mentorship, research, patience, motivation, enthusiasm, immense knowledge and continuous support all these years. Without his persistent efforts and guidance, this thesis would not have been accomplished. His guidance helped me research and writing of this thesis. He is genuinely the best advisor and mentor.

My sincere thanks also go to **Prof. Yogesh Singh**, Ex-Hon'ble Vice-Chancellor, DTU, **Prof. Jai Prakash Saini**, Hon'ble Vice-Chancellor, DTU and other officials for their valuable support and for providing ample facilities to conduct this research. I would also like to acknowledge the DTU's financial support to attend the 44^{th} and 46^{th} European Physical Society Conference on Plasma Physics in 2017 and 2019, respectively.

I would also thank **Prof. Rinku Sharma**, Head of the Department of Applied Physics, DTU, and all other faculty and staff members for their help and cooperation throughout my research. Thanks to the **Department of Applied Physics, Delhi Technological University (DTU),** for providing the required facilities so that I can work voraciously, barring the time limit.

I express my gratitude to my seniors, **Dr. Neha Gupta, Dr. Ravi Gupta, Dr. Jyotsna Panwar, and Dr. Monika Yadav,** for their valuable suggestions and

continuous help during the initial stage of my research work. I would also like to express huge and warm thanks to my other fellow lab mates in Plasma & Nano Simulation Research Laboratory; **Ms. Anshu, Ms. Shruti Sharma, Mr. Rajesh Gupta, Mr. Sagar Khanna, Ms. Jyoti, Mr. Rajesh Kumar, Mr. Harender Mor, Ms. Mansha Kansal, Ms. Sangeeta, Mr. Ramesh Kumar, Mr. Aditya and Ms. Ritu** for their scientific inputs, fruitful discussions, motivation, and all the fun we had, kept me going in this challenging yet beautiful journey. Our fun in the last few years kept me sane during my ups and downs. Their personal and professional help, moral support and encouragement have put me at ease. The time I spent with them will remain a memorable golden time in my life. I also explicitly thank my colleagues, **Dr. Aman Prasad, Dr. Harpreet Kaur, Mr. Rajat Bajaj, and Mr. Abhishek Bhardwaj,** for their generous support.

I want to pay high regard to my father, **Mr. Rajeev Kumar Sharma**, my mother, **Mrs. Sunita Sharma**, and my younger brother **Mr. Harivansh**, for their love, constant care, and emotional support throughout my life. Their faith, trust and confidence in me always pushed me toward my goal. I want to thank my husband, **Mr. Sanyam Kaushik,** for always being there and encouraging me when I lost optimism or felt disheartened. I owe a special thanks to my family-in-law, my grandfather-in-law **Mr. Om Prakash Sharma**, my mother-in-law **Mrs. Archana Kaushik**, father-in-law **Mr. Ravikant Kaushik** and brother-in-law, **Mr. Sarthak Kaushik,** as without their love, patience and support. My family's cooperation, understanding, patience and encouragement were the sustaining factors in this challenging journey. I am also indebted to my lovely friend **Ms. Alankrita Negi** for cheering me at every step.

I want to acknowledge the **Department of Science and Technology (DST), Government of India**, for providing financial assistance under the **DST-INSPIRE Fellowship** to conduct my research.

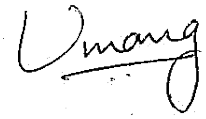

Umang Sharma

ABSTRACT

Carbon nanotubes (CNTs) are allotropes of carbon with sp^2 hybridization and could be considered a sheet of graphene (a hexagonal lattice composed of carbon atoms) rolled up in cylindrical geometry. They were first discovered by Sumio Iijima in 1991 while synthesizing fullerene in an arc discharge apparatus. CNTs have significantly contributed in many scientific fields such as physics, chemistry, mathematical modelling, and material sciences since their discovery. CNTs are the most extensively studied allotrope of carbon as it possess a hollow structure which gives astonishing thermal, electrical, and mechanical properties including high tensile strength, enhanced thermal conductivity compared to diamond, high electrical conductivity, etc. hence, they seem as the best fit for several applications. CNTs are used in biosensors, nano-scale electronics, field emission, and hydrogen storage. They can be synthesized using various methods such as laser ablation, arc discharge, thermal chemical vapour deposition (CVD) or plasma-enhanced CVD. However, CNTs made with the assistance of a reactive plasma medium are known to be vertically aligned. The plasma synthesis conditions influencing the CNT growth and optimizing their field emission properties are studied thoroughly in the current thesis.

The thesis explores the effects of plasma operating conditions, plasma parameters, etc. on the nucleation and growth of CNTs in a reactive plasma environment. Various analytical models have been considered in the work which accounts for the plasma aided vertical alignment of nanotubes; plasma pre-treatment of metal catalyst thin film for CNT synthesis and effect of different catalyst nanoparticles; growth of an array of vertically aligned CNTs; and effect of varying gas ratio and different carrier gases, respectively. Each model is divided into two parts. The first part encompasses the kinetics of all the plasma species (ions, electrons, and neutrals) which involves processes such as their ionization, dissociation, and excitation; and kinetics of catalyst nanoparticle including all the variations of the operating conditions. The second part comprises of all the processes leading to

deposition of nanotube. These processes include adsorption and desorption of hydrocarbon ions and neutral atoms onto/from the surface of catalyst, generation of carbon and hydrogen species on the active area of catalyst, surface diffusion of carbon over the surface of the catalyst, bulk diffusion of carbon into the volume of the catalyst, precipitation of carbon from the saturated catalyst nanoparticle which gives rise to graphitic tubular structure (CNT growth initiates), hydrogen etching of amorphous carbon that hinders the CNT growth, and simultaneous vertical alignment of CNTs due to plasma sheath induced electric field that gives rise to an alignment force. All these process are contained within the model equations and are solved for experimentally determined operating conditions and glow-discharge parameters. It was found that plasma sheath induces and electric field that produces an electrostatic force which is responsible for vertical alignment of nanostructures in plasma. Also this electric field and the consequent force are also dependent upon various plasma parameters. The plasma pre-treatment of catalyst thin films and the effect of process parameters, i.e. power, pressure, gas flow and plasma temperature, was deliberated. The effect of the nature and thickness of the catalyst on CNT growth parameters such as diameter, length, number of CNT walls, etc. was studied. The relation between the catalyst diameter and nanotube walls was established. The substrate temperature, plasma concentration, power and pressure greatly influence the CNT array growth. The change in average length and diameter of CNTs of the array with power and pressures is revealed. The effect of gas ratio and substrate temperature on the width of a carbon film deposited on the substrate between CNTs is also discussed. The field enhancement characteristics of the nanotube array are also studied. It is examined that on increasing the hydrogen ion density, CNT radius decreases due to decease in deposition rate. Also, with the increase in hydrogen ion densities, the hydrocarbon density decreases which endorses the decreases in CNT radius. The results indicate the decline in the CNT radius with increasing gas ratio. Also, the height of CNT decreases with the increasing gas ratio. With the increasing gas ratio i.e., as the concentration of hydrocarbon gas increases, CNTs of smaller radius and height were produced as abundance of carbon atoms are produced compared to hydrogen atoms and the amorphous carbon layer which hinders the

CNT growth generates rapidly. We have compared the effects of several carrier gases on the structure of CNT using acetylene as the hydrocarbon source. As a result of the study, it was concluded that whereas argon promotes the formation of CNTs, ammonia and nitrogen inhibit their growth. The results of the models have been assessed and compared with the existing experimental observations which accredit the proposed mechanisms. Since the field emission properties of the carbon nanotubes depend on their geometrical aspects, i.e., radius and length, the current work of the thesis can be expanded to construct the ideal vertically aligned carbon nanotubes for their potential application as field emitters. The current research work can potentially be expanded to understand the synthesis of other carbon-based nanostructures.

LIST OF PUBLICATIONS

International journals

1. **Umang Sharma** and Suresh C. Sharma, "Impact of plasma process parameters on the growth of vertically aligned carbon nanotube array and its optimization as field emitters", *European Physical Journal Plus* **137**, 823 (2022).
2. **Umang Sharma** and Suresh C. Sharma, "Investigations on Plasma Pretreatment of Catalyst Film and Catalyzed Growth of Carbon Nanotube", *IEEE Transactions on Plasma Science* **50**, 888-898 (2022).
3. **Umang Sharma** and Suresh C. Sharma, "A parametric study to unravel the alignment mechanism of carbon nanotubes during its plasma-assisted growth", *Physics of Plasmas* **25**, 103509 (2018).

International peer reviewed proceedings

1. **Umang Sharma** and Suresh C. Sharma, "Investigating the effect of different carrier gases on plasma-assisted multiwalled carbon nanotube growth", *46th European Physical Society Conference on Plasma Physics*, ECA Volume **43C**: P2.3009 (2019).
2. **Umang Sharma**, Suresh C. Sharma, Ravi Gupta and Neha Gupta, "Theoretical Investigations to Study the Effect of C_2H_2/H_2 gas ratio on the Multi-walled Carbon Nanotubes Growth", *44th European Physical Society Conference on Plasma Physics*, ECA Volume **41F**: P2.309 (2017).

3. **Umang Sharma**, Neha Gupta, Ravi Gupta, and Suresh C. Sharma, "Analytical modelling to study the effect of hydrogen plasma on the growth of multi-walled carbon nanotubes", *IOP: Journal of Physics: Conference Series*, Volume **36**: 012017 (2017).

CONTENTS

LIST OF FIGURES

Chapter 2

Chapter 3

Chapter 4

LIST OF TABLES

Chapter 4

Chapter - 1

INTRODUCTION

1

INTRODUCTION

1.1 BACKGROUND

Nanomaterials today are the fastest developing field in material science and engineering. At the nanometer-scale, the materials' properties differ from their three-dimensional bulk forms due to differences in bond strength and short- and long-range bond order. The current worldwide research is developed to comprehend the relation between the properties and structure of the materials in their nano-meter diameter and varying micron length scale.

The three primary configurations of elemental carbon are - *graphite*, that is made up of stacked planar graphitic sheets; *diamond*, where the carbon atoms are bonded tetrahedrally to each other, creating a huge three-dimensional structure; and *fullerenes*, which are a large and diverse class of hollow spheres, ellipses, and tubes made of sp^2 hybridized carbon atoms[1,2]. When fullerenes[3] and *carbon nanotubes* (CNTs)[4] were initially reported, it created the emergence of an innovative field of study where the understanding of physics, chemistry, and the possibility of technology applications has risen steadily[5,6]. Fig. 1.1 depicts several forms of carbon nanostructures. Each of the findings has predicted a revolution in materials science and electronics, especially in the last two[7,8]. In the early 1990s, Iijima [4] described the discovery of multi-walled carbon nanotubes, tubular carbon nanostructures that had crystallized and been repeatedly stacked. A laser ablation technique was used to quickly show the synthesis of single-walled carbon nanotubes (SWCNT)[9]. Multi-walled carbon nanotubes (MWCNTs) are made up of co-axial concentric tubes of single-walled carbon nanotubes (SWCNTs), which are represented as flawlessly rolled-up sheets of

graphene. Hence, there is a vast interest in researching carbon nanotubes' production, characterization, growth mechanism, chemical alterations, and possible applications.

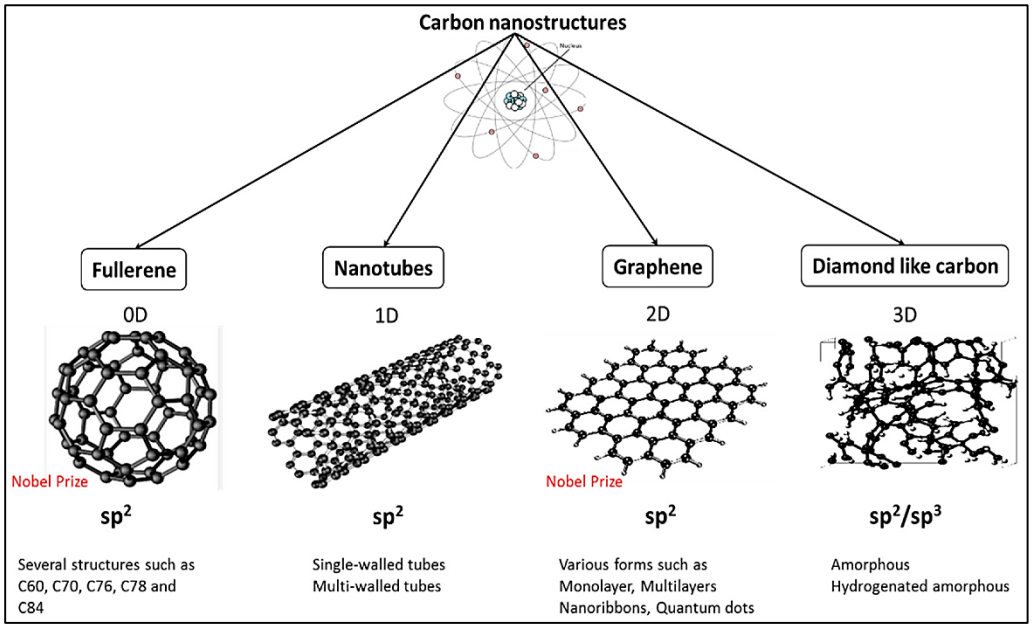

Figure 1.1 Different forms of carbon nanostructures[10].

1.2 CARBON NANOTUBES

Carbon nanotubes (CNTs) can be described as elongated fullerenes with graphitic shells arranged in the form of cylinders having their radii and lengths in the ranges of nano-meter and microns, respectively. Although CNTs could be produced using the same catalyst and have comparable morphology, they can vary in their diameters and crystalline structure. The positioning of graphitic planes with the axis of CNT growth symbolizes the difference between CNTs and controls their properties[11].

Since their discovery, they have drawn extensive and long way attention—the exponential boom in patent filings and courses devoted to this fascinating material. On the one hand, it demonstrates ever-growing technological and educational interests and, on the alternative hand, indicates that there nonetheless exist many perplexing situations towards their practical and bulk applications. Actually, on the way to realizing the capability of CNTs in reality, a few critical limitations along with CNT

cost, polydispersity in CNT type, CNT quality and purity, and challenges in processing and assembling have to be resolved.

1.3 TYPES OF CARBON NANOTUBES

Carbon nanotubes (CNTs) and fullerene (C_{60}) are adherents of the same family of carbon allotropes. A CNT can be considered a fullerene split in half and connected with a graphitic cylinder, whereas the latter is a spherical molecule. CNTs are divided into three categories: single, double, and multiple "walls". Single-walled carbon nanotubes (SWCNTs) and multi-walled carbon nanotubes (MWCNTs) differ significantly in their sizes (Figure 1.2). Although CNTs have minimal diameters, most miniature tubes can have extremely high aspect ratios and diameters. CNTs are therefore regarded as quasi-one-dimensional materials[12]. Typically, there are two categories of CNTs: (1) single-walled CNTs (SWCNTs), which have only one graphene layer, and (2) multi-walled CNTs (MWCNTs), which have nested co-axial arrays of SWCNTs and are spaced apart by 0.34 nm on average, which is marginally more significant than the interlayer separation of graphite.

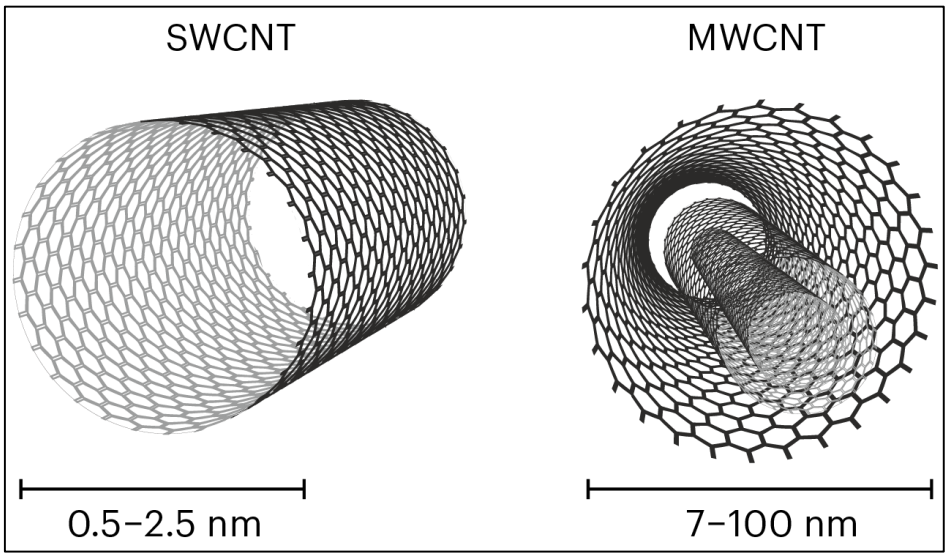

Figure 1.2 Types of CNTs; SWCNT (singe-walled carbon nanotubes) and MWCNT (multi-walled carbon nanotubes)[13].

1.4 STRUCTURE OF CARBON NANOTUBES

Owing to its high aspect ratio, CNT is considered a 1D nanostructure (i.e., the length over diameter). A graphene lattice's schematic diagram is shown in Figure 1.3, created by $|a_1| = |a_2| = a\sqrt{3}a_{C-C}$ ($a_{C-C} = 0.142\,nm$ describes the nearest-neighbor distance)[14] where $\boldsymbol{a_1}$ and $\boldsymbol{a_2}$ are the basis vectors. The radius of a CNT is determined by the chiral vector ***C***. To create the CNT, the graphitic sheet is rolled up in the direction of ***C***; hence it is known as the chiral vector of the CNT. The initial lattice point of the 2D graphene sheet through which vector ***T*** passes, also known as the translation vector, is parallel to the CNT axis but normal to ***C***. The unit cell of the CNT in real space is specified by the rectangle produced by ***C*** and ***T*** (as illustrated in Figure 1.3).

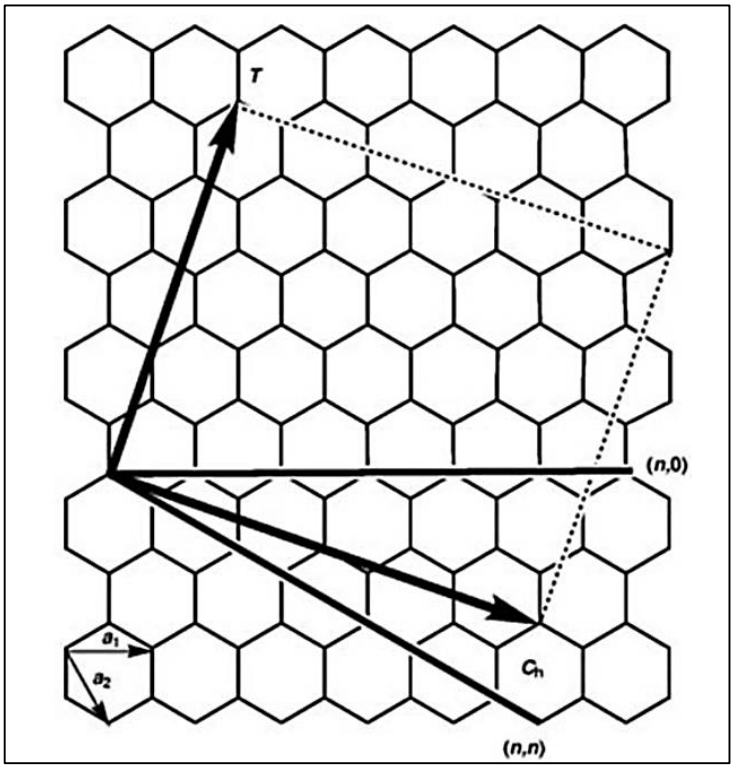

Figure 1.3 Schematic of graphene lattice with ***C*** as the chiral vector; ***T*** as the translation vector; and $\boldsymbol{a_1}$ and $\boldsymbol{a_2}$ as basis vectors, respectively[14].

The basis vectors $\boldsymbol{a_1}$ and $\boldsymbol{a_2}$ of the graphitic lattice are used to define $\boldsymbol{C}$:

$$\boldsymbol{C} = n\boldsymbol{a_1} + m\boldsymbol{a_2} \equiv (n, m) \tag{1.1}$$

where *n* and *m* are integers, and $0 \leq m \leq n$. *(n, m)* is the chiral index or chirality of the CNT.

The diameter of the CNT, *d*, is defined by $|C|/\pi$:

$$d = |C|/\pi = (a/\pi)\sqrt{n^2 + m^2 + nm} \tag{1.2}$$

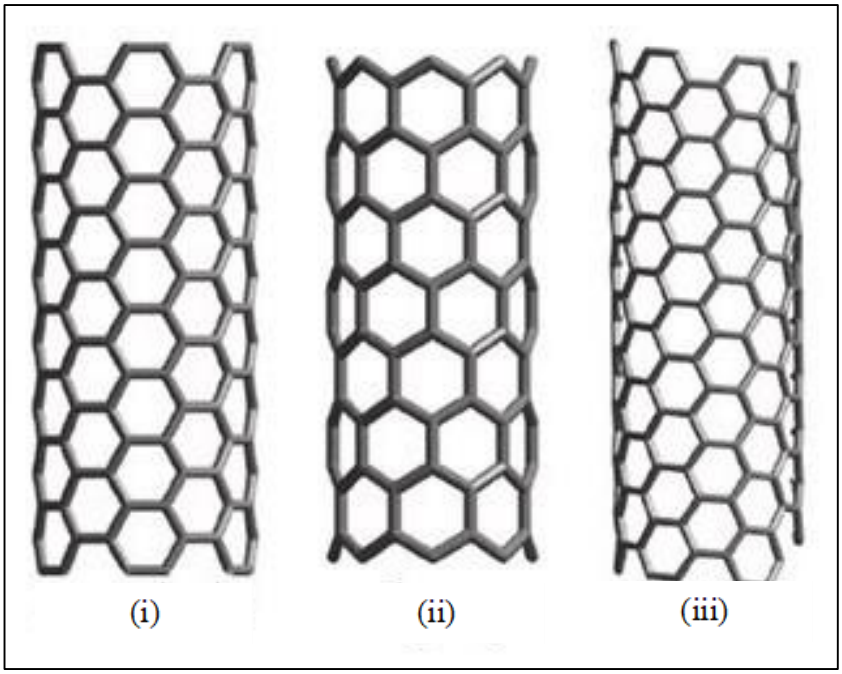

Figure 1.4 Classification of CNT though chirality; (i) armchair, (ii) zigzag, and (iii) chiral, respectively[15].

As *C* may be described with any practical arrangement of *n* and *m*, CNT can be rolled from graphitic sheets in various ways. This indicates many possible assemblies for CNTs even though the CNTs are nanoscale cylinders. CNTs may be classified as both achiral and chiral based on their symmetry. If the CNT mirror image is equal to the original one, it is an achiral CNT. Figure 1.4 (i) and (ii) suggest forms of achiral nanotubes, i.e., armchair and zigzag nanotubes. These forms of achiral CNTs are

named from the form of the cross-sectional ring, as seen from the edge of the nanotubes. Figure 1.4 (iii) suggests the schematic diagram of a chiral nanotube. Chiral nanotubes show spiral symmetry, and the CNT mirror image is not equivalent to the original one. The diameter and chirality of the tubes affect the band gap of CNTs. The characteristics of the individual tube layers in MWCNTs may vary. Theoretically, one-third of all *(n, m)* CNTs could be metallic, while *(n + 1, m)* CNTs could be semiconducting. However, the structural variations between the two groups can be pretty insignificant. Two types of chiral vector *C* deserve special mention. First is the zigzag CNT, whose chiral vectors lie simply along with one of the basis vectors, $C = (n, 0)$. The other is armchair CNT, whose chiral vectors are alongside the path precisely among the basis vectors, $C = (n, n)$. All different (n, m) CNTs with $n \neq m \neq 0$ correspond to chiral nanotubes.

1.4.1 ELECTRICAL PROPERTIES

The transport of charge carriers in CNT is in one dimension as they have an excellent aspect ratio and hollow structure. At room temperature, their resistivity is 10^{-6} Ω cm, considerably lower compared to silver and copper[9,16]. The mobility of holes in semiconducting CNTs (~2×10^4 cm^2 /Vs) is more than the mobility of electrons (~1.5×10^3 cm^2 /Vs) and holes (~4.5×10^2 cm^2 /Vs) in silicon. The CNTs also show a large current density (10^7-10^9 A/cm^2)[17,18].

The diameter-dependent energy gap makes CNT appealing to numerous nanoelectronics devices. CNT-based field-effect transistors (FETs) have the most practical geometry, including metal electrodes connected through a CNT on the high substrate point capped through an insulating layer. Due to the 1D nature of CNT, electron delivery in the 1-D nanostructure is restrained, so CNTs have an inherent benefit over bulk semiconducting materials to work as the vital component in a single-electron transistor (SET). As CNTs have a massive surface to volume ratio, conductance in CNTs is very sensitive to the electrostatic surroundings across the CNTs. The excessive sensitivity makes the CNT a perfect candidate for recollection

application. Because of these particular properties, CNTs were studied intensively throughout the decade.

1.4.2 THERMAL PROPERTIES

The computing scales to measure the thermal properties of any materials are specific heat and thermal conductivity. The CNT heat-conducting properties are far better than a diamond. The CNT thermal conductivity at room temperature[19,20] is 3000-6600 W/mK. The specific heat of SWNT bundles having a typical diameter of 1.25 nm was in the range 300 – 4K as reported by Hone *et al.*[21]. Beyond this, the experimental and theoretical curves agreed but differed vastly from graphitic curves up to 100K. Mizel et al.[22] indicated that the specific heat for SWCNT reformed its dependency on temperature (T) from $T^{1/2}$ to T. As identified by Yi *et al.*[23], the specific heat for MWCNT showed linear dependency on temperature for 10K to 300K. For carbon-based material, the thermal conductivity is through atomic vibrations. The diamond is an excellent thermal conductor with sp^3 bond, while CNT shows high thermal conductivity with sp^2 bond. The thermal conductivity of CNT bulk samples aligned by high magnetic fields was more significant than 200 W/mK, while for unaligned samples, it was one order smaller than a diamond, as observed by Berber *et al.*[19].

1.4.3 MECHANICAL PROPERTIES

To determine the mechanical properties of the solid material, it is necessary to analyze Young's modulus and tensile strength. Young's modulus is the ability of the material to withstand the linear extension/compression, while tensile strength examines the resistance provided by the material under the breaking tension. The experimental range for CNT Young's modulus[24-29] is 0.7-1.8 TPa, whereas theoretically[30], it is 0.5-5 TPa. This shows that CNTs are more robust and stiffer than steel[31,33], with Young's modulus of about 0.18-0.2 TPa. The tensile strength of the CNTs[27,38] is in the range of 11-200 GPa, while the tensile strength of steel[31,32] is about 0.38-1.55 GPa. Additionally, CNTs can retain their original form after experiencing an extreme deformation displaying high elastic properties.

1.5 APPLICATIONS OF CARBON NANOTUBES

CNT is an exquisite case of good nanotechnology: they have diameters of few nano-meters; however, their molecules may be altered chemically and physically in beneficial ways. CNTs expose a remarkable diversity of applications in material science, electronics, chemical processing, and many different fields. Growing commercial interest in CNTs worldwide is pondered in a manufacturing potential that exceeds numerous thousand tons per year. CNT bulk powders are included in many industries, including automotive parts, rechargeable batteries, and water filters. Vertically aligned CNTs (VACNTs) have numerous applications, as mentioned in the image below[33] in the field of field emission, fiber lasers, photonics, solar and nano applications (as a vertical CNT-field effect transistor), etc., owing to their high aspect ratio, excellent electrical conductivity, and outstanding mechanical strength.

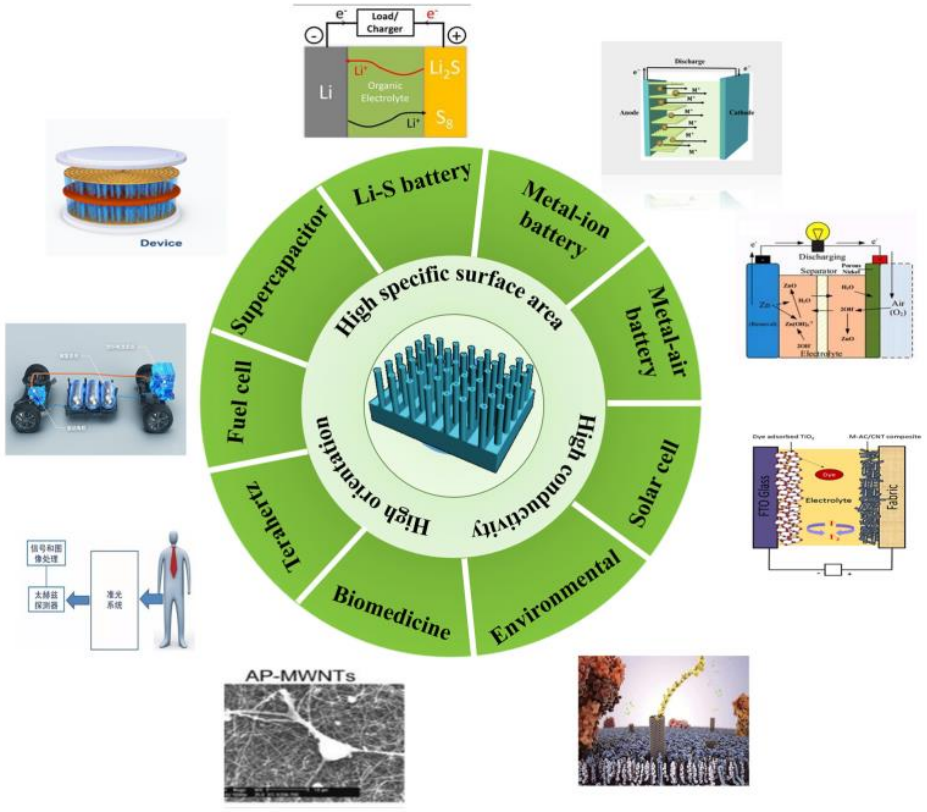

1.5.1 ENERGY STORAGE

CNTs show the inherent characteristics required for their use as electrodes in the rapidly developing field of battery and capacitors. They have an enormous surface area and excellent electrical conductivity; thus, their surface area is significantly readily available to the electrolyte due to linear geometry. Due to CNT's highest reversible capacity compared to other nanomaterials is being used in lithium-ion batteries [34]. Also, CNTs are now being marketed as an ideal material for supercapacitor electrodes[35]. CNTs are also used in various fuel cells, such as electrode catalyst supports in PEM fuel cells. Due to high electrical conductivity, CNT can also be advantageous in gas diffusion layers. CNT's High strength and toughness-to-weight properties could also benefit their use as composite components in fuel cells installed in transport applications.

1.5.2 MOLECULAR ELECTRONICS

The idea of using molecules of the material to build electronic circuits has recently been revived and is vital for nanotechnology applications. The interconnections between switches and other active devices become crucial in any electronic circuit with nanoscale dimensions. CNT's physical and chemical properties have made them perfect contenders for contacts in molecular electronics. Moreover, they had established themselves as switches.

1.5.3 THERMAL MATERIALS

As CNTs are pure carbon polymers, they can be controlled and influenced using the established chemistry of carbon. Their structure could be modified, and solubility and dispersion could be enhanced. CNTs are usually free from structural flaws as they are molecularly perfect. The incomparable CNT thermal conductivity enables various applications where heat transfer is necessary. Such application can be established in electronics, mainly in advanced computation, where uncooled chips usually range over 100 ^{o}C. The synthesis of aligned CNT structures and ribbons is crucial in making highly

effective heat conduits[36]. Furthermore, CNT composites have increased their bulk thermal conductivity dramatically.

1.5.4 STRUCTURAL MATERIALS

The extraordinary CNT properties are not restricted only to electrical and thermal conductivities; however additionally consist of mechanical properties, like strength, toughness, and stiffness. This leads to numerous applications owing to CNT properties and advanced composites that require more outstanding merit of more than one of those properties.

1.5.5 FABRICS AND FIBRES

In early 2000, pure CNT fibers spun were established and are under rapid development along with CNT composite fibres[37]. Such excellent robust fibers could have many applications, including body and automobile armor, transmission cables, woven textiles, and fabrics. CNTs also are getting used to make textiles stain-resistant.

1.5.6 CATALYTIC SUPPORTS

CNTs have a tremendously high surface area, i.e., each atom is on two CNT surfaces, inside and outside of the CNT. Their capability to affix primarily any reactive species to its walls (functionalization) delivers an application for CNT for use as distinctive catalyst supports. The CNT electrical conductivity might also be advantageous for exploring new catalytic actions.

1.5.7 AIR AND WATER FILTRATION

Several researchers have advanced air and water filtration devices using CNTs. It is indicated that those filters, along with blocking the tiniest debris, can also kill maximum bacteria. CNTs have already been commercialized in this area, and the products are now available in the marketplace.

1.5.8 BIOMEDICAL APPLICATIONS

The investigation of CNT in biomedical applications is ongoing and has substantial potential. The human body is mainly composed of carbon; hence it is assumed to be highly biocompatible. Cells grown over CNTs show no toxic effects. These cells give rise to the use of CNT in the biomedical field, such as prosthetics coatings and anti-fouling coatings for ships. CNT's property of sidewall functionalization paves the way for their other biomedical demands, such as neuron growth, regeneration, and vascular stents. Also, a single DNA strand could be fused to a CNT and can be implanted in a cell effectively.

1.5.9 HYDROGEN STORAGE

The structural variety displayed by 1-D CNTs gives rise to their use in hydrogen storage devices. Hydrogen is one of the most valuable energy sources that can be quickly produced with high utilization. One of the most significant disadvantages of using hydrogen as the energy source is its storage, but storage of hydrogen (liquid hydrogen) is expensive and dangerous. CNTs can absorb highly dense hydrogen at standard temperature and pressure (STP) conditions via H-bonding with van der Waals forces in CNTs[38] and show hydrogen condensation of about 5-10 % by weight. However, potassium and lithium doped CNTs show 14% and 20% by weight hydrogen condensation, respectively[39].

1.5.10 FIELD-EFFECT TRANSISTORS

CNT that show semiconducting behavior can be used as the channel in field-effect transistor (FET)[40,41]. A CNT-FET schematic is displayed in Fig. 1.5. The p-type CNT-FET show very high transconductance and high carrier velocity, i.e., at 0.6 V gate voltage, the current density of 1500 A/m are observed, whereas p-type MOSFET (metal-oxide-semiconductor field-effect transistor) shows ~ 500 A/m at the overdrive voltage.

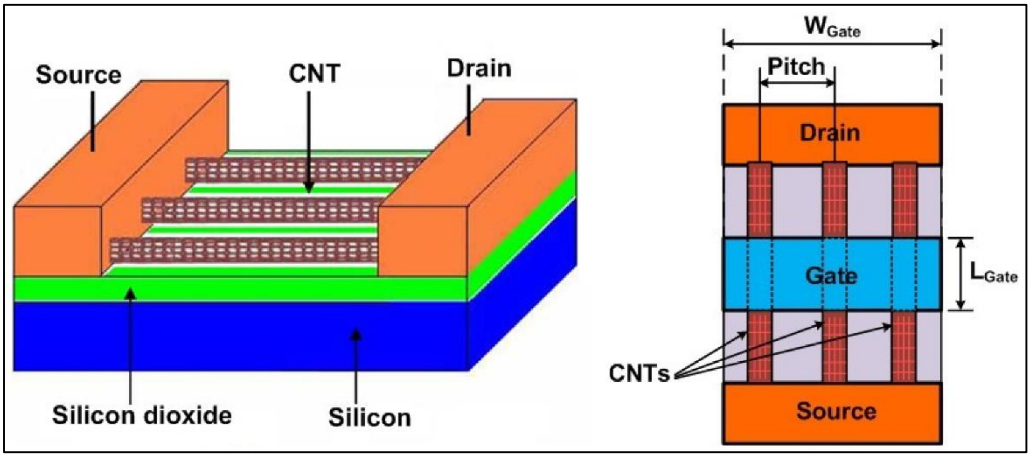

Figure 1.5 Carbon nanotube field-effect transistors (CNT-FET)[42].

1.5.11 ELECTRON EMITTERS

CNTs are regarded as excellent field emitters agreeing to their outstanding electric conductivity and the tremendous sharpness in their tip. This is because CNT's tip radius is smaller, and the electric field would be more focused, leading to elevated field emission. The tip sharpness also helps emission at an extremely low voltage, an essential feature for building low-power electrical devices. CNTs carry an astonishingly large and highly stable current density of 10^{13} A/cm^2. Flat-panel displays are garnering significant interest. CNT displays have a single electron gun for every pixel, unlike traditional CRT displays, which have a single electron gun. CNT's current density, low operating voltages, and steady, long-lived behavior make them efficient field emitters. Additional applications using the CNT field emitters comprise a low-voltage cold-cathode light source, electron microscope source, and lightning arrestors[43].

1.6 FIELD EMISSION CHARACTERISTICS

The field enhancement factor is crucial to understanding the field emission aspects. When an external electric field of adequate strength (more significant than the material's work function) is applied around the tip of the nanotube, it leads to electron emission. Carbon nanotubes are considered pre-eminent electron field mission

materials attributed to their high aspect ratio, i.e., length to radius ratio. Fowler and Nordheim stated the relation between applied electric field (E), work function (ϕ), and field emission current (I) of the material[44]

$$I = \frac{q^3 E^2 \alpha}{8\pi l \phi t^2(y)} \exp\left[\frac{-8\pi v(y)\sqrt{2m_e\phi^3}}{3lqE}\right] \tag{1.3}$$

where α is the field area of the emission sites, v*(y)* and *t(y)* are the Nordheim functions, and all other symbols have their usual meaning. Fig. 1.6 shows two experimental setups for determining field emission characteristics. The field emission characteristics of any material could be characterized by the field enhancement factor (β).

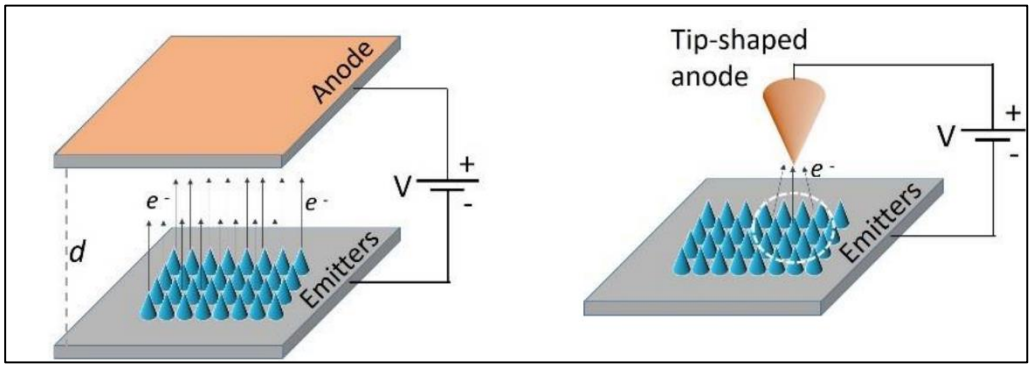

Figure 1.6 Experimental arrangement for field emission determination in (i) parallel plate and (ii) tip configuration for average and local characterization, respectively[45].

In general, β for individual CNT is proportional to the ratio of its length to the radius.

$$\beta = \frac{l}{r} \tag{1.4}$$

Thus, it can be believed that enhanced field emission properties displayed by the CNTs result from their geometry rather than their crystalline structure[46].

Also, the local electric field is greatly influenced by the surface shape and could be considerably enhanced at the top of sharp structures; hence β is expressed in terms of

the CNT tip electric field and the macroscopic electric field ratio. If E_a (actual electric field at CNT tip) and E_m (macroscopic electric field) -

$$\beta = \frac{E_a}{E_m} \tag{1.5}$$

This β factor is usually measured higher for individual CNTs around 30000 – 50000 than for CNT films around 1000 – 3000 which reduces furthermore for dense films due to the electric field screening from the close nanotubes. The factor is known to be dominated by the length of nanotubes and spacing between them; hence it is essential to recognize their effects to achieve optimum field emission properties[47].

Considering the spacing s between VACNTs, the geometrical field enhancement factor β for CNT films[48] can be estimated by Eq. (1.6), where β_0 is the field enhancement factor for individual CNT.

$$\beta = \beta_0 \left[1 - \exp\left(-2.3172 \frac{s}{l} \right) \right] \tag{1.6}$$

1.7 CNT SYNTHESIS METHODS

For industrial and research purposes, the chief characteristics of CNTs are their length, thickness, chiral angle, and inclination about the growth axis are the central aspect. There are many routes through which heterogeneous CNTs can be synthesized, but adopting easy and cost-effective methods is always necessary. CNTs can be synthesized through various techniques. Some of those techniques are discussed below.

- Laser ablation
- Arc discharge
- Thermal chemical vapor deposition (TCVD)
- Plasma-enhanced chemical vapor deposition (PECVD)

1.7.1 LASER ABLATION

This technique produced high-quality CNTs in more than 70% yield[9]. An intense and continuous laser beam (ND-YAG laser or CO_2 laser) is concentrated onto a 6-7mm carbon target loaded with 0.5 at. % nickel and cobalt as the metal catalyst is needed to form SWCNTs[49]. The target is heated to 1200 ^{O}C during this synthesis method, and the beam ablates the carbon target. An inert gas flow is introduced into the furnace to carry the grown nanotubes to the cold finger. This technique produces a high-quality single-walled carbon nanotube (SWCNT). These nanotubes self-organize into "ropes" consisting of 100–500 SWCNTs in a 2D triangular lattice due to van der Waals forces. The plume containing nanotubes and other products are condensed on the collector. This method is specifically known for producing high-quality and pure CNTs with minimal defects density. The schematic of the laser ablation method is shown in Fig. 1.7.

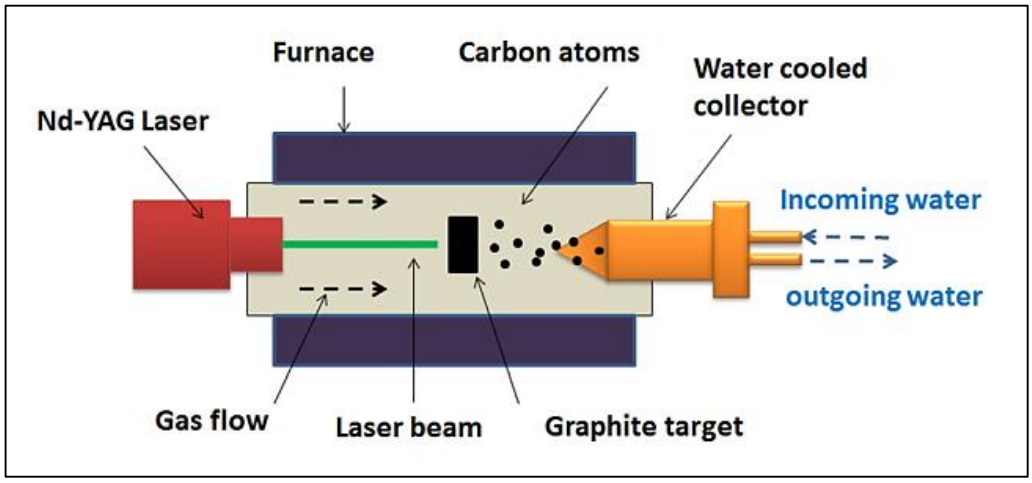

Figure 1.7 Schematic of laser ablation synthesis method[50].

Since the solid graphite target is vaporized at the atomic level, a highly energetic laser pulse is required[51-53]. The CNT diameters can be controlled by varying the furnace temperature, gas flow rate, and metal catalyst[52-56]. An excellent production rate of SWCNTs at ~ 1.5 g/hr was reported by Eklund *et al.*[57] using an ultrafast laser pulse. If laser pulses run at maximum power, the production rate increases to ~ 45 g/hr. In CO_2 laser ablation, SWCNT with a 5 g/hr production rate was obtained[58].

1.7.2 ARC DISCHARGE

In an electric arc-discharge method[59], the arc is produced in Helium or Argon inert atmosphere at high temperature and low pressure (100-1000 Torr)[60] using low voltage and high current power source between two graphite electrodes in a reactor. The schematic of the arc discharge method is displayed in Fig. 1.8.

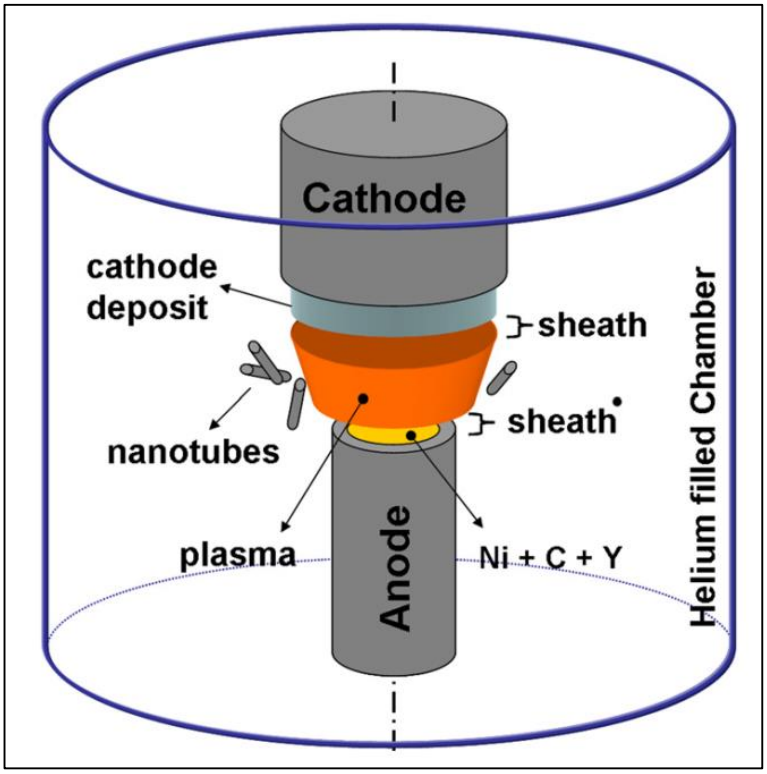

Figure 1.8 Schematic of arc discharge synthesis method[61].

The anode is filled with a mixture of metallic catalyst (commonly Fe or Co) and graphite powder. When a high current is passed through an anode and cathode, the plasma of He gas created by large currents evaporates the carbon atoms and deposits them at the cathode surface in the form of 1D CNTs. This method produces a large number of SWCNTs along with MWCNTs and fullerenes. The presence of hydrogen in the growth atmosphere produces a high crystalline product. Due to high growth temperature, the technique produces crystalline CNTs with a high yield, but it is not easy to produce aligned CNTs. Bethune *et al.*[62] have generated SWCNT as soot when a graphite rod used as an anode was doped with catalysts such as iron (Fe) or cobalt

(Co). SWCNTs were produced at an immense scale by Journet *et al.*[63] using this method and attained gram quantities. Using 1 at. % Y and 4.2 at. % Ni as catalyst, SWCNT yield was obtained between 70–90%.

1.7.3 THERMAL CHEMICAL VAPOUR DEPOSITION (TCVD)

In a classic thermal chemical vapor deposition (CVD) process, heat is the leading cause of chemical reactions; thus, it is frequently denoted as thermal CVD (TCVD)[64]. In catalytic CVD (CCVD), the decomposition of gaseous species over the catalytic particle surface supports the synthesis. A catalyst film is deposited over the substrate, and under high temperature, it fragments into nanoparticles over which hydrocarbon gas decomposes, diffuses, and gives rise to nanostructures upon saturation of carbon atoms over the catalysts[65]. The catalysts are generally heated from the temperature range 750 ^{O}C –1200 ^{O}C for the synthesis of nanostructures. The applied heat energy (from high temperatures) fragments the metal catalyst film into many catalyst nanoislands or particles, which act as the seeds for the nanostructure growth. Fe, Co, Ni, or a combination supported on oxides are commonly used as catalysts in CVD to synthesize CNTs[66]. Fig. 1.9 shows the schematic of the thermal CVD system. The following steps are involved in the growth of nanostructures through TCVD:

a. The hydrocarbon gas (carbon-bearing gas like acetylene or methane) decomposes and gets adsorbed onto the catalyst surface to create carbon and hydrogen species via various intermediary processes.
b. These carbon species diffuse over the surface and bulk of catalyst particle, and upon saturation of catalyst with carbon, carbon starts to precipitate out from the heated surface of the catalyst due to temperature gradient.
c. This precipitation gave rise to tubular layers of carbon nanotubes over the catalyst surface, and added carbon species are incorporated into the growing graphitic layers.
d. A surplus accretion of carbon species happens on the façade since the quantity of carbon here is extra to prevent blocking of the active surface. Thus, carbon species create a covering around the main body. The process continues until the façade of the metal catalyst is deactivated. This deactivation occurs due to the excess carbon

around the catalyst particle, which hinders the hydrocarbon species from reaching the catalyst and finally terminating the growth.

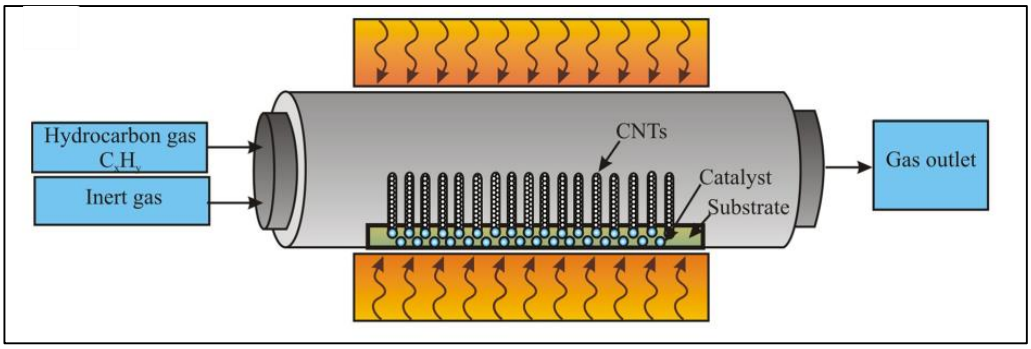

Figure 1.9 Schematic of chemical vapour deposition method[67].

Furthermore, the catalyst would either be found at the tip of CNT or the base during the growth, depending upon the interaction between catalyst and substrate surface[68]. The contact angle between the catalyst and substrate at constant operating conditions such as temperature and applied power describes their interaction. The large contact angle between catalyst and substrate results in strong interaction, and the catalyst remains anchored to the substrate; hence, the catalyst is found at the base of CNT (base-mode growth), while for small contact angles, this interaction is weak and catalyst lifts off from the substrate surface; hence catalyst is found at the tip of CNT (tip-mode growth). These growth modes are depicted in Fig. 1.10. Also, the layers of CNT, i.e., the number of graphitic walls, could be controlled by the system's temperature. For low system temperatures (600 ^{O}C – 900 ^{O}C), MWCNTs are formed, while for high system temperatures (900 ^{O}C – 1200 ^{O}C), SWCNTs are formed[69-76]. Along with temperature, the type of gaseous species and catalysts are other important parameters to control the growth of the nanotubes.

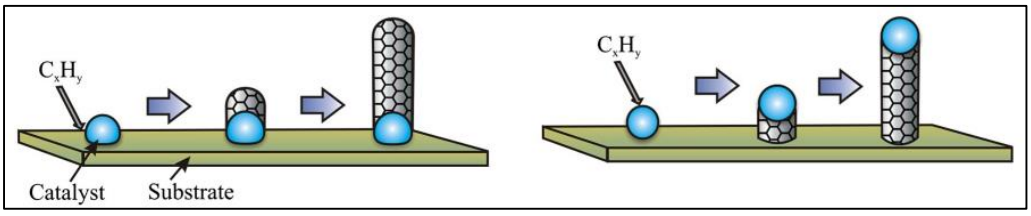

Figure 1.10 Base-mode and tip-mode growth of CNTs[77].

1.7.4 PLASMA-ENHANCED CHEMICAL VAPOR DEPOSITION (PECVD)

The CVD synthesis of CNTs involves temperatures greater than ~ 750°C as heat is the primary source for chemical reactions. This is far beyond the temperature limit of ~ 400–500°C fabrication in micro-electronics. Plasma-enhanced chemical vapor deposition (PECVD) synthesized CNTs at a much lower temperature, hence could also be referred to as low-temperature synthesis. The gaseous species are dissociated by the energy generated by plasma (a quasineutral state consisting of electrons, ionic species, neutrals, radicals, and others). The electric field generated by the plasma sheath aligns the CNTs in the direction normal to the substrate (along the electric field) hence vertically aligned CNTs (VACNTs), which will align the CNTs with the electric field lines. The catalyst deactivation rate, i.e., the creation rate of the amorphous carbon layer over the catalyst's active area, could be reduced due to the plasma etching of etchant species and ultra-long CNTs. Although, extreme etching could also be undesirable for CNT growth.

The high-temperature growth of CNTs via TCVD is a vapor-liquid-solid mechanism. The catalyst is in a liquid drop state for TCVD-CNT growth, and carbon species obtained from the gaseous species are dissolved into it. CNTs are precipitated from the supersaturated eutectic liquid. The activation energies required for synthesis in TCVD for ~ 700 ^{O}C is stated to be ~ 1.2 – 1.8 eV.

A low-temperature CNT growth mechanism is needed since the catalysts could stay solid at these temperatures. The activation energies required for low-temperature plasma-assisted CNT growth[78] are stated to be ~ 0.2 – 0.4 eV. This is nearby the activation energy of carbon atom surface diffusion[79] on Ni (0.3 eV). Carbon diffusion over the catalyst surface at low temperature was proposed as the rate-limiting step for plasma-assisted CNT growth[78].

PECVD method is used most frequently to synthesize carbon-based nanostructures because of its simplicity, controllability, and low temperature and pressure. As mentioned, the PECVD method uses plasma source energy for CNT synthesis. A few of these plasma sources are –

- radio frequency plasma-enhanced chemical vapor deposition (RF-PECVD)
- microwave plasma-enhanced chemical vapor deposition (MW-PECVD)
- inductively coupled plasma-enhanced chemical vapor deposition (IC-PECVD)
- direct current plasma enhanced chemical vapor deposition system (DC-PECVD)

The electric field strength in the plasma sheath increases with the increase in input power, which causes highly energetic ion bombardments. Powerful ionization in the locality of electrodes in PECVD occurs when the ion strikes the electrodes, and secondary electrons are produced and accelerated by the electric field into the plasma sheath. This intense plasma persuades plasma heating of catalyst and damage nanotubes. Thus, the plasma significantly influences CNT synthesis, and the detrimental ion substrate bombardment should be minimalized. Luo *et al.*[80] explored the ion bombardment effects and produced high-quality VACNTs in a plasma sheath using capacitively coupled RF-PECVD by enhancing the plasma parameters such as input power and pressure. In a primary ion space-charge-limited model[81], the plasma ion flux (n_{ion}) and ion energy (E_{ion}) are associated with gas pressure (P) and sheath voltage (V) in the following way-

$$E_{ion} \propto V^{4/5} P^{-1/2} \tag{1.7}$$

$$n_{ion} \propto V P^{3/4} \tag{1.8}$$

The increase in plasma power at a fixed pressure increases the ion flux impacting nanotubes; however, the ion energy is moderately increased. Contrastingly, the pressure and plasma sheath vary at constant plasma power $V \propto P^{1/2}$. The ion flux and energy varies as $E_{ion} \propto P^{-1/10}$ and $n_{ion} \propto P^{5/4}$, suggesting that ion etching is dominated by ion flux. Hence, reducing the incoming ion flux is necessary to synthesize high-quality nanotubes in a plasma sheath. Luo *et al.*[80] also revealed that nanotubes resisted ion etching at higher synthesis temperatures (more than 600 °C).

1.7.4.1 MW-PECVD

For MW-PECVD, a high frequency up to 2.45GHz is used to generate plasma. This high-density plasma produces highly energetic electrons that increase the gaseous species' dissociation. The technique dissociates atomic hydrogen to create hydrogen radicals which help in the effective etching of amorphous carbon species and promotes the formation of CNT[65]. In this method, plasma is created at high MW power and low pressures, or the plasma becomes unstable. Srivastava *et al.*[82] synthesized bamboo-like nanotubes that were deposited by MW-PECVD setup and also studied the effect of compositions of gases on the CNT growth and morphology. It was perceived that CNT growth and morphology could be controlled by gaseous plasma composition. The schematic diagram of the MW-PECVD system is shown in Fig. 1.11.

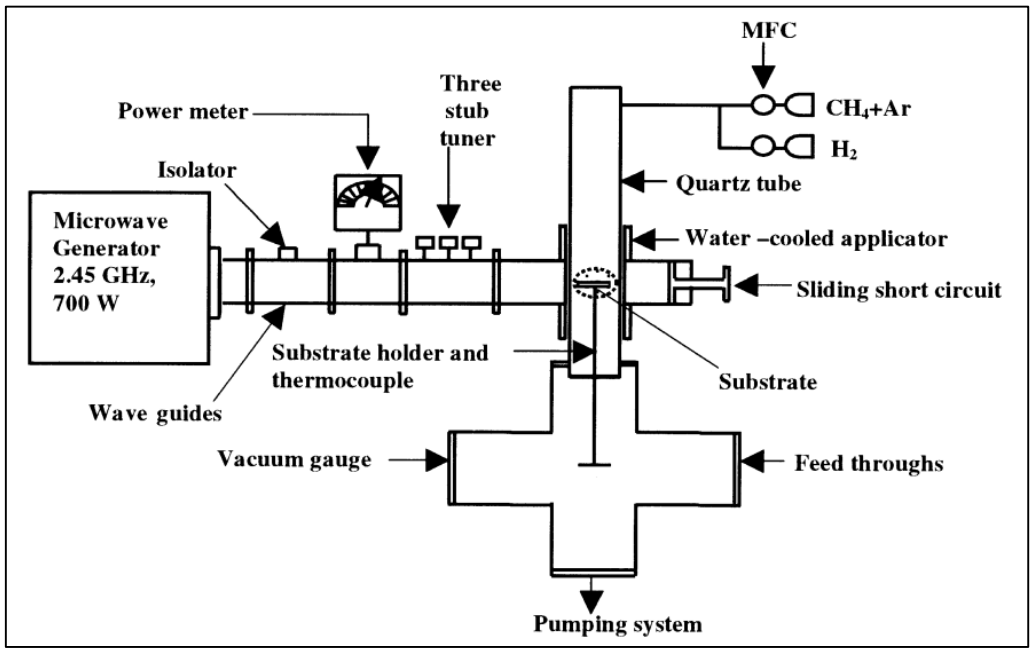

Figure 1.11 Schematic of MW-PECVD setup[83].

1.7.4.2 DC-PECVD

DC-PECVD synthesis of vertically aligned carbon nanostructures has been realized on two geometric setups [see Fig.1.12 & Fig.1.13]. First is the parallel plate method in which dc voltage between cathode and anode at low-pressure gas dissociates the gaseous species. This gaseous ionization is gas composition, pressure, and electrode distance dependent[84]. The substrate is either placed over the cathode or serves as the cathode itself. The cathode sheath electric field accelerates the ions towards the substrate and exerts the alignment force in the normal to the substrate. The second is the pin-to-plate method, which uses a non-uniform plasma source with asymmetric electrodes, i.e., tungsten tip and planar substrate. Merkulov *et al.*[64] have successfully prepared vertically aligned carbon nanofibres using dc-PECVD. This method results in the non-uniformity in the substrate's morphology and structure of carbon nanostructures. The requirement of a conductive substrate is the main disadvantage of this technique.

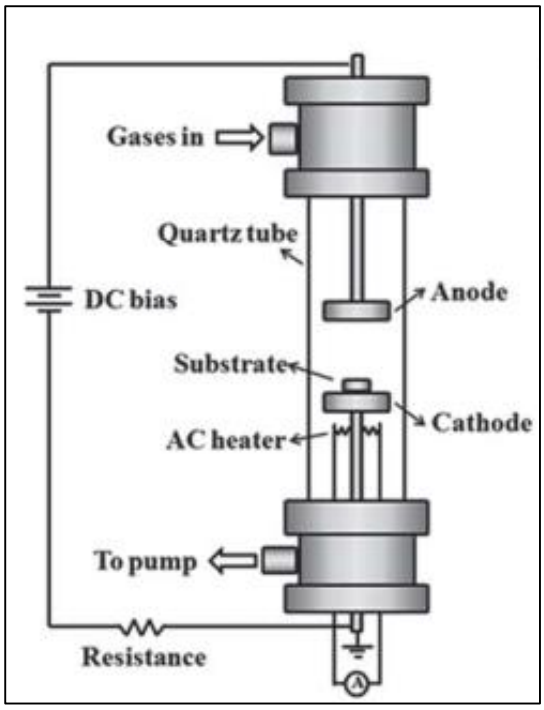

Figure 1.12 Schematic of parallel plate DC-PECVD setup[85].

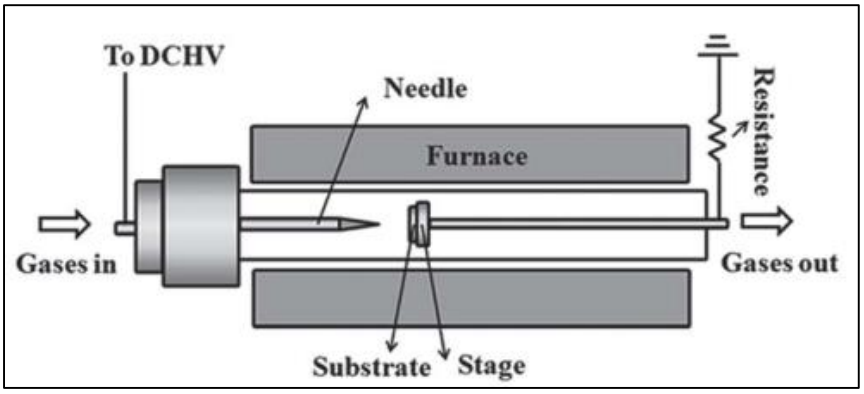

Figure 1.13 Schematic of pin to plate DC-PECVD setup[85].

1.7.4.3 RF-PECVD & IC-PECVD

Due to the limitations of DC-PECVD, the substrate placed over one electrode is attached to a radio frequency (13.56 MHz) voltage source to generate plasma. RF-PECVD technique has two types - inductively coupled RF-PECVD and capacitively coupled RF-PECVD. In the former technique, inductive coils connected to an RF generator are the plasma source, and two types of coils are used as the coil antenna; planar and cylindrical. The time-varying magnetic field is generated via a time-varying current around the coil. This induces an electric current in the gas, which dissociates it. Using magnetron-type RF plasma, Hirata *et al.*[86] synthesized nanostructures similar to nanofibres grown by DC-PECVD. Two types of RF-PECVD used are capacitively coupled RF-PECVD and inductively coupled RF-PECVD. Using IC-PECVD, CNTs are synthesized by Delzeit *et al.*[87], free-standing nanofibres by Caughman *et al.*[88], Honda *et al.*[89] and Lee *et al.*[90]. IC-PECVD is preferred over the capacitively coupled PECVD due to the creation of high-density plasma. RF-PECVD synthesis of vertically aligned carbon nanostructures has been depicted in Fig. 1.14.

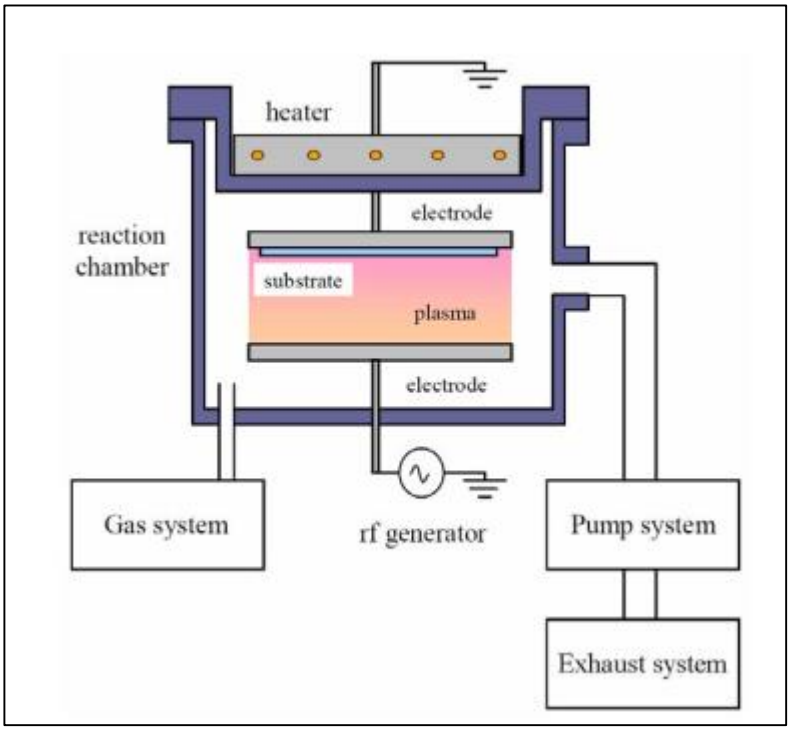

Figure 1.14 Schematic of RF-PECVD setup[91].

1.8 PLASMA AND PLASMA SHEATH

Definition: Plasma can be considered a quasineutral gas consisting of ions, electrons, neutrals species, and others.

Plasma is one of the naturally occurring states of matter in our universe apart from solid, liquid, and gas. The thermal energy of the atoms/molecules and the interparticle binding energy decides the state of matter. The binding energy of the particles is strongest in solids, weakest in liquids, and nearly insignificant in gases. Upon heating, the thermal energy of particles in solids overcomes the potential energy, bonds break, and phase transition from solid to liquid. Similarly, upon heating a liquid, a gaseous state is attained. When the gaseous state is heated to very high temperatures (10,000 ^{O}K or above), the atomic species of the gas gain enormously high thermal energy and collide with each other, thus kicking out electrons from the atoms. The resultant state consists of electrons, ions, neutrals, and other radical species, known as plasma or ionized gas. Although not every ionized gas can be referred to as plasma, certain

conditions known as quasineutrality and collective behaviour[92] need to be fulfilled for it to be called plasma. The condition of quasineutrality describes the state when ion number density and electron number density are at equilibrium in plasma of length more than the Debye length (λ_D), i.e., $l \gg \lambda_D$. The characteristic distance over which the potential due to a charge inside plasma can be shielded out is known as Debye length $\lambda_{D,}$ which is related to the electron density (ne) and temperature (T) as-

$$\lambda_D = \left(\frac{\varepsilon_0 k_B T_e}{n_e e^2} \right)^{1/2} \tag{1.9}$$

This quasineutrality exists everywhere except at the boundary/wall if there is a surface in contact (like substrate) in a PECVD reactor. Since the plasma is generated by heating the gas or utilizing electrical energy, it is in a high-energy state but is neutral. Within the bulk of plasma, no space–charge region is formed due to quasineutrality. The electrons owing to a higher temperature, and lower mass than ions, are much more mobile in plasma and thus have more significant fluxes. Hence, the materials interacting with the plasma will acquire a negative charge with reference to the plasma potential. In plasma sheath, the density of positively charged ions is slightly more significant than that of electrons. A pre-sheath region is formed, which is relatively positively charged due to the scarcity of electrons. Thus, an electric field is set up between the bulk plasma and the walls, providing a net flux of positive charge to the walls and offering the barrier for the electrons. This plasma sheath region is represented in Fig.1.15.

For the synthesis of nanostructures via the PECVD method, the formation of this plasma sheath is crucial because the substrate or surface of the material also interacts with the plasma. Besides this, nanostructures grow in this plasma sheath region. A negatively biased substrate is placed beneath the bulk plasma to induce a strong electric field between the bulk plasma and substrate, forming the vital plasma sheath region. A few of the parameters known to describe the plasma sheath region are sheath width

(λ_S), ion current density (J_{ij}), electron current density (J_e), Bohm velocity of ions (u_{ij}), thermal velocity of electrons (u_{th}), and plasma sheath electric field (E_0).

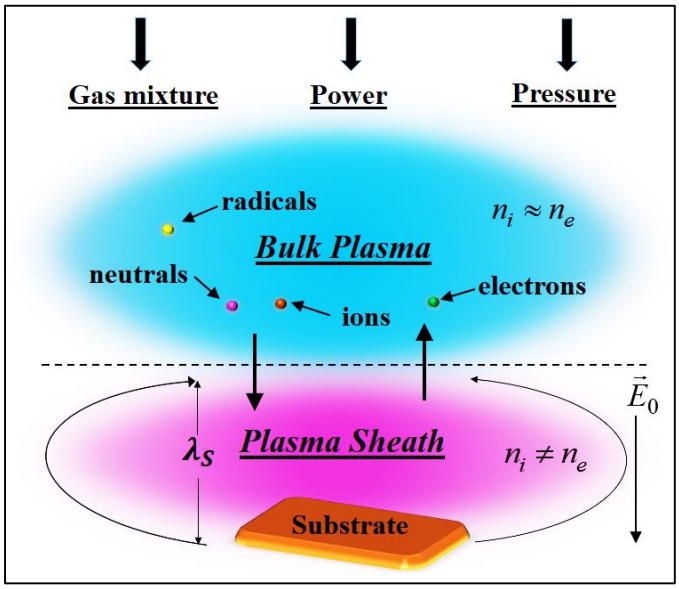

Figure 1.15 Schematic of plasma sheath region[93].

$$\lambda_s = \left\{ \frac{2}{3} \left(\frac{2e\varepsilon_0^2}{m_{ij}} \right)^{1/4} \frac{U_S^{3/4}}{J_{ij}^{1/2}} \right\} \tag{1.10}$$

$$J_{ij} = n_{ij} e u_{ij} \tag{1.11}$$

$$J_e = \left(\frac{-n_e e u_{th}}{4} \right) \tag{1.12}$$

$$u_{ij} = \left(\frac{k_B T_e}{m_{ij}} \right)^{1/2} \tag{1.13}$$

$$u_{th} = \left(\frac{8 k_B T_e}{\pi m_e} \right)^{1/2} \tag{1.14}$$

$$E_0 = \left\{ \left(\frac{6m_{ij}}{e\varepsilon_0^2} \right)^{1/3} J_{ij}^{2/3} \lambda_s^{1/3} \right\} = \left\{ 2 \left(\frac{k_B e}{2\varepsilon_0^2} \right)^{1/4} n_{ij}^{1/2} T_e^{1/4} U_S^{1/4} \right\} \qquad (1.15)$$

In the Eqs. (1.9) – (1.15), n_{ij}, n_e represents the number density of ions and electrons; m_{ij}, m_e represents the mass of ions and electrons; T_e is the electron temperature, and U_S is the bias applied at the substrate, respectively.

1.9 NUCLEATION AND GROWTH OF CARBON NANOTUBES

For nanostructure growth to proceed in a PECVD process, plasma pre-treatment of a metal catalyst thin film is essential. A catalyst thin film deposited over the substrate for the catalytic method transforms into catalyst nanoparticles (via plasma processing or etching) which act as the seed layer, essential for the nucleation of CNTs. Numerous experiments determine that the catalyst's nature and size govern the nanotube's growth, which can be altered under varying plasma conditions. The transition metals, namely iron (Fe), cobalt (Co), and nickel (Ni), can be used as a pure metal catalyst for CNT synthesis. A metal nanofilm pre-deposited over a substrate is etched in the presence of etchant plasma to obtain metal catalyst nanoparticles. The heavy bombardment of highly energetic etchant species leads to the thin film's physical sputtering and chemical etching, which ultimately results in the fragmentation of the catalyst film into the many catalyst particles. A schematic representation of plasma-assisted CNT growth is represented in Fig. 1.16. This pre-treatment can alter the surface with preferred characteristics by adjusting the plasma chemistry and operating conditions. The initialization of nanotube growth starts on the facet of these catalyst nanoparticles required to disintegrate hydrocarbon species. The CNT growth over the catalyst-substrate surface initiates via carbon species generated on the active surface of the catalyst by different surface processes, viz., adsorption and desorption of hydrocarbon and hydrogen species, diffusion of carbon atoms on the surface and bulk of catalyst particle, thermal dehydrogenation of hydrocarbon species, and many others. The carbide formation allows the decomposition-segregation of carbon atoms to penetrate

through the nanoparticle and regenerate into graphitic cylinders. Simultaneous vertical alignment of CNT during the growth process owing to various plasma operating parameters. The consistent sticking of neutral species on the growing nanotube leads to catalyst poisoning, eventually ceasing the growth process.

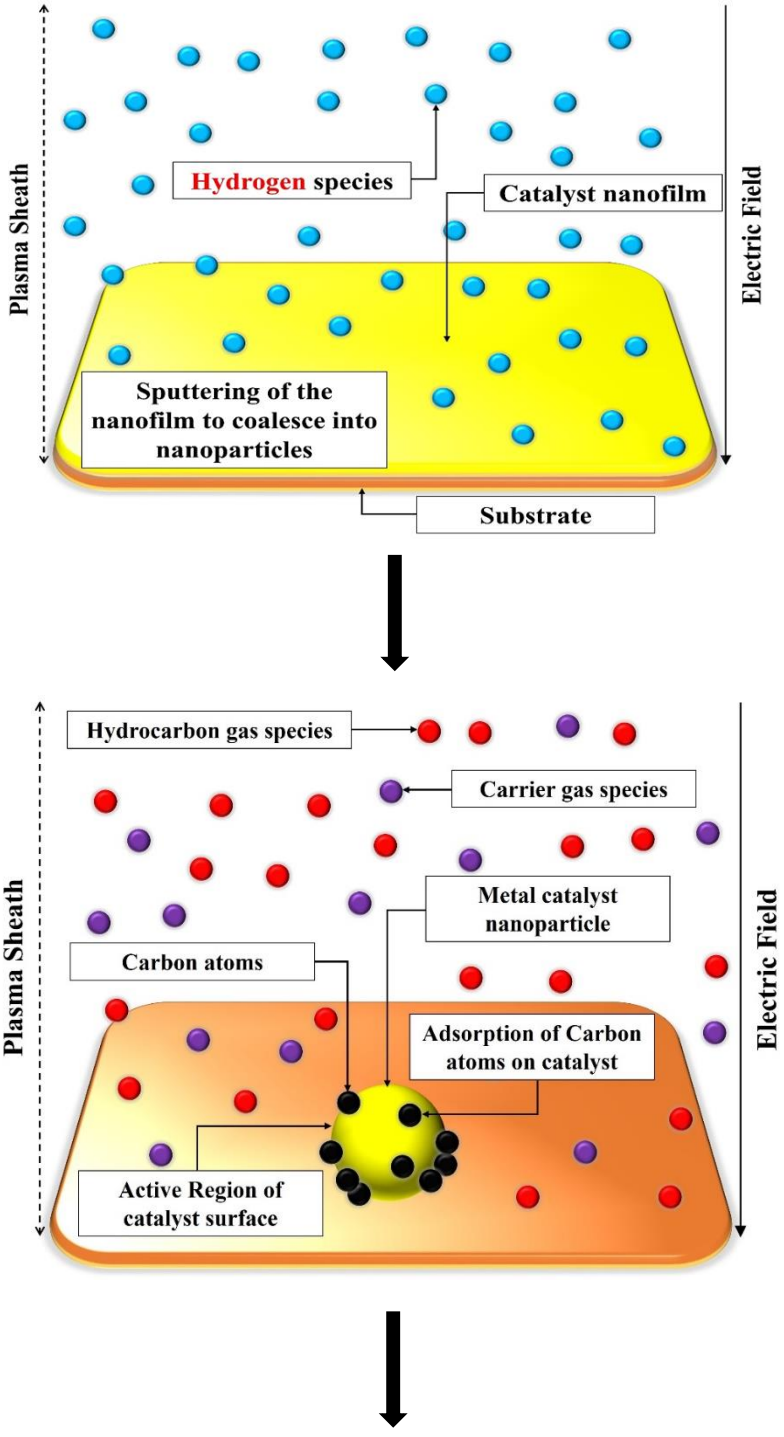

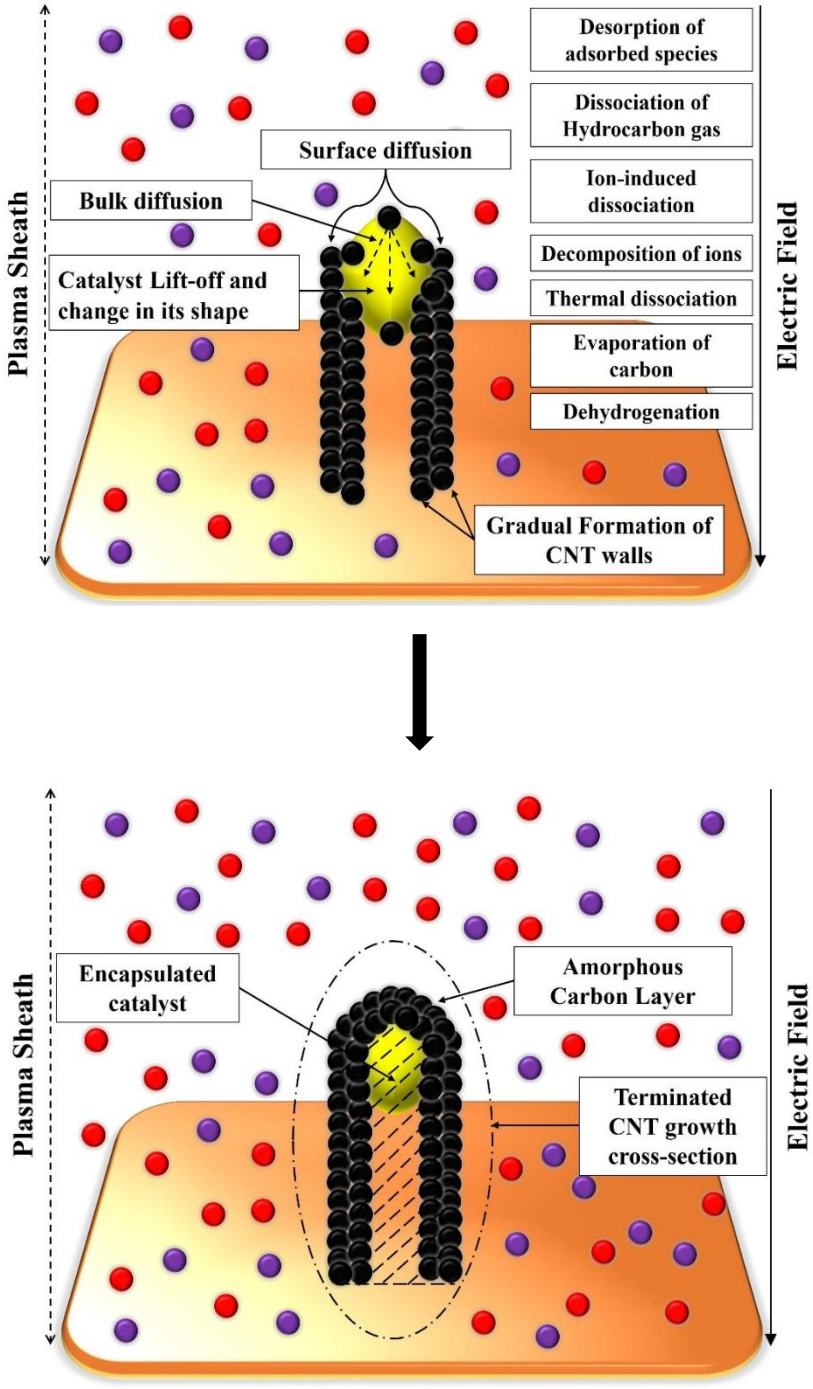

Figure 1.16 Schematic representation of CNT growth in plasma.

1.10 REVIEW OF THE EFFECT OF PLASMA PROCESS PARAMETERS

In-depth knowledge of plasma process parameters' effect in the PECVD method is essential for controlling and modifying the growth of CNTs. These process parameters include the source gases, plasma power, pressure, temperature, type of catalyst and substrate involved, etc. All these factors significantly affect the growth of CNTs.

Many research groups observed the effect of various parameters, including gas composition, nature of catalyst precursor, and various plasma parameters, influence the growth characteristics of CNTs. Few of the literature on these parameters and their impact on CNT growth are mentioned below.

Bower *et al.*[94] studied the electric field effect of carbon nanotube alignment unambiguously in an MW-PECVD chamber with acetylene and ammonia as source gases. Primarily, when the plasma was created in the chamber, vertical MWCNTs were obtained. On turning off the plasma and continuing with CNT growth (i.e., in a TCVD mode), the obtained CNTs were unaligned and curly. Upon further investigation, they stated that CNTs always oriented themselves normally to the substrate surface irrespective of the substrate shape, orientation or position. After their findings, extensive research has been conducted to investigate the plasma-dependent orientation of PECVD-grown CNTs, which is revealed to be better than that obtained from thermal CVD.

Merkulov *et al.*[95] concluded experimentally how the presence of a catalyst at the tip of CNF is vital for its alignment in plasma. The interaction of the force applied to the CNF tip where the catalyst is located favours the vertically aligned growth. They also suggested that the crowding effect is essential for the alignment mechanism and the electric field effect.

Bocharov *et al.*[96] indicated the electric field effect on the alignment and orientation of CNT. They concluded that the electric field created owing to the potential difference between the nanotube and the substrate affects the alignment of CNT to a certain degree.

Pal *et al.*[97] successfully performed experiments growing arrays of CNT in dc glow discharge and showed that the interaction of CNTs with the electric field influences its growth.

Zhang *et al.*[98] experimented with the growth of chemical vapour deposition grown CNT with the electric field and concluded the effects of large aligning torques and forces on nanotube orientation.

Huang *et al.*[99] and Lee *et al.*[100] investigated the growth of CNTs experimentally for different catalyst nanoparticles, namely nickel, iron, and cobalt. They stated that the catalyst nanoparticles affected the diameter of CNTs and their growth rate.

Kim *et al.*[101], Lee *et al.*[102], Lee *et al.*[103], Chen *et al.*[104,] and several others investigated the effect of different plasmas on the growth of carbon nanotubes in PECVD. The experiments were carried out using various compositions of plasmas, and their results were presented.

Delzeit *et al.*[105] revealed that on increasing the applied substrate bias, MWCNTs could transition to MWCNFs. Also, on increasing argon dilution, MWCNFs can transition to MWCNTs. They discussed that in these cases, the variation in atomic hydrogen around the vicinity of the wafer could be accounted for the perceived transition. It is crucial to know that the substrate temperature is not fixed in DC-HFCVD (direct current – hot filament CVD). When the substrate bias and plasma power increase, the substrate temperature also increases, which can cause the reorganization of catalytic species into large bunches. This change could alter the finally obtained CNT morphology.

On comparing the results of the PECVD in the literature, it is discovered that initially, the growth rate is 0.5–6 µm/min. The PECVD growth rate is usually lower than that of TCVD, which could be a consequence of the atmospheric pressure operation of TCVD.

For 3 Torr pressure, 100 W IC power, 200 W RF power at the substrate, and a 10 nm Fe catalyst over a Si substrate, the effect of deposition temperature on the synthesis of MWCNT in a C_2H_4 + H_2 mixture is studied. At temperatures lower than 600 ^{O}C, diminished growth appears; beyond 700 ^{O}C, strong growth appears. A careful reveals

that the average MWCNF diameter increases with the rise in deposition temperature. Also, this temperature rise could reorganize the catalytic species into big bunches. The average MWCNF length decrease with increasing temperature. Hence, it can be said that thicker carbon fibres grow slower.

Baker *et al.*[106] showed an analysis depicting the carbon flux leaving the catalyst's growth side of the catalyst, and thus, the CNT growth rate depends inversely on the particle radius. This radius also depends on the thickness of catalyst film, substrate temperature, ionic species energy, etc. For similar temperature or applied bias, thicker catalytic particles forms thicker and smaller MWCNFs. A 0.5 nm Ni catalyst was used for this study, and a decent growth was obtained. Although, in the absence of such a catalyst, no such growth was observed. At low quantities of hydrocarbon gases in plasma mixtures (CH_4, C_2H_2, C_2H_4 and other stable species for catalytic dissociation) which is rate-limiting, leads to in CNT growth rate[107]. However, extremely high hydrocarbon content can adversely affect CNT growth due to the generation of excessive amorphous carbon species.

1.11 ORGANIZATION OF THESIS

The aims of the thesis are highly motivated by the vital interest of theoretical and experimental areas towards a better understanding of the PECVD technique to produce the carbon nanostructure, namely Carbon Nanotubes (CNTs) of high quality in a controllable environment. Many researchers have tried to investigate the plasma processing of these carbon nanotubes and the relation between the plasma parameters and the CNT nucleation and growth. Several issues raised regarding the effect of plasma parameters on the growth, structure and field enhancement factor have so far gone unexplored (experimental as well as theoretical). The study has provided a deeper insight into the physics of carbon nanotubes in the presence of plasma environments and the technical feasibility of carbon nanotubes. Our analytical model and the results from numerical simulations would help us understand the experimental results from several leading experimental groups. This study would also pave the way for highly efficient CNTs-based field emitters.

- **Chapter 2** – The alignment and catalyst-assisted growth mechanism of carbon nanotubes in an H_2-diluted methane plasma are demonstrated in this chapter. The consequence of plasma parameters (plasma density and temperature) and substrate potential on the plasma sheath electric field are examined. The repercussions of the plasma sheath electric field in establishing the alignment force and its effect on the growth of aligned carbon nanotubes in the plasma are studied by taking into contemplation the steady-state fluid equations, the kinetics of the plasma sheath, charged species dynamics (ions, electrons, and others) and neutrals in the complex plasma, catalyst kinetics, carbon and hydrogen species generation on the catalyst surface and including other processes responsible for the CNT growth in plasma. Considering the initial boundary conditions and plasma glow-discharge factors determined experimentally for the model, the theoretical model is solved. The result reveals the dependence of CNT alignment on the force applied by the sheath electric field at the CNT tip, where the catalyst is located. This force is a consequence of the electric field that depends on various factors and the applied substrate bias voltage. This alignment force is also CNT radius and length-dependent and constantly adjusts during the growth. The results of the study are compared to the available experimental data, which accredit the proposed mechanisms.

- **Chapter 3** – In this chapter, a computational model was developed and studied for the plasma pre-treatment of nanofilms, and the effect of process parameters, i.e., power, pressure, gas flow and plasma temperature, was deliberated. We have also deliberated different catalyst nanoparticles and their consequence on nanotube growth, considering a theoretical model which includes the dynamics of catalyst nanoparticles, plasma sheath, and plasma species (ions, neutrals, and electrons) and the generation of atomic C and H species on the catalyst surface, taking into contemplation several processes essential for the plasma-assisted CNT growth. The theoretical study aims to improve the understanding of using different catalysts for various scientific fields by unravelling their effect on CNT growth. The pre-treatment effects on the catalyst nanofilm for nanoparticle formation are deliberated. The effects of increasing catalyst nanofilm thickness on catalyst size and density

were attained. Different metal catalysts (Ni, Fe, and Co) were studied for their influence on CNT growth under the same plasma conditions.

- **Chapter 4** – In this chapter, a computational study is modelled to investigate a vertically aligned carbon nanotube (VACNT) array in plasma and structures its growth based on the variation of plasma operating conditions and process parameters. We have investigated the consequence of plasma concentration, power, pressure, and substrate temperature on the aspects of the VACNT array. Furthermore, the amorphous carbon deposition between the CNTs of the array is also examined. As field emission is one of the most outstanding applications of the VACNT array, the field enhancement factor for the array is also deliberated and optimized. The results are modelled, considering the balance of plasma species, plasma and CNT energy exchange, hydrocarbon and hydrogen generation over the catalyst nanoparticle, CNT array growth, and carbon deposition over the substrate between CNTs in VACNT array growth using plasma-enhanced chemical vapor deposition (PECVD). The model is numerically solved by deliberating the experimental literature's initial conditions and plasma parameters. The aspects of an array, i.e., its length and average CNT diameter, can be optimized as desired by altering the operating conditions and glow discharge plasma parameters. The influence of array aspects on the field emission properties is also observed. The results of the study are in fair agreement with the available experimental data.

- **Chapter 5** – This chapter consists of three different plasma environments. In case 1, the plasma-based model analyses the effect of hydrogen ion density and changing gas ratio on the growth of carbon nanotubes. The first environment considers a model composed of electrons, neutral atoms, and positively charged ions of methane CH_4 and hydrogen H_2, while the second considers acetylene C_2H_2 and hydrogen H_2. Using the model described in the previous chapter, the first-order simultaneous differential equations are solved using the initial conditions determined experimentally and plasma glow discharge parameters. It was analyzed that on increasing hydrogen ion density, nanotube radius decreases due to a decrease in deposition rate. It can also be observed that the hydrocarbon density decreases with

increasing hydrogen ion densities, which endorses the decrease in CNT radius. The results indicate the decline in the CNT radius with an increasing gas ratio. Also, the height of CNT decreases with the increasing gas ratio. With the increasing gas ratio, i.e., as the concentration of C_2H_2 increases in plasma, nanotubes of lesser radius and height were produced as an abundance of carbon atoms are produced compared to hydrogen atoms, and the amorphous carbon layer which hinders the CNT growth generates rapidly. The plasma-based model analyses the consequence of different carrier gases on PECVD-CNT growth for the third plasma environment. The investigative model deliberates a plasma mixture of C_2H_2 as the hydrocarbon source gas; NH_3, N_2, or Ar as carrier gases. The effect of different carrier gases on the CNT structure was compared. It was concluded that while Ar promotes the CNT growth, NH_3 and N_2 diminish the growth of carbon nanotubes in plasma.

- **Chapter 6** – The last chapter incorporates the thesis's conclusion and future research scope. The research work in the present thesis is not limited to the growth of one-dimensional nanostructures in plasma; instead, it can be expanded to study nanostructures of various dimensionalities. This chapter also includes the future work that can be performed to study plasma-assisted growth of nanotubes more thoroughly and efficiently to make its production more accessible and enhance its applications in various fields.

REFERENCES

[1] J. L. Delgado, M. A. Herranz, and N. Martín, Journal of Materials Chemistry **18**, 1417 (2008).

[2] A. Mostofizadeh, Y. Li, B. Song, and Y. Huang, Journal of Nanomaterials **2011**, 685081 (2011).

[3] W. H. Kroto, J. R. Heath, S. C. O'Brien, R. F. Curl, and R. E. Smalley, Nature **318**, 162 (1985).

[4] S. Iijima, Nature **354**, 56 (1991).

[5] M. S. Dresselhaus, G. F. Dresselhaus, and P. C. Eklund, *Science of Fullerenes and Carbon Nanotubes*, 1st Edition (Academic Press San Diego, CA, 1996).

[6] D. M. Guldi and N. Martín, *Carbon Nanotubes and Related Structures*, 1st Edition (Wiley-VCH, Weinheim, 2010).

[7] M. Terrones, W. K. Hsu, H. W. Kroto, and D. R. M. Walton, Topics in Current Chemistry **199**, 189 (1999).

[8] S. K. Pati, T. Enoki, and C. N. R. Rao, *Graphene and Its Fascinating Attributes*, 1st Edition (World Scientific, Hackensack, NJ, 2011).

[9] A. Thess, R. Lee, P. Nikolaev, H. J. Dai, J. Robert, C. H. Xu, Y. H. Lee, S. G. Kim, A. G. Rinzler, D. T. Colbert, G. E. Scuseria, D. Tomanek, J. E. Fischer, and R. E. Smalley, Science **273**, 483 (1996).

[10] A. Al-Jumaili, S. Alancherry, K. Bazaka, M. V. Jacob, Materials **10**, 1066 (2017).

[11] V. I. Merkulov, A. V. Melechko, M. A. Guillorn, D. H. Lowndes, and M. L. Simpson, Chemical Physics Letters **361**, 492 (2002).

[12] B. Trauzettel and D. Loss, Nature Physics **5**, 317–318 (2009).

[13] *https://tuball.com/articles/multi-walled-carbon-nanotubes*

[14] A. Hirsch, Angew. Chem. **114**, 1933 (2002).

[15] V. Choudhary, and A. Gupta, in *Carbon Nanotubes – Polymer Nanocomposites* by S. Yellampalli, IntechOpen (2011), pp. 65.

[16] L. Forro and C. Schnonenberger, in *Carbon Nanotubes Synthesis, Structure, Properties and Applications* by M. S. Dresselghaus, G. Dresselhaus, and P. Avouris (Springer-verlag, Newyork, 2001), pp. 329.

[17] C. Schonenberger, A. Bachtold, C. Strunk, J. P. Salvetat, and L. Forro, Appl. Phys. A **69**, 283 (1999).

[18] W. A. De Heer and R. Martel, Phys. World **13**, 49 (2000).

[19] S. Berber, Y. K. Kown, and D. Tomanek, Phys. Rev. Lett. **84**, 4613 (2000).

[20] P. Kim, L. Shi, A. Majumdar, and P. L. McEuen Phys. Rev. Lett. **87**, 215502 (2001).

[21] J. Hone, B. Batlogg, Z. Benes, A. T. Johnson, and J. E. Fischer, Science **289**,1730 (2000).

[22] A. Mizel, L. X. Benedict, M. L. Cohen, S. G. Louie, A. Zettl, N. K. Budraa, and W. P. Beyermann, Phys. Rev. B. **60**, 3264 (1999).

[23] W. Yi, L. Lu, Zhang Dian-lin, Z. W. Pan, and S. S. Xie, Phys. Rev. B **59**, R9015 (1999).

[24] B. Bhushan, *Springer Handbook of Nanotechnology* (Springer - Verlag., 2007).

[25] R. Saito, G. Dresselhaus, M. S. Dresselhaus, *Physical properties of carbon nanotubes* (Imperial College Press, London, 1998).

[26] K. E. Geckelar and E. Rosenburg, *Functional Nanomaterials* (American Scientific Publishers, California, 2006).

[27] E. W. Wong, P. E. Sheehan, and C. M. Lieber, Science **277**, 1971 (1997).

[28] M. F. Yu, O. Lourie, M. J. Dyer, K. Moloni, T. E. Kelly, and R. S. Ruoff, Science **287**, 637 (2000).

[29] M. F. Yu, B. S. Files, S. Arepalli, and R. S. Ruoff, Phys. Rev. Lett. **84**, 5552 (2000).

[30] H. Bates, O. Brand, G. Fedder, C. Hierold, J. Korvink, and O. Tabata, *Enabling Technology for MEMS and Nanodevices* (Weinheim, Germany, Wilely-VCH, 2004).

[31] *Properties of Stainless Steel* by Australian Stainless Steel Development Association.

[32] W. D. J. Callister, *Material Science and Engineering an introduction*, 6th Edition (Wiley, New York 2003).

[33] S. Huang, X. Du, M. Ma, and L. Xiong, Nanotechnology Reviews **10**, 1592 (2021).

[34] B. Gao, Chem. Phys. Lett. **327**, 69 (2000).

[35] R. Ma, B. Wei, C. Xu, J. Liang, and D. Wu, Sci. China Ser. E-Technol. Sci. **43**, 178 (2000).

[36] D. A. Walters, M. J. Casavant, X. C. Qin, C. B. Huffman, P. J. Boul, L. M. Ericson, E. H. Haroz, M. J. O'Connell, K. Smith, D. T. Colbert, and R. E. Smalley, Chem. Phys. Lett. **338**, 14 (2001).

[37] R. H. Baughman, Science **290**, 1310 (2000).

[38] A. C. Dillon, K. M. Jones, T. A. Bekkedahl, C. H. Kiang, D. S. Bethune, and M. J. Heben, Nature **386**, 377 (1997).

[39] P. Chen, X. Wu, J. Lin, and K. L. Tan, Science **285**, 91 (1999).

[40] A. Javey, J. Guo, D. B. Farmr, Q. Wang, E. Yenilmez, R. G. Goprdon, M. Lundstrom, and H. Dai, Nano Lett. **4**, 1319 (2004).

[41] A. P. Graham, G. S. Duesberg, W. Hoenlein, F. Kreupl, M. Liebau, R. Martin, B. Rajasekharan, W. Pamler, R. Seidel, W. Steinhoegl, and E. Unger, Appl. Phys. A **80**, 1141 (2005).

[42] M. Masud, A. A'ain, I. Khan, and N. Husin, Electronics **8**, 95 (2019).

[43] B. Q. Wei, R. Vajtai, and P. M. Ajayan, Appl. Phys. Lett. **79**, 1172 (2001).

[44] R. H. Fowler and L. Nordheim, Proc. R. Soc. London Ser. A **119**, 173 (1928).

[45] F. Giubileo, A. Di Bartolomeo, L. Iemmo, and G. Luongo, F. Urban, Appl. Sci. **8**, 526, (2018).

[46] T. M. Minea, S. Point, A. Granier, and M. Touzeau, Appl. Phys. Lett. **85**, 1244 (2004)

[47] K. B. K. Teo, M. Chhowalla, G. A. J. Amaratunga, W. I. Milne, G. Pirio, P. Legagneux, F. Wyczisk, D. Pribat, and D. G. Hasko, Appl. Phys. Lett. **80**, 2011 (2002).

[48] J. M. Bonard, N. Weiss, H. Kind, T. Stöckli, L. Forró, K. Kern, and A. Châtelain, Adv. Mater. **13**, 184 (2001).

[49] T. Guo, P. Nikolaev, A. Thess, D.T. Colbert, and R.E. Smalley, Chem. Phys. Lett. **243**, 49 (1995).

[50] F. Kazemizadeh, S. M. Bellah, and R. Malekfar, Journal of Laser Applications **29**, 042004 (2017).

[51] A. A. Puretzky, D. B. Geohegan, X. Fan, and S. J. Pennycook, Appl. Phys. A **70**, 153 (2000)

[52] R. Sen, Y. Ohtsuka, T. Ishigaki, D. Kasuya, S. Suzuki, H. Kataura, and Y. Achiba, Chem. Phys. Lett. **332**, 467 (2000)

[53] F. Kokai, K. Takahashi, M. Yudasaka, and S. Iijima, J. Phys. Chem. B **104**, 6777 (2000).

[54] S. Bandow, S. Asaka, Y. Saito, A. M. Rao, L. Grigorian, E. Richter, and P. C. Eklund, Phys. Rev. Lett. **80**, 3779 (1998).

[55] H. Kataura, Y. Kumazawa, Y. Maniwa, Y. Ohtsuka, R. Sen, and S. Suzuki, Carbon **38**, 1691 (2000).

[56] H. Kataura, A. Kimura, Y. Ohtsuka, S. Suzuki, Y. Maniwa, T. Hanyu, and Y. Achiba, Jpn. J. Appl. Phys. Part 2 **37**, L616 (1998).

[57] P. C. Eklund, B. K. Pradhan, U. J. Kim, Q. Xiong, J. E. Fischer, A. D. Friedman, B. C. Holloway, K. Jorgan, and M. W. Smith, Nano Lett. **2**, 561 (2002).

[58] A. P. Bolshakov, S. A. Uglov, A. V. Saveliev, V. I. Konov, A. Gorbunov, W. Pompe, and A. Graff, Diamond Relat. Mater. **11**, 927 (2002).

[59] E. G. Gamaly, and T. W. Ebbesen, Phys. Rev. B **52**, 2083 (1995).

[60] M. O'Connell, Carbon Nanotubes: Properties and Applications (CRC Press, Boca Raton, 2006).

[61] M. Kundrapu, J. Li, A. Shashurin and M. Keidar, J. Phys. D: Appl. Phys. **45**, 315305 (2012).

[62] D. S. Bethune, C. H. Kiang, M. S. De vries, G. Gorman, R. Savoy, J. Vazquez , and R. Beyers, Nature **363**, 605 (1993).

[63] C. Journet, W. K. Maser, P. Bernier, A. Loiseau, M. Lamy de la Chapelle, S. Lefrant, P. Deniard, R. Leek and J. E. Fischer, Nature **388**, 756 (1997).

[64] V. I. Merkulov, D. K. Hensley, A. V. Melechko, M. A. Guillorn, D. H. Lowndes, and M. L. Simpson, J. Phys. Chem. B **106**, 10570 (2002).

[65] A. V. Melechko, V. I. Merkulov, T. E. McKnight, M. A. Guillorn, K. L. Klein, D. H. Lowndes, and M. L. Simpson, J. Appl. Phys. **97**, 041301 (2005).

[66] M. L. Terranova, V. Sessa, and M. Rossi, Chem. Vap. Deposition **12**, 315 (2006).

[67] O. Zaytseva and G. Neumann, Chem. Biol. Technol. Agric. **3**, 17 (2016).

[68] R. T. K. Baker, Carbon **27**, 315 (1989).

[69] S. Karthikeyan, P. Mahalingam, and M. Karthik, Journal of Chemistry **6**, 756410, (2009).

[70] Z. B. He, J. L. Maurice, C. S. Lee, A. Gohier, D. Pribat, P. Legagneux, and C. S. Cojocaru, Carbon **49**, 435 (2011).

[71] H. Dai, A. G. Rinzler, P. Nikolaev, A. Thess, D. T. Colbert, and R. E. Smalley, Chem. Phys. Lett. **260**, 471 (1996).

[72] H. M. Cheng, F. Li, X. Sun, S. D. M. Brown, M. A. Pimenta, A. Marucci, G. Dresselhaus, and M. S. Dresselhaus, Chem. Phys. Lett. **289**, 602 (1998).

[73] B. C. Satishkumar, A. Govindaraj, R. Sen, and C. N. R. Rao, Chem. Phys. Lett. **293**, 47 (1998).

[74] J. H. Hafner, M. J. Bronikowski, B. R. Azamian, P. Nikolaev, A. G. Rinzler, D. T. Colbert, K. A. Smith, and R. E. Smalley, Chem. Phys. Lett. **296**, 195 (1998).

[75] J. Kong, A. M. Cassell, and H. J. Dai, Chem. Phys. Lett. **292**, 567 (1998).

[76] E. Flahaut, A. Govindaraj, A. Peigney, C. Laurent, A. Rousset, and C. N. R. Rao, Chem. Phys. Lett. **300**, 236 (1999).

[77] X. D. Wang, K. Vinodgopal and G. P. Dai in Perspective of Carbon Nanotubes by H. M. Saleh, Intechopen (2019).

[78] S. Hoffmann, B. Kleinsorge, C. Ducati, A. C. Ferrari, and J. Robertson, Diamond Relat. Mater. **14**, 1171 (2004).

[79] J. F. Mojica, and L. L. Levenson, Surf. Sci. **59**, 447 (1976).

[80] Z. Luo, S. Lim, Y. You, J. Miao, H. Gong, J. Zhang, S. Wang, J. Lin, and Z. Shen, Nanotechnology **19**, 255607 (2008).

[81] A. Godyak, R. B. Piejak, and B. M. Alexandrovich, IEEE Trans. Plasma Sci. **19**, 660 (1991).

[82] S. K. Srivastava, V. D. Vankar and V. Kumar, Thin Solid Films **515**, 1552 (2006).

[83] S. K. Srivastava, A. K. Shukla, V. D. Vankar, and V. Kumar, Thin Solid Films **492**, 124 (2005).

[84] F. Paschen, Ann. Phys. Chem. **273**, 69 (1889).

[85] Z. Bo, Y. Yang, J. Chen, K. Yu, J. Yan and K. Cen Nanoscale **5**, 5180 (2013).

[86] T. Hirata, N. Satake, G. H. Jeong, T. Kato, R. Hatakeyama, K. Motomiya, and K. Tohji, Appl. Phys. Lett. **83**, 1119 (2003).

[87] L. Delzeit, I. McAninch, B. A. Cruden, D. Hash, B. Chen, J. Han, and M. Meyyappan, J. Appl. Phys. **91**, 6027 (2002).

[88] J. B. O. Caughman, L. R. Baylor, M. A. Guillorn, V. I. Merkulov, D. H. Lowndes, and L. F. Allard, Appl. Phys. Lett. **83**, 1207 (2003).

[89] S. Honda, M. Katayama, K. Y. Lee, T. Ikuno, S. Ohkura, K. Oura, H. Furuta, and T. Hirao, Jpn. J. Appl. Phys., Part 2 **42**, L441 (2003).

[90] K. Y. Lee, M. Katayama, S. Honda, T. Kuzuoka, T. Miyake, Y. Terao, J. G. Lee, H. Mori, T. Hirao and K. Oura, Jpn. J. Appl. Phys., Part 2 **42**, L804 (2003).

[91] Jimmy Melskens, *Optimization of a protocrystalline hydrogenated amorphous silicon top solar cell for highest stabilized efficiency*, Masters Thesis, Delft University of Technology, Netherlands (2007).

[92] J. A. Bittencourt, *Fundamentals of Plasma Physics* (Springer-Verlag, New York 2004).

[93] Umang Sharma and Suresh C. Sharma, Phys. Plasmas **25**, 103509 (2018).

[94] C. Bower, W. Zhu, S. Jin, and O. Zhou, Appl. Phys. Lett. **77**, 830 (2000).

[95] V. I. Merkulov, D. H. Lowndes, Y. Y. Wei, G. Eres, and E. Voelkl, Appl. Phys. Lett. **76**, 3555 (2000).

[96] G. S. Bocharov, A. A. Knizhnik, A. V. Eletskii, and T. J. Sommerer, Surface Electron and Ion Emission **57**, 270 (2012).

[97] A. F. Pal, T. V. Rakhimova, N. V. Suetin, M. A. Timofeev, and A V Filippov, Low Temperature Plasma **33**, 43 (2007).

[98] Y. Zhang, A. Chang, J. Cao, Q. Wang, W. Kim, Y. Li, N. Morris, E. Yenilmez, J. Kong and H. Dai, Appl. Phys. Lett. **79**, 19 (2001).

[99] Z. P. Huang, D. Z. Wang, J. G. Wen, M. Sennett, H. Gibson, and Z. F. Ren, Applied Physics A **74**, 387 (2002).

[100]M. W. Lee, M. A. S. M. Haniff, A. S. Teh, D. C. S. Bien and S. K. Chen, Journal of Experimental Nanoscience **10**, 16 (2015).

[101]S. G. Kim, S. Y. Kim, and H. W. Lee, Trans. Nonferrous Met. Soc. China **21**, 130 (2011).

[102]T. Y. Lee, J. H. Han, S. H. Choi, J. B. Yoo, C. Y. Park, T. Jung, S. Yu, W. K. Yi, I. T. Han and J. M. Kim, Diamond and Related Materials **12**, 851 (2003).

[103]S. F. Lee, Y. P. Chang and L. Y. Lee, J Mater Sci: Mater Electron **20**, 851 (2009).

[104]M. Chen, C. M. Chen, H. S. Koo, and C. F. Chen, Diamond and Related Materials **12**, 1829 (2003).

[105]L. Delzeit, I. McAninch, B. A. Cruden, D. Hash, B. Chen, J. Han, M. J. Meyyappan, Appl. Phys. **91**, 6027 (2002).

[106]R. T. K. Baker, P. S. Harris, R. B. Thomas, R. J. Waite, J. Catal. **30**, 86 (1973).

[107]K. Matthews, B. Cruden, B. Chen, M. Meyyappan, L. Delzeit, J. Nanosci. Nanotechnol. **2**, 475 (2001).

Chapter - 2

STUDY THE ALIGNMENT MECHANISM DURING THE PLASMA-ASSISTED GROWTH OF CARBON NANOTUBES

PUBLICATION

- **Umang Sharma** and Suresh C. Sharma, "A parametric study to unravel the alignment mechanism of carbon nanotubes during its plasma-assisted growth", *Physics of Plasmas* **25**, 103509 (2018).

2

STUDY THE ALIGNMENT MECHANISM DURING THE PLASMA-ASSISTED GROWTH OF CARBON NANOTUBES

2.1 BRIEF OUTLINE OF THE CHAPTER

The alignment and catalyst-assisted growth mechanism of carbon nanotubes (CNTs) in a hydrogen-diluted methane plasma are demonstrated in the analysis. The consequence of plasma parameters (plasma density and temperature) and bias potential of the substrate on the sheath electric field are examined. The role of the electric field in the plasma sheath to provide the necessary electrostatic force and its repercussion on the carbon nanotubes alignment in the plasma is studied by taking into contemplation the steady state fluid equations, kinetics of the plasma sheath, charged species dynamics (positive ions and electrons) and neutral atoms in a reactive plasma, kinetics of the catalyst particle, creation of atomic species of carbon and hydrogen over the surface of catalyst nanoparticle and incorporating various processes vital for the growth of carbon nanotube in plasma. Taking into deliberation the initial conditions and the glow discharge parameters determined experimentally for the model, the numerical solutions for the equations are obtained. The outcomes of the studies revealed that the alignment of the nanotube depends on the force exerted at the tip of CNT i.e., the catalyst nanoparticle. This force is a consequence of the plasma sheath electric field which is dependent on the plasma parameters and the bias voltage at the substrate. This electrostatic force is also dependent upon the dimensions of the nanotube growing in the plasma environment and modifies itself continuously conferring to the instantaneous nanotube measurement and alignment during the growth. The study can be apprehended to manufacture carbon nanotubes aligned vertically in plasma for better applications in the areas of field emission devices. The results of the study have been assessed and compared with the existing experimental observations which accredit the proposed mechanisms.

2.2 INTRODUCTION

The forces acting on CNT due to the plasma sheath electric field during its growth helps in its vertical alignment in the plasma. Over the years, several experimental groups worldwide have produced vertically aligned carbon nanotubes (VACNTs) using plasma and have derived various observations regarding its vertical orientation.

Bower *et al.*[1] reported that the growth of CNT is always oriented perpendicular to the substrate irrespective of the inclination or shape of the substrate and the self-bias potential can be considered as the primary reason behind the alignment of CNTs.

Chhowalla *et al.*[2] showed that in the absence of applied bias, randomly oriented or spaghetti-like nanotubes grow whereas on applying bias voltages, the nanotubes begin to align themselves. They also revealed that for small bias voltages, the nanotubes did not align completely with the substrates, in contrast to high bias voltages leading to the higher electric field, CNTs appeared to be perfectly aligned.

Tanemura *et al.*[3] have observed the catalyst material dependence alignment of CNTs, and the positive ions supplied selectively to the tip of nanotube due to biasing at the substrate which controls the morphology could be the possible reason for the alignment of the CNTs.

Merkulov *et al.*[4] anticipated that the non-uniform stresses (tensile, compressive) across the catalyst interface and force acting on the CNTs/CNFs associates a feedback mechanism which initiates the alignment of the nanostructure.

Chen *et al.*[5] proposed that under the effect of electric field, the charged catalyst particle at the tip of nanotube gets pulled in the electric field direction i.e. normal to the substrate which governs the direction of growth of CNT and hence its alignment.

Zhang *et al.*[6] demonstrated that the growth of CNTs by CVD is directed by electric field and studied the CNT alignment with the electric field and gas flow. The nanotubes grown under no electric field exhibited random orientation in contrast to aligned CNTs grown under bias voltages.

Yu *et al.*[7] obtained highly aligned growth of CNT under applied substrate bias and random growth of CNT without the bias voltage. Henceforth, hypothesized that the chemical bonds formed between the charged species along the direction of the electric field and hence, induce the vertical alignment.

Maiti *et al.*[8,9] deliberated the growth of CNT in arc discharge and showed that the position of atoms constituting the nanotube tends to straighten the tube under the effect of potential and restrict it from curving and ultimately closing.

Merchan *et al.*[10] synthesized well aligned graphitized concentric graphitic cylinder and suggested the alignment of the CNT array growing on a substrate is under the effect of a metal catalytic support in presence of electric field. They proposed that the axial stresses produced by the electric charges on CNT aids in its growth and the electric field influences the transport of species.

Blazek *et al.*[11] mathematically computed electric field in the plasma sheath, the forces exerted on the catalyst particle and the resistivity of the substrate.

Bao *et al.*[12] simulated the electric forces on the catalyst tip and nanotube with varying density, length and diameter of nanotube which guides the field for probable nanotube alignment and its use in field emitter devices.

Wei *et al.*[13] experimentally verified the change in the electrostatic force acting on a CNF with plasma parameters and inspected the mechanism for possible detachment of CNF from the substrate.

Bocharov *et al.*[14] computed the effect of the externally applied electric field on the inclination of an initially grown CNT and showed the dependence of bending angle of CNT on the local value of electric field due to the polarization of charges.

Pal *et al.*[15] stated that the CNT growth gets influenced by the existence of an electric field which applies a pondermotive force on the nanotube sufficient for its alignment along the field direction.

In the chapter, we explain that the vertically-aligned CNT growth is owed to the electric field persuaded in plasma sheath and the growth of nanotubes can be guided by varying

the operational plasma parameters. The plasma sheath induced electric field produces an electrostatic force on the CNT growing on a substrate immersed in plasma which governs its alignment. The role of the plasma sheath electric field and corresponding electrostatic force in aligning the CNT is explained.

2.3 MODEL DESCRIPTION

In the model, a collisional plasma with finite electron and ion temperature constituted by plasma species (electrons, positively charged ions, and neutrals atoms) of methane CH_4 and hydrogen H_2, where CH_4 acts as the main hydrocarbon source gas, and H_2 as the etchant gas is considered. The methane and hydrogen species are denoted as type A and B, respectively. Table 2.1 details all the ionic and neutral species of methane and hydrogen considered in the model. Under the influence of plasma, irrespective of the type of plasma source considered (dc, rf, microwave, ICP etc.), vertically aligned CNTs are obtained experimentally. The plasma parameters, namely plasma density and electron temperature considered in the work are of the rf plasma source range.

Type	Neutral species	Positively charged ions
A	CH, CH_2, CH_3, CH_4,	CH^+, CH_2^+, CH_3^+, CH_4^+,
	C_2H, C_2H_2, C_2H_3, C_2H_4,	CH_5^+, C_2H^+, $C_2H_2^+$, $C_2H_3^+$,
	C_2H_5, C_2H_6, C_3H_8,C_4H_{10}	$C_2H_4^+$, $C_2H_5^+$, $C_2H_6^+$
B	H, H_2	H^+, H_2^+, H_3^+

Table 2.1 Plasma species considered in the present computation.

The detailed analysis of the growth model of CNT in a plasma is demonstrated subsequently. The elementary course followed in the nucleation and growth of CNT in specified plasma are[16–18]

a. A pre-deposited nickel Ni metal catalyst film is disintegrated into many catalyst nanoparticles owing to the bombardment of highly energetic etchant species in the reactive plasma. These catalyst nanoparticles positioned over a negatively biased substrate are the sites for nucleation of CNT growth.

b. The hydrocarbon species act as the main source for the generation of carbon species for CNT growth. The hydrogen gas present in the plasma aids in the effective shaping of the nanotube.
c. The CNT growth over the catalyst-substrate surface initiates via carbon species generated on the active surface of the catalyst by different surface processes viz., adsorption and desorption of hydrocarbon and hydrogen species, diffusion of carbon atoms on the surface and bulk of catalyst particle to form a graphitic tubular structure, thermal dehydrogenation of hydrocarbon species, and many others.
d. Simultaneous vertical alignment of CNT during the growth process owing to various plasma operating parameters.
e. The consistent sticking of neutral species on the growing nanotube leads to catalyst poisoning which eventually ceases the growth process.

The theoretical model of catalyst-assisted growth and alignment mechanisms of CNT growing in a complex plasma considered in the analysis is depicted in Fig. 2.1. The growth of CNT initiates at the surface of catalyst nanoparticle due to the decomposition process of hydrocarbons species, the diffusion processes of the C-atoms, the precipitation process through the posterior of the catalyst, lifting it off the substrate surface and formation of graphitic cylindrical layers, hence primarily the CNT grows perpendicular to the planar substrate. After the initialization of growth, the catalyst-nanotube interface experience tensile-compressive stresses due to inhomogeneous C-precipitation at this interface which deviates the CNT from its initial orientation. As the growth progresses, these stresses tend to balance each other and the electrostatic force then provides the necessary feedback mechanism for CNT alignment. When there is no instability in the C-precipitation at the catalyst-nanoparticle, the CNTs are aligned in the direction of electrostatic force governed by sheath electric field. When the nanotube is aligned, this force holds a minimum value for the structure to be aligned and the growth carries on.

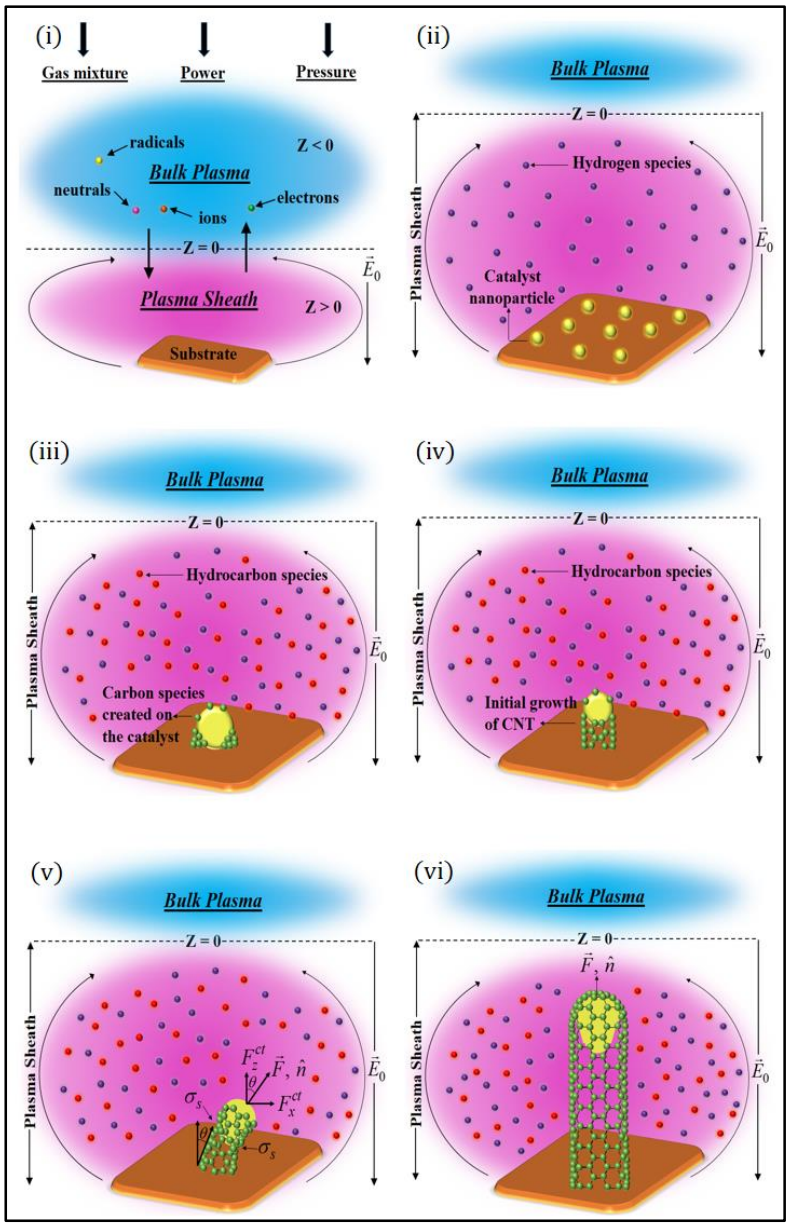

Figure 2.1 Schematic representation of the growth and alignment of CNT in a hydrogen-diluted hydrocarbon plasma **(i)** various regions of the plasma model considered, **(ii)** Formation of catalyst nanoparticles in hydrogen plasma, **(iii)** creation of carbon atoms on the nanoparticle surface, **(iv)** initialization of growth of nanotube in the direction of electric field, **(v)** deviation of CNT alignment due to various components of forces acting on the catalyst surface as well as the catalyst-nanotube interface, **(vi)** fully vertically aligned carbon nanotube with catalyst encapsulated within the carbonaceous layer.

To examine the structure of plasma sheath, energies and fluxes of the plasma species, a one-dimensional plasma sheath model is considered in the investigation. Assuming the position of the bulk plasma-sheath interface at $z=0$, $z<0$ is the neutral plasma region and $z>0$ is a non-neutral plasma region [see Fig. 2.1 (i)] governed by the following steady-state fluid equations[16,19]

$$\vec{\nabla}.(n_{ij}\overrightarrow{u_{ij}}) = \nu_{if} n_e \ , \tag{2.1}$$

$$\vec{\nabla}.(n_e\overrightarrow{u_e}) = \sum_{ij} \nu_{if} n_e \ , \tag{2.2}$$

$$m_{ij} n_{ij} u_{ij} \partial_z(u_{ij}) = e n_{ij} \partial_z(\varphi) - m_{ij} n_{ij} \nu_{cf} u_{ij}, \tag{2.3}$$

$$0 = e n_e \partial_z(\varphi) - m_e n_e \nu_{cf} u_e, \tag{2.4}$$

$$\partial_{zz}(\varphi) = 4\pi e (n_e - \sum_{ij} \zeta_{ij} n_{ij}). \tag{2.5}$$

The Eqs. (2.1) and (2.2) define the ion and electron particle balance equations, respectively. n_{ij}, u_{ij} and m_{ij} are the number densities, velocities and masses of the *j* type ionic species considered in the model. n_e, u_e and m_e are the number density, velocity and mass of the electron. The Eqs. (2.3) and (2.4) describe the ion and electron ion-momentum balance equations, respectively. The electrostatic sheath potential is denoted by φ, $\nu_{if}\left(=\psi_{ij}\zeta_j n_n\right)$ is the ionization frequency of the neutral atoms due to collision with electrons where ψ_{ij} is the ionization potential of the j^{th} ion, ζ_{ij} is the number density ratio for j^{th} ion to electron, $\sum_{ij}\zeta_{ij}=0$ and $0<\zeta_{ij}<1$, n_n defines the number density of neutrals. ν_{cf} is the collision frequencies of ions with neutrals. The Eq. (2.5) describes the Poisson's equation which determines the electrostatic potential by relating it to the electron and ion number density.

2.3.1 CHARGING OF CNT

The Eq. (2.6) represents the time evolution of charge attained by the CNT due to the accretion of positive ions and electrons at the tip and the cylindrical surface of CNT. Another assumption is made regarding the charge transfer and neutralization of the ionic species incident at the CNT surface.

$$\partial_\tau(Z) = \sum_j \left(\xi_{ij}^{tip} + \xi_{ij}^{cyl} \right) - \gamma_e \left(\xi_e^{tip} + \xi_e^{cyl} \right), \tag{2.6}$$

where Z is the extent of charge on the CNT surface and γ_e represents the electron sticking coefficient defining the adsorption probability of electrons at the surface.

$$\xi_{ij}^{tip} = n_{ij}(z)\pi r^2 \left(\frac{8k_B T_{ij}}{\pi m_{ij}} \right)^{1/2} \left[1 - Z\alpha_{ij} \right] \exp\left[-\frac{E_b}{k_B T_S} \right] \exp\left[-\frac{eU_S}{k_B T_S} \right], \tag{2.7}$$

$$\xi_{ij}^{cyl} = n_{ij}(z) r l \left(\frac{2\pi k_B T_{ij}}{m_{ij}} \right)^{1/2} \left\{ \frac{2}{\sqrt{\pi}} \left(\frac{eV_S}{k_B T_{ij}} \right)^{1/2} + \exp\left[\frac{eV_S}{k_B T_{ij}} \right] erfc\left[\left(\frac{eV_S}{k_B T_{ij}} \right)^{1/2} \right] \right\} \times \exp\left[-\frac{E_b}{k_B T_S} \right] \exp\left[-\frac{eU_S}{k_B T_S} \right], \tag{2.8}$$

$$\xi_e^{tip} = n_e(z)\pi r^2 \left(\frac{8k_B T_e}{\pi m_e} \right)^{1/2} \exp\left[Z\alpha_e + \frac{eU_S}{k_B T_S} \right], \tag{2.9}$$

$$\xi_e^{cyl} = n_e(z) r l \left(\frac{2\pi k_B T_S}{m_e} \right)^{1/2} \exp\left[\frac{eV_S}{k_B T_e} + \frac{eU_S}{k_B T_S} \right]. \tag{2.10}$$

The Eqs. (2.7) and (2.8) define the collection current of the ionic species at the tip and tubular surface of CNT, respectively. The Eqs. (2.9) and (2.10) define the collection current of electrons at the tip and the tubular surface of CNT, respectively. The potential at the tubular surface of the CNT is denoted by V_S, the substrate bias is

designated by U_S, the temperature of the substrate is defined by T_S, the energy required for the bulk diffusion is symbolized by E_b, r is the radius of the catalyst particle. $\alpha_e\left(=\frac{e^2}{rk_BT_e}\right)$, and $\alpha_{ij}\left(=\frac{e^2}{rk_BT_{ij}}\right)$. The plasma sheath ion and electron density are represented as $n_{ij}(z)=n_{ij0}\left(1-\frac{2e\varphi(z)}{m_{ij}u_{ij0}^2}\right)^{-1/2}$ and $n_e(z)=n_{e0}\exp\left(\frac{|e|\varphi(z)}{k_BT_e}\right)$, respectively, where n_{ij0} and n_{e0} are the initial number density for the ionic species and electrons, respectively. u_{ij0} is the initial ion velocity, and $\varphi(z)=\varphi_0\exp\left(-\frac{z}{\lambda_D}\right)$ is the electrostatic potential within the plasma sheath, where $\varphi_0\left(=U_S\right)$ is the negative substrate potential and $\lambda_D=\sqrt{\frac{k_BT_e}{n_ee^2}}$ is the Debye length. k_B represents the Boltzmann constant, T_{ij} and T_e symbolise the temperature of the ionic species and electrons, respectively.

2.3.2 DYNAMICS OF ELECTRON NUMBER DENSITY

The time evolution of electron density in the bulk plasma is described by Eq. (2.11).

$$\partial_\tau(n_e)=\sum_j\beta_jn_j-\sum_j\alpha_jn_en_{ij}-\gamma_e\frac{n_{CNT}}{\lambda_s}\left(\begin{matrix}tip\\ \xi\\ e\end{matrix}+\begin{matrix}cyl\\ \xi\\ e\end{matrix}\right)-\mathrm{K}_{wall}^{e}n_e, \qquad (2.11)$$

where β_j is the neutral atom ionization coefficient, $\alpha_j\left(T_e\right)=\left\{\alpha_{j0}\left(300/T_e\right)^k\right\}$ is the recombination coefficient for the ionic species and electrons, where $k=-1.2$ is a constant[20]. n_e, n_j and n_{ij} represent the electron, neutral and ion number density,

respectively. The CNT number density is represented by n_{CNT}. The last term denotes the electronic species loss rate per unit volume on the discharge wall where $K_{wall}^{e} = \left(\frac{\gamma_e u_e A_{chm}}{4V} \right)$, A_{chm} and V are the surface area and volume of a cylindrical plasma chamber, respectively, having interior diameter of $2R = 32\,\text{cm}$ and length $L = 23\,\text{cm}$[21].

In Eq. (2.11), the first term accounts the increase in number density of electrons due to dissociative ionization of j type neutral species, the second term accounts for the decrease in the number density of electrons owing to the recombination process between ions and electrons, the third term accounts the decrease in the number density of electrons due to electron collection at the surface of CNT, and the last term denotes the discharge loss to the wall.

2.3.3 DYNAMICS OF POSITIVE ION NUMBER DENSITY

The Eqs. (2.12) and (2.13) represent the time evolution of A and B type ion density in the bulk plasma.

$$\partial_\tau (n_{iA}) = \beta_A n_A - \alpha_A n_e n_{iA} - \frac{n_{CNT}}{\lambda_s} \left(\begin{matrix} tip \\ \xi \\ iA \end{matrix} + \begin{matrix} cyl \\ \xi \\ iA \end{matrix} \right) + \sum_{\ell AB} k_\ell n_A n_{iB} - \sum_{qBA} k_q n_B n_{iA} - K_{wall}^{iA} n_{iA} + \left(\frac{P}{E_{CH}^{diss} V} \right), \tag{2.12}$$

$$\partial_\tau (n_{iB}) = \beta_B n_B - \alpha_B n_e n_{iB} - \frac{n_{CNT}}{\lambda_s} \left(\begin{matrix} tip \\ \xi \\ iB \end{matrix} + \begin{matrix} cyl \\ \xi \\ iB \end{matrix} \right) + \sum_{qBA} k_q n_B n_{iA} - \sum_{\ell AB} k_\ell n_A n_{iB} - K_{wall}^{iB} n_{iB} + \left(\frac{P}{E_{H}^{diss} V} \right), \tag{2.13}$$

where $\mathrm{K}_{wall}^{ij} = \left(\frac{\gamma_{ij} u_{ij} A_{chm}}{4V} \right)$ represents the discharge loss of *j* type ions to the wall, γ_{ij} is the sticking coefficient of respective ions[21], k_q and k_l are the neutral-ion reaction rate coefficients, P is the applied power, $\delta E_{CH}^{diss} (\approx 2.1\, eV)$ and $\delta E_{H}^{diss} (\approx 2.1\, eV)$ are the hydrocarbon and hydrogen dissociation energies, respectively[19].

In Eqs. (2.12) and (2.13), the first term characterizes the increase in ion number density owing to the *j* type neutral species dissociative ionization, the second term incorporates the loss in the ion number density due to electron-positive ion recombination process, the third term indicates the loss in the ion number density because of the collection of ions on the CNT surface, the fourth and fifth terms denotes the positive ion-neutral reactions in the plasma at different reaction rates, respectively, the sixth term indicates the ion discharge loss to the wall of the chamber and lastly, the increase in ion number density owed to the dissociation by plasma power.

2.3.4 DYNAMICS OF NEUTRAL ATOM NUMBER DENSITY

The time evolution of A and B type neutral atoms in the bulk plasma is represented as

$$\begin{aligned} \partial_\tau (n_A) = {} & \alpha_A n_e n_{iA} - \beta_A n_A + \frac{n_{CNT}}{\lambda_s}\left(1-\gamma_{iA}\right)\begin{pmatrix} tip & cyl \\ \xi & \xi \\ iA & iA \end{pmatrix} - \frac{n_{CNT}}{\lambda_s}\gamma_A \begin{pmatrix} tip & cyl \\ \xi & \xi \\ A & A \end{pmatrix} \\ & + \mathrm{Q}_A^{IF} - \mathrm{Q}_A^{OF} - \sum_{lBA} k_l n_A n_{iB} + \sum_{qAB} k_q n_B n_{iA} - J_A^{adsp} + J_A^{desp} \\ & - \mathrm{K}_{wall}^{A} n_A, \end{aligned} \tag{2.14}$$

$$\begin{aligned} \partial_\tau (n_B) = {} & \alpha_B n_e n_{iB} - \beta_B n_B + \frac{n_{CNT}}{\lambda_s}\left(1-\gamma_{iB}\right)\begin{pmatrix} tip & cyl \\ \xi & \xi \\ iB & iB \end{pmatrix} - \frac{n_{CNT}}{\lambda_s}\gamma_B \begin{pmatrix} tip & cyl \\ \xi & \xi \\ iB & iB \end{pmatrix} \\ & + \mathrm{Q}_B^{IF} - \mathrm{Q}_B^{OF} - \sum_{qBA} k_q n_B n_{iA} + \sum_{\ell AB} k_\ell n_A n_{iB} - J_B^{adsp} + J_B^{desp} \\ & + J_{thd} - \mathrm{K}_{wall}^{B} n_B, \end{aligned} \tag{2.15}$$

where $Q_j^{IF} = \left(\frac{4.4\times10^{17}}{V} J_j \right)$, and $Q_j^{OF} = \left(\frac{\upsilon_{pump}}{V} n_j \right)$ are the influx and outflux rates of j type species from the chamber, respectively[21]. γ_j is the neutral atoms sticking coefficient, J_j is the inlet flow of the respective gas, and υ_{pump} is the pumping rate. J_j^{adsp} and J_j^{desp} are the fluxes of adsorption and desorption on/from the catalyst-substrate surface, respectively. J_{thd} is the thermal dehydrogenation flux of the hydrogen species, $K_{wall}^{j} = \sigma_j \frac{D_j}{\Lambda^2}$ signifies the discharge loss of j type neutrals, σ_j is the wall reaction coefficient, D_j is the diffusion coefficient which considers the motion of respective species within the plasma constituents which is defined by binary diffusion coefficients $D_{j,j'}$ of j type species on j' through Blanc's law, $\frac{1}{D_j} = \frac{1}{D_{j,CH_4}} + \frac{1}{D_{j,H_2}}$ as the dominant species are CH_4 and H_2, and $\Lambda = \frac{RL}{\left\{(2.405L)^2 + (\pi R)^2\right\}^{1/2}}$ is the effective diffusion length of the chamber for a cylindrical setup[16,22]. In Eqs. (2.14) and (2.15), the first term represents the rise in the neutral atom density owing to the electron-positive ion recombination process, the second term represents the loss due to dissociative ionization of j type neutrals, the third term represents the increase in neutral atom density due to neutralization of ionic species after their collection at the CNT surface, and the fourth term represents the loss of neutrals due to collection on CNT surface. The fifth and sixth terms define the plasma chamber influx and outflux of the j type neutral species, respectively. The seventh and eighth term define the change in the density of the neutral atoms due to the neutral-positive ion reactions considered in the model (see Table 2.2). The ninth and tenth term describe the neutral species adsorption and desorption onto/from the surface of the catalyst. The eleventh term of Eq. (2.15) incorporates the thermal dehydrogenation process corresponding to the rate of increase in hydrogen species density[23]. The last terms of both equations represent the discharge loss of j type neutrals

to the cylindrical chamber wall. The wall reaction coefficient σ_j is incorporated to take into account neutral losses to the wall (see Table 2.3). This term represents the rate at which the neutral species are lost to the wall by embedding or recombination. This implies that only fractions of species are lost via diffusion to the walls and the remaining return to the plasma.

Reactions	k (cm^3sec^{-1})
$CH_4^+ + CH_4 \rightarrow CH_5^+ + CH_3$	1.5×10^{-9}
$CH_3^+ + CH_4 \rightarrow CH_4^+ + CH_3$	1.36×10^{-10}
$H_2^+ + H_2 \rightarrow H + H_3^+$	2.5×10^{-9}
$CH_3^+ + CH_4 \rightarrow C_2H_5^+ + H_2$	1.2×10^{-9}
$H_3^+ + C_2H_6 \rightarrow C_2H_5^+ + 2H_2$	2.0×10^{-9}
$H_3^+ + CH_4 \rightarrow CH_5^+ + H_2$	1.6×10^{-9}
$H_3^+ + C_2H_4 \rightarrow C_2H_5^+ + H_2$	1.9×10^{-9}
$H_3^+ + C_2H_2 \rightarrow C_2H_3^+ + H_2$	1.94×10^{-9}
$C_2H_2^+ + CH_4 \rightarrow C_2H_3^+ + CH_3$	4.1×10^{-9}
$C_2H_2^+ + CH_4 \rightarrow C_3H_4^+ + H_2$	6.25×10^{-10}
$C_2H_2^+ + CH_4 \rightarrow C_3H_5^+ + H$	1.44×10^{-9}
$C_2H_4^+ + C_2H_4 \rightarrow C_3H_5^+ + CH_3$	3.9×10^{-10}
$C_2H_4^+ + C_2H_4 \rightarrow C_4H_8^+$	4.3×10^{-10}
$CH_5^+ + C_2H_6 \rightarrow C_2H_5^+ + H_2 + CH_4$	5.0×10^{-10}
$C_2H_5^+ + C_2H_2 \rightarrow C_4H_7^+$	6.7×10^{-10}

$C_2H_5^+ + C_2H_4 \rightarrow C_3H_5^+ + CH_4$	3.1×10^{-10}
$C_2H_5^+ + C_2H_4 \rightarrow C_4H_9^+$	3.0×10^{-10}

Table 2.2 Ion-neutral reactions taken into consideration in the plasma model, as well as their reaction rate coefficients (Ref. 33).

Reactions	Rate coefficient(σ)
$CH_4 \xrightarrow[\sigma]{wall} CH_4$	$\sigma = 0$
$CH_3 \xrightarrow[\sigma]{wall} CH_3$	$\sigma = 0.01$
$CH_2 \xrightarrow[\sigma]{wall} CH_2$	$\sigma = 0.01$
$CH \xrightarrow[\sigma]{wall} CH$	$\sigma = 0.01$
$C_2H_2 \xrightarrow[\sigma]{wall} C_2H_2$	$\sigma = 0.01$
$C_2H_3 \xrightarrow[\sigma]{wall} C_2H_3$	$\sigma = 0.01$
$C_2H_4 \xrightarrow[\sigma]{wall} C_2H_4$	$\sigma = 0.01$
$C_2H_5 \xrightarrow[\sigma]{wall} C_2H_5$	$\sigma = 0.01$
$C_2H_6 \xrightarrow[\sigma]{wall} C_2H_6$	$\sigma = 0.01$
$H_2 \xrightarrow[\sigma]{wall} H_2$	$\sigma = 0.07$
$H \xrightarrow[\sigma]{wall} H$	$\sigma = 1$

$2H \xrightarrow[\sigma]{wall} H_2$	$\sigma = 0.05$

Table 2.3 Neutral-wall reactions for discharge losses considered in the model and their rate coefficients (Ref. 22).

2.3.5 CARBON AND HYDROGEN SPECIES GENERATED OVER THE CATALYST SURFACE

The hydrocarbon and hydrogen precursors decompose over the catalyst surface undergoing numerous surface processes. This decomposition results in the generation of carbon species and hydrogen radicals crucial for the growth of CNT. The time evolution of the carbon and hydrogen species created per unit area over the surface of the catalyst are given by

$$\begin{aligned}\partial_\tau(n_C) = \Bigg[& \sum_A \left\{ J_A(1-\theta_t) + n_A^{surf}\upsilon \exp\left(-\frac{\delta E_{CH}^{diss}}{k_B T_S}\right) - n_A \upsilon \exp\left(-\frac{\delta E_{dCH}}{k_B T_S}\right)\right\} \\ & + \sum_{iA}\left\{\left(\sum_A \frac{n_A^{surf} y_d}{\upsilon_0}\right) J_{iA} + J_{iA}\right\} + J_C + \sum_{iB}\left(\sum_{iA}\frac{J_{iA}\sigma_{ads}}{\upsilon}\right) J_{iB} \\ & - \sum_B\left(\sum_A n_A^{surf}\sigma_{ads}\right) J_B - n_C \upsilon \exp\left(-\frac{\delta E_{ev}}{k_B T_S}\right) - n_C \sigma_{ads} \upsilon n_H \Bigg] \\ & \times d_\tau(\Omega_C),\end{aligned} \tag{2.16}$$

$$\begin{aligned}\partial_\tau(n_H) = \sum_B \Bigg\{ & J_B(1-\theta_t) + n_B^{surf}\upsilon \exp\left(-\frac{\delta E_H^{diss}}{k_B T_S}\right) - n_B^{surf}\upsilon \exp\left(-\frac{\delta E_{dH}}{k_B T_S}\right) \\ & - n_B^{surf}\sigma_{ads} J_B - n_B^{surf}\sigma_{ads} J_{iB}\Bigg\} + \sum_{iA}\left(\sum_A \frac{n_A^{surf} y_d}{\upsilon_0}\right) J_{iA} \\ & + \sum_{iB} J_{iB} - n_H \sigma_{ads} \upsilon n_C,\end{aligned} \tag{2.17}$$

where n_C and n_H are the number density of carbon and hydrogen species generated per unit area on the catalyst surface, respectively. The functional terms and parameters mentioned in Eqs. (2.16) and (2.17) are described in Table 2.4. The rate of generation of carbon species over the surface of the catalyst is represented by Eq. (2.16). The first and second term designates the increase in carbon number density due to the adsorption of neutral hydrocarbons over the surface of the catalyst and the hydrocarbon thermal dissociation, respectively. The third term denotes decrease in carbon number density owed to the desorption of hydrocarbon species from the surface of the catalyst, the fourth and fifth terms indicate increase in carbon density due to the hydrocarbon ion-induced dissociation and positive ion decomposition, respectively. The sixth term represents the carbon influx directly towards the particle surface, the seventh term denotes increase due to the ion-ion interaction of hydrocarbon and hydrogen ions. The eighth term shows the decrease in carbon species owing to the hydrocarbon neutrals and hydrogen interaction. The ninth and tenth term incorporates the reduction due to evaporation of carbon species and interaction between the carbon and hydrogen species generated on the catalyst nanoparticle, respectively. The incessant dissociation of hydrocarbon species on the catalyst active regions creates an abundance of carbon species. This leads to the amorphous carbon layer formation, which over time poisons the catalyst and restricts the dissociation of hydrocarbon species any further due to the absence of an active region on the catalyst surface. The term $d_\tau(\Omega_C)=\left(1-4n_C\pi r^2\right)$ of Eq. (2.16) indicates the rate of poisoning of the catalyst which depends upon the carbon number density over the catalyst surface generated throughout the growth[24]. The creation of hydrogen species on the surface of the catalyst is represented by Eq. (2.17). The first and second term denotes the increase in hydrogen species due to adsorption of hydrogen neutral species on the surface of the catalyst and thermal dissociation of the hydrocarbons, respectively. The third term denotes the loss due to desorption of hydrogen from the surface of the catalyst. The fourth and fifth term represents the interaction between the hydrogen adsorbed on the surface with the incoming neutrals and ions of hydrogen, respectively. The sixth and seventh term denotes the increase due to the hydrocarbon ion-induced dissociation and hydrogen

influx near the particle surface. The last term signifies the loss in hydrogen caused by interaction between the generated hydrogen and carbon species on the nanoparticle.

Functions/parameters	Description
$\upsilon_0 (\approx 10^{15}\ cm^{-2})$	Adsorption sites per unit area[23]
$\upsilon (\approx 10^{13}\ Hz)$	Thermal vibration frequency[25]
$\sigma_{ads}\left(=6.8\times10^{-16} cm^2\right)$	Cross-section of interaction amongst various species[23]
$n_j^{surf}\left(=\theta_j \upsilon_0\right)$	Surface number density of the neutral atom[23,26]
θ_j	Surface coverage by the neutral species[25]
$\delta E_{ev} (=1.8\ eV)$	Evaporation energy of the carbon atoms[19]
$\delta E_{dCH}\left(=1.8\ eV\right)$	Desorption energy for hydrocarbon species[19]
$\delta E_{dH} (=1.8\ eV)$	Desorption energy for hydrogen species[19]
Ω_C	Blocking function for the catalyst particle[24]

Table 2.4 Description of the functions/parameters mentioned in Eqs. (2.16) and (2.17).

2.3.6 GROWTH EQUATION AND ALIGNMENT MECHANISM OF CNT

The growth of CNT in a reactive plasma is evaluated in Eq. (2.18) i.e., a volumetric change in the CNT (variation of radius and height) with the number densities of carbon and hydrogen species generated over the surface of the catalyst by considering various growth processes.

$$\partial_\tau\left(\pi r^2 l\right)=\left[\left\{D_S+D_b+2\kappa\upsilon r^2\right\}\times\frac{P(8\pi r)n_C}{\upsilon\rho_{CNT}\sum_{Ai}\xi_{iA}}+\left\{\frac{D_m}{4\pi r^2}+n_H\left(4\pi r^2\right)\sum_{Bi}\xi_{iB}\right\}\right]\times\frac{m_{ct}}{\rho_{ct}}, \tag{2.18}$$

The functional terms and parameters mentioned in Eq. (2.18) are described in Table 2.5. The first term represents the carbon species diffusion over the surface of the catalyst. The diffusion over the catalyst surface is dominant for the growth of outer

shells of the CNT. However, the second term denotes the carbon species bulk diffusion through the catalyst. The third term signifies the incorporation or precipitation of carbon species around the posterior of the catalyst particle and forms an inner cylindrical shell. The dominance of bulk diffusion over the surface diffusion leads to the formation of MWCNTs otherwise SWCNTs are formed and this generally depends on the substrate temperature and catalyst particle size[27,28]. The formation of graphitic shells develops the stress between the graphene sheet and catalyst rear interface. The fourth term denotes the metal catalyst particle self-diffusion along the growth direction of CNT. An etching gas, here hydrogen, is added to etch out the terminally stuck carbon atoms and promote the CNT growth along the vertical direction. Thus, the last term represents the hydrogen etching of the growing CNT walls.

Functions/parameters	Description
$D_S = a_0^2 \upsilon \exp\left(-\frac{E_S}{k_B T_S}\right)$	Surface diffusion coefficient of carbon atoms[23]
$D_b = \frac{\upsilon r}{\pi} \exp\left(-\frac{E_b}{k_B T_S}\right)$	Bulk diffusion coefficient of carbon atoms[23]
$D_m = D_{m0} \exp\left(-\frac{\delta E_{sd}}{k_B T_S}\right)$	Self-diffusion coefficient for metal atoms[23]
$\kappa = a_0 \upsilon \exp\left(-\frac{\delta E_{inc}}{k_B T_S}\right)$	Incorporation rate of carbon atoms into the CNT wall[23,26]
$a_0 \left(= 0.34\ nm\right)$	Interatomic distance between carbon atoms
$E_S \left(= 0.3\ eV\right)$	Energy barrier for carbon species surface diffusion over catalyst surface[23]
$E_b \left(= 1.6\ eV\right)$	Energy barrier for carbon species surface diffusion through the catalyst[23]
$P\ (\approx 20\ GPa)$	Pressure which the graphitic layers exert on the nanoparticle[29]

$\delta E_{inc}\left(=\delta E_d=0.8\ eV\right)$	Energy barrier for carbon species to diffuse along the nanotube-catalyst boundary[26]

Table 2.5 Description of the functions/parameters mentioned in Eqs. (2.18).

For a strongly negative biased substrate, the positively charged ions entering the plasma sheath gets accelerated by the plasma potential. The ion flux towards the substrate is defined as ion current density, J_{ij} directed towards the substrate due to negative biasing. The electron current density, J_e is electron flux directed away from the substrate and antiparallel to J_{ij}. These particle fluxes in the plasma sheath can be represented as $J_{ij}=n_{ij}eu_{ij}$, and $J_e=\left(\frac{-n_e e u_{th}}{4}\right)$, where $u_{ij}=\left(\frac{k_B T_e}{m_{ij}}\right)^{1/2}$ is the Bohm velocity of ions, $u_{th}=\left(\frac{8k_B T_e}{\pi m_e}\right)^{1/2}$ is the thermal velocity of electrons. As there are no electrons present in the high voltage sheath region, Poisson's equation can be solved considering $\varphi(0)=0,$ and $d_z\varphi(0)=0,$ as the boundary conditions, giving

$$-\varphi(z)=\left\{\left(\frac{3}{2}\right)^{4/3}\left(\frac{J_{ij}}{\varepsilon_0}\right)^{2/3}\left(\frac{2e}{m_{ij}}\right)^{-1/3}z^{4/3}\right\}. \tag{2.19}$$

Taking $\varphi(\lambda_s)=-U_S$ in Eq. (2.19) and solving gives,

$$\lambda_s=\left\{\frac{2}{3}\left(\frac{2e\varepsilon_0^2}{m_{ij}}\right)^{1/4}\frac{U_S^{3/4}}{J_{ij}^{1/2}}\right\}. \tag{2.20}$$

The Eq. (2.20) is notably known as Child law for space-charge-limited current. The sheath electric field near the substrate $\left(E_0\right)$ i.e., where $z=\lambda_s$ can be estimated using the Child law, substitution of Eq. (2.20) in Eq. (2.19) and as $E(z)=-d_z(\varphi),$ gives

$$E_0 = \left\{ \left(\frac{6m_{ij}}{e\varepsilon_0^2} \right)^{1/3} J_{ij}^{2/3} \lambda_s^{1/3} \right\} = \left\{ 2 \left(\frac{m_{ij}}{2e\varepsilon_0^2} \right)^{1/4} J_{ij}^{1/2} U_S^{1/4} \right\},$$

$$E_0 = \left\{ 2 \left(\frac{m_{ij}}{2e\varepsilon_0^2} \right)^{1/4} \left(n_{ij} e u_{ij} \right)^{1/2} U_S^{1/4} \right\} = \left\{ 2 \left(\frac{k_B e}{2\varepsilon_0^2} \right)^{1/4} n_{ij}^{1/2} T_e^{1/4} U_S^{1/4} \right\}. \quad (2.21)$$

This electric field varies increasingly with the bias voltage of the substrate as well as the ion current density. To evaluate the force exerted on a CNT and to study the influence of plasma on the CNT alignment, a simple model is considered where a single CNT with a hemispherical catalyst top is grown in the presence of a complex plasma. During the growth of CNT, the generation of carbon species over the catalyst surface form graphitic layers due to various surface processes and their inhomogeneous C-precipitation leads to the introduction of compressive and tensile stresses between the catalyst-nanotube interfaces leading to the deviation from CNT vertical alignment. These stresses can perhaps aid in the carbon diffusion at the CNT where the carbon concentration is less thereby providing a feedback mechanism[4]. The stress introduced at this interface can be assessed as $\sigma_s = F_n^{ct} / \pi r^2$ where r is the radius of the hemispherical catalyst top[10]. The electric field E_0 is present nearby the surface of the substrate in the plasma sheath. Following basic electrostatics, it is known that a conducting surface experiences a downward electrostatic pressure, $p = \left(\frac{1}{2} \varepsilon_0 E^2 \right)$ due to the local electric field E outward normal to the surface. The pressure acting on the catalyst surface induces a net upward force which causes the vertical alignment. The electric force acting upon the catalyst nanoparticle per unit area is given by $dF_n^{ct} = \frac{1}{2} \varepsilon_0 E^2 dA$, where dA is the unit surface area of the catalyst nanoparticle. The pressure acting on the wall of the cylindrical surface is negligible or due to cylindrical symmetry, it cancels out. The local electric field acting upon this geometry creates a dipole which produces components of a dipolar field. This electric field at the apex of

the CNT is estimated using a simple floating sphere model which gives the corresponding field enhancement factor $\beta = \left(\frac{l}{r} + 0.5 + 3\cos\theta\right)$, where r is the radius of the hemispherical catalyst top, l is the distance of the hemisphere from the substrate surface namely the length of CNT, θ denotes the angle between the vertical axis and normal to the hemisphere[30]. The total field acting on top of the catalyst particle will be given by $E_{top} = \beta E_0$, where E_0 is the plasma sheath electric field around the substrate vicinity. The electrostatic force acting in the planar direction to the substrate is given as[13]

$$F_x^{ct} = \left\{\frac{1}{2}\varepsilon_0 \int \left(E_{top}\right)^2 dA\hat{r} \,.\, \hat{x}\right\},$$

$$F_x^{ct} = \left\{\frac{1}{2}\varepsilon_0 \int \left(E_0\beta\right)^2 \sin\theta dA\right\},$$

$$F_x^{ct} = \left\{\frac{1}{2}\varepsilon_0 \int \left[\frac{l}{r} + 0.5 + 3\cos\theta\right]^2 E_0^2 \left(2\pi r^2 \sin\theta\right)\sin\theta d\theta\right\}, \qquad (2.22)$$

Now, the electrostatic force F_z^{ct} acting in the z direction of a unit area dA on the catalyst particle responsible for vertical alignment is given as

$$F_z^{ct} = \left\{\frac{1}{2}\varepsilon_0 \int \left(E_{top}\right)^2 dA\hat{r} \,.\, \hat{z}\right\},$$

$$F_z^{ct} = \left\{\frac{1}{2}\varepsilon_0 \int \left(E_0\beta\right)^2 \cos\theta dA\right\},$$

$$F_z^{ct} = \left\{\frac{1}{2}\varepsilon_0 \int \left[\frac{l}{r} + 0.5 + 3\cos\theta\right]^2 E_0^2 \left(2\pi r^2 \sin\theta\right)\cos\theta d\theta\right\}, \qquad (2.23)$$

$$F_z^{ct} = \left\{ \int 4\pi \left(\frac{k_B e}{2} \right)^{1/2} \left(n_{ij} T_e^{1/2} U_S^{1/2} \right) \left[l + \left(0.5 + 3\cos\theta \right) r \right]^2 \sin\theta \cos\theta d\theta \right\}. \quad (2.24)$$

In Eq. (2.22), the force F_x^{ct} represents the repulsive force acting between the neighbouring CNTs if a CNT array is considered. If an array of nanotubes is considered with *s* being the inter-CNT separation, the effective electric field at the tip of the catalyst particle will consist of a screening factor defined by $S = 1 - \exp\left(-1.1586s\right)$ [13]. For simplification of the model and calculations, only a single carbon nanotube is considered. It may be assumed that the axial stresses and the planar force component together, resolve any further fluctuations prevailing in the feedback of carbon precipitation and the force F_z^{ct} represented by Eq. (2.24) holds the responsibility of aligning the CNT in the direction perpendicular to the substrate.

Some may hypothesize that the alignment of CNT was due to the selective supply of positive ions at the tip of CNT under the effect of an applied substrate bias. This would mean that on undertaking this form of supply under the effect of a small negative bias also, only vertically aligned CNTs and no random CNTs should be observed but experimentally, for a small negative bias, only randomly oriented CNTs were observed. Moreover, this selective supply of positive ions greatly to the tip of the CNT where the catalyst is present, will lead to a more rapid poisoning of the catalyst due to the increase in generation of carbon atoms on the nanoparticle surface and saturate the growth further. Another hypothesis could be that the electrostatic attraction between neighbouring nanotubes. Bower *et al.*[1] performed an experiment where they grow CNT by thermal as well as PECVD. During the growth process via PECVD, vertically aligned nanotubes were obtained and on turning off the plasma i.e., in the thermal environment, nanotubes were observed to be growing in a curly or random way. Similar results demonstrating the electrostatic deflection of nanotube have been obtained by Poncharal *et al.*[31]. Thus, if the alignment was a consequence of the Van der Waals forces or the crowding effect amongst the CNTs, the growth would have proceeded to

be in an aligned way during thermally assisted growth as was in the case of the plasma-assisted growth.

The growth axis of the CNT coincides with the electrostatic force direction exerted over the catalyst. This force produces an even stress around the CNT-catalyst interface. The carbon species precipitates out of this interface, forming a vertically aligned cylindrical graphitic structure. A compressive stress is produced at the CNT-catalyst interface where superior growth rate is present and a tensile stress where lesser growth rate is existent. These contradictory stresses acting on the interface, support the carbon incorporation in the region where lesser growth is observed. This effect of stress-induced diffusion equalizes the growth rate around the nanotube-catalyst interface and maintains the vertical alignment of CNT.

2.4 RESULTS AND DISCUSSION

The first order simultaneous differential equations described in the previous section are solved using the initial conditions determined experimentally and plasma glow discharge parameters[32–36] that are mentioned in Table 2.6 and 2.7 to study the effect of plasma on the corresponding electrostatic force exerted over the growing CNT structure.

Species	**Mass (1 amu=1.66×10^{-27} kg)**	**Number density (cm^{-3})**
e	0.0005486 *amu*	1.0×10^{10}
CH	13 *amu*	1.0×10^{10}
CH_2	14 *amu*	0.2×10^{10}
CH_3	15 *amu*	0.1×10^{13}
CH_4	16 *amu*	1.0×10^{14}
C_2H	25 *amu*	1.0×10^{9}
C_2H_2	26 *amu*	0.2×10^{14}
C_2H_3	27 *amu*	0.4×10^{11}

C_2H_4	28 *amu*	0.4×10^{13}
C_2H_5	29 *amu*	0.1×10^{11}
C_2H_6	30 *amu*	0.8×10^{12}
C_3H_8	44 *amu*	1.0×10^{10}
H	1 *amu*	0.7×10^{14}
H_2	2 *amu*	1.0×10^{15}
CH^+	13 *amu*	0.7×10^{6}
CH_2^+	14 *amu*	1.0×10^{7}
CH_3^+	15 *amu*	0.2×10^{9}
CH_4^+	16 *amu*	0.2×10^{9}
CH_5^+	17 *amu*	0.5×10^{9}
C_2H^+	25 *amu*	0.1×10^{7}
$C_2H_2^+$	26 *amu*	0.2×10^{10}
$C_2H_3^+$	27 *amu*	0.2×10^{10}
$C_2H_4^+$	28 *amu*	0.3×10^{9}
$C_2H_5^+$	29 *amu*	0.1×10^{10}
$C_2H_6^+$	30 *amu*	0.4×10^{8}
H^+	1 *amu*	0.4×10^{9}
H_2^+	2 *amu*	0.6×10^{9}
H_3^+	3 *amu*	0.1×10^{8}

Table 2.6 Parametric initialization of the number density of various plasma species deliberated in the present computation assumed by the literature of plasma composition of the glow discharge.

Parameter	Initial value
RF power	50-200 W
Working pressure	50 $mTorr$
T_e (electron temperature)	2.5 eV
T_{ij} (ion species temperature)	0.20 eV
T_n (neutral atom temperature)	0.20 eV
$T_s = T_{ct}$ (substrate and catalyst temperature)	300 $^{\circ}C$
ρ_{ct} (nickel catalyst density)	8.96 gm/cm^3
γ_e (electron sticking coefficient)	1
γ_{ij} (ions sticking coefficient)	1
γ_j (neutral atoms sticking coefficient)	1
U_S (negative substrate bias voltage)	500 V
θ_t (total surface coverage)	0.01
J_{CH_4} (methane gas flow)	30 $sccm$
J_{H_2} (hydrogen gas flow rate)	100 sccm
α_{j0} (ion-electron recombination coefficient)	1.12×10^{-7} cm^3/sec

Table 2.7 Parametric initialization of the various parameters deliberated in the present computation assumed by the experimentally determined conditions.

2.4.1 Variation of CNT dimensions with growth time

Fig. 2.2 (i) and (ii) shows the temporal behaviour of the CNT radius and length grown in the plasma, respectively, for different number densities of hydrocarbon ions and electron temperature.

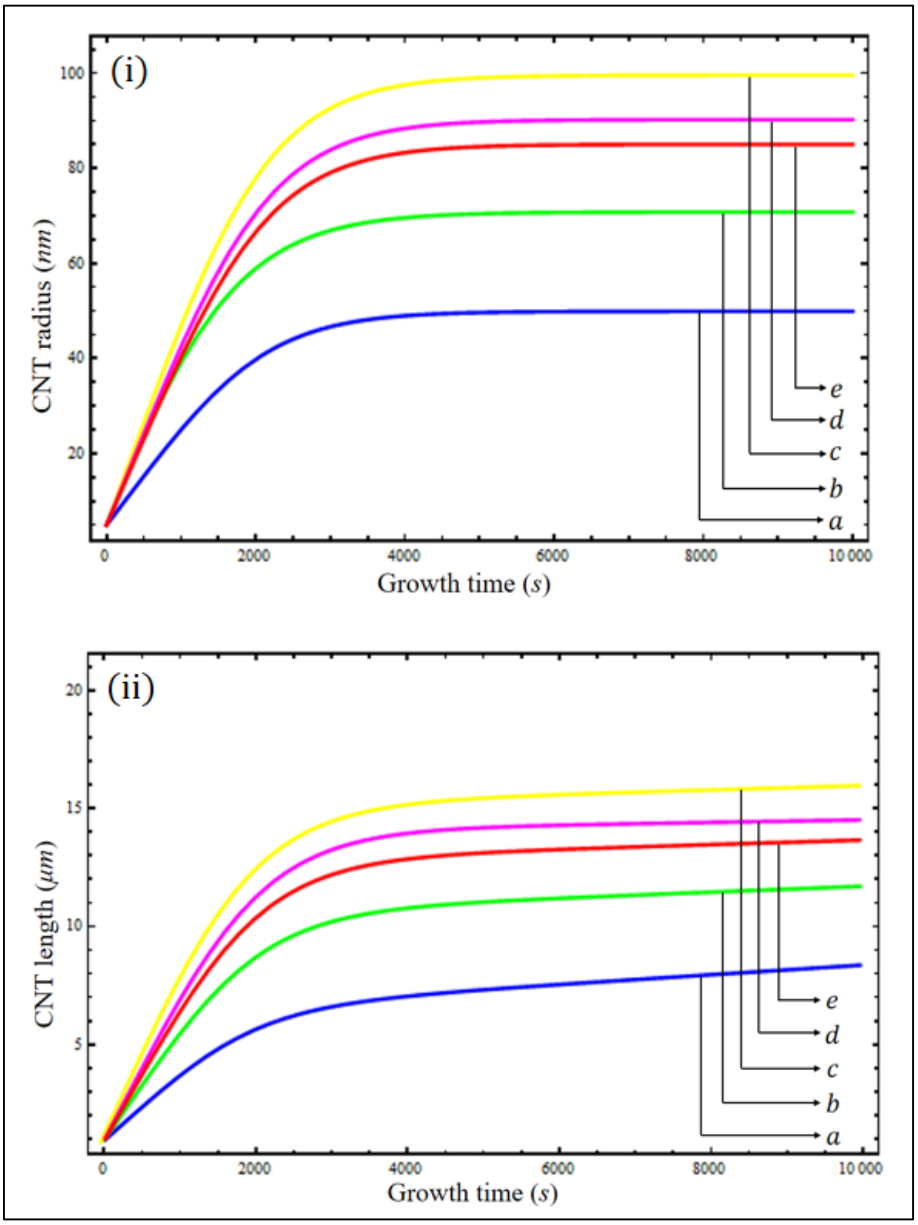

Figure 2.2 Time evolution of **(i)** CNT radius and **(ii)** CNT length with changing plasma parameters where a, b, c, d and e corresponds to $(n_{iA0}, T_{e0}) = (0.2\times10^{9}\ cm^{-3}, 1.5\ eV); (0.4\times10^{9}\ cm^{-3}, 1.75\ eV); (0.6\times10^{9}\ cm^{-3}, 2.0\ eV); (0.8\times10^{9}\ cm^{-3}, 2.25\ eV); (1.0\times10^{9}\ cm^{-3}, 2.5\ eV)$.

The result indicates that the CNT radius and length increases with time and attains saturation for a fixed value of number density of hydrocarbon ions and electron temperature. Primarily, the carbon species generated over the surface of the catalyst are deposited and the subsequently the amorphous carbon is etched by the hydrogen species which enriches the growth of CNT. With time, progressive growth of

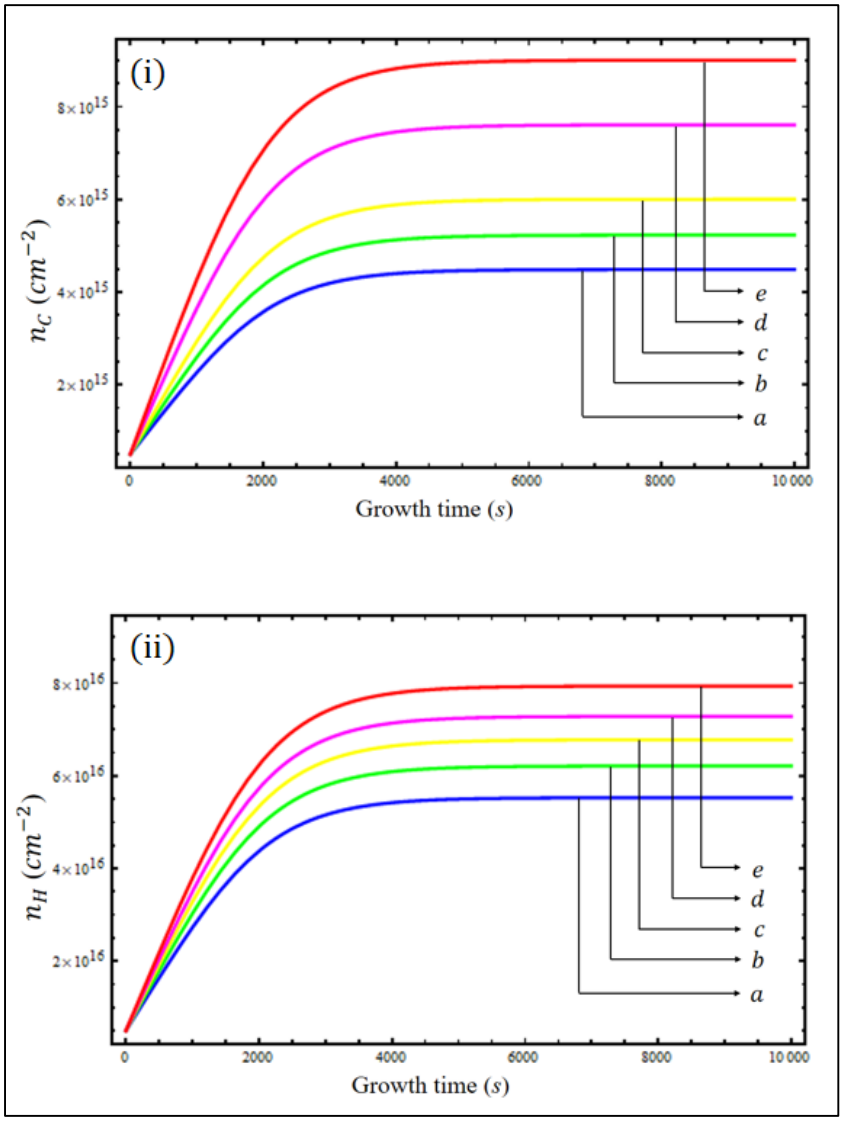

Figure 2.3 Temporal behaviour of **(i)** carbon and **(ii)** hydrogen species number density created on the catalyst surface as a function of different plasma parameters where a, b, c, d and e corresponds to $(n_{iA0}, T_{e0}) = (0.2\times10^9\ cm^{-3}, 1.5\ eV); (0.4\times10^9\ cm^{-3}, 1.75\ eV); (0.6\times10^9\ cm^{-3}, 2.0\ eV); (0.8\times10^9\ cm^{-3}, 2.25\ eV); (1.0\times10^9\ cm^{-3}, 2.5\ eV)$.

amorphous carbon layer leads to the catalyst poisoning, and thereby, saturating the CNT growth. For lower hydrocarbon ion density, the ion dissociation and ion-induced dissociation over the catalyst surface decreases and leads to the lower carbon surface concentration as compared to hydrogen radicals [cf. Fig. 2.3 (i) and (ii)]. Whereas on increasing the ion number density, carbon species are generated over the particle surface increases resulting in enhanced CNT growth. However, it should also be noted that going beyond an optimum value of ion number density, the carbon concentration over the surface of the catalyst increases rapidly which in turn poisons the catalyst quickly. This can be interpreted from the blocking function that for a greater number of carbon species the catalyst particle gets poisoned rapidly.

2.4.2 Variation of the electric field with plasma parameters

Fig. 2.4 (i) and (ii) display the variation of the electric field of the plasma sheath in the substrate vicinity with the electron temperature and negative substrate bias, respectively. The increase in electron temperature decreases the sheath width which leads to an increase in the electron thermal kinetic energy. This leads to the loss of electrons from the plasma bulk to the boundary wall and hence, increases the electric field strength. On increasing the negative bias over the substrate, the plasma potential increases due to a decrease in sheath width leading to a rise in the electric field near the substrate. This high field strength accelerates the positive ions towards the substrate i.e., high current density due to high plasma potential, which leads to their abundance in the substrate vicinity.

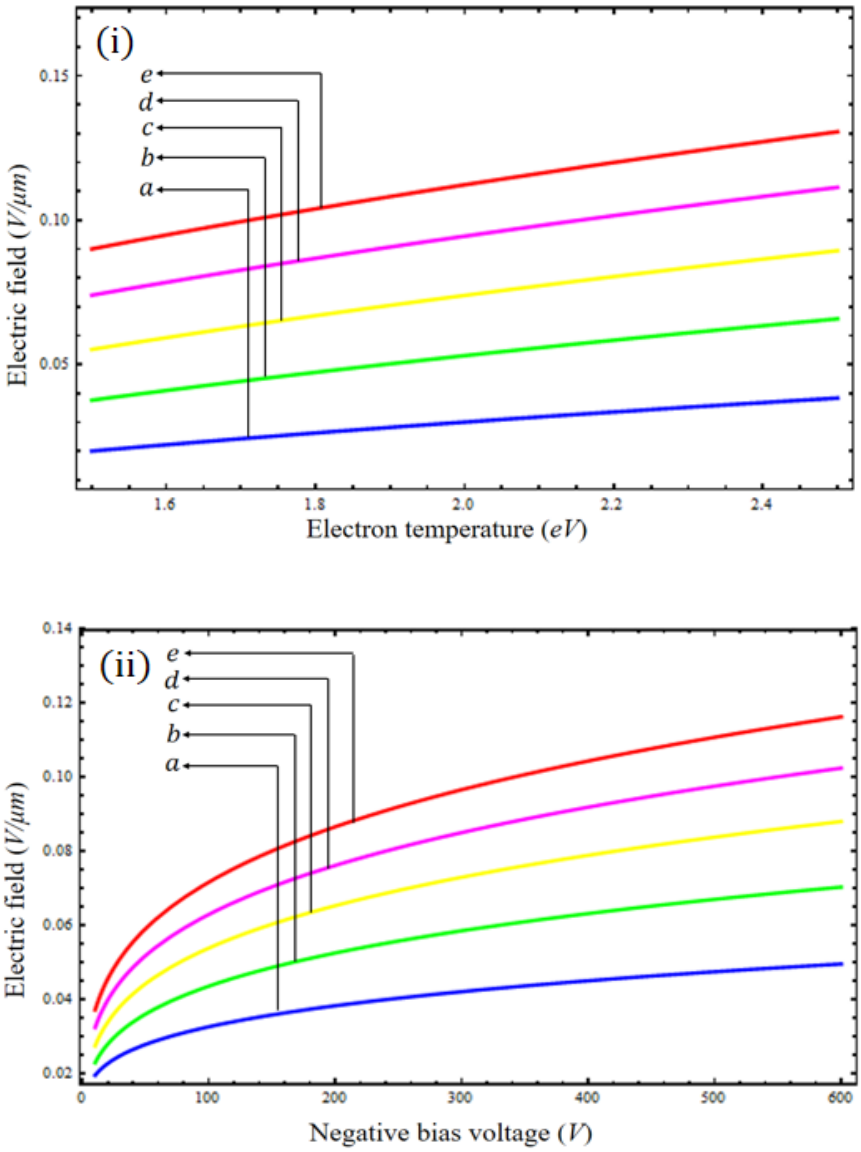

Figure 2.4 (i) Effect of electron temperature in plasma on the electric field (where a, b, c, d and e corresponds to $(n_{iA0}, U_S) = (0.2\times10^9\ cm^{-3}, 100V); (0.4\times10^9\ cm^{-3}, 200\ V); (0.6\times10^9\ cm^{-3}, 300\ V); (0.8\times10^9\ cm^{-3}, 400\ V); (1.0\times10^9\ cm^{-3}, 500\ V)$.

(ii) Effect of bias voltage on the electric field where a, b, c, d and e corresponds to $(n_{iA0}, T_{e0}) = (0.2\times10^9\ cm^{-3}, 1.5\ eV); (0.4\times10^9\ cm^{-3}, 1.75\ eV); (0.6\times10^9\ cm^{-3}, 2.0\ eV); (0.8\times10^9\ cm^{-3}, 2.25\ eV); (1.0\times10^9\ cm^{-3}, 2.5\ eV)$.

2.4.3 Temporal behaviour of the electric field

Fig. 2.5 (Inset) represents the time evolution of the plasma sheath electric field. The electric field nearby the substrate region shows a strong dependency on the electron temperature and negative bias voltage over the substrate as depicted in Fig. 2.4. The continuous drop in electron temperature over the growth time in the plasma due to incessant collisions of electrons with gaseous atoms, sheath width increases which decrease the ion current density towards the substrate and thereby, decreases the plasma potential. For a given sheath voltage, this leads to a lower sheath electric field strength in the substrate vicinity. Hence, the electric field decreases over the growth period. The result also attributes to the change in the electric field over time on changing the negative substrate bias. When the negative bias over the substrate increases, the plasma sheath electric field increase due to increase in plasma potential.

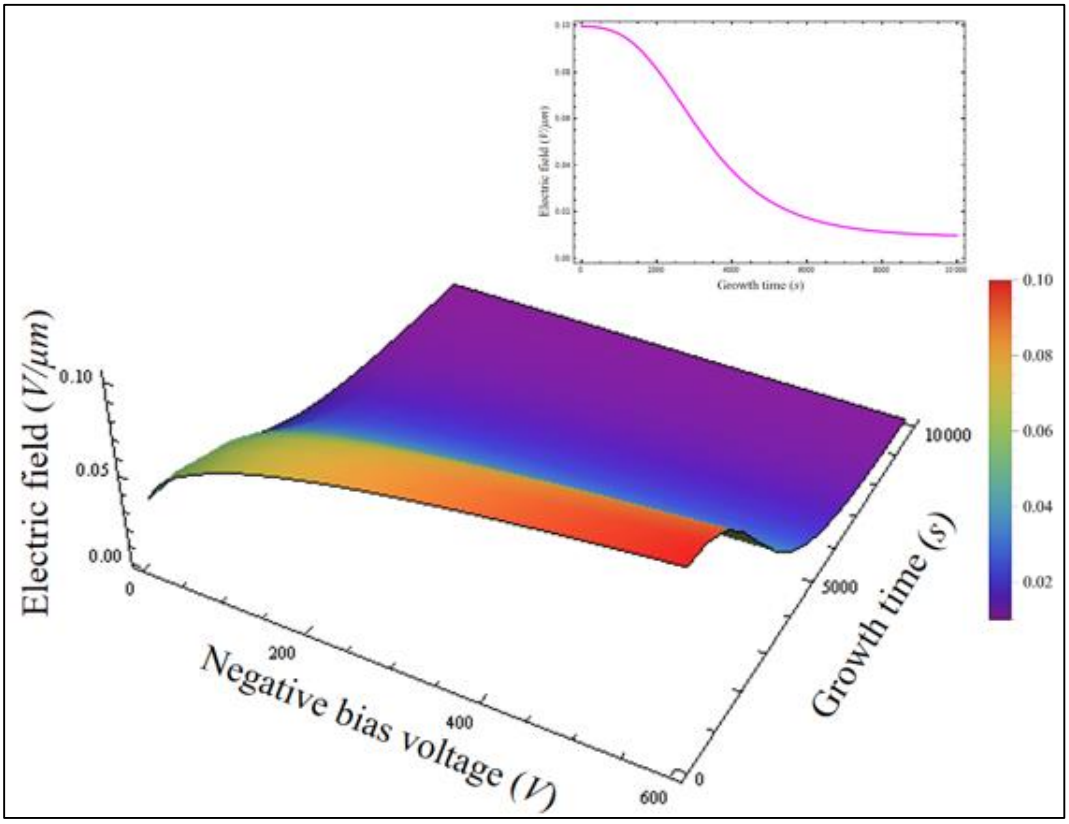

Figure 2.5 Variation of the electric field with growth time and negative substrate bias. Inset: Temporal behavior of electric field at $U_S = 500\ V$.

2.4.4 Variation of temporal electrostatic force with temporal plasma parameters and electric field

Fig. 2.6 (i), (ii), and (iii) display the relation between the temporal plasma parameters (hydrocarbon ion number density and electron temperature) and plasma electric field with the concurrent force exerted on the CNT tip. The decrease in electric field strength with time as shown in Fig 2.5 (i), decreases the ion density in the plasma sheath owing to the low plasma potential. The electron temperature in plasma also decreases with growth time due to the loss in electron energy due to continuous collisions in the sheath region. The initial increase in electrostatic force can be comprehended to its dependence on the tip surface area which increases due to increase in growth rate and the alignment angle of CNT [cf. Eq. (2.24)]. This increasing force produces stresses on the catalyst-nanotube interface and deviates the CNT from its vertical growth axis. Once the alignment reaches near about 30 degrees, these stresses start to balance each other and the electrostatic force decreases owing to the decrease in plasma parameters with time which starts to decrease the deviation produced in CNT. The increase in the negative substrate bias leads to the higher plasma potential and the electric field. The family of curves can be elucidated by the increase in electrostatic force exerted on the CNT with the increase in this negative bias over the substrate.

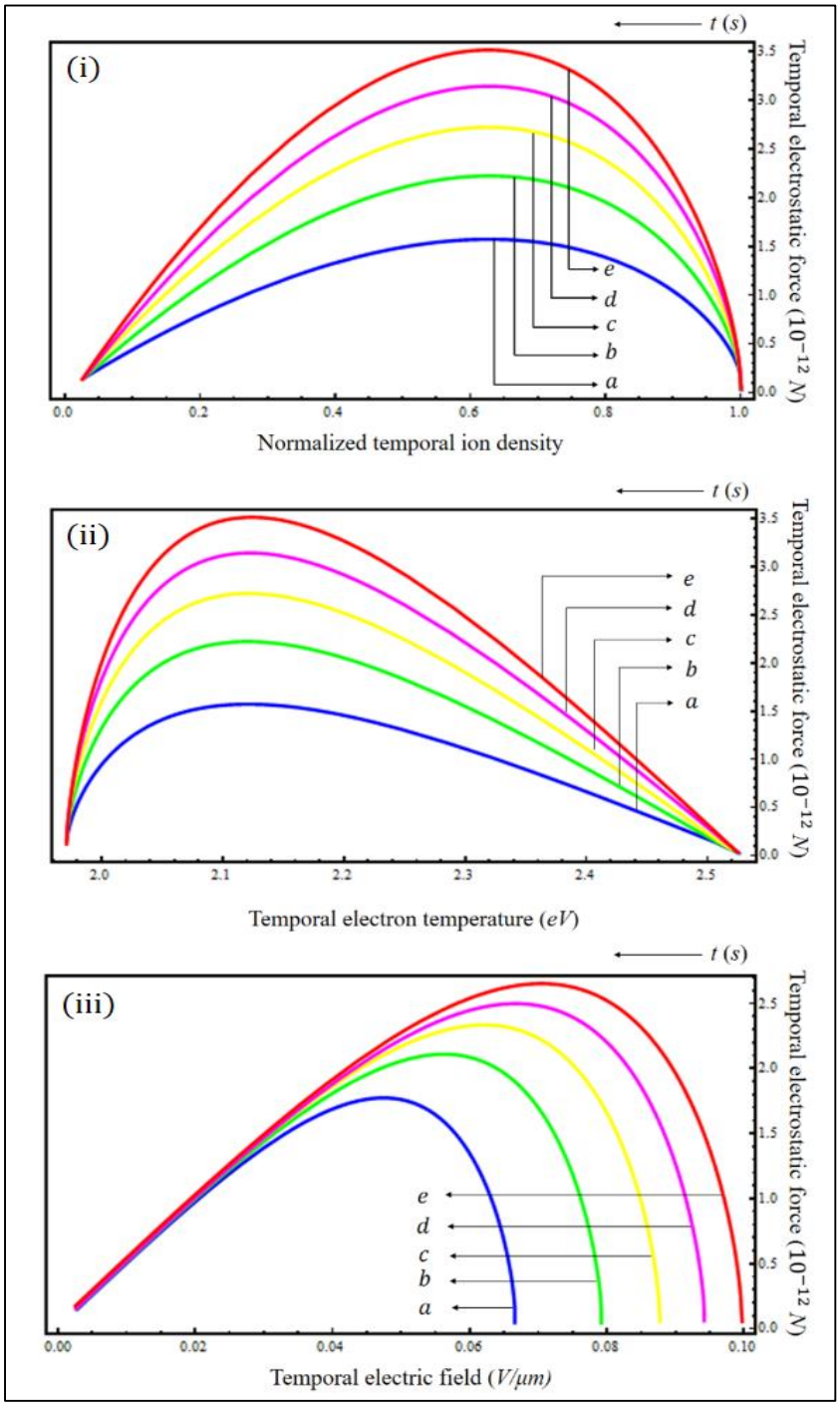

Figure 2.6 Variation of temporal electrostatic force with the concurrent **(i)** ion number density, **(ii)** electron temperature and **(iii)** electric field (where a, b, c, d and e corresponds to $U_S = 100\ V,\ 200\ V,\ 300\ V,\ 400\ V$ and $500\ V$, respectively).

2.4.5 Variation of electrostatic force with CNT dimensions

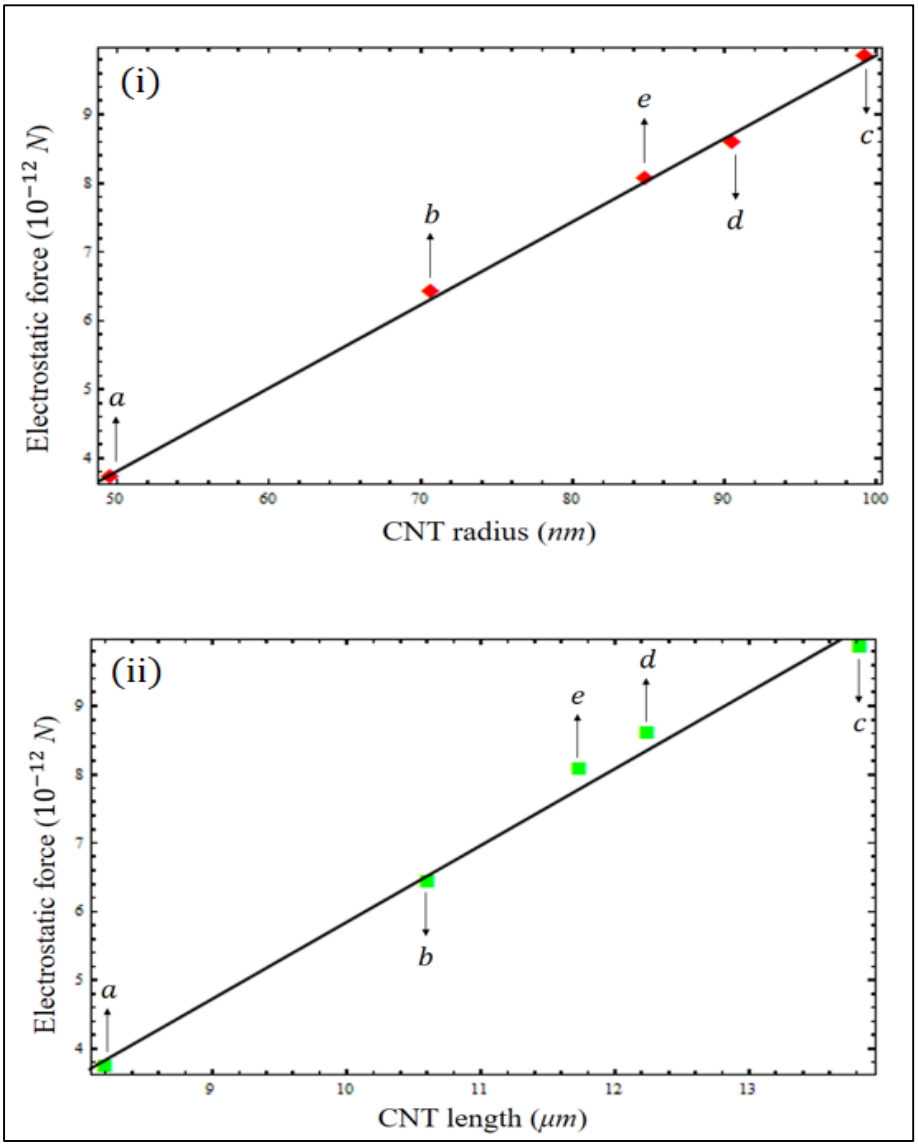

Figure 2.7 Effect of **(i)** CNT radius and **(ii)** CNT length on the electrostatic force (where a, b, c, d and e corresponds to $(n_{iA0}, T_{e0}) = (0.2\times10^9\ cm^{-3}, 1.5\ eV); (0.4\times10^9\ cm^{-3}, 1.75\ eV); (0.6\times10^9\ cm^{-3}, 2.0\ eV); (0.8\times10^9\ cm^{-3}, 2.25\ eV); (1.0\times10^9\ cm^{-3}, 2.5\ eV)$.

Fig. 2.7 (i) and (ii) characterizes the relation between the CNT radius and length grown in the plasma with the electrostatic force acting on it. For an initial number density of hydrocarbon ions and electron temperature, the variation in the radius and length of the CNT in the plasma is depicted in Fig. 2.2. The increase in the radius and length of the

nanotube increases the ultimate electrostatic force exerted at the tip of CNT in plasma. The increase in the growth of CNT enhances the electric field at the tip of the catalyst which leads to a higher electrostatic force. Hence, for the plasma conditions (denoted by points) leading to a greater CNT growth, results in a stronger electrostatic force. The linear best fit for the points denoting different plasma process conditions shows the linear relation of electrostatic force with the CNT radius and length.

2.4.6 Temporal behaviour of alignment angle

Fig. 2.8 shows the temporal variation of the alignment angle of CNT. During the nucleation stage, when the growth of CNT initiates the carbon species starts to precipitate out around the bottom of the catalyst which helps in lifting it up from the substrate forming graphitic layers beneath it. Hence originally, the CNT is growing aligned in the vertical direction. As discussed previously, due to non-uniformity in the growth rate of CNT around catalyst-nanotube interfaces, the axial stresses acting on the nanotube deviate it from its initial vertical alignment and CNT begins to incline. On reaching an inclination near 30 degrees, the electrostatic force acting on it CNT tip dominates these axial stresses and tend to decrease this inclination angle. As the CNT reaches its original vertical configuration, the force acting on its tip also decreases and reaches a saturation to maintain its alignment [cf. Fig. 2.1 (iv-vi)].

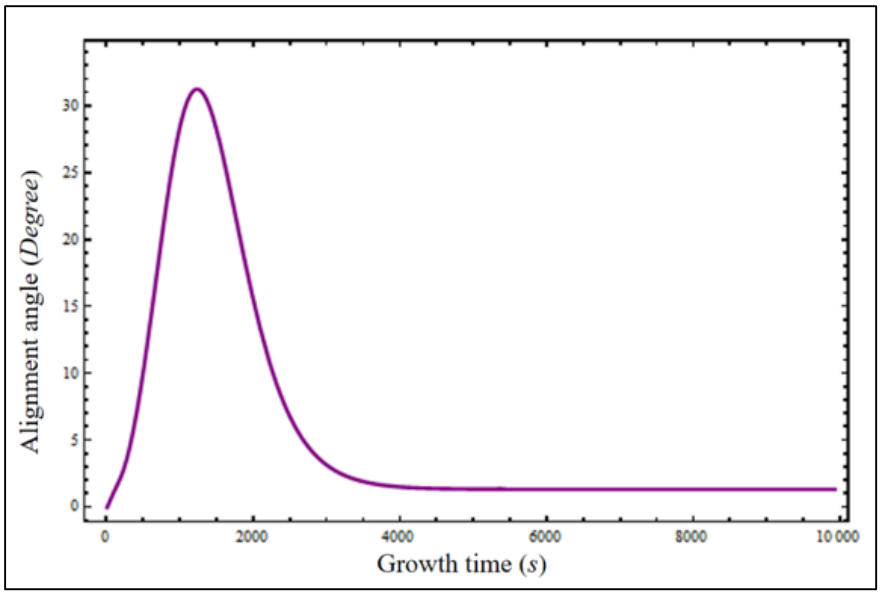

Figure 2.8 Temporal variation of alignment angle of CNT.

2.4.7 Temporal behaviour of the force acting on CNT

Fig. 2.9 signifies the time variation of the force employed on the carbon nanotube by the plasma. The electrostatic force depends strongly on the inclination angle of CNT [cf. Eq. (2.24)]. As the initial alignment of CNT in its nucleation stage is vertical, the force acting on it holds a small value. As the spatial variation in the C precipitation around the rear of catalyst tends to deviate the nanotube from its initial growth direction during the growth stage, the electrostatic force produces the axial stresses between the catalyst and CNT increases. The compressive and tensile stress act opposing to the higher and lower growth rate, respectively. These conflicting stresses support the C precipitation at the interface undergoing a lower growth rate. This balances the growth rate around the boundary of catalyst and CNT. Hereafter, the CNT tends to align itself again along the field. This electrostatic force attains a saturation value when the CNT reaches its original alignment. The result also features the change in the electrostatic force with time on changing the negative substrate bias. On increasing the negative bias over the substrate, the electrostatic force on CNT increases due to increase in plasma sheath electric field.

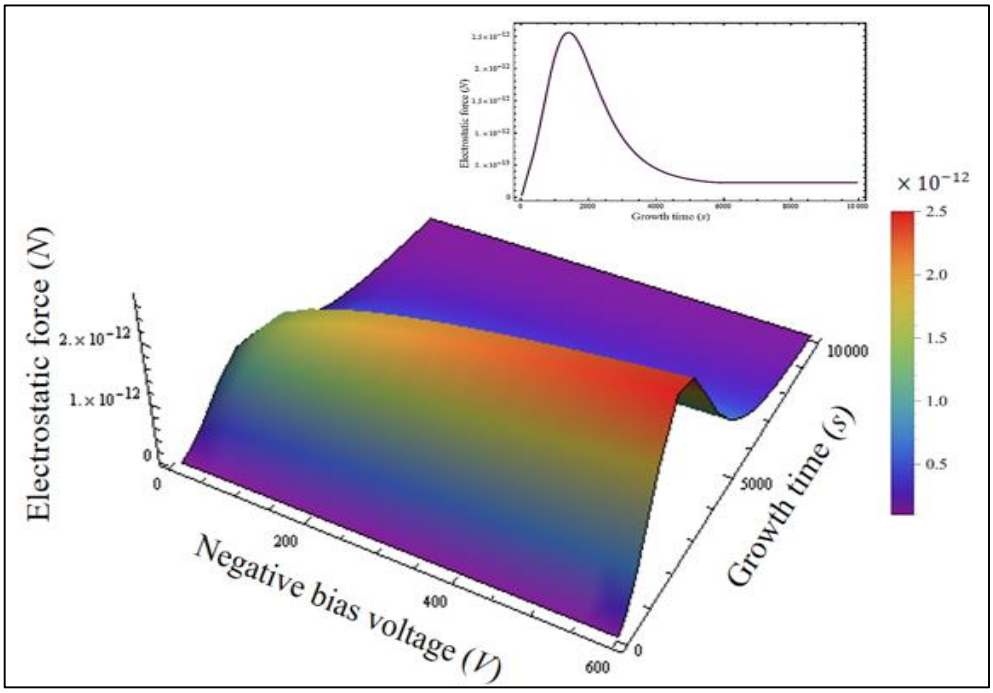

Figure 2.9 Variation of the electrostatic force with growth time and negative substrate bias. Inset: Temporal behavior of electrostatic force at $U_S = 500\ V$.

2.4.8 Variation of force with alignment angle

Fig. 2.10 shows the influence of an electrostatic force in the alignment of CNT in the plasma. As discussed before when the growth of CNT initiates, the CNT grows aligned with the electric field and slowly deviates from its initial axis due to all the axial stresses acting on it due to the electrostatic force. As these opposing stresses (compressive and tensile) start balancing the C precipitation around the catalyst-nanotube interface, this deviation starts to decrease again and align itself along its initial growth axis. Once the nanotube is aligned vertical to the substrate, the force sustains a constant value to retain the alignment and the growth process continues till it reaches a saturation. The Fig. 2.10 shows the effect of electrostatic force on aligning back the deviated CNT to its vertical growth axis.

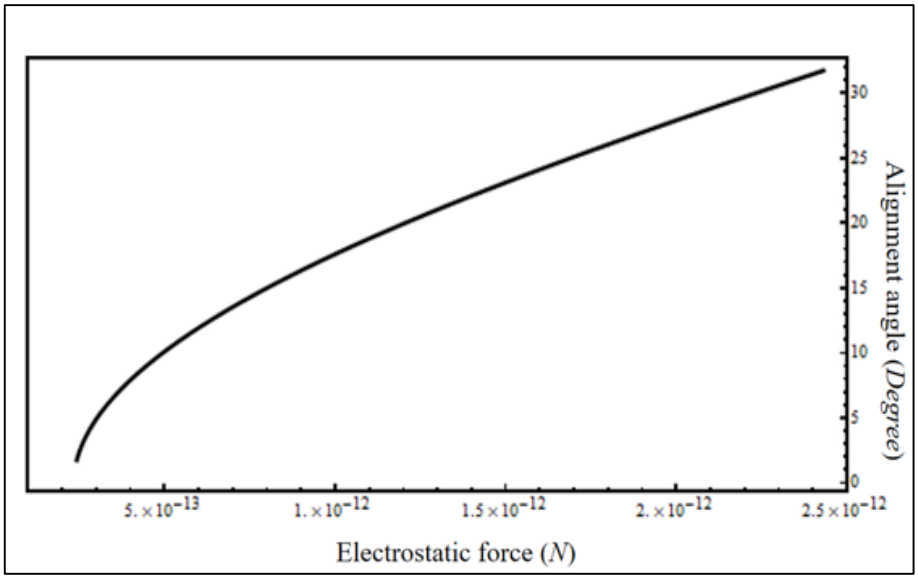

Figure 2.10 Variation of the alignment angle of CNT with the electrostatic force.

2.4.9 Comparison with the experimental outcomes

The theoretical outcomes of the analysis are found out to be in agreement with variously available observations as follows. The results from the work of Zhang *et al.*[6], Merchan *et al.*[10] and Pal *et al.*[15] showed the strong effect of electric field in aligning the CNTs along the field direction which are in compliance with our results. The results from Bower *et al.*[1] exhibited the importance of plasma in aligning the CNT perpendicular to the substrate surface, regardless of its orientation or shape. This

suggests the importance of plasma parameters in the alignment of CNT as revealed in our study. Roettgen *et al.*[37] studied the time-resolved plasma parameters in pulse discharges and suggested the decrease in plasma density and electron temperatures with time. Hence, this comprehends to the decrease in the plasma sheath electric field and the corresponding electrostatic force as indicated in the chapter. Bao *et al.*[12] simulated the electric field influence on the MWCNT and found that the force acting on the nanotubes govern their alignment and their results for the effect of the dimensions of CNT on this force are in direct compliance with the outcomes of the analysis. This indicates the faster alignment of CNT with higher electrostatic force due to the high negatively biased substrate. Wang et al.[38] studied experimentally the evolution of CNT growth by PECVD and presented differently aligned nanotubes during the growth time. This justifies the time evolution of CNT alignment angle during its growth. Tanemura *et al.*[3] suggested the dependence of alignment of CNT on the negative bias of the substrate which is in accordance with our results. The influence of negative substrate bias on the electrostatic force and the variation of CNT alignment angle with this force are obtained.

2.5 CONCLUSIONS

A theoretical analysis has been carried out to focus on the alignment mechanism along with the growth of carbon nanotube on a catalyst nanoparticle in a complex plasma. The several phenomena involved in the growth of CNT have been contemplated and consequence of plasma parameters on the growth as well as the establishment of electrostatic force responsible for the alignment of CNT has been studied in the present work. The alignment force is comprehended to increase with the growth in the dimensions of CNT. When the growth starts to decline due to catalyst poisoning, the aligning force acting on the CNT also decays and as the growth saturates, this force holds minimum value to sustain the alignment. The time evolution of the electric field and force in the plasma sheath is also studied. The current study can prove to be beneficial for the production of various 1D nanostructures, namely CNTs/CNFs and their use in various field emission devices due to the great dependency of its properties on the structure, morphology and alignment of CNTs.

REFERENCES

[1] C. Bower, W. Zhu, S. Jin, and O. Zhou, Appl. Phys. Lett. **77**, 830 (2000).

[2] M. Chhowalla, K.B.K. Teo, C. Ducati, N.L. Rupesinghe, G.A.J. Amaratunga, A.C. Ferrari, D. Roy, J. Robertson, and W.I. Milne, J. Appl. Phys. **90**, 5308 (2001).

[3] M. Tanemura, K. Iwata, K. Takahashi, Y. Fujimoto, F. Okuyama, H. Sugie, and V. Filip, J. Appl. Phys. **90**, 1529 (2001).

[4] V.I. Merkulov, A. V. Melechko, M.A. Guillorn, D.H. Lowndes, and M.L. Simpson, Appl. Phys. Lett. **79**, 2970 (2001).

[5] Y. Chen, L. Guo, S. Patel, and D. Shaw, J. Mater. Sci. **5**, 5517 (2000).

[6] Y. Zhang, A. Chang, J. Cao, Q. Wang, W. Kim, Y. Li, N. Morris, E. Yenilmez, J. Kong, and H. Dai, Appl. Phys. Lett. **79**, 3155 (2001).

[7] J. Yu, X.D. Bai, J. Ahn, S.F. Yoon, and E.G. Wang, Chem. Phys. Lett. **323**, 529 (2000).

[8] A. Maiti, C.J. Brabec, C.M. Roland, and J. Bernholc, Phys. Rev. B **52**, 14850 (1995).

[9] A. Maiti, C.J. Brabec, C.M. Roland, and J. Bernholc, Phys. Rev. Lett. **73**, 2468 (1994).

[10] W. Merchan-Merchan, A. V. Saveliev, and L.A. Kennedy, Carbon N. Y. **42**, 599 (2004).

[11] J. Blažek, P. Špatenka, F. Pácal, C. Täschner, and A. Leonhardt, Diam. Relat. Mater. **13**, 503 (2004).

[12] Q. Bao, H. Zhang, and C. Pan, Comput. Mater. Sci. **39**, 616 (2007).

[13] H.W. Wei, K.C. Leou, M.T. Wei, Y.Y. Lin, and C.H. Tsai, J. Appl. Phys. **98**, 044313 (2005).

[14] G.S. Bocharov, A.A. Knizhnik, A. V Eletskii, and T.J. Sommerer, Tech. Phys. **57**,

270 (2012).

[15] A.F. Pal, T. V Rakhimova, N. V Suetin, M.A. Timofeev, and A. V Filippov, Plasma Phys. Reports **33**, 43 (2007).

[16] M.A. Lieberman and A.J. Lichtenberg, *Principles of Plasma Discharges and Materials Processing: Second Edition* (John Wiley & Sons, 2005).

[17] A. Tewari and S.C. Sharma, Phys. Plasmas **21**, 063512 (2014).

[18] R. Gupta, S.C. Sharma, and R. Sharma, Plasma Sources Sci. Technol. **26**, 024006 (2017).

[19] Z. Marvi, S. Xu, G. Foroutan, and K. Ostrikov, Phys. Plasmas **22**, 013504 (2015).

[20] M.S. Sodha, S. Misra, S.K. Mishra, and S. Srivastava, J. Appl. Phys. **107**, 103307 (2010).

[21] I.B. Denysenko, S. Xu, J.D. Long, P.P. Rutkevych, N.A. Azarenkov, and K. Ostrikov, J. Appl. Phys. **95**, 2713 (2004).

[22] Antonio Miguel da Cruz Baptista Dias, Modeling of Low Pressure Plasmas in CH4-H2 Mixtures, Instituto Superior Técnico, Universidade de Lisboa, 2012.

[23] I. Denysenko and K. Ostrikov, J. Phys. D. Appl. Phys. **42**, 015208 (2009).

[24] R. Gupta and S.C. Sharma, Phys. Plasmas **24**, 073504 (2017).

[25] H. Mehdipour, K. Ostrikov, and A.E. Rider, Nanotechnology **21**, 455605 (2010).

[26] I. Denysenko and N.A. Azarenkov, J. Phys. D. Appl. Phys. **44**, 174031 (2011).

[27] I. Denysenko and K. Ostrikov, Appl. Phys. Lett. **90**, 10 (2007).

[28] S. Hofmann, G. Csányi, A.C. Ferrari, M.C. Payne, and J. Robertson, Phys. Rev. Lett. **95**, 036101 (2005).

[29] M. Yudasaka, R. Kikuchi, T. Matsui, Y. Ohki, S. Yoshimura, and E. Ota, Appl. Phys. Lett. **67**, 2477 (1995).

[30] R.G. Forbes, C.. Edgcombe, and U. Valdrè, Ultramicroscopy **95**, 57 (2003).

[31] P. Poncharal, Z.L. Wang, D. Ugarte, and W.A. De Heer, Science **283**, 1513 (1999).

[32] C. Bower, O. Zhou, W. Zhu, D.J. Werder, and S. Jin, Appl. Phys. Lett. **77**, 2767 (2000).

[33] M. Mao and A. Bogaerts, J. Phys. D. Appl. Phys. **43**, 205201 (2010).

[34] D. Herrebout, A. Bogaerts, M. Yan, R. Gijbels, W. Goedheer, and E. Dekempeneer, J. Appl. Phys. **90**, 570 (2001).

[35] M.S. Bell, K.B.K. Teo, R.G. Lacerda, W.I. Milne, D.B. Hash, and M. Meyyappan, Pure Appl. Chem. **78**, 1117 (2006).

[36] W. Wunderlich, Diam. Relat. Mater. **16**, 369 (2007).

[37] A. Roettgen, I. Shkurenkov, M. Simeni Simeni, V. Petrishchev, I. V. Adamovich, and W.R. Lempert, Plasma Sources Sci. Technol. **25**, 055009 (2016).

[38] H. Wang and Z.F. Ren, Nanotechnology **22**, 405601 (2011).

Chapter - 3

STUDY OF PLASMA PRE-TREATMENT EFFECTS ON THE CATALYST NANOPARTICLE AND CORRESPONDING CNT GROWTH

PUBLICATION

- **Umang Sharma** and Suresh C. Sharma, "Investigations on Plasma Pretreatment of Catalyst Film and Catalyzed Growth of Carbon Nanotube", *IEEE Transactions on Plasma Science* **50**, 888-898 (2022).

3

STUDY OF PLASMA PRE-TREATMENT EFFECTS ON CATALYST NANOPARTICLE AND CNT GROWTH

3.1 BRIEF OUTLINE OF THE CHAPTER

The catalyzed-growth process of carbon nanotubes (CNTs) in a C_2H_2/H_2 plasma is established theoretically in this chapter to explore the effect of plasma pre-treatment of catalyst nanofilm and its effect on CNT growth. We have also deliberated different catalyst nanoparticles and their consequences on the nanotube growth considering a theoretical model which includes the dynamics of catalyst nanoparticle, plasma sheath and plasma species (ions, neutrals and electrons), the generation of atomic C and H species on the catalyst surface and taking into contemplation several processes essential for the plasma-assisted CNT growth. The theoretical study aims to improve the understanding of using different catalysts for various scientific fields by unravelling their effect on CNT growth. The pre-treatment effects on the catalyst nanofilm for nanoparticle formation is deliberated. The effects of increasing catalyst nanofilm thickness on catalyst size and density were attained. For same plasma conditions, different metal catalysts (Ni, Fe, Co) were studied for their influence on CNT growth. The results of this theoretical study were compared to the SEM, TEM and other experimental observations and can provide a better insight into plasma aided catalytic synthesis of CNT growth for various applications.

3.2 INTRODUCTION

The synthesis of CNTs can be of catalytic or non-catalytic type. The catalytically grown CNTs have improved characteristics such as yield and quality of the CNTs[1,2]. The transition metals nanoparticles are of utmost effectiveness owing to their high diffusion rate and carbon solubility. Thorough studies on the simple in-situ production of heteroatom-doped carbon nanomaterials for efficient catalytic applications has recently been demonstrated[3,4]. A catalyst nanofilm deposited over the substrate for the catalytic method transforms into catalyst nanoparticles (via plasma processing or etching)[5] which acts as the seed layer, essential for the nucleation of CNTs[6,7]. Numerous experiments determine that the catalyst nature and size govern the nanotube's growth, which can be altered on varying the plasma conditions[8,9]. The transition metals, namely iron (*Fe*), cobalt (*Co*) and nickel (*Ni*), can be used as a pure metal catalyst for CNT synthesis[10–14]. A metal nanofilm pre-deposited over a substrate is etched in the presence of plasma to obtain metal catalyst nanoparticles. This pre-treatment can alter the surface with preferred characteristics by adjusting the plasma chemistry and plasma operating conditions.

Yen *et al.*[15] suggested that hydrogen pre-treatment is essential for catalytic activity preceding CNT growth for the CVD process. They obtained worm-like CNFs for thermally annealed nanofilm and spaghetti-like CNTs for hydrogen plasma etching of the film.

Chang *et al.*[9,16] used pure hydrogen for pre-treatment of nickel catalyst film to break it into nanoparticles and showed that plasma pressure and power influence the catalyst size greatly and hence the diameter of CNT.

Yang *et al.*[17] showed plasma treatment using hydrogen, nitrogen and oxygen for a nickel film and deliberated improvement in CNT number density and quality.

Wang *et al.*[18] exhibited consistent growth of multiwalled CNTs on pre-treatment of catalyst nanofilm with NH_3. They also described the influence of hydrogen gas flow on the dimension of nickel catalyst[19]. The catalyst and CNT parameters were plasma power and pre-treatment time-dependent.

Hoyos-Palacio *et al.*[13] produced chemical vapor deposition (CVD) grown CNTs using nickel, cobalt, iron and molybdenum as catalysts and observed the finest growth with nickel. Huang *et al.*[14] studied the effect of Ni, Fe and Co catalyst on nanotube growth via plasma-enhanced chemical vapor deposition (PECVD).

Valentini *et al.*[20] observed the effect of catalyst layer thickness on CNT growth parameters. Labbaye *et al.*[10] also investigated the catalytic effect on CNT production. Wang *et al.*[12] studied the formation of catalyst nanoparticles and their underlayer for the CNT growth.

Chang *et al.*[16] and Jian *et al.*[21] obtained that CNTs synthesized on catalsyt were well-aligned and had a similar diameter and density as catalyst on treatment with H_2 or H_2/N_2 plasmas.

In the this chapter, we examine plasma pre-treatment effects on catalyst nanoparticles and CNT growth. The dynamics of catalyst film thickness, catalyst size and their effects on the growth parameters of the nanotube is also studied. The model will also consider the consequences of using different catalysts for CNT nucleation and growth in plasma.

3.3 MODEL DESCRIPTION

The catalyst-assisted growth of CNTs aims to increase nanotube production, better growth, enhance properties, or modify their structures for various applications. The most commonly used catalyst for CNT production via PECVD are transition metals such as iron (*Fe*), cobalt (*Co*) and nickel (*Ni*). The nanoparticles are achieved from the nanofilms via the plasma processing technique. Along with being fast, this method helps achieve catalyst nanoparticles of high quality and activity compared to conventional methods. Plasma processing leads to well-dispersed and smaller catalyst particles having a strong interaction with the substrate leading to better activity and support. Many chemical reactions and species are considered to demonstrate the phenomena of nucleation and growth mechanism of CNTs[22]. An analytical study has been performed investigating the effect of plasma pre-treatment on the catalyst nanoparticles and their result on the CNT growth. The role of different catalyst nanoparticles on the growth of CNT is also deliberated. The chapter incorporates

particle balance equations, energy-momentum balance equations, and Poissons equation that are solved numerically for a reactive plasma constituted by a primary hydrocarbon gas - acetylene (C_2H_2) represented as A and etchant gas - hydrogen (H_2) represented as B throughout the work, respectively. The most prevailing hydrocarbon and carrier species considered in the model are listed in Table 3.1.

Type	Neutral species	Positive species
A	$C_2H, C_2H_2, C_2H_3, C_2H_4$	$C_2H_2^+, C_2H^+, C_2H_3^+, C_2H_4^+$
	$C_4H_3, C_4H_2, C_6H_2, C_6H_4$	$C_4H_3^+, C_4H_2^+, C_6H_4^+, C_6H_2^+$
B	H, H_2	H^+, H_2^+

Table 3.1 Plasma species considered in the computation.

The study considers eight acetylene ions, two hydrogen ions, eight acetylene neutrals, and two hydrogen neutrals, respectively. The remaining species were omitted because they primarily sputter and etch out amorphous carbon from the catalyst surface and have a diminishing role in the CNT growth. The graphic illustration of the catalytic CNT growth model in a reactive plasma is represented in Fig. 3.1. The initialization of nanotube growth starts on the facet of metallic catalyst nanoparticles required to disintegrate hydrocarbon species. The carbide formation allows the decomposition-segregation of carbon atoms to penetrate through the nanoparticle and regenerate into graphitic cylinders. An interface between the bulk plasma and plasma sheath at z = 0 is considered to study the plasma sheath model, electronic, ionic, neutral fluxes, and plasma species energies. The following steady-state fluid equations[23,24] constitute this 1-D model within the plasma, which is composed of a neutral (z < 0) and a non-neutral region (z > 0):

$$\frac{\partial}{\partial z}(n_{ij}u_{ij}) = n_e \nu_{if}, \tag{3.1}$$

$$\frac{\partial}{\partial z}(n_e u_e) = \sum_{ij} n_e \nu_{if}, \tag{3.2}$$

where n_{ij} and n_e are the number densities; u_{ij} and u_e are the velocities; m_{ij} and m_e are masses of the ionic and electronic species undertaken in the investigative model,

respectively. The above equations represent the particle balance equations for charged plasma species.

$$m_{ij}u_{ij}\left(\frac{\partial u_{ij}}{\partial z}+\nu_{cf}\right)=e\frac{\partial\varphi}{\partial z} \tag{3.3}$$

$$m_e u_e \nu_{cf} = e\frac{\partial\varphi}{\partial z} \tag{3.4}$$

The Eqs. (3.3) and (3.4) describe the momentum balance equations for charged plasma species, respectively. ν_{cf} is defined as the neutral-ion collision frequency, ν_{if} is the neutral atom ionization frequency due to electron collision. The sheath potential of the plasma is defined as φ.

$$\frac{1}{4\pi e}\frac{\partial^2\varphi}{\partial z^2}=n_e-\sum_{ij}\zeta_{ij}n_{ij}\,. \tag{3.5}$$

Equation (3.5) defines Poisson's equation that defines the sheath potential by considering the ion and electron density, where ζ_{ij} is the ratio of number density for j^{th} an ion to the electron, $\sum_{ij}\zeta_{ij}=0$ and $0<\zeta_{ij}<1$.

The nanoparticles on the substrate are charged due to immersion in the reactive plasma as it contains various charged species (i.e., electrons, ions, etc.). The nanoparticles usually attain a negative charge, and the magnitude of this charge developed depends significantly upon the plasma conditions and particle sizes. Following Fig. 3.1,

(i) A catalyst thin film is pre-deposited over the substrate and is treated with hydrogen plasma to obtain the fundamental growth point i.e., metal catalyst nanoparticles over the substrate[25].

(ii) The hydrocarbon gases decay on the particle's surface due to substrate heating and high power plasma. Some of these adsorbed ions are desorbed from the catalyst's surface due to thermal dehydrogenation and dissociation. The active area of the catalyst nanoparticle generates numerous carbon atoms that diffuse over the surface and the volume of the catalyst[26–28].

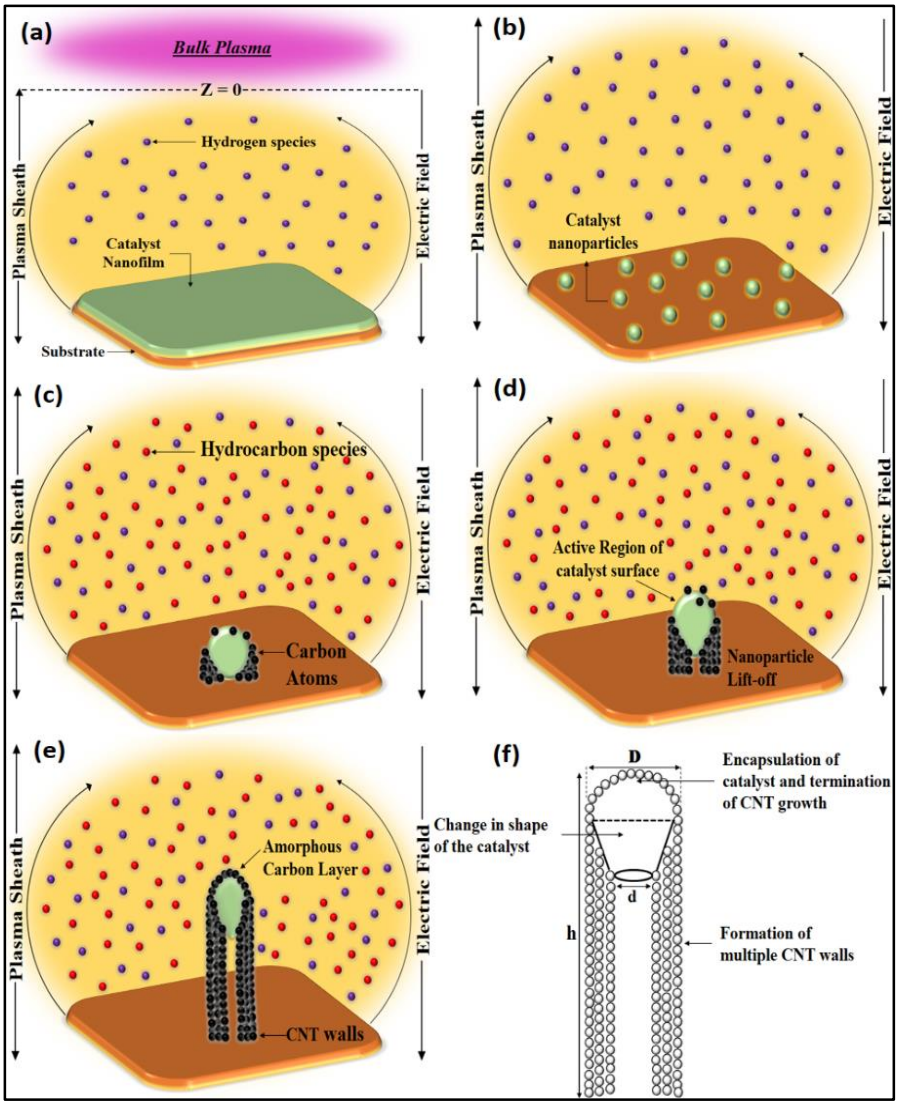

Figure 3.1 Catalytic CNT growth representation **(a)** nanofilm deposited on substrate, **(b)** hydrogen plasma segregates nanofilm into nanoparticles, **(c)** hydrocarbon species dissociate on catalyst surface into C atoms which diffuse over catalyst surface and bulk and initiate growth, **(d)** with diffusion, C atoms precipitate at the rear end of catalyst forming graphitic walls, **(e)** when catalyst is covered with amorphous carbon layer, growth terminates **(f)** catalyst gets fully encapsulated inside CNT, multiple walls are formed and catalyst shape also changes due to wall stresses.

(iii) These carbon atoms dissolve into the catalyst until it is supersaturated, after which they start precipitating out of the rear end of the metal nanoparticle and initiate the formation of graphitic layers around the nanoparticle.

(iv) The growth of CNT and the etching due to etchants species present in the plasma happen simultaneously. The nanoparticle's shape starts to deform due to the stresses exerted by these graphitic layers on the catalyst[29,30].

(v) The CNT growth concludes due to the encapsulation of the catalyst under amorphous carbon layers that covers the nanoparticle's active area[7].

(vi) The nanotube is aligned vertically simultaneous to the growth due to the electrostatic forces provided by the plasma sheath[22].

3.3.1 PRE-TREATMENT OF NANOFILM AND CREATION OF NANOPARTICLES

Prior to CNT growth, a catalyst nanofilm is pre-deposited on the substrate surface. The nanofilm is processed in hydrogen plasma (plasma processing) to convert it into a seed layer of catalyst nanoparticles. The energy balances in plasma processing, i.e. the total power input on the surface of the substrate is the sum of contributions from different energy fluxes per unit area[31], i.e. power interchange of plasma species (neutrals, ions and electrons), various reactions involving recombination or collection and sputtering of the nanofilm.

$$Power\ Input = \begin{pmatrix} P_{neutrals} + P_{ions\,\&\,electrons} + \\ P_{processes} + P_{reactions} + P_{external} \end{pmatrix}$$

Considering this power balance which takes into account the input plasma power of the PECVD reactor and its effect on the power gain and loss over substrate surface and nanofilm which fragments it into nanoparticles, we get-

$$\partial_\tau (m_{nf} C_{nf} T_S) = T_S C_{nf} A_{nf} \rho_{nf} \partial_\tau \left(V_{ct} n_{ct} \right)$$
$$= T_S C_{nf} A_{nf} t_{nf} \rho_{nf} \frac{1}{n_{ct}} \partial_\tau \left(n_{ct} \right)$$

$$T_S C_{nf} A_{nf} t_{nf} \rho_{nf} \frac{1}{n_{ct}} \partial_\tau \left(n_{ct}\right) = \left[\underset{p}{\overset{nf}{\xi}} \varepsilon_p^{nf} + \underset{ip}{\overset{nf}{\xi}} \varepsilon_{ip}^{nf} + \underset{e}{\overset{nf}{\xi}} \varepsilon_e^{nf} \right] + \left[\frac{3}{2} k_B T_S \left(1-\gamma_{ip}\right) \underset{ip}{\overset{nf}{\xi}} + \delta\left(1-\gamma_e\right)\left[2k_B T_e - \frac{3}{2} k_B T_S \right] \underset{e}{\overset{nf}{\xi}} \right] + A_{nf} \left[\begin{array}{l} \upsilon_0 \sigma_{ads} U_B n_p \left(k_B T_p / m_B\right)^{1/2} \\ + y_d E_i \left(1-\theta_t\right) n_{ip} \left(k_B T_{ip} / m_{ip}\right)^{1/2} \end{array} \right] \quad (3.6)$$

Equation (3.6) refers to the disintegration of nanofilm into nanoparticles deliberating the dynamics involved at the nanofilm surface. m_{nf} is the nanofilm mass, C_{nf} denotes the nanofilm specific heat and ρ_{nf} is the nanofilm density. $V_{ct}\left(=\frac{2\pi R_{ct}^3}{3}\right)$ is the catalyst volume, where R_{ct} is catalyst radius. A_{nf} and t_{nf} are nanofilm area and thickness, and n_{ct} is density of nanoparticles. y_d is the sputtering yield. U_B is the surface binding energy for the catalyst. ε_e^{nf}, ε_{ip}^{nf}, and ε_p^{nf} are the mean energies of the electrons, ionic and neutral species of hydrogen at the metal nanofilm surface given by $\varepsilon_k^{nf} = \left[\left(\frac{2-Z\gamma_k}{1-Z\gamma_k}\right) - Z\gamma_k\right] k_B T_k$ and $\gamma_k = \frac{E_b}{k_B T_k}$. n_{ip}, n_p and n_e are the number densities of plasma species. Also, $\underset{ik}{\overset{nf}{\xi}}$, $\underset{k}{\overset{nf}{\xi}}$ and $\underset{e}{\overset{nf}{\xi}}$ are the collection current of the ions, neutrals and electrons at the nanofilm surface defined as-

$$\underset{ip}{\overset{nf}{\xi}} = n_{ip}(z) A_{nf} \left(\frac{8k_B T_{ip}}{\pi m_{ip}}\right)^{1/2} \exp\left[-\frac{E_b}{k_B T_S}\right] \exp\left[-\frac{eU_S}{k_B T_S}\right],$$

$$\xi_p^{nf} = n_p(z) A_{nf} \left(\frac{8 k_B T_p}{\pi m_p} \right)^{1/2},$$

$$\xi_e^{nf} = n_e(z) A_{nf} \left(\frac{8 k_B T_e}{\pi m_e} \right)^{1/2} \exp\left[\frac{eV_S}{k_B T_e} + \frac{eU_S}{k_B T_S} \right].$$

The left part of the Eq. (3.6) refers to the increased power due to the catalyst nanofilm etching. On the right part of the equation, the first term takes into account the change in energy due to the collection of neutral, ionic and electronic species at nanofilm surface, the second term considers neutral atom formation and loss of electrons due to sticking and collisions, and the last term denotes plasma etching and sputtering of the nanofilm[32].

3.3.2 CHARGE BALANCE OF CARBON NANOTUBES

$$\partial_\tau(Z) = \sum_{A=1}^{8} (\xi_{iA}^{tip} + \xi_{iA}^{cyl}) + \sum_{B=1}^{2} (\xi_{iB}^{tip} + \xi_{iB}^{cyl}) - \gamma_e (\xi_e^{tip} + \xi_e^{cyl}) \tag{3.7}$$

The time progression of charge over the nanotube surface is represented by Eq. (3.7). Due to positive ions and electronic species deposition, a charge is developed over the nanotube's tip and cylindrical surface. The above equation considers *Z* as the charge generated on the CNT surface and γ_e is the sticking coefficient of electrons. The first and second term of Eq. (3.7) can be expanded in the form of Eq. (3.8) and (3.9), respectively (where *j=A,B).*

$$\xi_{ij}^{tip} = n_{ij}(z) \pi r^2 \left(\frac{8 k_B T_{ij}}{\pi m_{ij}} \right)^{1/2} \left[1 - Z\alpha_{ij} \right] \exp\left[-\frac{E_b}{k_B T_S} \right] \exp\left[-\frac{eU_S}{k_B T_S} \right] \tag{3.8}$$

$$\xi_{ij}^{cyl} = n_{ij}(z) rl \left(\frac{2\pi k_B T_{ij}}{m_{ij}} \right)^{1/2} \exp\left[-\frac{E_b}{k_B T_S} \right] \exp\left[-\frac{eU_S}{k_B T_S} \right] \times \left\{ \frac{2}{\sqrt{\pi}} \left(\frac{eV_S}{k_B T_{ij}} \right)^{1/2} + \exp\left[\frac{eV_S}{k_B T_{ij}} \right] erfc\left[\left(\frac{eV_S}{k_B T_{ij}} \right)^{1/2} \right] \right\} \tag{3.9}$$

These equations define the amount of charge collected due to ionic species at the nanotube's tip and cylindrical regions, respectively. The third term in Eq. (3.7) can be expanded in the form of Eq. (3.10) and (3.11), respectively.

$$\xi_e^{tip} = n_e(z)\pi r^2 \left(\frac{8k_B T_e}{\pi m_e}\right)^{1/2} \exp\left[Z\alpha_e + \frac{eU_S}{k_B T_S}\right] \tag{3.10}$$

$$\xi_e^{cyl} = n_e(z) r l \left(\frac{2\pi k_B T_S}{m_e}\right)^{1/2} \exp\left[\frac{eV_S}{k_B T_e} + \frac{eU_S}{k_B T_S}\right] \tag{3.11}$$

These equations define the charge collected due to electrons at the nanotube's tip and cylindrical regions, respectively. $\alpha_e \left(= \frac{e^2}{r k_B T_e}\right)$ and $\alpha_{ij} \left(= \frac{e^2}{r k_B T_{ij}}\right)$. The other terms in the above equations are termed in Table 3.2.

Terms	Description
V_S	CNT tubular surface potential
U_S, T_S	Substrate bias and temperature
E_b	Energy necessary for bulk diffusion
$n_{ij}(z) = n_{ij0}\left(1 - \frac{2e\varphi(z)}{m_{ij}u_{ij0}^2}\right)^{-1/2}$	Plasma sheath ion density
$n_e(z) = n_{e0}\exp\left(\frac{\lvert e\rvert \varphi(z)}{k_B T_e}\right)$	Plasma sheath electron density
$\varphi(z) = \varphi_0 \exp\left(-\frac{z}{\lambda_D}\right)$	Electrostatic sheath potential

Table 3.2 Interpretation of functions/parameters termed in Eqs. (3.8 - 3.11).

3.3.3 TIME-EVOLUTION OF PLASMA ELECTRON DENSITY

$$\partial_\tau(n_e)=\left[\sum_{A=1}^{8}\beta_A n_A+\sum_{B=1}^{2}\beta_B n_B\right]-\left[\sum_{A=1}^{8}\alpha_A n_e n_{iA}+\sum_{B=1}^{2}\alpha_B n_e n_{iB}\right] \\ \frac{n_{CNT}}{\lambda_s}\begin{pmatrix} tip & cyl \\ \xi & \xi \\ e & e \end{pmatrix}\gamma_e-n_e\,\mathrm{K}_{wall}^{e}, \tag{3.12}$$

The time progression of bulk plasma electron density is defined by Eq. (3.12). The first term in the above equation defines the gain in density owing to the dissociative-ionization of neutrals *j=(A, B)*; the second term calculates loss due to the ion-electron recombination. The decrease in electron density due to the accumulation of electrons at the nanotube surface is interpreted in the third term, and lastly, the fourth term is the electron discharge loss to the reactive plasma chamber walls. Other terms in Eq. (3.12) are mentioned in Table 3.3.

Terms	Description
β_j	Ionization coefficient of neutrals
$\alpha_j(T_e)=\alpha_{j0}\left(300/T_e\right)^k$	Recombination coefficient for ions and electrons where $k=-1.2$ [32]
$\mathrm{K}_{wall}^{e}=\left(\frac{\gamma_e u_e A_{chm}}{4V}\right)$	Loss rate of electrons over the volume on the discharge wall[33]
A_{chm}, V	Cylindrical plasma chamber's surface area and volume (L=23cm and D=32cm)[33]

Table 3.3 Interpretation of functions/parameters termed in Eqs. (3.12).

3.3.4 TIME-EVOLUTION OF PLASMA ION DENSITY

$$\partial_\tau(n_{iA}) = \overbrace{\left\{\beta_A n_A + \left(\sum_{\ell AB} k_\ell n_A n_{iB} - \sum_{qBA} k_q n_B n_{iA}\right) + \left(\frac{P}{E_{CH}^{diss} V}\right)\right\}}^{Gain} - \overbrace{\left\{\alpha_A n_e n_{iA} + \frac{n_{CNT}}{\lambda_s}\begin{pmatrix} tip & cyl \\ \xi & \xi \\ iA & iA \end{pmatrix} + n_{iA}\begin{matrix} iA \\ \mathrm{K} \\ wall \end{matrix}\right\}}^{Loss} \tag{3.13}$$

$$\partial_\tau(n_{iB}) = \overbrace{\left\{\beta_B n_B + \left(\sum_{qBA} k_q n_B n_{iA} - \sum_{\ell AB} k_\ell n_A n_{iB}\right) + \left(\frac{P}{E_H^{diss} V}\right)\right\}}^{Gain} - \overbrace{\left\{\alpha_B n_e n_{iB} + \frac{n_{CNT}}{\lambda_s}\begin{pmatrix} tip & cyl \\ \xi & \xi \\ iB & iB \end{pmatrix} + n_{iB}\begin{matrix} iB \\ \mathrm{K} \\ wall \end{matrix}\right\}}^{Loss} \tag{3.14}$$

Equations (3.13) and (3.14) denote the time progression of bulk plasma ion number density of A and B type ions. In the above equations, the first part refers to the rise in the ion density owing to dissociative-ionization of neutrals *j=(A, B)*, changes due to ion-neutral atom plasma reactions, and ion dissociation by plasma power, respectively. The second part of the equations refers to the fall in ion number density as the ions and electrons recombine, accumulation of ions on the nanotube surface, and discharge loss of ions to the reactive plasma chamber walls. $\begin{matrix} ij \\ \mathrm{K} \\ wall \end{matrix}$ is the ion discharge loss to the chamber[33], k_q, k_l are the neutral-ion reaction coefficients[34], $\delta E_{CH}^{diss} (\approx 2.1\, eV)$, $\delta E_H^{diss} (\approx 2.1\, eV)$ are the hydrocarbon and hydrogen dissociation energies[24], and P is applied plasma power.

3.3.5 TIME-EVOLUTION OF PLASMA NEUTRAL ATOM DENSITY

Equations (3.15) and (3.16) denote the time progression of bulk plasma neutrals of A and B types.

$$\partial_\tau(n_A)=\overbrace{\left\{\alpha_A n_e n_{iA}+\frac{n_{CNT}}{\lambda_s}\begin{pmatrix} tip & cyl \\ \xi & \xi \\ iA & iA \end{pmatrix}\left(1-\gamma_{iA}\right)+J_A^{desp}+\left(\mathrm{Q}_A^{IF}-\mathrm{Q}_A^{OF}\right)\right.}^{Gain}$$
$$\overbrace{\left.+\left(\sum_{qAB} k_q n_B n_{iA}-\sum_{lBA} k_l n_A n_{iB}\right)\right\}}^{Gain}-\overbrace{\left\{\beta_A n_A+\frac{n_{CNT}}{\lambda_s}\begin{pmatrix} tip & cyl \\ \xi & \xi \\ A & A \end{pmatrix}\gamma_A\right.}^{Loss} \quad (3.15)$$
$$\overbrace{\left.+J_A^{adsp}+n_A\begin{matrix} A \\ \mathrm{K} \\ wall \end{matrix}\right\}}^{Loss}$$

$$\partial_\tau(n_B)=\overbrace{\left\{\alpha_B n_e n_{iB}+\frac{n_{CNT}}{\lambda_s}\begin{pmatrix} tip & cyl \\ \xi & \xi \\ iB & iB \end{pmatrix}\left(1-\gamma_{iB}\right)+J_B^{desp}+\left(\mathrm{Q}_B^{IF}-\mathrm{Q}_B^{OF}\right)\right.}^{Gain}$$
$$\overbrace{\left.+\left(\sum_{\ell AB} k_\ell n_A n_{iB}-\sum_{qBA} k_q n_B n_{iA}\right)\right\}}^{Gain}-\overbrace{\left\{\beta_B n_B+\frac{n_{CNT}}{\lambda_s}\begin{pmatrix} tip & cyl \\ \xi & \xi \\ iB & iB \end{pmatrix}\gamma_B\right.}^{Loss} \quad (3.16)$$
$$\overbrace{\left.+J_B^{adsp}+\begin{matrix} B \\ \mathrm{K} \\ wall \end{matrix} n_B\right\}}^{Loss}+J_{thd}$$

In the above equations, the first part denotes the gain in the number density of neutrals due to ion-electron recombination, ion neutralization after their accumulation at the nanotube surface, ion desorption from the catalyst surface, changes due to neutral species inflow and outflow in the chamber, and changes owing to neutral atom-ion reactions deliberated in the study[34], respectively. The second part of the equations refers to the loss in density due to the neutral atom dissociative ionization, loss owing to the collection of neutrals on nanotube surface, neutral atom adsorption, and neutral atom discharge loss to the reactive plasma chamber walls, respectively. In Eq. (3.16),

the last term determines the rise in hydrogen neutral density due to the thermal dehydrogenation process[35]. Other terms described in the Eqs. (3.15-3.16) are designated in Table 3.4.

Terms	Description
$Q_j^{IF} = \left(\frac{4.4\times10^{17}}{V} J_j \right)$	Inflow of neutrals from the reactive plasma chamber[33]
$Q_j^{OF} = \left(\frac{\upsilon_{pump}}{V} n_j \right)$	Outflow of neutrals from the reactive plasma chamber[33]
J_j^{adsp}, J_j^{desp}	adsorption and desorption fluxes from the catalyst-substrate surface
J_{thd}	thermal dehydrogenation flux[36]
$K_{wall}^{j} = \sigma_j \frac{D_j}{\Lambda^2}$	neutral atom discharge loss with Λ as cylindrical chamber effective diffusion length[23,37]
σ_j, D_j	wall reaction and diffusion coefficient respective species[23,37]

Table 3.4 Interpretation of functions/parameters termed in Eqs. (3.15-3.16).

3.3.6 EVOLUTION OF C AND H ATOMS OVER THE CATALYST

$$\partial_\tau (n_C) = \left[\overbrace{\left\{ \sum_{A=1}^{8} (1-\theta_t) J_A + \sum_{A=1}^{8} n_A^{surf} \upsilon \exp\left(-\frac{\delta E_{CH}^{diss}}{k_B T_S} \right) + \sum_{iA=1}^{8} \left(\sum_{A=1}^{8} \frac{n_A^{surf} y_d}{\upsilon_0} \right) J_{iA} \right.}^{Gain} \right.$$

$$\left. \overbrace{+ \sum_{iA=1}^{8} J_{iA} + J_C + \sum_{iB=1}^{2} \left(\sum_{iA=1}^{8} \frac{J_{iA} \sigma_{ads}}{\upsilon} \right) J_{iB} \right\}}^{Gain} - \overbrace{\left\{ \sum_{A=1}^{8} n_A \upsilon \exp\left(-\frac{\delta E_{dCH}}{k_B T_S} \right) \right.}^{Loss} \quad (3.17)$$

$$\left. \left. \overbrace{+ \sum_{B=1}^{2} \left(\sum_{A=1}^{8} n_A^{surf} \sigma_{ads} \right) J_B + n_C \upsilon \exp\left(-\frac{\delta E_{ev}}{k_B T_S} \right) + n_C \sigma_{ads} \upsilon n_H \right\}}^{Loss} \right] \times d_\tau (\Omega_C)$$

The C species density n_c over the catalyst is signified by Eq. (3.17). The first part of the equation construes the rise in carbon density as the acetylene neutrals get adsorbed over the catalyst, thermal dissociation, ion-induced hydrocarbon dissociation, positive ion decomposition, direct carbon influx, and hydrocarbon and hydrogen ion-ion interaction, respectively. The second part of the equation construes the fall in the density of carbon owing to the hydrocarbon desorption from catalyst surface, hydrocarbon-hydrogen interaction, C species evaporation, and interaction between catalyst surface generated C and H species. Finally, the continuous hydrocarbon species dissociation over the active area of catalyst nanoparticles creates an excessive amount of carbon species, leading to an amorphous carbon layer formation that decreases the active area over the catalyst and concludes nanotube growth. The last term of Eq. (3.17) indicates the catalyst-poisoning rate that depends on the density of C atoms generated throughout the growth over the catalyst surface.

$$\partial_{\tau}(n_H) = \overbrace{\left\{\sum_{B=1}^{2} J_B(1-\theta_t) + \sum_{B=1}^{2} n_B^{surf}\upsilon\exp\left(-\frac{\delta E_{CH}^{diss}}{k_B T_S}\right) + \sum_{iA=1}^{8}\left(\sum_{A=1}^{8}\frac{n_A^{surf} y_d}{\upsilon_0}\right) J_{iA} + \sum_{iB=1}^{2} J_{iB}\right\}}^{Gain} - \overbrace{\left\{\sum_{B=1}^{2} n_B^{surf}\upsilon\exp\left(-\frac{\delta E_{dH}}{k_B T_S}\right) + \sum_{B=1}^{2} n_B^{surf}\sigma_{ads} J_B + \sum_{B=1}^{2} n_B^{surf}\sigma_{ads} J_{iB} + n_H\sigma_{ads}\upsilon n_C\right\}}^{Loss} \quad (3.18)$$

The hydrogen species number density n_H over the catalyst is signified by Eq. (3.18). The first part of the equation construes the rise in density owing to the hydrogen neutrals adsorption over catalyst surface, thermal dissociation, ion-induced dissociation of hydrocarbons, and inflow of hydrogen around the catalyst. The second part construes the fall in density owing to its desorption from the catalyst surface, the interaction between the hydrogen adsorbed over the catalyst and neutral atom, interaction between the adsorbed hydrogen over the catalyst and hydrogen ions, and C and H atom interaction. Other terms stated in Eqs. (3.17-3.18) are termed in Table 3.5.

Terms	Description
$\upsilon_0 (\approx 10^{15}\ cm^{-2})$	Adsorption sites per unit area[36]
$\upsilon (\approx 10^{13}\ Hz)$	Thermal vibration frequency[38]
$\sigma_{ads}\left(=6.8\times10^{-16} cm^2\right)$	Interaction cross-section amongst various species[36]
$n_j^{surf}\left(=\theta_j\upsilon_0\right)$	Surface number density of neutrals[2,36]
$\delta E_{CH}^{diss}\left(=2.1\ eV\right)$	Hydrocarbon dissociation energy[24]
$\delta E_{ev} (=1.8\ eV)$	Carbon evaporation energy[24]
$\delta E_{dCH}\left(=1.8\ eV\right)$	Hydrocarbon desorption energy[24]

$\delta E_{dH}\,(=1.8\ eV)$	Hydrogen desorption energy[24]
$d_{\tau}(\Omega_C)=\left(1-4n_C\pi r^2\right)$	Poisoning rate of catalyst governed by n_C that is generated throughout the growth process[22]

Table 3.5 Description of the functions/parameters mentioned in Eqs. (3.17) and (3.18).

3.3.7 CATALYTIC GROWTH OF CNT IN PLASMA

$$\partial_{\tau}\left[\pi\left(R_{ct}^2-r^2\right)l\right]=\left[\left\{D_{Surf}+D_{Bulk}+2\kappa\upsilon {R_{ct}}^2\right\}\times\frac{P\left(8\pi R_{ct}\right)n_C}{\upsilon\rho_{CNT}\sum_{A=1}^{8}\xi_{iA}}+\left\{\frac{D_m}{4\pi {R_{ct}}^2}+n_H\left(4\pi {R_{ct}}^2\right)\sum_{B=1}^{2}\xi_{iB}\right\}\right]\times\frac{m_{ct}}{\rho_{ct}} \tag{3.19}$$

The time progression of CNT growth is estimated by Eq. (3.19). The nanotube growth is assessed assuming a change in CNT volume (dependent on its radius and height). Several growth processes considered in the above equation are explained in Table 3.6.

The first part of the equation considers the surface diffusion over the catalyst surface, bulk diffusion of carbon through the catalyst volume, and the carbon atom precipitation from the rear end of the catalyst, respectively forming a tubular graphitic structure of the nanotube. The supremacy of one diffusion process over another mainly governs the synthesis of SWCNTs or MWCNTs, i.e., if bulk diffusion dominates over surface diffusion, MWCNTs are formed or else SWCNTs[39]. The second part of the equation contemplates the self-diffusion of catalyst as the CNT growth proceeds; and the amorphous carbon atom etching attached at the extremity that hinders nanotube growth. Finally, the growth and alignment of CNT proceed simultaneously due to the electrostatic force applied to the growing nanotube structure[22]. The change in the CNT diameter also changes the number of the graphitic layers or the CNT walls. For simplification, CNT walls can be estimated by the difference between the inner and outer diameter of the CNT, assuming these CNTs are perfectly aligned concentric

graphitic tubes, i.e., $\left(D_o - D_i\right)$~ number of CNT walls, where $D_o (\sim D_{ct})$ is the nanotube outer diameter which assumed to be comparable to catalyst diameter and D_i is the nanotube inner diameter.

Functions/parameters	*Description*
$D_{Surf} = a_0^2 \upsilon \exp\left(-\frac{E_{Surf}}{k_B T_S}\right)$	Surface diffusion coefficient of carbon atoms[36]
$D_{Bulk} = \frac{\upsilon r}{\pi} \exp\left(-\frac{E_{Bulk}}{k_B T_S}\right)$	Bulk diffusion coefficient of carbon atoms[36]
$D_m = D_{m0} \exp\left(-\frac{\delta E_{sd}}{k_B T_S}\right)$	Self-diffusion coefficient for metal atoms[36]
$\kappa = a_0 \upsilon \exp\left(-\frac{\delta E_{inc}}{k_B T_S}\right)$	Carbon atom incorporation rate into the CNT wall[2,36]
$a_0 \left(= 0.34\ nm\right)$	Interatomic distance between carbon atoms
$E_S \left(= 0.3\ eV\right)$	Carbon atom energy barrier for surface diffusion on the catalyst surface[36]
$E_b \left(= 1.6\ eV\right)$	Carbon atom energy barrier for bulk diffusion on the catalyst surface[36]
$\delta E_{inc} \left(= \delta E_d = 0.8\ eV\right)$	Carbon atom energy barrier to diffuse along nanotube-catalyst boundary[40]

Table 3.6 Description of the functions/parameters mentioned in Eqs. (3.19).

3.4 RESULTS AND DISCUSSION

The results for this study helps in understanding the catalyzed growth of CNT in acetylene-hydrogen plasma. To study the plasma pre-treatment, we have considered a Ni catalyst nanofilm of thickness 15 nm and the effect of plasma power, pressure and gas flow on the nanoparticles are investigated. Some of the initial plasma parameters used in the study are mentioned below. For studying the different catalyst effects, Ni, Fe and Co catalyst films are considered. The 1st order time-differential equations mentioned in the previous section are solved for CNT growth considering the experimentally obtained primary conditions and glow-discharge plasma parameters assumed from the literatures[41–44], and some are mentioned in Table 3.7.

Parameter	*Initial value*
RF power	300 *W*
Working pressure	50 *mTorr*
T_e (electron temperature)	2.0 *eV*
T_{ij} (ion species temperature)	0.20 *eV*
T_n (neutral atom temperature)	0.20 *eV*
$T_s = T_{ct}$ (substrate and catalyst temperature)	350 ℃
ρ_{ct} (nickel catalyst density)	8.96 gm/cm^3
γ_e (electron sticking coefficient)	1
γ_{ij} (ions sticking coefficient)	1
γ_j (neutral atoms sticking coefficient)	1
U_S (substrate bias)	-500 *V*
θ_t (total surface coverage)	0.01
$J_{C_2H_2}$ (methane gas flow)	50 *sccm*
J_{H_2} (hydrogen gas flow rate)	200 sc*cm*

A_{nf}	(catalyst nanofilm area)	1 cm^2

Table 3.7 Initial configuration of various parameters in the computational study.

3.4.1 Variation of catalyst diameter with plasma power and pressure

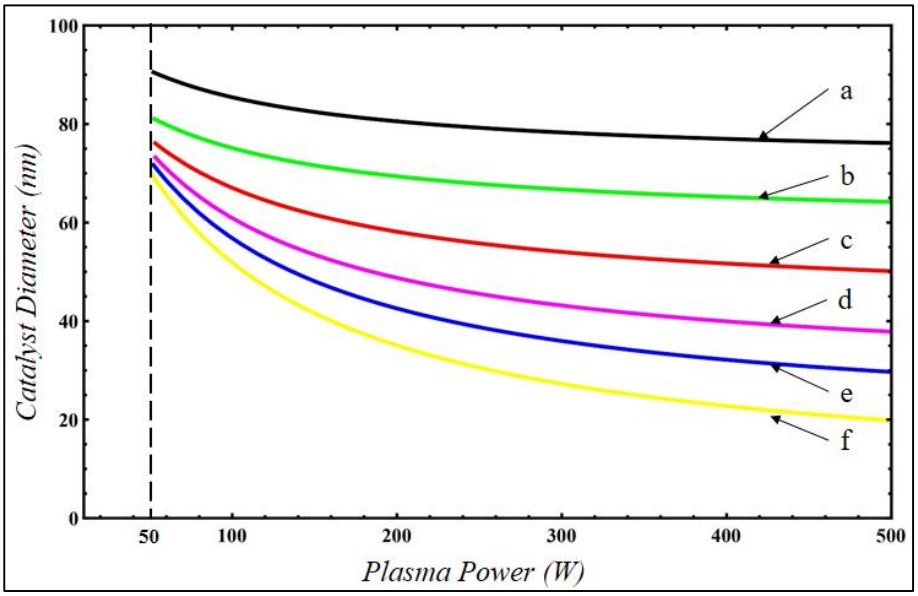

Figure 3.2 Variation of catalyst diameter with plasma power at different process pressures where a, b, c, d, e and f corresponds to 10, 20, 30, 40, 50 and 60 mTorr, respectively.

The variation of catalyst diameter with the plasma power is depicted in Fig. 3.2. For constant plasma pressure, increase in plasma power during plasma pre-treatment of nanofilm decreases the nanoparticle diameter. For high plasma power, the gaseous species' energy increases and bombarding effect on the nanofilm increases, leading to smaller nanoparticles. The result indicates that the CNT radius and length increases with time and attains saturation for a fixed value of number density of hydrocarbon ions and electron temperature. Primarily, the carbon species generated over the surface of the catalyst are deposited and the subsequently the amorphous carbon is etched by the hydrogen species which enriches the growth of CNT. With time, progressive growth of amorphous carbon layer leads to the catalyst poisoning, and thereby, saturating the CNT growth.

The effect of plasma processing pressure on the catalyst diameter is observed in Fig 3.3. For fixed plasma power, increase in the plasma pressure during pre-treatment decreases the nanoparticle diameter. This is attributed to the gas density increase for high pressure that decreases the mean free path of particles. This increases the collisional rate of gaseous species, increasing the gas flux towards the nanofilm and decreasing the nanoparticle size. The result agrees with the experimental observations of Chang *et al.*[9,16] whose SEM images of Ni nanofilm pre-treated with hydrogen shows similar trend of decreasing nanoparticle size with plasma power and pressure.

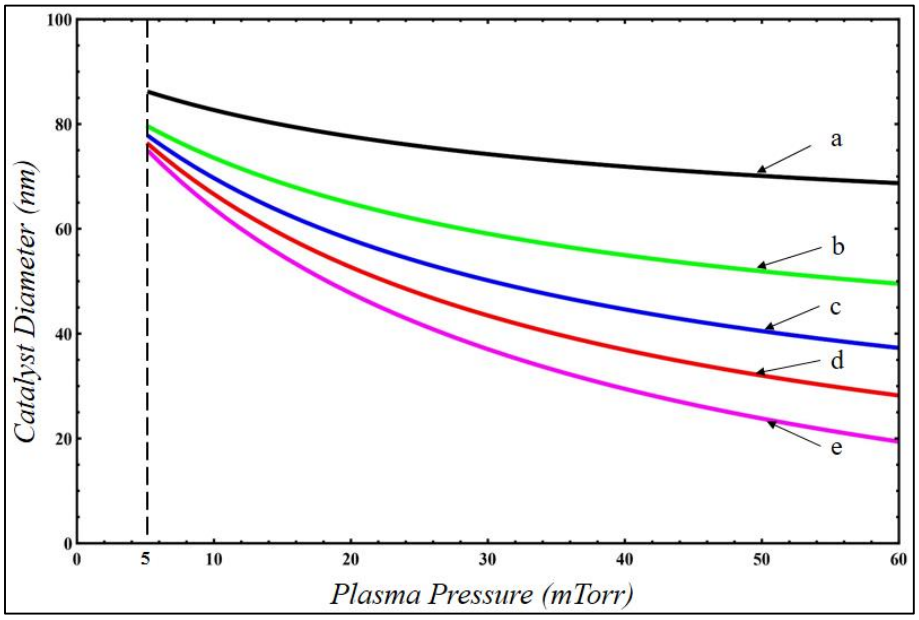

Figure 3.3 Variation of catalyst diameter with plasma pressure at different process powers where a, b, c, d and e corresponds to 100, 200, 300, 400 and 500 Watts, respectively.

3.4.2 Variation of the catalyst diameter with hydrogen flow rate

The effect of changing hydrogen flow rate during plasma pre-treatment is observed in Fig. 3.4. On increasing the hydrogen flow rate during pre-treatment, the flux of plasma species towards the nanofilm increases breaking it into smaller nanoparticles. In addition, it is also evident that smaller nanoparticles are obtained for higher pre-treatment temperature as the catalyst can move conveniently than at lower pre-treatment temperature. The SEM and TEM results from the experimental findings of Wang *et al.*[19] and Jian *et al.*[21,45] also suggest that hydrogen pre-treatment of nanofilm produce uniform and smaller particles for higher gas flow rate.

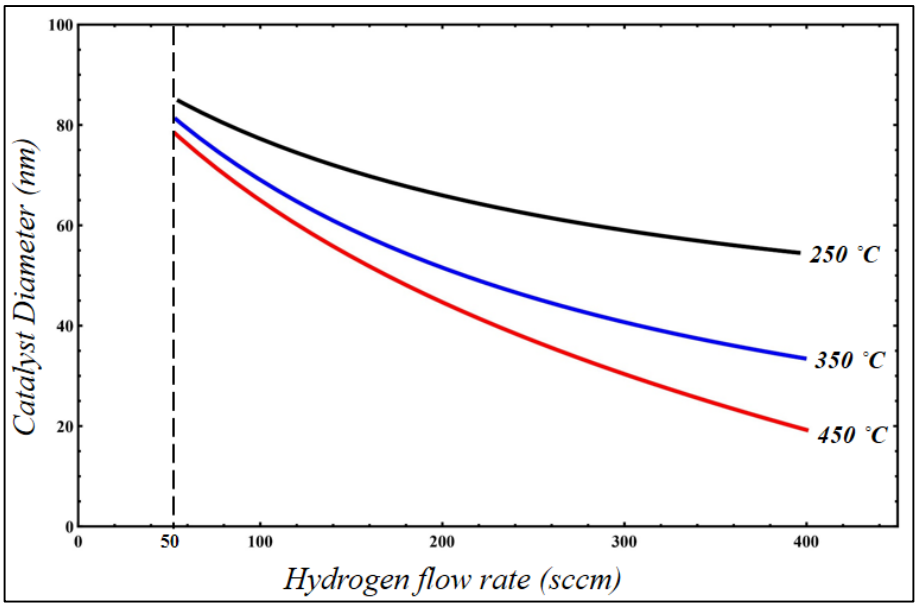

Figure 3.4 Variation of catalyst diameter with hydrogen gas flow rate at different substrate temperatures of 250 ºC, 350 ºC and 450 ºC, respectively.

3.4.3 Variation of the catalyst particle density with nanofilm thickness

The growth time variation of the catalyst particle density over the substrate for Ni catalyst for varying nanofilm thickness is represented in Fig. 3.5. It can be observed that the catalyst number density decreases on increasing the nanofilm thickness. This is attributed to the agglomeration of the larger catalyst particles on the substrate for a thicker nanofilm, decreasing their density over the substrate. Moreover, this number density increases with time as the hydrogen plasma species are rigorously and incessantly bombarded on the nanofilm until it is wholly converted to nanoparticles and attains saturation. It can be concluded that on increasing the film thickness, the catalyst obtained have increased diameter. Chhowalla *et al.*[46] and Bower *et al.*[47] showed similar dependency of nanofilm thickness on catalyst size experimentally through their SEM and TEM results for Ni and Co, respectively.

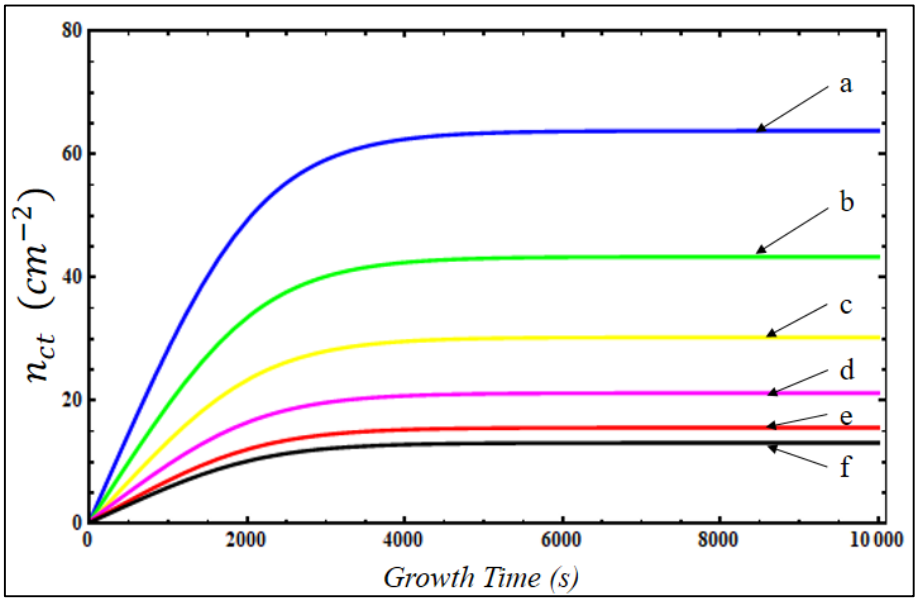

Figure 3.5 Time variation of catalyst number density for different nanofilm thickness for Ni catalyst where a, b, c, d, e, and f corresponds to 2, 4, 6, 8, 10 and 15 nm, respectively.

3.4.4 Variation of the catalyst diameter with nanofilm thickness

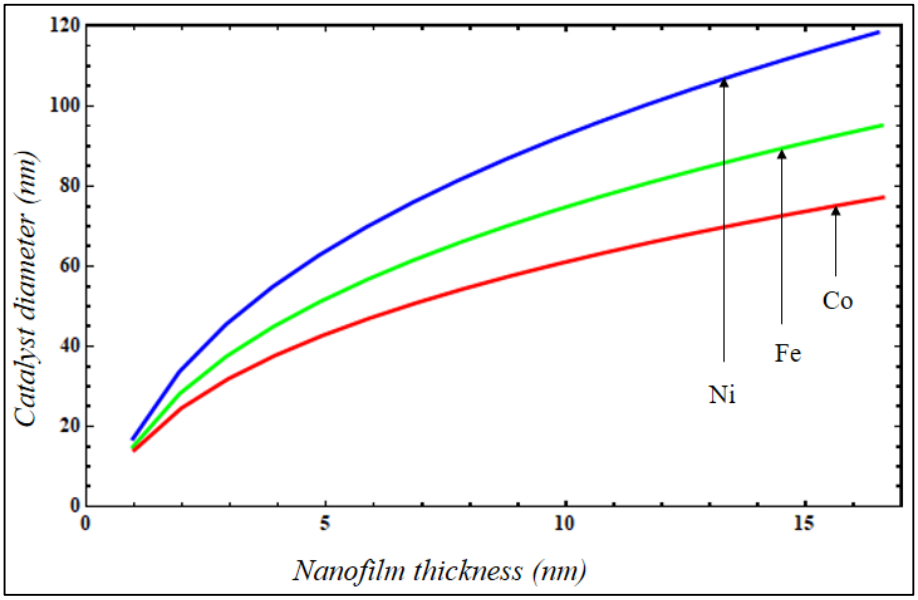

Figure 3.6 Variation of catalyst diameter with nanofilm thickness.

The variation of catalyst diameter with nanofilm thickness for Ni, Fe, and Co is represented in Fig. 3.6. It can be concluded that on increasing the film thickness, the catalyst nanoparticle obtained have increased diameter. It is also observed that Ni catalysts are bigger in diameter than Fe and Co catalysts. Huang *et al.*[14] in their experimental study showed the SEM and TEM images of plasma-assisted CNT growth for Ni, Fe and Co catalysts and observed that for the same nanofilm thickness, the grain size of Ni is more significant than that of Fe and Co and hence, observed that Ni-CNT had a larger diameter.

3.4.5 Carbon species generation with growth time

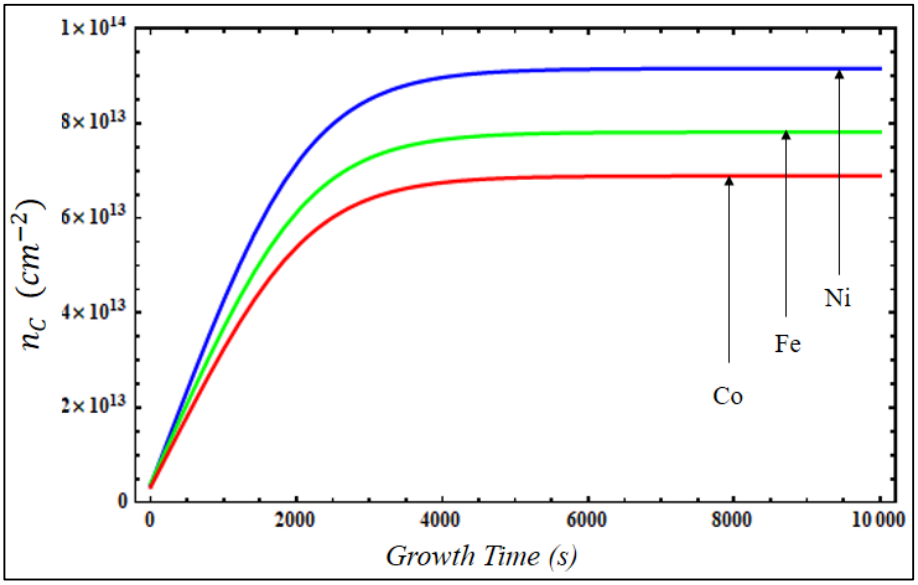

Figure 3.7 Rate of creation of C species on the catalyst.

The rate of carbon species generation over the nanoparticle for the different catalysts is denoted in Fig. 3.7. For a large catalyst, a larger active region over the catalyst surface allows more hydrocarbon species to dissociate into carbon species hence, creating more carbon species over the catalyst surface. From the observations of Fig. 3.6, it is comprehended that the carbon species generated over Ni is higher than Fe and Co for the same nanofilm thickness.

3.4.6 Variation of the nanotube inner and outer diameter

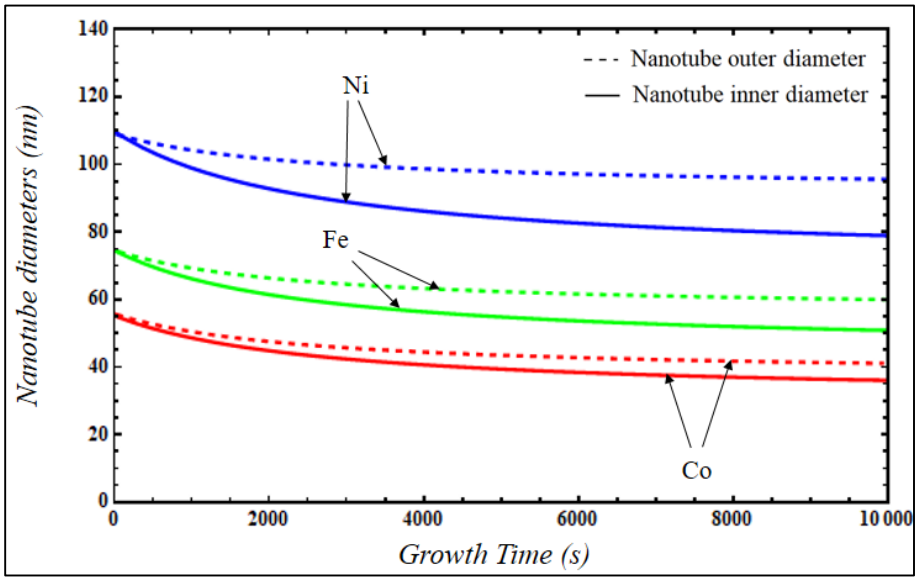

Figure 3.8 Temporal variation of CNT inner and outer diameters.

The temporal variation of CNT inner and outer diameter is depicted in Fig. 3.8. During the growth process, the carbon atoms generated over the nanoparticle diffuse out at its rear end, forming graphitic tubular layers and causing the nanoparticle to lift off. These layers exert stresses on the nanoparticle leading to its shape change. These walls produce compressive stress at the rear end of the nanoparticle surface. Hence, the inner diameter of the growing CNT is reduced due to these stresses and change the shape of the catalyst during CNT growth that gives rise to diameter reduction which is observed experimentally through SEM, HRTEM, and ETEM results of various groups[28,35,46]. The outer CNT diameter is assumed comparable to the catalyst diameter at the top of the catalyst surface; hence not much reduction is observed. Jung *et al.*[48] studied the PECVD growth of CNT over Ni catalyst film and suggested a lift-off mechanism. They also observed a more significant reduction in CNT diameter for an increasing catalyst film thickness. The nanoparticle surface produces carbon species and this region gets encapsulated once the catalyst gets saturated as these abundant carbon atoms form an amorphous carbon layer over the catalyst surface. The result shows that for a larger catalyst diameter, the reduction in the inner diameter is more. Also, CNT with Ni

catalyst has larger CNT diameters than Fe and Co. Experimentally, the FESEM and HRTEM results of Hoyos-Palacio *et al.*[13] and Huang *et al.*[14] comply with our observations.

3.4.7 Variation of CNT length with hydrocarbon density

The time variation in CNT length for different hydrocarbon densities are observed in Fig. 3.9 (i-iii) for Ni, Fe and Co, respectively. It can be seen that greater acetylene density leads to greater CNT length. When the acetylene density increases, more plasma species are present for dissociation at the catalyst surface that generate more carbon species leading to higher diffusion and precipitation on the catalyst surface. This rise in the CNT growth processes leads to a rise in the CNT length.

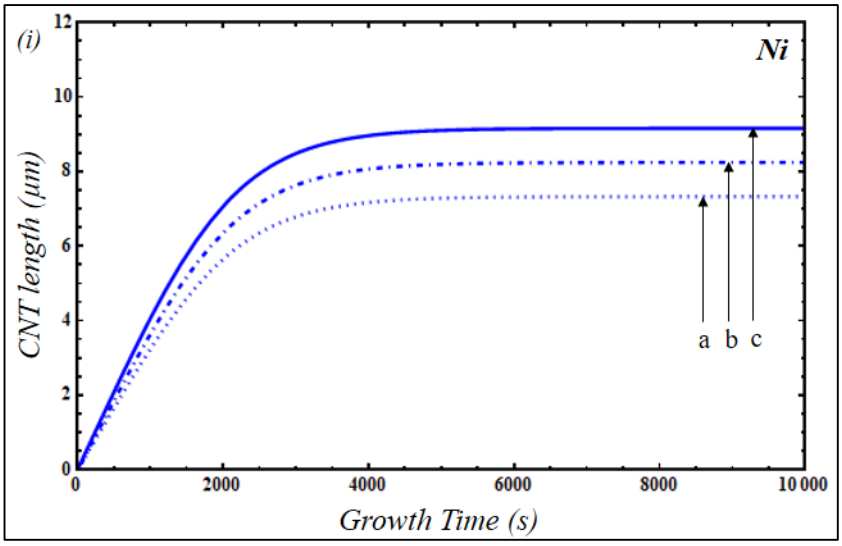

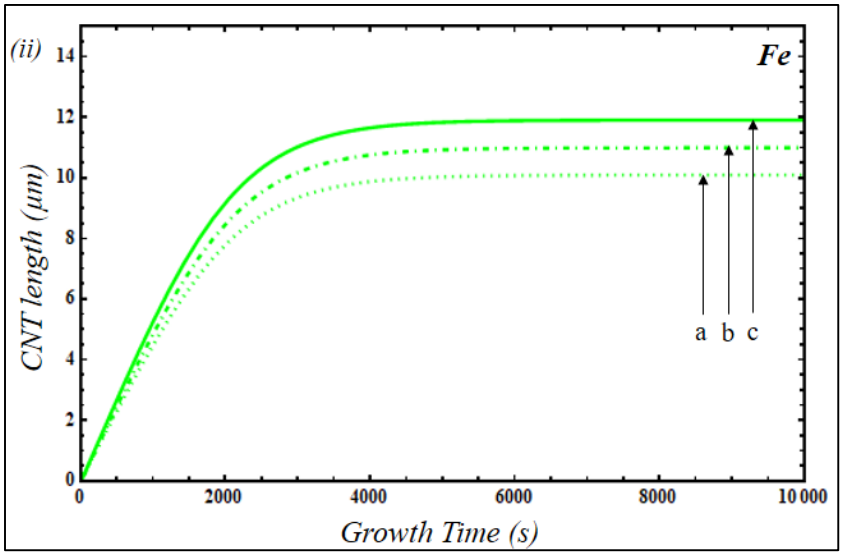

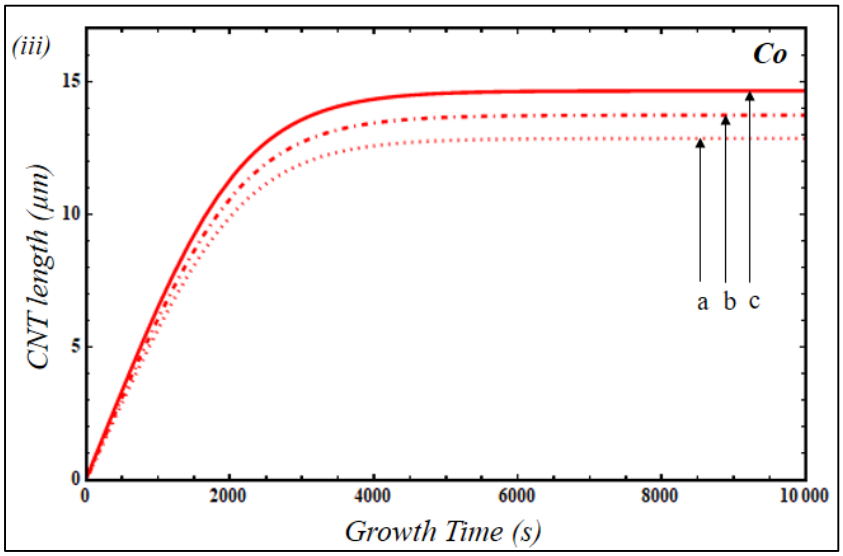

Figure 3.9 Temporal variation of CNT length for different hydrocarbon densities (where a, b and c corresponds to 10^{12}, 10^{13}, 10^{14} cm^{-3}, respectively) for (i) Ni (ii) Fe (iii) Co.

3.4.8 Variation of CNT length for different catalysts

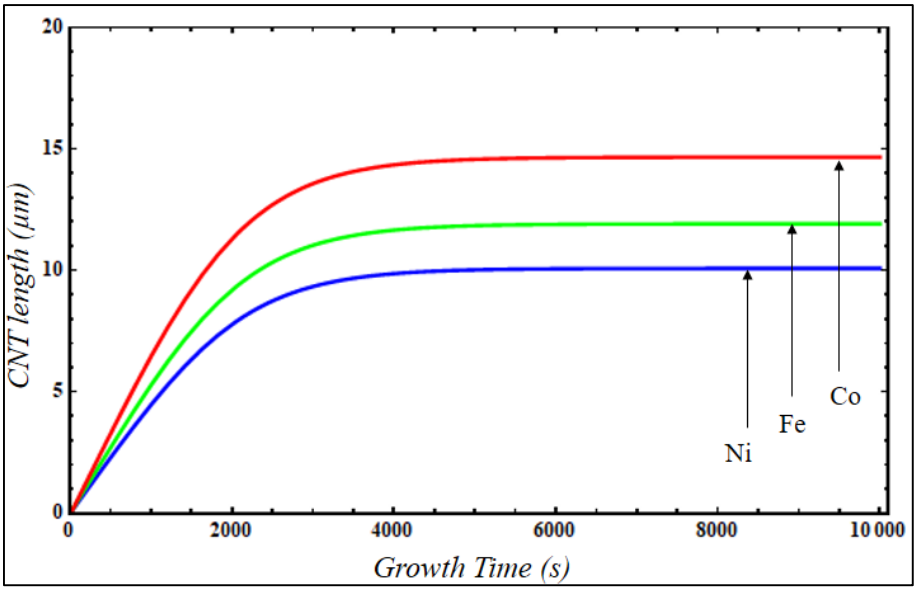

Figure 3.10 Growth time variation of CNT length for different catalysts.

The time variation of CNT length for the different catalysts is represented in Fig. 3.10. For a catalyst of smaller size, the carbon species that precipitate out at the rear end of the catalyst cannot circumvent the etching of carbon species by the hydrogen species.

Hence, the CNT starts growing in such a way that it promotes vertical growth by precipitating more at the catalyst rear end but a larger catalyst particle would cover CNT walls growing underneath from hydrogen etching, hence the number of layers increases. Chhowalla *et al.*[46] and Hofmann *et al.*[49] through their SEM results and data analysis showed this inverse proportionality of CNT length with diameter. Hence, CNT length for Co catalyst is greater than Ni and Fe.

3.4.9 Number of CNT walls with catalyst diameter

The dependency of number of walls on the Ni catalyst diameter is shown in Fig. 3.11. As catalyst diameter increases, amount of carbon species generated on the catalyst increases that diffuse and precipitate to form more graphitic tubular walls at the bottom of the catalyst. Hence, CNT with larger diameter would have more number of walls and is experimentally confirmed by Hoyos-Palacio *et al.*[13] and Huang *et al.*[14]. Similar dependency was observed for Fe and Co catalysts.

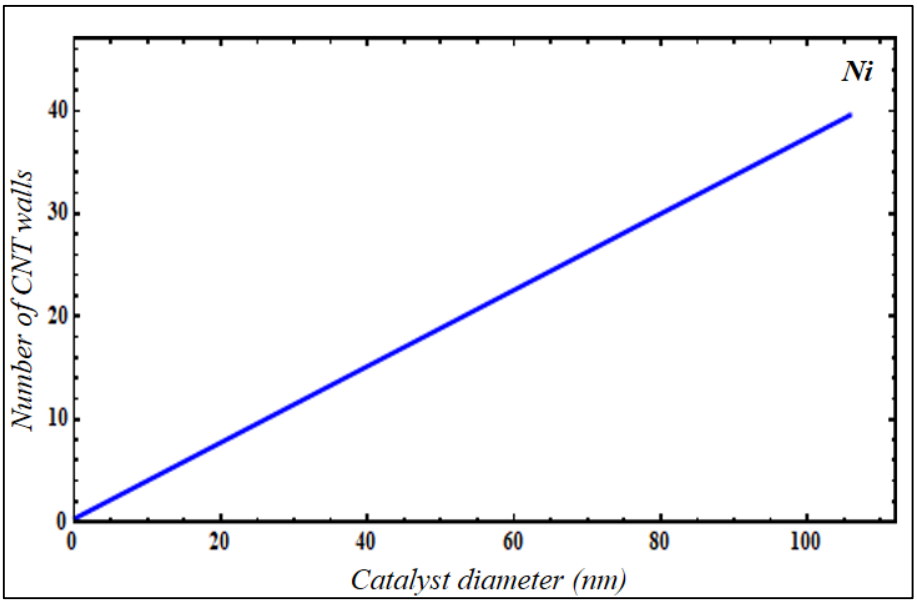

Figure 3.11 Dependence of the number of CNT walls on the catalyst diameter for Ni.

3.4.10 Time variation of number of CNT walls

Fig. 3.12 shows the time variation of the number of CNT walls for different catalysts. As CNT grows, the number of CNT walls also increases, and when the growth terminates, these walls attain a saturation. Ni having the bigger nanoparticle size has higher number of CNT walls compared to Fe and Co. The relationship of the number of CNT walls with the catalyst diameter and nanofilm thickness and its variation with growth time has been verified by the data analysis of Xie *et al.*[50], Ma *et al.*[51], and Prawoto *et al.*[52].

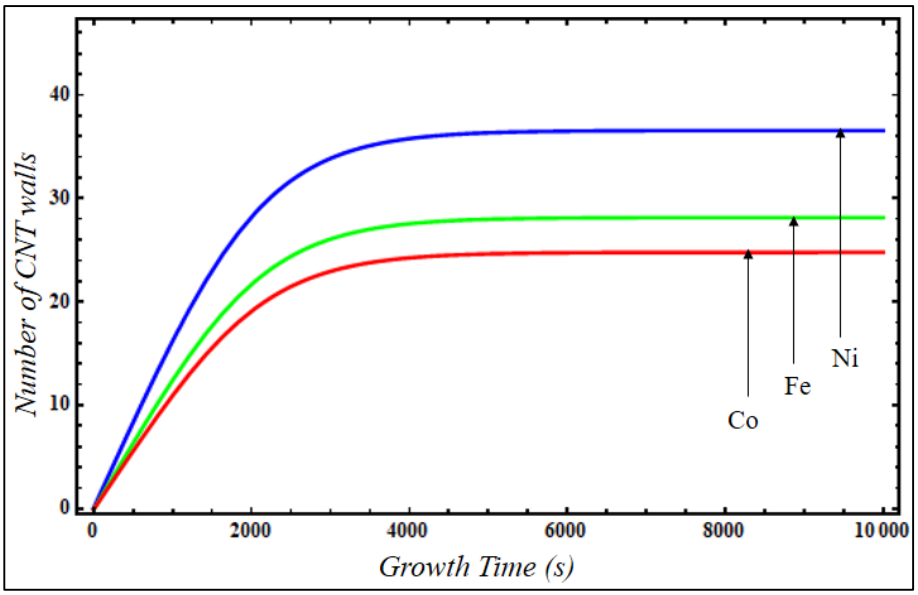

Figure 3.12 Time evolution of the number of CNT walls for different catalysts.

3.4.11 Variation of number of CNT walls with film thickness and time

The temporal variation of CNT walls along with catalyst thickness for Ni catalyst is depicted in Fig. 3.13. The result shows that CNT walls increase with time for varying nanofilm thickness. This is attributed to the increase in catalyst size with increasing nanofilm thickness [cf. Fig. 3.6]. This increase in catalyst size increases the number of CNT walls [cf. Fig. 3.11]. A similar outcome is observed using Fe and Co.

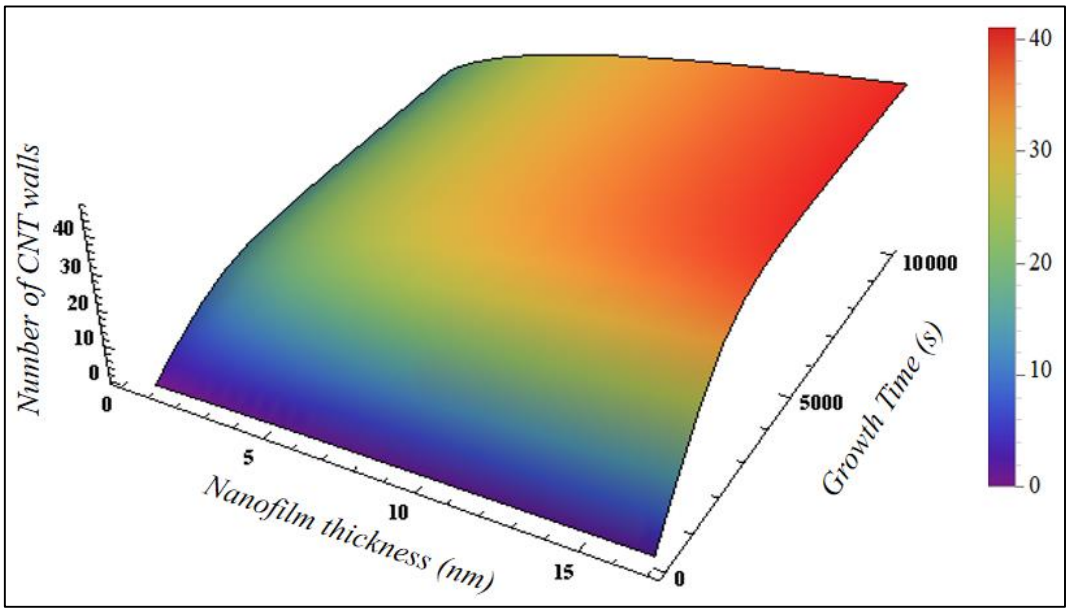

Figure 3.13 Variation of CNT walls with the film thickness and growth time for Ni.

3.5 CONCLUSIONS

A computational model was developed and studied for the plasma pre-treatment of nanofilms, and the effect of process parameters, i.e. power, pressure, gas flow and plasma temperature, was deliberated. The model also accomplishes the catalyzed growth of CNTs in a reactive plasma considering different catalysts, namely iron (Fe), nickel (Ni), and cobalt (Co). The effect of the nature and thickness of the catalyst and its nanofilm on CNT growth parameters such as nanotube diameter, nanotube length, number of CNT walls, etc. was deliberated in this chapter. The relation between the catalyst diameter and nanotube walls was established. The time evolution of various parameters (CNT diameter, length, and number of CNT walls) for different catalysts was also studied. The study would also be helpful in producing various other nanostructures and altering their properties to serve the necessary objective for their use in various applications.

REFERENCES

[1] C. Ducati, I. Alexandrou, M. Chhowalla, J. Robertson, and G.A.J. Amaratunga, J. Appl. Phys. **95**, 6387 (2004).

[2] I. Denysenko and N.A. Azarenkov, J. Phys. D. Appl. Phys. **44**, 174031 (2011).

[3] X. Wang, A. Dong, Y. Hu, J. Qian, and S. Huang, Chem. Commun. **56**, 10809 (2020).

[4] J. Ding, L. Zhong, Q. Huang, Y. Guo, T. Miao, Y. Hu, J. Qian, and S. Huang, Carbon N. Y. **177**, 160 (2021).

[5] R. Mohan, *Plasma Processing of Nanomaterials* (CRC Press Taylor & Francis Group, 2017).

[6] M. Cantoro, S. Hofmann, S. Pisana, C. Ducati, A. Parvez, A.C. Ferrari, and J. Robertson, Diam. Relat. Mater. **15**, 1029 (2006).

[7] S. Hofmann, M. Cantoro, B. Kleinsorge, C. Casiraghi, A. Parvez, J. Robertson, and C. Ducati, J. Appl. Phys. **98**, 034308 (2005).

[8] S.K. Srivastava, A.K. Shukla, V.D. Vankar, and V. Kumar, Thin Solid Films **492**, 124 (2005).

[9] S.C. Chang, T.C. Lin, and C.Y. Pai, Microelectronics J. **38**, 657 (2007).

[10] T. Labbaye, E. Kovacevic, T. Lecas, M.R. Ammar, A. Canizarès, N. Raimboux, T. Strunskus, C. Jaeger, P. Simon, and C. Boulmer-Leborgne, Appl. Surf. Sci. **453**, 436 (2018).

[11] M.W. Lee, M.A.S.M. Haniff, A.S. Teh, D.C.S. Bien, and S.K. Chen, J. Exp. Nanosci. **10**, 1232 (2015).

[12] Y. Wang, Z. Luo, B. Li, P.S. Ho, Z. Yao, L. Shi, E.N. Bryan, and R.J. Nemanich, J. Appl. Phys. **101**, 1 (2007).

[13] L.M. Hoyos-Palacio, A.G. García, J.F. Pérez-Robles, J. González, and H. V.

Martínez-Tejada, IOP Conf. Ser. Mater. Sci. Eng. **59**, 012005 (2014).

[14] Z.P. Huang, D.Z. Wang, J.G. Wen, M. Sennett, H. Gibson, and Z.F. Ren, Appl. Phys. A Mater. Sci. Process. **74**, 387 (2002).

[15] J.H. Yen, I.C. Leu, C.C. Lin, and M.H. Hon, Diam. Relat. Mater. **13**, 1237 (2004).

[16] S.C. Chang, T.C. Lin, T.S. Li, and S.H. Huang, Microelectronics J. **39**, 1572 (2008).

[17] D.J. Yang, Q. Zhang, S.F. Yoon, J. Ahn, S.G. Wang, Q. Zhou, Q. Wang, and J.Q. Li, Surf. Coatings Technol. **167**, 288 (2003).

[18] S. Wang, P. Wang, and O. Zhou, Diam. Relat. Mater. **15**, 361 (2006).

[19] W.P. Wang, H.C. Wen, S.R. Jian, J.Y. Juang, Y.S. Lai, C.H. Tsai, W.F. Wu, K.T. Chen, and C.P. Chou, Appl. Surf. Sci. **253**, 9248 (2007).

[20] L. Valentini, J.M. Kenny, L. Lozzi, and S. Santucci, J. Appl. Phys. **92**, 6188 (2002).

[21] S.R. Jian, Mater. Chem. Phys. **115**, 740 (2009).

[22] U. Sharma and S.C. Sharma, Phys. Plasmas **25**, 103509 (2018).

[23] M.A. Lieberman and A.J. Lichtenberg, *Principles of Plasma Discharges and Materials Processing: Second Edition* (John Wiley & Sons, 2005).

[24] Z. Marvi, S. Xu, G. Foroutan, and K. Ostrikov, Phys. Plasmas **22**, 013504 (2015).

[25] R.T.K. Baker, Carbon N. Y. **27**, 315 (1989).

[26] M. Pérez-Cabero, E. Romeo, C. Royo, A. Monzón, A. Guerrero-Ruíz, and I. Rodríguez-Ramos, J. Catal. **224**, 197 (2004).

[27] N.M. Rodriguez, A. Chambers, and R.T.K. Baker, Langmuir **11**, 3862 (1995).

[28] C.S. Cojocaru, A. Senger, and F. Le Normand, J. Nanosci. Nanotechnol. **6**, 1331 (2006).

[29] A. Malesevic, H. Chen, T. Hauffman, A. Vanhulsel, H. Terryn, and C. Van Haesendonck, Nanotechnology **18**, 455602 (2007).

[30] G. Bin Zheng, K. Kouda, H. Sano, Y. Uchiyama, Y.F. Shi, and H.J. Quan, Carbon N. Y. **42**, 635 (2004).

[31] H. Kersten, H. Deutsch, H. Steffen, G.M.W. Kroesen, and R. Hippler, Vacuum **63**, 385 (2001).

[32] M.S. Sodha, S. Misra, S.K. Mishra, and S. Srivastava, J. Appl. Phys. **107**, 103307 (2010).

[33] I.B. Denysenko, S. Xu, J.D. Long, P.P. Rutkevych, N.A. Azarenkov, and K. Ostrikov, J. Appl. Phys. **95**, 2713 (2004).

[34]UMIST Database Astrochem. (2012).

[35] S. Hofmann, R. Sharma, C. Ducati, G. Du, C. Mattevi, C. Cepek, M. Cantoro, S. Pisana, A. Parvez, F. Cervantes-Sodi, A.C. Ferrari, R. Dunin-Borkowski, S. Lizzit, L. Petaccia, A. Goldoni, and J. Robertson, Nano Lett. **7**, 602 (2007).

[36] I. Denysenko and K. Ostrikov, J. Phys. D. Appl. Phys. **42**, 015208 (2009).

[37] Antonio Miguel da Cruz Baptista Dias, Modeling of Low Pressure Plasmas in CH4-H2 Mixtures, Instituto Superior Técnico, Universidade de Lisboa, 2012.

[38] H. Mehdipour, K. Ostrikov, and A.E. Rider, Nanotechnology **21**, 455605 (2010).

[39] S. Hofmann, G. Csányi, A.C. Ferrari, M.C. Payne, and J. Robertson, Phys. Rev. Lett. **95**, 036101 (2005).

[40] I. Denysenko and N.A. Azarenkov, J. Phys. D. Appl. Phys. **44**, 174031 (2011).

[41] C. Bower, W. Zhu, S. Jin, and O. Zhou, Appl. Phys. Lett. **77**, 830 (2000).

[42] M.S. Bell, K.B.K. Teo, R.G. Lacerda, W.I. Milne, D.B. Hash, and M. Meyyappan, Pure Appl. Chem. **78**, 1117 (2006).

[43] M. Mao and A. Bogaerts, J. Phys. D. Appl. Phys. **43**, 315203 (2010).

[44] J. Benedikt, J. Phys. D. Appl. Phys. **43**, 043001 (2010).

[45] S.R. Jian, Y.T. Chen, C.F. Wang, H.C. Wen, W.M. Chiu, and C.S. Yang, Nanoscale Res. Lett. **3**, 230 (2008).

[46] M. Chhowalla, K.B.K. Teo, C. Ducati, N.L. Rupesinghe, G.A.J. Amaratunga, A.C. Ferrari, D. Roy, J. Robertson, and W.I. Milne, J. Appl. Phys. **90**, 5308 (2001).

[47] C. Bower, O. Zhou, W. Zhu, D.J. Werder, and S. Jin, Appl. Phys. Lett. **77**, 2767 (2000).

[48] H.K. Jung and H.W. Lee, J. Nanomater. **2014**, 1 (2014).

[49] S. Hofmann, M. Cantoro, B. Kleinsorge, C. Casiraghi, A. Parvez, J. Robertson, and C. Ducati, J. Appl. Phys. **98**, 034308 (2005).

[50] R. Xie, G. Zhong, C. Zhang, B. Chen, C.S. Esconjauregui, and J. Robertson, J. Appl. Phys. **114**, 244302 (2013).

[51] Z. Ma, S. Zhou, C. Zhou, Y. Xiao, S. Li, and M. Chan, Nanomaterials **10**, 1 (2020).

[52] C. Prawoto, S. Li, and M. Chan, 2018 IEEE Int. Conf. Electron Devices Solid State Circuits, EDSSC 2018 (2018).

Chapter - 4

MODELING A VERTICALLY ALIGNED CNT ARRAY IN PLASMA AND OPTIMIZING IT FOR FIELD EMISSION APPLICATIONS

PUBLICATION

- **Umang Sharma** and Suresh C. Sharma, "Impact of plasma process parameters on the growth of vertically aligned carbon nanotube array and its optimization as field emitters", *European Physical Journal Plus* **137**, 823 (2022).

4

MODELING A VERTICALLY ALIGNED CNT ARRAY IN PLASMA AND OPTIMIZING IT FOR FIELD EMISSION APPLICATIONS

4.1 BRIEF OUTLINE OF THE CHAPTER

The theoretical study models a vertically aligned carbon nanotube (VACNT) array in plasma and structures its growth based on the variation of plasma operating conditions and process parameters. We investigate the consequence of plasma concentration, power, pressure, and substrate temperature on the aspects of the VACNT array. Furthermore, the amorphous carbon deposition between the CNTs of the array is also examined. As field emission is one of the most outstanding applications of the VACNT array, the field enhancement factor for the array is also deliberated and optimized. The results are modelled, considering the balance of plasma species, plasma and CNT energy exchange, hydrocarbon and hydrogen generation over the catalyst nanoparticle, CNT array growth, and carbon deposition over the substrate between CNTs in VACNT array growth using plasma-enhanced chemical vapour deposition (PECVD). The model is numerically solved by deliberating the experimental literature's initial conditions and plasma parameters. The aspects of an array, i.e., its length and average CNT diameter can be optimized as desired by altering the operating conditions and glow discharge parameters. Additionally, the influence of array aspects on the field emission properties is observed. The results of the study are validated by the available experimental data. This theoretical study can be effectively used to grow the VACNT array and its optimization to obtain better field emitters.

4.2 INTRODUCTION

The alignment of CNTs is critical for various applications, and vertically aligned carbon nanotubes (VACNTs) are stated to be used for electronic applications like field emission displays, field-effect transistor channels, and quantum wires[1–3]. The synthesis of VACNTs forest is obtained via various processes such as thermal CVD (TCVD), one-step catalytic chemical vapour deposition (CCVD), and PECVD over a metal catalyst. As mentioned before, PECVD can produce VACNT arrays at lower temperatures. The VACNTs have good alignment, uniform length, and coverage of the catalyst-substrate surface. The properties of VACNT arrays can be influenced by their pattern and intertube distance and are demonstrated in fibre lasers, photonics, solar and nano applications (as a vertical CNT-field effect transistor). As the VACNT arrays deteriorate the shielding of the electric field, thus improving the electric field distribution, the upkeep of closely packed VACNT array areal density is essential for its use in field emission and nanoelectrode arrays[4]. The pre-patterned catalyst sites for the growth of nanotubes is used to decrease the areal density. This vertical alignment of carbon nanotubes results from an electrostatic force acting on growing nanotubes' tips, resulting from the sheath electric field.

The growth of CNT forest is a consequence of continuous carbon species diffusion through the catalyst surface either via tip-mode growth (where the nanoparticle is detected on the nanotube tip) or base-mode growth (where the nanoparticle is detected at the nanotube base, i.e., on the substrate). A catalyst metal thin film (commonly Fe, Ni, Co) deposited over the substrate fragments into catalyst nanoparticles upon heating, serving as a seed layer for nanotube nucleation and growth[5]. The feedstock gases dissociate due to plasma power and over the catalyst surface into carbon species which stimulates the growth of the nanotubes. Several dissociations and diffusion processes are liable for carbon species movement over the catalyst. Various groups have acknowledged the base-mode growth of VACNTs, suggesting the feedstock gases transport through the CNT array to reach the catalyst located on the substrate and contribute to the growth. Although the CVD growth of VACNTs has been enlightened

experimentally and theoretically, the studies done for the plasma-assisted growth of CNT arrays are ambiguous.

Kato *et al.*[6] demonstrated a pioneering work by synthesizing single-walled CNTs (SWCNTs) in the form of SWCNT bundles and individual SWCNT using PECVD. Hoffman *et al.*[7] revealed a controlled PECVD synthesis of VA-carbon nanofibers on pre-marked substrates at very low temperatures, i.e., 120 ^{o}C, suggesting a diffusion growth mechanism. Srivastava *et al.*[8] synthesized CNTs using the MPECVD (microwave plasma-enhanced chemical vapour deposition) technique to study the influence of gas composition on their growth. They also synthesized nitrogen-doped CNT films using a similar technique to study their growth morphology and field emission characteristics[9]. Hayashi *et al.*[10] grew well-aligned CNTs under the influence of a high plasma sheath electric field and pressure for the rf-dc PECVD method. Bell *et al.*[11,12] synthesized a VACNT film via a dc PECVD set up to study the plasma chemistry of species, calculated the optimum gas ratio for nanotube film growth and dominant precursor. In our previous work[13], we have developed a parametric model for the vertical alignment of a CNT, where we established that an electrostatic force acting on the CNT during its growth is responsible for its vertical alignment in plasma. We have also studied the effect of process parameters such as plasma temperature, plasma density, and negative substrate voltage on the growth and alignment of CNTs.

Okuyama *et al.*[14] made an effort to control the density and diameter of VACNTs in a dc-plasma setup using a Ni catalyst. They suggested that the density can be maximized by optimizing the plasma pre-treatment time. Ikuno *et al.*[15] examined the relation between film morphology and PECVD plasma conditions. They proposed that the growth was stimulated due to increasing inter-electrode distance, which increases the generation of radicals and increases in self-bias, which induces vertical alignment in nanotubes. Lee *et al.*[16] provided new insights into the CVD growth of CNT forest and hypothesized that the film growth is mass transport limited. Louchev *et al.*[17] provided a detailed analysis of CVD growth of nanotubes involving the diffusion processes over metal catalyst surfaces. Zhong *et al.*[18] synthesized VA-SWCNT mats via point-arc

microwave plasma chemical vapour deposition over Fe catalyst and confirmed that gas-phase diffusions of feedstock gases bound the film growth rate.

Few applications such as field emitter devices require a patterned growth of CNTs to avoid any screening effects of high-density films. The spacing between the CNTs must be high to disregard the field screening effect. Thapa *et al.*[19] synthesized VACNT arrays on a stainless steel substrate in a dc-PECVD setup and studied field emission characteristics of these arrays. They also simulated the effect of bundling of CNTs and observed that field emission from individual CNTs or less dense CNT bundles was better in comparison to denser CNT bundles. Campo *et al.*[20] synthesized SWNTs via alcohol catalytic chemical vapour deposition (AC-CVD) on TiN conductive substrates and further tested them for field emission concluding that SWNTs grown directly on these substrates showed excellent field emission characteristics. Morassutto *et al.*[21] synthesized dense arrays of aligned CNTs via thermal CCVD over Fe catalyst on a thin Ta layer. They observed that the catalyst particle size and density govern the growth of VACNTs and addition of Au or Pt between substrate and Ta layer increases the CNT conductivity and improves field emission.

Various literature has already established that plasma-assisted growth of nanotubes provides high quality and uniformly deposited array. Also, using highly ionized gaseous fluxes enhances the array growth uniformity and quality, which are critical for their electron-emitting and dimensional characteristics; hence studying the effects of plasma parameters on VACNTs growth becomes significant. This study investigates the impact of plasma conditions on VACNT array growth in a PECVD setup. We propose that the catalyst is attached to the substrate during the growth so that the gaseous species are required to travel through the growing CNT array, i.e., the growth occurs via base mode. CNT growth only occurs at the catalyst sites, enabling a patterned or selective growth approach. The geometrical field enhancement factor of the array is also studied.

4.3 MODEL DESCRIPTION

The following section is an extensive study of the growth model of a VACNT film in a PECVD set up to provide a deep understanding of the kinetics of all the species involved and various nucleation and growth processes involved. The feedstock gases considered in the model are acetylene (C_2H_2) as a hydrocarbon and hydrogen (H_2) as a carrier gas, respectively.

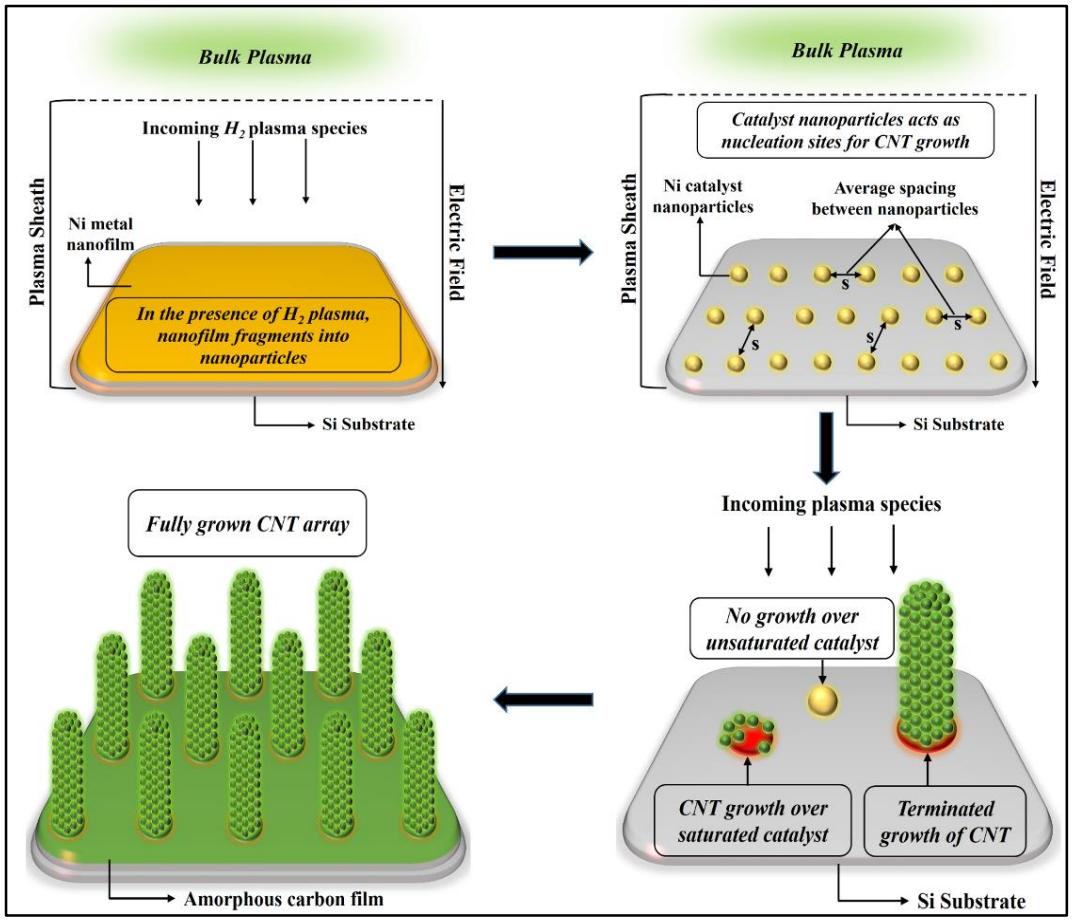

Figure 4.1 Schematic illustration of CNT array growth in plasma.

The growth of VACNT arrays in a complex reactive plasma follows the scenario illustrated schematically in Fig. 4.1 – A metal catalyst film deposited over a substrate surface under the effect of hydrogen plasma gets fragmented into nanoparticles which are nucleation sites for the carbon nanotubes. The plasma species are dissociated into carbon species owing to many dissociation processes and surface decomposition over catalyst surface. These carbon atoms diffuse over the catalyst's surface and volume,

initiating CNT growth. This growth begins when the carbon precursors deposit on the substrate area between the catalyst nanoparticles and diffuse into and over the catalyst until the nanoparticles become saturated with carbon. Once the saturation of metal catalysts is achieved, nanotubes start to nucleate on their surface by increasing their proportions. Few carbon atoms get deposited on the substrate surface due to the diffusion of gaseous fluxes between these growing nanotubes leaving a deposition layer (typically amorphous carbon layer). These nanotubes continue to grow until the metal catalysts get poisoned.

A plasma sheath region is formed near the substrate (space charge separation region), where a negative bias is supplied. This region starts at $z = 0$, and substrate is located at $z = \lambda_s$, where the plasma sheath potential equals the substrate potential. An electric plasma sheath field is established due to the charge separation that prevails along the z-axis, which directs all the ionic species towards the negatively biased substrate while the electrons are averted. Following the 1D fluid steady-state model, the particle energy and momentum balance equations are calculated from Boltzmann's transport equation, and the electric field is calculated from Poisson's equation combined with balance equations to make the model self-consistent. The ionization and collisional effects of electrons and ions with the neutral species are considered; however, ion-electron collisions are neglected. The temperatures of electrons, ionic and neutral species are presumed to be constant throughout the plasma sheath, and additionally, ions and neutrals have an equivalent temperature, i.e. $T_i = T_n$. The study considers acetylene (C_2H_2) as a hydrocarbon gas and hydrogen (H_2), denoted as A and B in the script. Only dominant gaseous species are considered in the model, mentioned in Table 4.1.

Type	A	B
Neutral species	C_2H_2, C_2H, C_2H_3, C_2H_4, C_4H, C_4H_3, C_4H_2, C_6H, C_6H_4, C_6H_2 (10)	H, H_2 (2)
Positive species	$C_2H_2^+$, C_2H^+, $C_2H_3^+$, $C_2H_4^+$, C_4H^+ $C_4H_2^+$, $C_4H_3^+$, $C_6H_2^+$, C_6H^+, $C_6H_3^+$ (10)	H^+, H_2^+ (2)

Table 4.1 Plasma species considered in the computation.

For all the plasma species (ions, neutrals and electrons), the balance equations are represented as[22,23] –

$$\frac{\partial}{\partial z}\left(n_{ij}u_{ij}\right)=\nu_{ij}n_e, \tag{4.1}$$

$$\frac{\partial}{\partial z}\left(n_e u_e\right)=\sum_j \nu_{ij}n_e, \tag{4.2}$$

$$m_{ij}n_{ij}u_{ij}\left(\frac{\partial u_{ij}}{\partial z}+\nu_{cj}\right)=-n_{ij}\left(e\frac{\partial \varphi}{\partial z}+\frac{T_{ij}}{n_{ij}}\frac{\partial n_{ij}}{\partial z}\right), \tag{4.3}$$

$$m_e u_e \nu_{ce}=\left(e\frac{\partial \varphi}{\partial z}-\frac{T_e}{n_e}\frac{\partial n_e}{\partial z}\right). \tag{4.4}$$

Using Poisson's equation, we obtain the potential φ and electric field E as –

$$\frac{d^2\varphi}{dz^2}=-\frac{e}{\varepsilon_o}\left(\sum_{ij}^{A,B}\sigma_{ij}n_{ij}-n_e\right), \qquad E=-\frac{d\varphi}{dz}. \tag{4.5}$$

where $\sigma_{ij}=\left\{\begin{matrix}\sum\sigma_{ij}=0\\0<\sigma_{ij}<1\end{matrix}\right\}$ defines the j^{th} ion-electron ratio. Using the solutions of Eqs. (4.1-4.5), the plasma sheath is investigated around the substrate region and essential parameters of the CNT growth are determined with the following boundary conditions–

$$u_e\big|_z=0,\ u_{ij}\big|_z=v_{ij0}\big|_z\left(=\frac{T_e}{m_{ij}}\right),\ \varphi=0,\ \frac{\partial\varphi}{\partial z}=-\frac{T_e}{e\lambda_i},$$

where $\lambda_i=\frac{T_n}{\sigma p_0}$ and, v_{ij} and p_0 are the ion-acoustic speed and gas pressure, respectively.

In this complex numerical model, we have presumed that the catalyst nanoparticles remain anchored to the substrate throughout the nanotube growth, i.e. the base-mode growth of CNT is deliberated. As perceived from Figure 4.2, on a substrate with an

area of 5000 x 5000 μm^2, a pre-patterned Ni metal nanoparticle film is considered with 1000 metal catalysts with an average diameter of 40 nm and a minimum average spacing of 100 nm (centre-to-centre distance between catalysts). As the catalyst nanoparticles act as nucleation sites for carbon nanotubes; hence, 1000 nanotubes for this pre-patterned catalyst film would be accomplished. The main equations accounting for the nucleation and CNT array growth in a reactive plasma are preceded by the bulk plasma balance equations taking into account all the process changes loss during the growth. Other predetermined parameters considered for the computation are mentioned in Sec. 4.4.

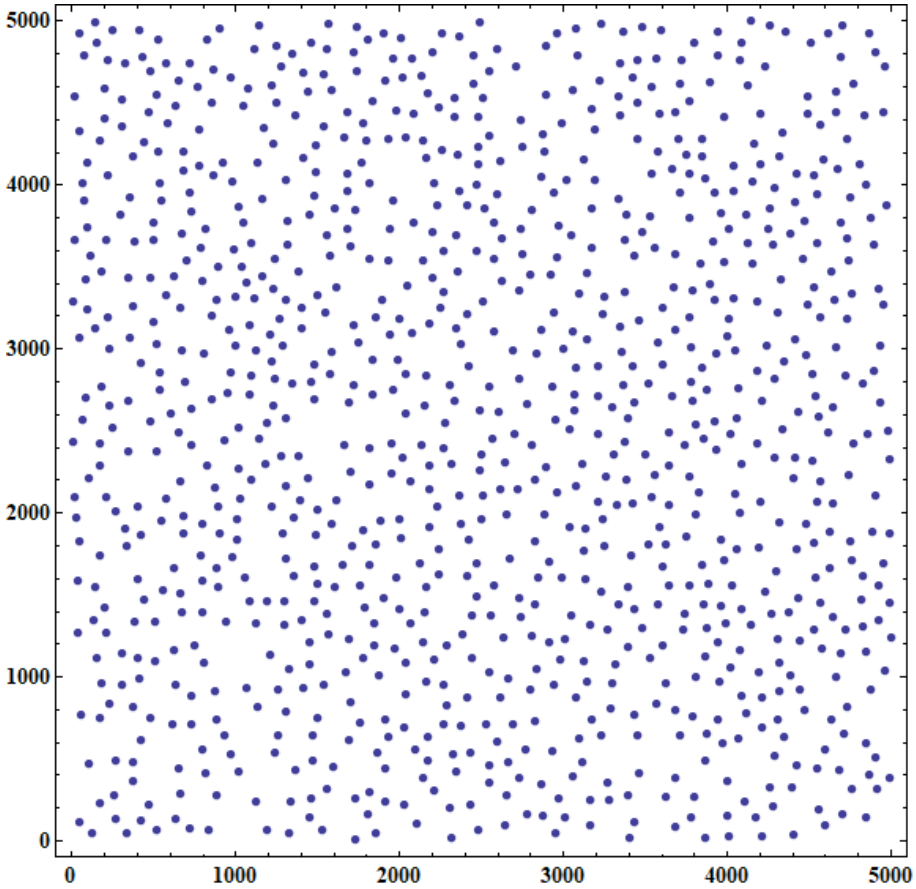

Figure 4.2 Computational domain with 1000 catalytic nanoparticles over 5000 x 5000 μm^2 substrate area.

4.3.1 FORMATION OF HYDROGEN RADICALS AND CARBON SPECIES OVER THE CATALYST NANOPARTICLE

$$\sum_{p=1}^{N} \partial_{\tau}(n_C^p) =$$

$$\Bigg[\underbrace{\Bigg\{ \sum_{p=1}^{N}\Bigg[\sum_{A=1}^{10}(1-\theta_t)J_A^p\Bigg] + \sum_{p=1}^{N}\Bigg[\sum_{A=1}^{10} n_A^{surf\,p}\,\upsilon\exp\left(-\frac{\delta E_{CH}^{diss}}{k_B T_S}\right)\Bigg] + \sum_{p=1}^{N}\Bigg[\sum_{iA=1}^{10}\Bigg(\sum_{A=1}^{10} n_A^{surf\,p}\,\frac{y_d}{\upsilon_0}\Bigg)J_{iA}^p\Bigg]}_{First\ Part\ (Gain)}$$

$$\underbrace{+ \sum_{p=1}^{N}\Bigg(\sum_{iA=1}^{10} J_{iA}^p\Bigg) + \sum_{p=1}^{N} J_C^p + \sum_{p=1}^{N}\Bigg[\sum_{iB=1}^{2}\Bigg(\sum_{iA=1}^{10}\frac{J_{iA}^p\sigma_{ads}}{\upsilon}\Bigg)J_{iB}^p\Bigg]\Bigg\}}_{First\ Part\ (Gain)}$$

$$\underbrace{-\Bigg\{\sum_{p=1}^{N}\Bigg[\sum_{A=1}^{10} n_A^{surf\,p}\,\upsilon\exp\left(-\frac{\delta E_{dCH}}{k_B T_S}\right)\Bigg] + \sum_{p=1}^{N}\Bigg[\sum_{B=1}^{2}\Bigg(\sum_{A=1}^{10} n_A^{surf\,p}\,\sigma_{ads}\Bigg)J_B^p\Bigg]\Bigg\}}_{Second\ Part\ (Loss)} \tag{4.6}$$

$$\underbrace{+ \sum_{p=1}^{N}\Bigg[n_C^p\upsilon\exp\left(-\frac{\delta E_{ev}}{k_B T_S}\right)\Bigg] + \sum_{p=1}^{N}\left(n_C^p\sigma_{ads}\upsilon n_H^p\right)\Bigg\}}_{Second\ Part\ (Loss)} \Bigg] \times d_{\tau}(\Omega_C)$$

Eq. (4.6) describes the carbon atoms produced over the p^{th} catalyst nanoparticle's surface. The increase in carbon atom density is described in the first part of the equation. This gain is ascribed to the hydrocarbon neutrals absorption over the nanoparticle's surface, hydrocarbon thermal dissociation, hydrocarbon ion-induced dissociation, positive ion decomposition, direct carbon influx onto the nanoparticle, and hydrocarbon-hydrogen ion interaction, respectively. The decrease in carbon atom density is described in the second part of the equation. This loss is ascribed to the hydrocarbon desorption from the nanoparticle's surface, the interaction of hydrocarbon-hydrogen neutrals, carbon species evaporation from the nanoparticle, and interaction between catalyst surface created carbon and hydrogen species. The incessant hydrocarbon dissociation over the p^{th} nanoparticle's surface generates an enormous amount of amorphous carbon that forms a vague layer over it, which depletes the active area of the catalyst and gradually saturates the CNT growth. Hence, the last

part of the Eq. (4.6) administers the catalyst contamination rate due to the creation of this carbon layer as a function of carbon number density.

$$\sum_{p=1}^{N} \partial_{\tau}(n_H^p) = \underbrace{\left\{ \sum_{p=1}^{N} \left(\sum_{B=1}^{2} J_B^p (1-\theta_t) \right) + \sum_{p=1}^{N} \left[\sum_{B=1}^{2} n_B^{surf\,p} \upsilon \exp\left(-\frac{\delta E_{CH}^{diss}}{k_B T_S} \right) \right] + \sum_{p=1}^{N} \left[\sum_{iA=1}^{10} \left(\sum_{A=1}^{10} n_A^{surf\,p} \frac{y_d}{\upsilon_0} \right) J_{iA}^p \right] \right.}_{First\ Part\ (Gain)}$$

$$\underbrace{\left. + \sum_{p=1}^{N} \left(\sum_{iB=1}^{2} J_{iB}^p \right) \right\}}_{First\ Part\ (Gain)} - \underbrace{\left\{ \sum_{p=1}^{N} \left[\sum_{B=1}^{2} n_B^{surf\,p} \upsilon \exp\left(-\frac{\delta E_{dH}}{k_B T_S} \right) \right] + \sum_{p=1}^{N} \left(\sum_{B=1}^{2} n_B^{surf\,p} \sigma_{ads} J_B^p \right) \right.}_{Second\ Part\ (Loss)}$$

$$\underbrace{\left. + \sum_{p=1}^{N} \left[\sum_{iB=1}^{2} \left(\sum_{B=1}^{2} n_B^{surf\,p} \sigma_{ads} J_{iB}^p \right) \right] + \sum_{p=1}^{N} n_H^p \sigma_{ads} \upsilon n_C^p \right\}}_{Second\ Part\ (Loss)} \tag{4.7}$$

Eq. (4.7) describes the hydrogen atoms produced over the p^{th} catalyst nanoparticle's surface. The increase in hydrogen atom density is described in the first part of the equation. This gain is ascribed to the hydrogen neutrals adsorption over the nanoparticle's surface, hydrocarbons thermal dissociation, hydrocarbons ion-induced dissociation, and the influx of hydrogen ion on p^{th} catalyst. The decrease in hydrogen atom density is described in the second part of the equation. This loss is ascribed to the hydrogen desorption from the p^{th} nanoparticle's surface, the surface adsorbed hydrogen and neutral hydrogen interaction, the surface adsorbed hydrogen and ionic hydrogen interaction, and interaction between catalyst surface created carbon and hydrogen species. The functions/parameters stated in Eqs. (4.6-4.7) are termed in Table 4.2.

Parameters/functions	Description
$\upsilon_0 (\approx 10^{15}\ cm^{-2})$	Adsorption sites per unit area[24]
$\sigma_{ads}\left(=6.8\times10^{-16} cm^2\right)$	Cross-section of plasma species interaction[24]
$n_j^{surf}\left(=\theta_j \upsilon_0\right)$	Surface density of the neutral atom[24]
$\upsilon (\approx 10^{13}\ Hz)$	Thermal vibration frequency[25]
$\delta E_{CH}^{diss}\left(=2.1\ eV\right)$	Hydrocarbon dissociation energy[23]
$\delta E_{ev} (=1.8\ eV)$	C-atom evaporation energy[23]
$\delta E_{dCH} (=1.8\ eV)$	Hydrocarbon desorption energy[23]
$\delta E_{dH} (=1.8\ eV)$	Hydrogen desorption energy[23]
$d_\tau(\Omega_C)=\left(1-n_C \pi d_p^2\right)$	Rate of contamination of catalyst with Ω_C as catalyst particle blocking function[13]

Table 4.2 Particulars of functions/parameters termed in Eqs. (4.6-4.7).

4.3.2 PLASMA SPECIES EQUILIBRIUM IN THE GLOW DISCHARGE (NEUTRALS, IONS, ELECTRONS)

The Eqs. (4.8) and (4.9) describes the evolution of neutral density *j = (A, B)* type in bulk plasma as a consequence of various processes. The gain in neutral atom density represented in the first part of the equations is attributed to ion-electron recombination, ion neutralization on sticking to the nanotube surface, desorption of ions from catalyst surface, variation in chamber inflow and outflow of neutrals, and influence of ion-neutral reactions considered in the study[26] (listed in Table 4.3), respectively.

$$\partial_\tau(n_A) = \underbrace{\alpha_A n_e n_{iA} + \sum_{p=1}^{N} \frac{n_{CNT}}{\lambda_s}\left(1-\gamma_{iA}\right)\begin{pmatrix} tip^p & cyl^p \\ Q & + Q \\ iA & iA \end{pmatrix}}_{First\ Part\ (Gain)}$$

$$\underbrace{+ \sum_{p=1}^{N} \frac{desp^p}{A} J + \left(V_A^{IF} - V_A^{OF}\right) + \left(\sum_{qAB} k_q n_B n_{iA} - \sum_{lBA} k_l n_A n_{iB} \right)}_{First\ Part\ (Gain)}$$

$$\underbrace{-\left\{ \beta_A n_A + \sum_{p=1}^{N} \frac{n_{CNT}}{\lambda_s} \gamma_A \begin{pmatrix} tip^p & cyl^p \\ Q & + Q \\ A & A \end{pmatrix} + \sum_{p=1}^{N} \frac{adsp^p}{A} J + \mathrm{K}_{wall}^{A} n_A \right\}}_{Second\ Part\ (Loss)} \quad (4.8)$$

$$\partial_\tau(n_B) = \underbrace{\alpha_B n_e n_{iB} + \sum_{p=1}^{N} \frac{n_{CNT}}{\lambda_s}\left(1-\gamma_{iB}\right)\begin{pmatrix} tip^p & cyl^p \\ Q & + Q \\ iB & iB \end{pmatrix}}_{First\ Part\ (Gain)}$$

$$\underbrace{+ \sum_{p=1}^{N} \frac{desp^p}{B} J + \left(V_B^{IF} - V_B^{OF}\right) + \left(\sum_{\ell AB} k_\ell n_A n_{iB} - \sum_{qBA} k_q n_B n_{iA} \right)}_{First\ Part\ (Gain)}$$

$$\underbrace{-\left\{ \beta_B n_B + \sum_{p=1}^{N} \frac{n_{CNT}}{\lambda_s} \gamma_B \begin{pmatrix} tip^p & cyl^p \\ Q & + Q \\ B & B \end{pmatrix} + \sum_{p=1}^{N} \frac{adsp^p}{B} J + \mathrm{K}_{wall}^{B} n_B \right\}}_{Second\ Part\ (Loss)} + J_{thd} \quad (4.9)$$

The loss in neutral atom density represented in the second part of the equations is due to the dissociative neutral ionization, neutral accretion at the nanotube surface, neutrals species adsorption, and reactive chamber wall discharge loss of neutrals, respectively. The final term in Eq. (4.9) analyses the rise in carrier gas neutrals density due to thermal dehydrogenation. The specifics of the equations mentioned above are given in Table 4.4.

Reactions	k (cm^3sec^{-1})
$H^+ + C_4H \rightarrow C_4H^+ + H$	2.0 x 10^{-9}
$H^+ + C_6H \rightarrow C_6H^+ + H$	2.0 x 10^{-9}
$H^+ + C_2H_2 \rightarrow C_2H^+ + H_2$	4.3 x 10^{-9}
$H^+ + C_4H_2 \rightarrow C_4H^+ + H_2$	2.0 x 10^{-9}
$H_2^+ + H \rightarrow H^+ + H_2$	6.4 x 10^{-10}
$H_2^+ + C_2H_2 \rightarrow C_2H_2^+ + H_2$	5.3 x 10^{-9}
$H_2^+ + C_4H \rightarrow C_4H_2^+ + H$	1.7 x 10^{-10}
$H_2 + C_2H^+ \rightarrow C_2H_2^+ + H$	1.7 x 10^{-9}
$C_2H + C_4H^+ \rightarrow C_6H^+ + H$	6.0 x 10^{-10}
$C_2H + C_4H_2^+ \rightarrow C_6H_2^+ + H$	1.3 x 10^{-9}
$C_2H_2 + C_2H^+ \rightarrow C_4H_2^+ + H$	1.2 x 10^{-9}
$C_2H_2 + C_2H_3^+ \rightarrow C_4H_3^+ + H_2$	2.4 x 10^{-10}
$C_2H_2 + C_4H^+ \rightarrow C_6H_2^+ + H$	1.5 x 10^{-9}
$C_2H_2 + C_4H_2^+ \rightarrow C_6H_4^+$	1.4 x 10^{-10}
$C_2H_2 + C_2H_2^+ \rightarrow C_4H_3^+ + H$	9.5 x 10^{-10}
$C_2H_2 + C_2H_2^+ \rightarrow C_4H_2^+ + H_2$	1.2 x 10^{-9}
$C_2H_2^+ + H_2 \rightarrow C_2H_3^+ + H$	1.0 x 10^{-11}
$C_2H_2^+ + C_6H_2 \rightarrow C_6H_2^+ + C_2H_2$	5.0 x 10^{-10}
$C_2H_2^+ + C_2H_3 \rightarrow C_4H_3^+ + H_2$	3.3 x 10^{-10}
$C_4H_2^+ + C_2H_3 \rightarrow C_6H_4^+ + H$	1.2 x 10^{-9}
$C_4H_3^+ + C_2H_3 \rightarrow C_6H_4^+ + H_2$	5.0 x 10^{-10}

$C_2H_3^+ + H \rightarrow C_2H_2^+ + H_2$	6.8 x 10^{-11}
$C_2H_3^+ + C_4H \rightarrow C_6H_2^+ + H_2$	4.0 x 10^{-10}
$C_2H_3^+ + C_6H \rightarrow C_6H_2^+ + C_2H_2$	5.0 x 10^{-10}

Table 4.3 Ion-neutral reactions with their reaction rates considered in the study.

Parameters/functions	Description
$V_j^{IF} = \left(\frac{4.4\times10^{17}}{vol} J_j \right)$	Inflow of neutrals from the reactive plasma chamber[27]
$V_j^{OF} = \left(\frac{\upsilon_{pump}}{vol} n_j \right)$	Outflow of neutrals from the reactive plasma chamber where υ_{pump} is the pumping rate[27]
J_{thd}	Thermal dehydrogenation flux[24]
J_j^{adsp} , J_j^{desp}	Adsorption and desorption fluxes
$K_{wall}^j = \sigma_j \frac{D_j}{\Lambda^2}$	Neutral atom discharge loss[28]
$\Lambda = \frac{RL}{\left\{(2.405L)^2 + (\pi R)^2\right\}^{1/2}}$	Cylindrical chamber effective diffusion length[28]
σ_j, D_j	Wall reaction and diffusion coefficient of respective species[28]

Table 4.4 Particulars of functions/parameters termed in Eqs. (4.8-4.9).

$$\partial_\tau(n_{iA}) = \underbrace{\left\{\beta_A n_A + \left(\sum_{\ell AB} k_\ell n_A n_{iB} - \sum_{qBA} k_q n_B n_{iA}\right) + \left(\frac{P}{E_{CH}^{diss} vol}\right)\right\}}_{First\ Part\ (Gain)} - \underbrace{\left\{\alpha_A n_e n_{iA} + \sum_{p=1}^{N} \frac{n_{CNT}}{\lambda_s}\begin{pmatrix} tip^p & cyl^p \\ Q & + Q \\ iA & iA \end{pmatrix} + K_{wall}^{iA} n_{iA}\right\}}_{Second\ Part\ (Loss)} \tag{4.10}$$

$$\partial_\tau(n_{iB}) = \underbrace{\left\{\beta_B n_B + \left(\sum_{qBA} k_q n_B n_{iA} - \sum_{\ell AB} k_\ell n_A n_{iB}\right) + \left(\frac{P}{E_H^{diss} vol}\right)\right\}}_{First\ Part\ (Gain)} - \underbrace{\left\{\alpha_B n_e n_{iB} + \sum_{p=1}^{N} \frac{n_{CNT}}{\lambda_s}\begin{pmatrix} tip^p & cyl^p \\ Q & + Q \\ iB & iB \end{pmatrix} + K_{wall}^{iB} n_{iB}\right\}}_{Second\ Part\ (Loss)} \tag{4.11}$$

The Eqs. (4.10) and (4.11) describes the evolution of positive ion density *j = (A, B)* type in bulk plasma as an outcome of various processes. The gain in ion density represented in the first part of the equations is due to dissociative ionization of neutrals, the influence of ion-neutral reactions considered in the study (listed in Table 4.3), and the plasma power ion dissociation process, respectively. The loss in ion number density represented in the second part of the equations is due to ion-electron recombination, ion accretion on the nanotube's surface, and reactive chamber wall discharge loss of ions, respectively. The specifics of the equations mentioned above are given in Table 4.5.

Parameters/functions	Description
$K_{wall}^{ij} = \left(\frac{\gamma_{ij} u_{ij} A_{chm}}{4 vol} \right)$	Ion discharge loss to the wall[27]
$k_q,\ k_l$	Neutral-ion reaction rate coefficients[29]
$\delta E_{CH}^{diss} (\approx 2.1\, eV)$, $\delta E_{H}^{diss} (\approx 2.1\, eV)$	Hydrocarbon and hydrogen dissociation energies[23]
P	Plasma power

Table 4.5 Particulars of functions/parameters termed in Eqs. (4.10-4.11).

$$\partial_\tau (n_e) = \underbrace{\left\{ \sum_{A=1}^{10} \beta_A n_A + \sum_{B=1}^{2} \beta_B n_B \right\}}_{First\ Part\ (Gain)} - \underbrace{\left\{ \left[\sum_{A=1}^{10} \alpha_A n_{iA} n_e + \sum_{B=1}^{2} \alpha_B n_{iB} n_e \right] + \sum_{p=1}^{N} \frac{n_{CNT}}{\lambda_s} \gamma_e \begin{pmatrix} tip^p & cyl^p \\ Q & + Q \\ e & e \end{pmatrix} + K_{wall}^{e} n_e \right\}}_{Second\ Part\ (Loss)} \tag{4.12}$$

Eq. (4.12) describes the evolution of electron density in the bulk plasma attributed to various processes. The increase in electron density represented in the first term of the equation is attributed to the dissociative ionization of neutral. The second part of the equation represents the loss in electron density owing to ion-electron recombination, electron accretion on the nanotube surface, and reactive chamber wall discharge loss of electrons, respectively. The specifics of the equation mentioned above is given in Table 4.6.

Parameters/functions	Description
β_j	Ionization coefficient of neutral atom
$\alpha_j\left(T_e\right)=\alpha_{j0}\left(300/T_e\right)^k$	Recombination coefficient for ions and electrons ($k=-1.2$ constant)[30]
$n_e,\ n_j,\ n_{ij}$	Electron, neutral, and ion density, respectively
n_{CNT}	Number density of CNT
$K_{wall}^{e}=\left(\frac{\gamma_e u_e A_{chm}}{4\,vol}\right)$	Loss rate of electrons over the volume on the discharge wall[27]
$A_{chm},\ vol$	Cylindrical plasma chamber's area and volume (length $L=23cm$ and internal diameter $D=32\,cm$)[27]

Table 4.6 Particulars of functions/parameters termed in Eq. (4.12).

In Eqs. (8-12), the surface collection currents of ions, electrons and neutrals define the amount of charge collected by the nanotube's tip and cylindrical surfaces which are given by-

$$Q_j^{tip\,p}=n_j(z)\pi d_p^2\left(\frac{8k_BT_j}{\pi m_j}\right)^{1/2},$$

$$Q_j^{cyl\,p}=n_j(z)\pi d_p l\left(\frac{2\pi k_BT_j}{m_j}\right)^{1/2},$$

$$Q_e^{tip\,p}=n_e(z)\pi d_p^2\left(\frac{8k_BT_e}{\pi m_e}\right)^{1/2}\exp\left[Z\alpha_e+\frac{eU_S}{k_BT_S}\right]$$

$$Q_e^{cyl\,p} = n_e(z) d_p l \left(\frac{2\pi k_B T_S}{m_e}\right)^{1/2} \exp\left[\frac{eV_S}{k_B T_e} + \frac{eU_S}{k_B T_S}\right],$$

$$Q_{ij}^{tip\,p} = n_{ij}(z)\pi d_p^2 \left(\frac{8k_B T_{ij}}{\pi m_{ij}}\right)^{1/2} \left[1 - Z\alpha_{ij}\right] \exp\left[\frac{-E_b}{k_B T_S}\right] \exp\left[\frac{-eU_S}{k_B T_S}\right],$$

$$Q_{ij}^{cyl\,p} = n_{ij}(z) d_p l \left(\frac{2\pi k_B T_{ij}}{m_{ij}}\right)^{1/2} \exp\left[-\frac{E_b}{k_B T_S}\right] \exp\left[-\frac{eU_S}{k_B T_S}\right] \times \left\{\frac{2}{\sqrt{\pi}} \left(\frac{eV_S}{k_B T_{ij}}\right)^{1/2} + \exp\left[\frac{eV_S}{k_B T_{ij}}\right] erfc\left[\left(\frac{eV_S}{k_B T_{ij}}\right)^{1/2}\right]\right\}.$$

The other terms are given in Table 4.7.

Parameters/functions	Description
V_S	CNT tubular surface potential
E_b	Energy necessary for bulk diffusion
$n_{ij}(z) = n_{ij0}\left(1 - \frac{2e\varphi(z)}{m_{ij} u_{ij0}^2}\right)^{-1/2}$	Plasma sheath ion density
$n_e(z) = n_{e0} \exp\left(\frac{\lvert e\rvert \varphi(z)}{k_B T_e}\right)$	Plasma sheath electron density
n_{e0}, n_{ij0}	Primary number density of electrons and ions
$\varphi(z) = \varphi_0 \exp\left(-\frac{z}{\lambda_D}\right)$	Electrostatic plasma sheath potential
$\lambda_D = \sqrt{k_B T_e / n_e e^2}$	Plasma debye length

Table 4.7 Particulars of functions/parameters in equations for collection currents.

4.3.3 CHARGE ACQUIRED BY THE CARBON NANOTUBES OF THE ARRAY

$$\partial_\tau (Z^p) = \sum_{j}^{A,B} \begin{pmatrix} tip^p & cyl^p \\ Q & + Q \\ ij & ij \end{pmatrix} - \gamma_e \begin{pmatrix} tip^p & cyl^p \\ Q & + Q \\ e & e \end{pmatrix} \tag{4.13}$$

Equation (4.13) evaluates the charge acquired by the p^{th} CNT's tip and cylindrical surfaces due to the accretion of $j = (A, B)$ type ions and electrons impending from the plasma. Z^p describes the aggregate charge on the p^{th} CNT on the array.

$$\mathbb{Q} = \frac{\sum_{p=1}^{N} \partial_\tau (Z^p)}{N} \tag{4.14}$$

Equation (4.14) estimates the average charge acquired by CNTs of an array growing in a reactive plasma surrounding. The equation considers the summation of surface charges over all N numbers of CNTs.

4.3.4 GROWTH OF CNT ARRAY IN PLASMA

$$\partial_\tau \left[\pi \left\{ \left(\frac{D_{ct}}{2} \right)^2 - \left(\frac{d_p}{2} \right)^2 \right\} l_p \right] =$$

$$\left[\left\{ D_{surf} + D_{volm} + 2\kappa\upsilon \left(\frac{D_{ct}}{2} \right)^2_p \right\} \times \frac{P \left\{ 8\pi \left(\frac{D_{ct}}{2} \right)_p \right\} n_C}{\upsilon \rho_{CNT} \sum_{A=1}^{8} Q^p_{iA}} \right.$$

$$\left. + \left\{ \frac{D_{sd}}{4\pi \left(\frac{D_{ct}}{2} \right)^2_p} + \left\{ 4\pi \left(\frac{D_{ct}}{2} \right)^2_p \right\} \sum_{B=1}^{2} Q^p_{iB} \right\} n_H \right] \times \frac{m_{ct}}{\rho_{ct}}. \tag{4.15}$$

Eq. (4.15) calculates the growth of p^{th} CNT growing over p^{th} catalyst nanoparticle where l_p and d_p are the length and diameter of p^{th} CNT. This growth rate is calculated by considering the total volumetric change (reliant on CNT diameter and height) during the continuous CNT growth on the p^{th} catalyst nanoparticle. The former part of the equation assesses the carbon surface and volume diffusion process over the nanoparticle surface and volume along with the precipitation process of carbon atoms from the catalyst surface, giving rise to graphitic cylindrical tubes. When volume diffusion dominates over surface diffusion, MWCNTs are produced otherwise SWCNTs; hence the supremacy of one diffusion process over the other administers the type of CNTs being produced. The former part of the equation considers the metal nanoparticle self-diffusion process and elimination of growth hindering amorphous layer formed over the catalyst due to its contamination. The removal of this layer promotes the CNT growth further by getting rid of carbon atoms attached to the extremities of growing CNT or on the nanoparticle's surface. The vertically aligned structure of CNT is attained due to a continuous electrostatic force resulting from the plasma sheath electric field[13]. Presuming the CNTs to have a perfectly aligned and concentric cylindrical structure, the difference in CNT diameters can estimate the number of CNT layers created, i.e. *outer CNT diameter (~D_{ct}) – inner CNT diameter(d) ≈ number of CNT layers*.

$$\gamma_{array}(d,l) = \frac{\sum_{p=1}^{N} \partial_{\tau}\left[\pi\left\{\left(\frac{D_{ct}}{2}\right)^2 - \left(\frac{d_p}{2}\right)^2\right\} l_p\right]}{N} \tag{4.16}$$

Hence, Eq. (4.16) estimates the average growth rate of CNTs in an array growing over catalyst nanoparticles in a reactive plasma where l and d are the average length and diameter of CNTs in an array. The equation considers the summation of the growth rate of all N numbers of CNTs. The details of various growth processes deliberated in Eq. (4.15) are given in Table 4.8.

Parameters/functions	Description
$D_{surf} = a_0^2 \upsilon \exp\left(-\frac{E_{surf}}{k_B T_S}\right)$	Surface diffusion coefficient of C-atoms[24]
$D_{volm} = \frac{\upsilon D_{ct}}{2\pi} \exp\left(-\frac{E_{volm}}{k_B T_S}\right)$	Volume diffusion coefficient of C-atoms[24]
$D_{sd} = D_{sd0} \exp\left(-\frac{\delta E_{sd}}{k_B T_S}\right)$	Self-diffusion coefficient for metal atoms[24]
$\kappa = a_0 \upsilon \exp\left(-\frac{\delta E_{inc}}{k_B T_S}\right)$	C-atom incorporation rate into the CNT wall[24,31]
$E_{surf}\left(=0.3\ eV\right)$	Surface diffusion C-atom energy barrier on the catalyst [24]
$E_{volm}\left(=1.6\ eV\right)$	Volume diffusion C-atom energy barrier through the catalyst[24]
$\delta E_{inc}\left(=\delta E_d = 0.8\ eV\right)$	C-atom energy barrier to diffuse along nanotube-catalyst boundary[31]

Table 4.8 Particulars of functions/parameters termed in Eq. (4.15).

4.3.5 AMORPHOUS CARBON FILM DEPOSITION

Along with VACNT array growth, an amorphous carbon film can also get deposited between the spaces of the nanotubes of the array. The ionic and neutral species get incorporated at the level where the catalysts are anchored on the substrate ($z = \lambda_s$). The deposition flux rate of carbon film can be determined as[32–34]

$$J_{cf} = J_{iA} + J_{iA}\theta_t y_s(\lambda_s) + n_C \nu \exp\left(\frac{-\delta E_f}{k_B T_S}\right)(\lambda_s) - \frac{1}{4}\left(1-\theta_t\right)\upsilon_0 \sigma_{bulk} J_H - J_{iA}\left(1-\theta_t\right) y_{sp} \tag{4.17}$$

The first term of Eq. (4.17) describes the direct absorption flux of hydrocarbon ions, the second term determines the neutral stitching owing to ion-induced incorporation with the stitching rate as $y_s = 2.49\times10^{-2} + 3.29\times10^{-2}\left(E_i\right)$, the third term is the incorporation of carbon atoms into the film, the fourth term expresses the atomic hydrogen etching assuming the concentration of carbon is higher than hydrogen. Lastly, the fifth term defines the sputtering loss of carbon atoms with sputtering yield as $y_{sp} = -3.89\times10^{-7}\left(E_i^2\right) + 7.04\times10^{-4}\left(E_i - 100\right) + 8.14\times10^{-2}$, where $E_i = 2.1eV$ is the ion energy. Other parameters in the equation are $\delta E_f = 2.3eV$, and $\sigma_{bulk} = 6.8\times10^{-15}\,cm^2$. The growth rate of this carbon film in terms of its width w_{cf} is expressed in Eq. (4.18)

$$\partial_\tau\left\{w_{cf}\right\} = \frac{J_{cf}M_{cf}}{\rho N_A}, \tag{4.18}$$

where J_{cf} is the deposition flux rate, M_{cf} is the film mole mass, ρ is the film density, N_A is the Avogadro number.

4.3.6 FIELD EMISSION FROM THE CNT ARRAY GROWN IN PLASMA

Carbon nanotubes are considered pre-eminent electron field mission materials attributed to their high aspect ratio, i.e. length to radius ratio. The field enhancement factor is crucial to understanding the field emission aspects. When an external electric field of adequate strength is applied around the tip of the nanotube, it leads to electron emission. This factor is usually measured higher for individual CNTs around 30000 – 50000 than for CNT films around 1000 – 3000 which reduces furthermore for dense films due to the electric field screening from the close nanotubes. The factor is known to be dominated by the length of nanotubes and spacing between them; hence it is essential to recognize their effects to achieve optimum field emission properties[35].

$$\beta_0 = 1.2\left(2.15 + \frac{2l}{d}\right)^{0.9} \tag{4.19}$$

Eq. (4.19) approximates the primary geometrical field enhancement factor for an individual VACNT where l and d signify the dimensions of VACNT[36]. The field emission factor is also defined as the ratio of the CNT tip electric field to the macroscopic electric field. Considering the spacing s between VACNTs, the geometrical field enhancement factor for CNT films[37] can be estimated by Eq. (4.20).

$$\beta = \beta_0 \left[1 - \exp\left(-2.3172 \frac{s}{l} \right) \right] \tag{4.20}$$

4.4 RESULTS AND DISCUSSION

The present computation would help to accomplish a catalyzed CNT array growth in C_2H_2/H_2 reactive plasma. The effect of substrate temperature, acetylene concentration, plasma power and plasma pressure on the CNT array aspects are examined. The consequence of gas ratio and substrate temperature on the width of amorphous carbon film between CNTs is also studied. The influence of CNT array aspects on the field enhancement factor of CNT films is also deliberated. The equations mentioned in the previous section are first-order time-varying equations that are solved for plasma aided CNT array growth considering the experimentally acquired primary conditions and glow-discharge parameters anticipated from the literature[11,38,39] and others mentioned in Table 4.9.

Terms	Initial value
Computational substrate area	5000 x 5000 μm^2
Average catalyst diameter D_{ct}	40 *nm*
Minimum spacing between catalysts	100 *nm*
T_e (electron temperature)	2.0 *eV*
T_n (neutral temperature)	0.20 *eV*
T_{ij} (ion species temperature)	0.20 *eV*
$T_s = T_{ct}$ (substrate and catalyst temperature)	750 *K*
Plasma power	300 *W*
Working pressure	100 *mTorr*
U_S (substrate voltage)	-400 *V*
θ_t (total coverage)	0.01
Acetylene gas flow	50 *sccm*
Hydrogen gas flow	200 sc*cm*
$\gamma_e, \gamma_{ij}, \gamma_j$ (sticking coefficients)	1

Table 4.9 Computational parameters considered in the model.

4.4.1 Time variation of CNT array length with substrate temperature

The time variation of average CNT length at different substrate temperatures is depicted in Figure 4.3. The CNT array growth proceeds via hydrocarbon and hydrogen dissociation, creation of diffusion through or over the catalyst nanoparticle, generation of amorphous carbon layer and termination of growth as catalyst gets encapsulated with carbon. As the substrate temperature increases, the ion dissociation increases; hence the incoming flux of carbon generating species increases. Therefore, more carbon atoms diffuse into and over the catalyst, which correspondingly increases the average length of the CNTs in an array. As the temperature is increased beyond an optimum value i.e. 750 ^{o}C, the accretion of carbon atoms increases excessively over the catalyst consuming rapidly its active area required for the growth. This accelerates the generation of the amorphous carbon layer and terminates its growth sooner. Hence, the average length of the array at a higher temperature is inferior. This theoretical result is consistent experimentally with the observation of Chhowalla *et al.*[40], Cui *et al.*[41], and Bulyarskiy *et al.*[42,43]

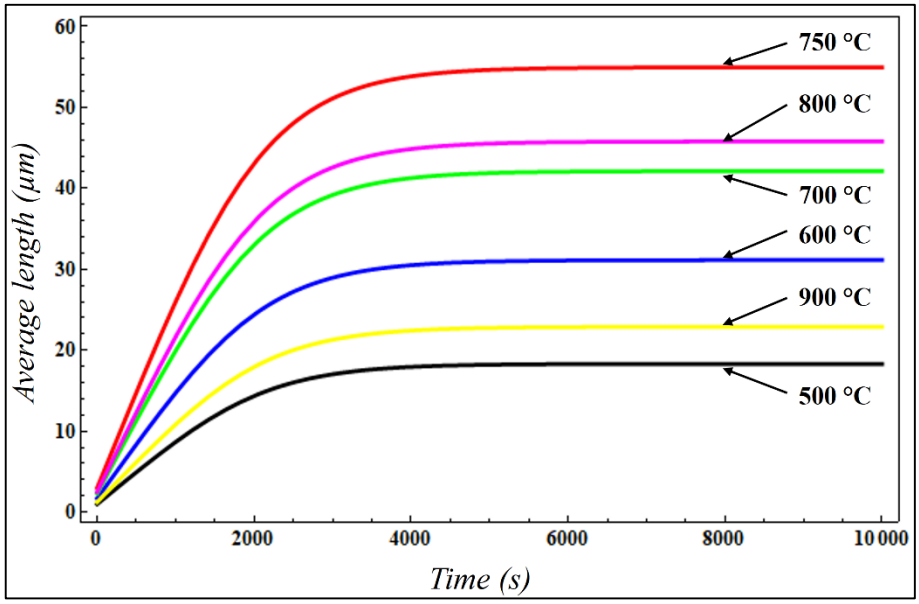

Figure 4.3 Time variation of average length of CNTs of the array during plasma-assisted growth for different substrate temperature.

4.4.2 Time variation of CNT array length with hydrocarbon concentration

The time variation of average CNT length at different acetylene concentrations is depicted in Figure 4.4. The presence of H_2 in C_2H_2/H_2 plasma has two roles in the growth of CNTs: the generation of atomic hydrogen and the removal of excess carbon and delay in creating amorphous carbon on the catalyst surface. This means that the etching rate of the amorphous layer decreases for lower hydrogen content. On the lower side of the increase in acetylene concentration in plasma, the carbon creating species essential for growth and hydrogen creating species required for excess carbon etching collectively gives the initial increase in the array length. However, increasing the C_2H_2 concentration over an ideal value i.e. 30 %, results in a plasma with excess carbon for growth and low hydrogen for etching. Hence, the growth rate dominates the etching rate giving rise to quick termination of growth and shorter nanotube arrays. The result is verified experimentally by Chhowalla *et al.*[40], Bell *et al.*[11] and Chen *et al.*[44].

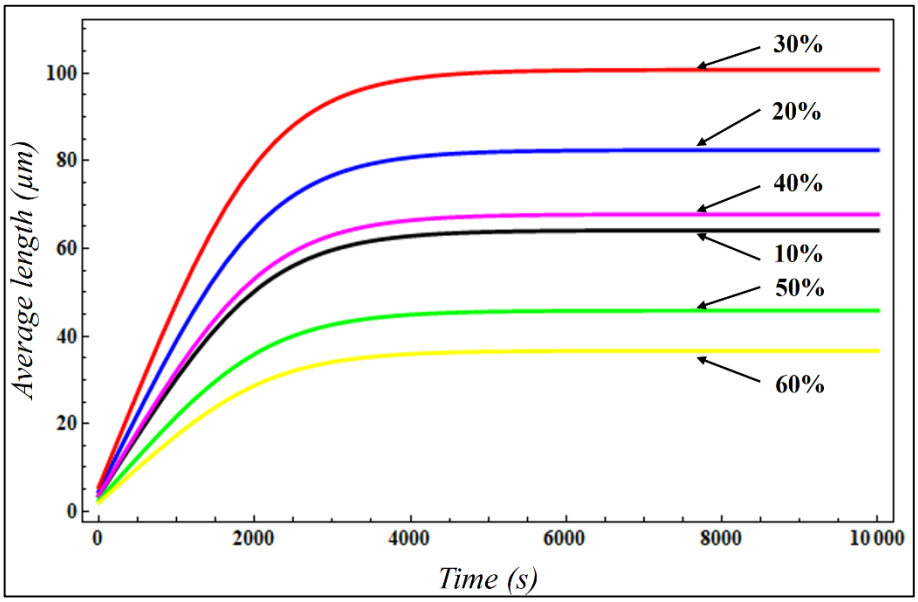

Figure 4.4 Time variation of average length of CNTs of the array during plasma-assisted growth for different C_2H_2%.

4.4.3 Variation of CNT array length and diameter with plasma power

When the plasma power increases, the plasma electron density and electron temperature also increase [45], which gives rise to plasma neutral atom ionization and an increase in plasma ion number density. Bell *et al.*[11] studied that the decomposition of hydrocarbon rises on increasing power. The increase in neutral decomposition enhances the ion-induced dissociation, which generates a significant amount of carbon and hydrogen species.

The time variations of carbon and hydrogen number density at different plasma power are depicted in Figure 4.5 (i) and (ii), respectively. Since carbon atoms are responsible for the growth of nanotubes and hydrogen atoms' etching, both the rates collectively heightens the nanotubes' array. The decrease in the nanotube diameter is due to stresses exerted by the graphitic walls and etching due to hydrogen species. For increasing plasma power, the hydrogen etching leads to the removal of graphitic walls of nanotubes, thereby diminishing its diameter (the initial diameter was comparable to the catalyst diameter). Thus, for higher power, the reduction in diameter is more significant.

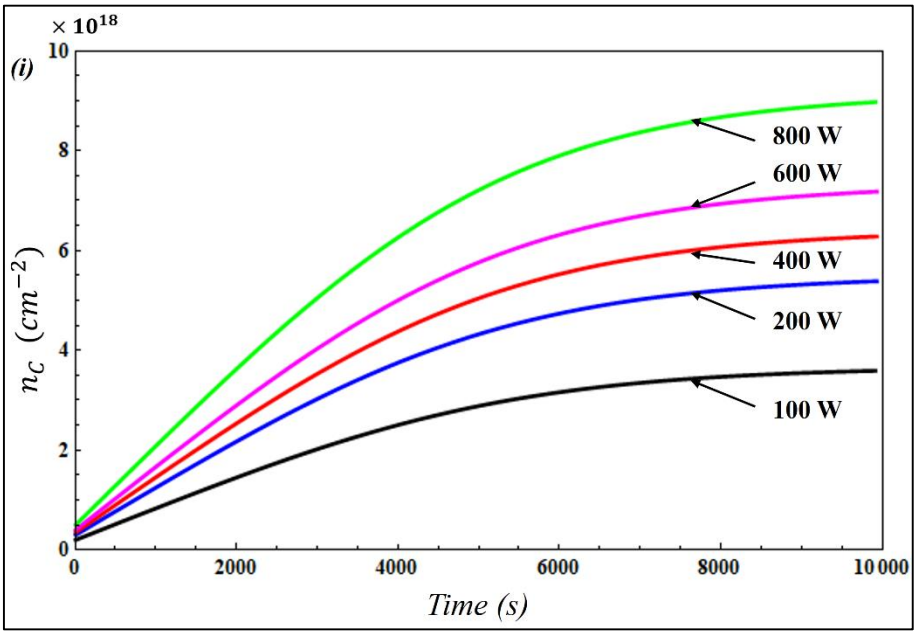

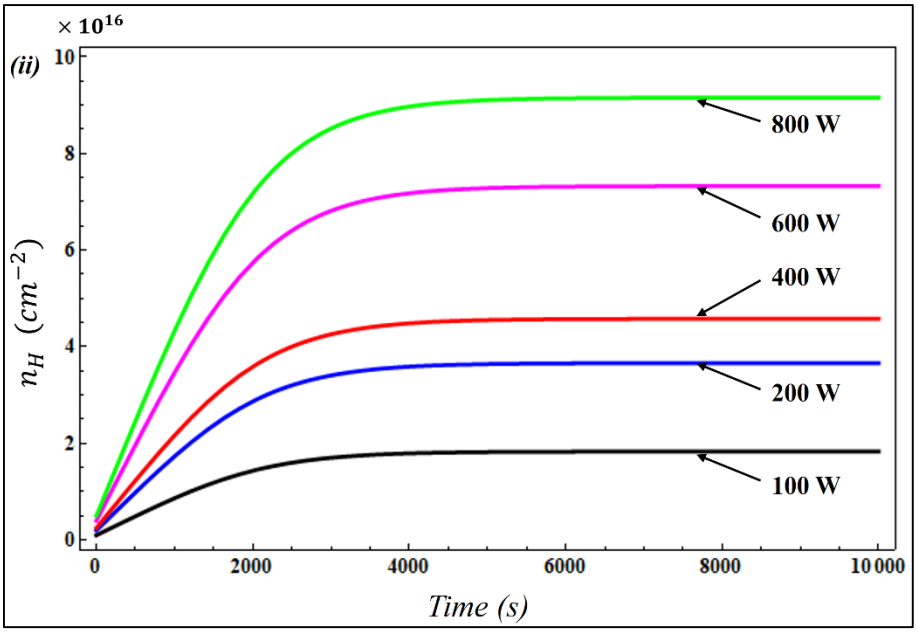

Figure 4.5 Time variations of (i) carbon density and (ii) hydrogen density during plasma-assisted growth of CNT array for different plasma power.

The variations of average length and average diameter of CNTs at different plasma power are depicted in Figure 4.6 (i) and (ii), respectively where the points represent the value of average length and diameter of CNTs of the array for specific plasma power and the line represents the best fit. The outcomes are comparable to the experimental observations of Ikuno *et al.*[46], Wei *et al.*[47], Merkulov *et al.*[48], and Chang *et al.*[49].

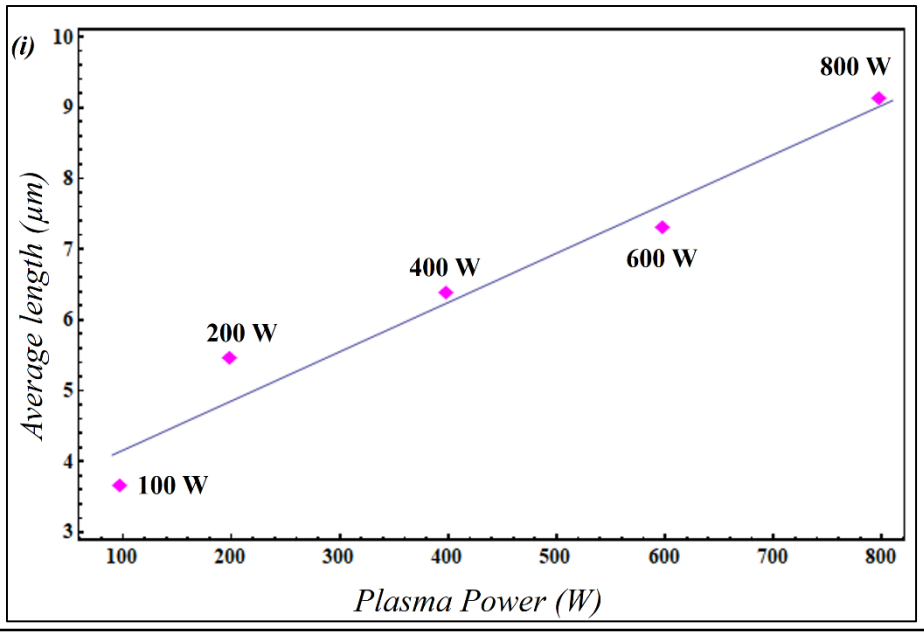

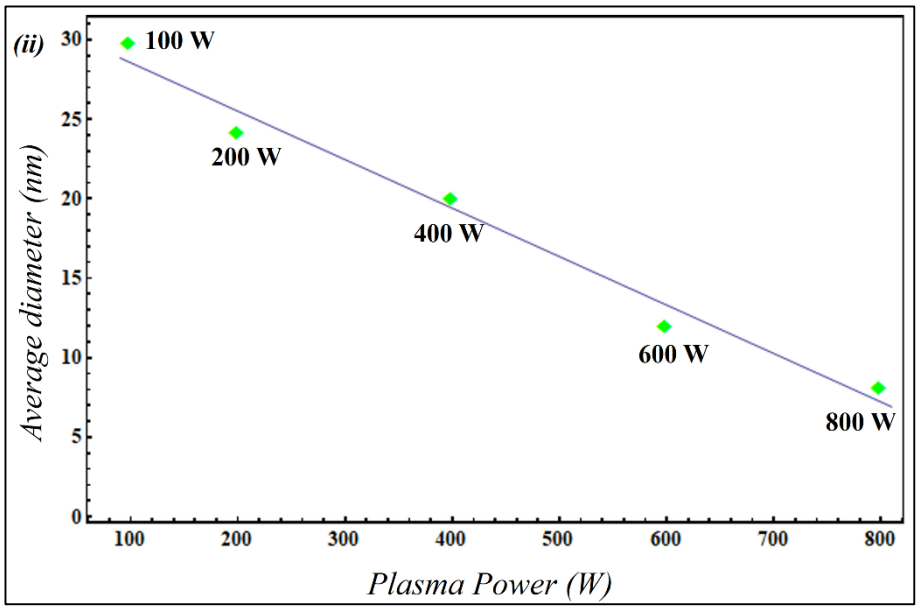

Figure 4.6 Variation of (i) average length and (ii) average diameter of CNTs of the array for different plasma power. (Line represents best fit curve)

4.4.4 Variation of CNT array length and diameter with plasma pressure

When the plasma pressure increases, the plasma electron density and electron temperature decrease [50], increasing the number of electrons and neutrals collisions. This indicates that plasma species would lose energy, decreasing the temperature of neutral species and resulting in lower neutral ionization, i.e. the number of neutrals in plasma (neutral species density) is higher at higher pressures. Hence, at higher pressures, the neutral flux to the catalyst increases, thus raising the amount of C and H atoms generated over the catalyst surface.

The time variations of carbon and hydrogen number density with plasma pressure are depicted in Figure 4.7 (i) and (ii), respectively. The increases in the density of carbon and hydrogen atoms leads to more significant nanotube growth; hence, the average length of CNTs of the array increases. At extremely high pressures, hydrogen neutrals dissociation is higher than hydrocarbons as they require lower energy to dissociate. This increases the number of carbon atoms excessively as opposed to hydrogen. Hence, deposition rate dominates etching rate, which rapidly consumes the catalyst active area

required for growth, leading to shorter nanotubes. The fall in average CNT diameter is the greatest for the lowest plasma pressure. The etching rate is lower for a high plasma pressure than the deposition rate; hence the diameter reduction is slight (the initial diameter was comparable to the catalyst diameter).

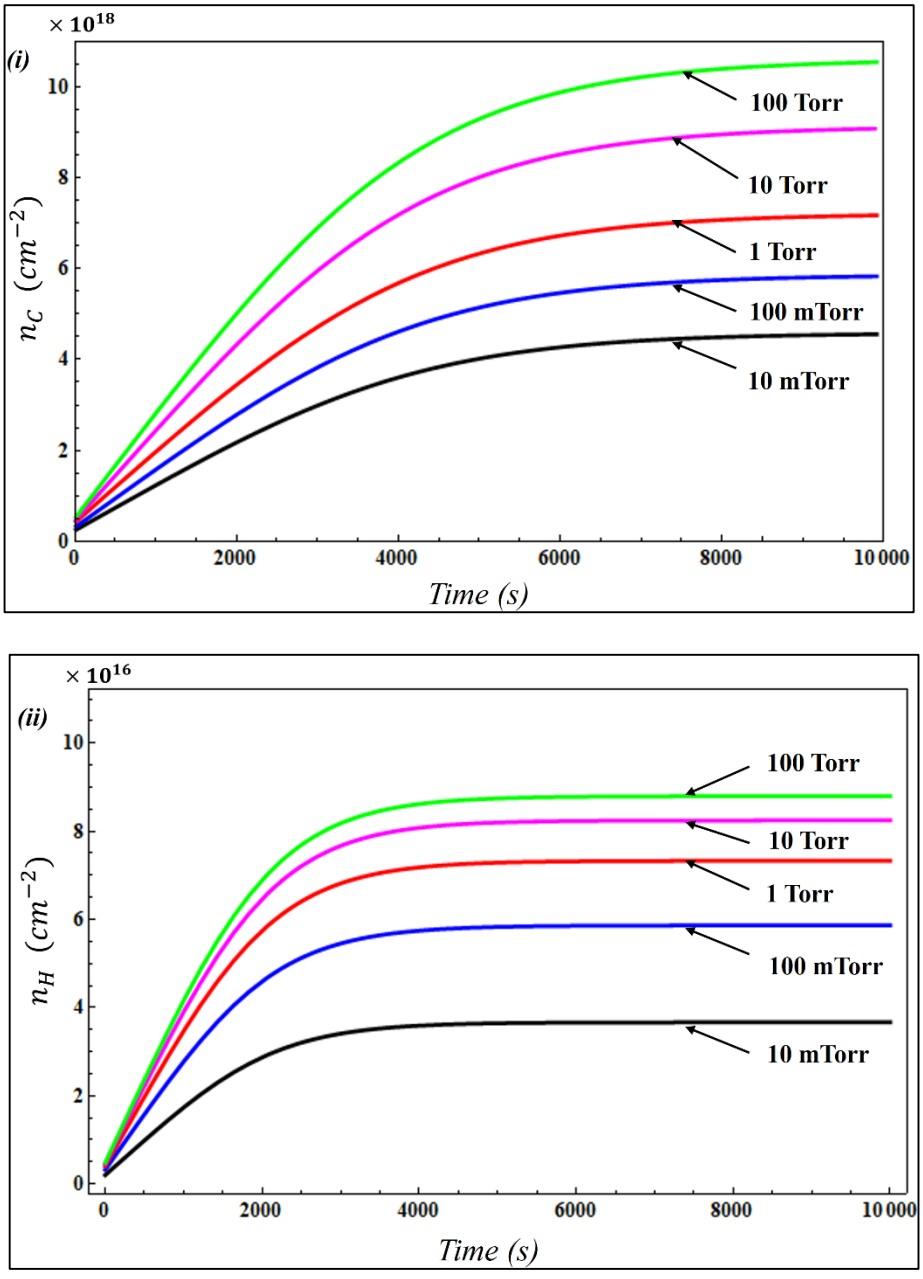

Figure 4.7 Time variations of (i) carbon density and (ii) hydrogen density during plasma-assisted growth of CNT array for different plasma pressure.

The variations of average length and average diameter of CNTs at different plasma pressure are depicted in Figure 4.8 (i) and (ii), respectively where the points represent the value of average length and diameter of CNTs of the array for specific plasma pressure and the line represents the best fit. The results for the initial increase in length for low pressure and decrease with higher pressures is experimentally detected by Cruden *et al.*[51], Tsakadze *et al.*[52] and Li *et al.*[53], whereas the increase in diameter with pressure is in agreement with Li *et al.*[53] and Tanemura *et al.*[54].

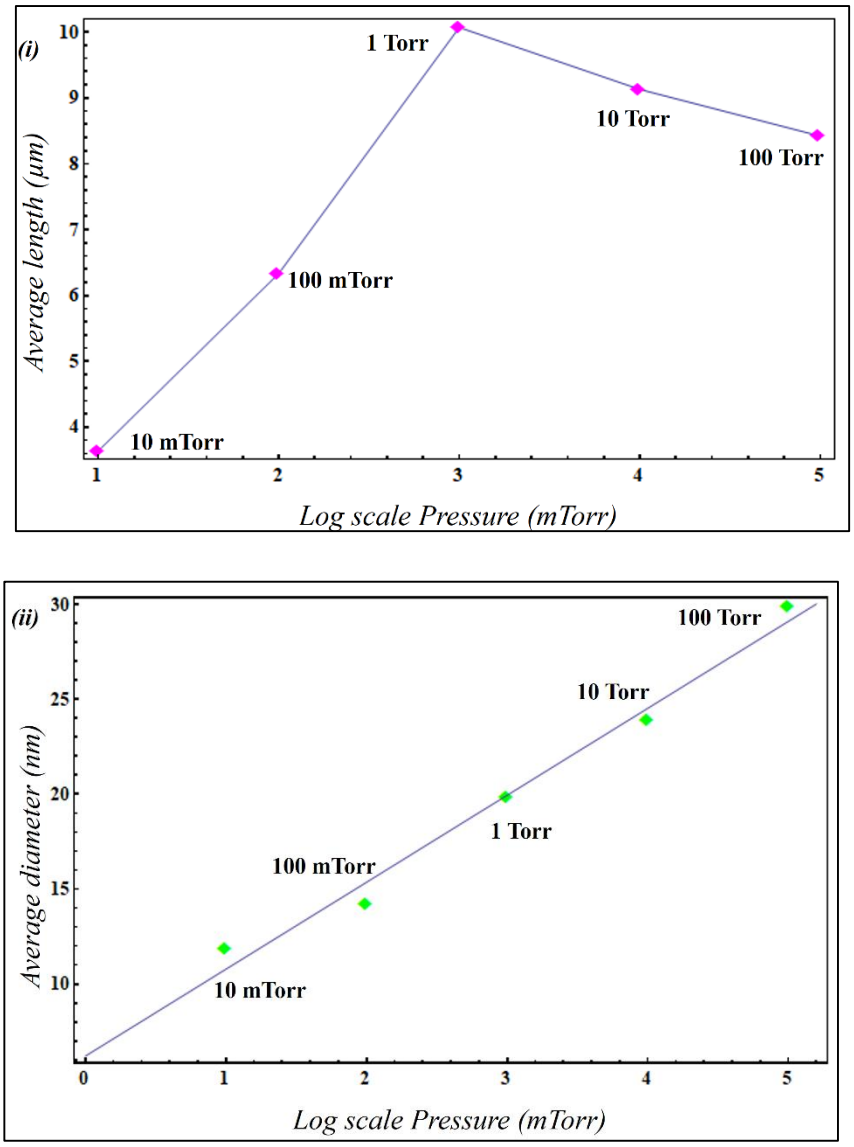

Figure 4.8 Variation of (i) average length and (ii) average diameter of CNTs of the array for different plasma pressure. (Line represents best fit curve)

4.4.5 Instantaneous growth of CNT and corresponding charge

A plot of the instantaneous change in length and corresponding charge attained by the CNT with time is depicted in Figure 4.9. As the substrate where the catalyst is anchored and array growth occur is attached to a negatively biased substrate, the CNTs of the array acquire a negative charge. With time, the average length of the CNTs of the array increases and attains a saturated value on termination [cf. Fig. 4.3 and 4.4]. At shorter CNT length, negative charge is less and at larger length, this negative charge is more. Hence the negative charge acquired by the growing CNTs would also increase due to increase in CNT length and lastly attain a constant value on growth termination *(l=55 μm)*. The variation of the nanotube with growth time is experimentally verified through various literature [40,47].

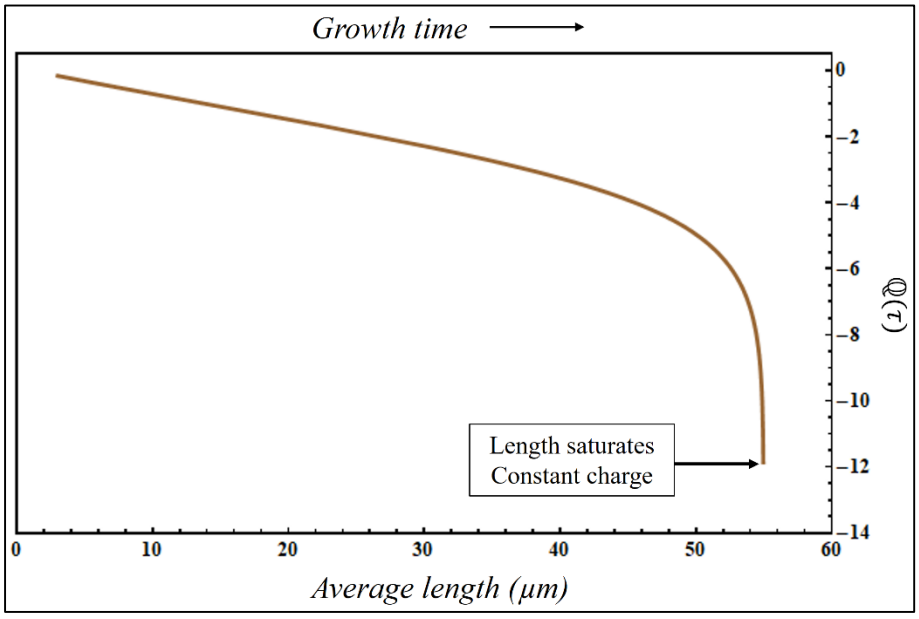

Figure 4.9 A plot of average CNT length and average charge of CNT with growth time.

4.4.6 Variation of the width of amorphous carbon film with gas ratio

The variation of the width or thickness of amorphous carbon film generated over the substrate between CNTs with C_2H_2/H_2 gas ratio is depicted in Figure 4.10. As the amount of acetylene compared to hydrogen in plasma increases, i.e. the C_2H_2/H_2 ratio increases, more hydrocarbon species are available for dissociation and incorporation,

which correspondingly increases carbon atoms density. This increases the flux of carbon atoms and creates an amorphous carbon film. In another way, if the amount of hydrogen in plasma increases, i.e. the C_2H_2/H_2 ratio decreases, the film etching increases due to an increase in hydrogen flux that produces a thinner amorphous carbon film. This result is comparable to the result numerically modelled by Denysenko et al.[34].

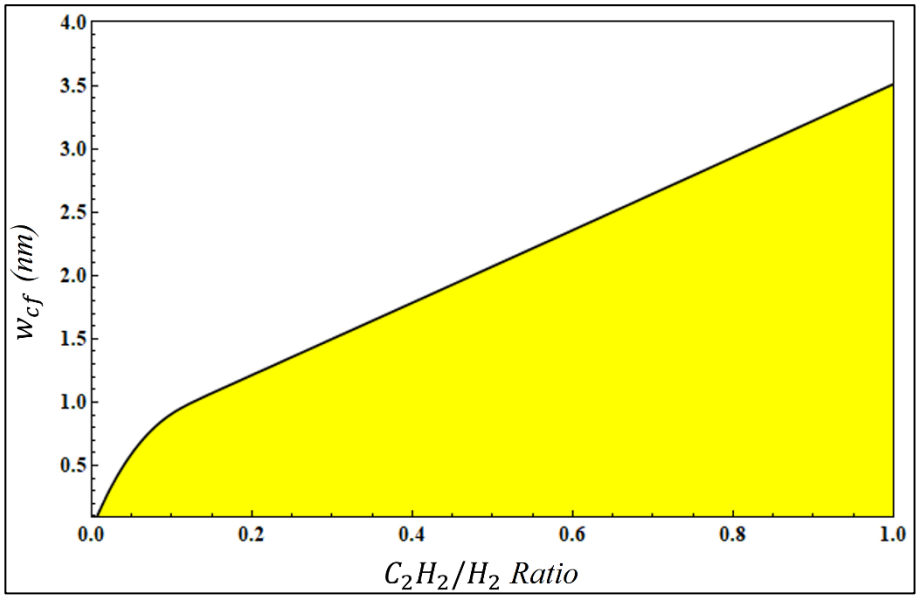

Figure 4.10 Width of carbon film formed between CNTs with changing gas ratio.

4.4.7 Variation of the width of amorphous carbon film with substrate temperature

The variation of the width of amorphous carbon film generated over the substrate between CNTs with substrate temperature for different hydrocarbon ion densities is depicted in Figure 4.11. As the substrate temperature increases, the width of carbon film decreases due to an increase in desorption flux, which decreases the total surface coverage. The deposition flux rate of carbon film decreases significantly, depositing a thin carbon film. Also, increasing the hydrocarbon ion density increases the ion flux increases, which collectively increases their direct and ion-induced incorporation to the carbon film [cf Eq. (4.17)], and the film gets thicker. This outcome is observed experimentally by Mantzaris *et al.*[32] and simulated numerically by Denysenko *et al.*[31].

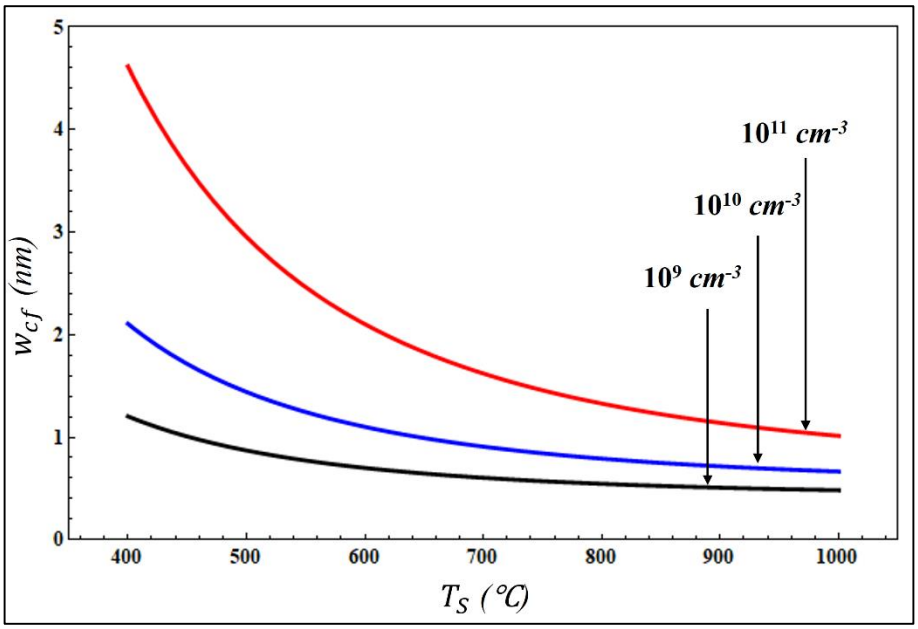

Figure 4.11 Width of carbon film formed between CNTs for changing substrate temperature for different hydrocarbon ion densities.

4.4.8 Variation of the ratio of geometrical field enhancement factor β / β_0

The variation of the ratio of geometrical field enhancement factor β of a CNT film and enhancement factor β_0 of an individual CNT (i.e. the ratio of field enhancement of an array film and an individual nanotube β / β_0) with spacing s for different arrays obtained from the pressure study mentioned in Table 4.10 is depicted in Figure 4.12 (i). The field emission property is significant for arrays with the highest β; therefore, arrays with the highest β / β_0 ratio would have the best field emission characteristics.

Case	*l (μm)*	*d (nm)*
I	3.64	11.88
II	6.34	14.19
III	10.07	19.81
IV	9.13	23.91
V	8.42	29.92

Table 4.10 Dimensions of the array obtained from the pressure study [cf Fig. 4.8 (i-ii)] which were considered for field enhancement study.

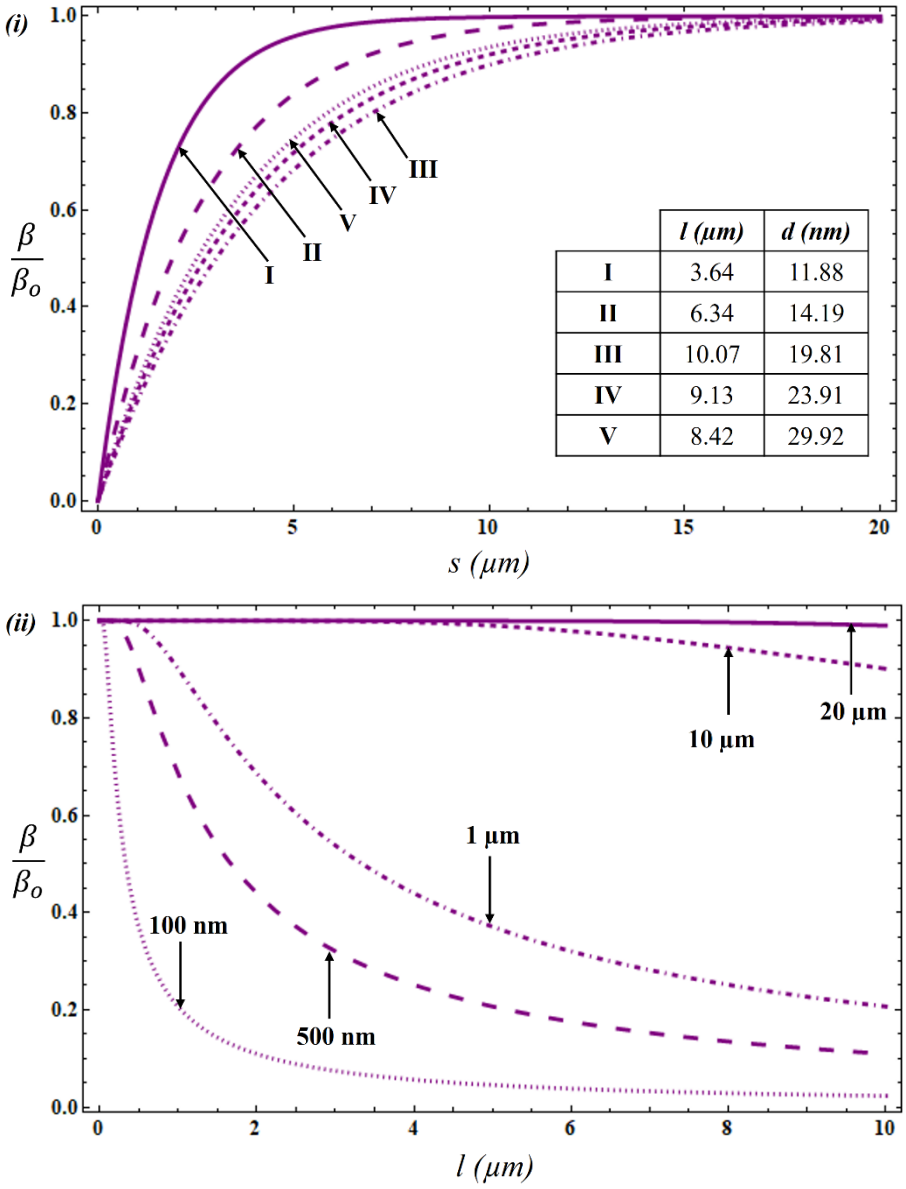

Figure 4.12 β / β_0 variation for an array with (i) spacing s between CNTs and (ii) length for different spacing between CNTs.

As seen from the figure, for less dense arrays, i.e. for greater spacing *s* between CNTs, β / β_0 increases. This can be attributed to the reduction in screening effects of individual CNTs of the array on one another. This suggests that the field emission from sparse nanotube arrays is better than denser ones. For case I, where *l* and *d* possess minimum values, β / β_0 is maximum signifying that small and thin CNT arrays are appropriate for best emission characteristics. Also, the result shows that as *s* increases beyond *2l*,

the exponential term in Eq. (4.20) becomes insignificant, and the CNTs of the array are spaced so far apart that they behave as individual emitters showing the best emission characteristics. Figure 4.12 (ii) shows the variation of β / β_0 with the length of the nanotubes of the array for different *s*. For constant $d=40$ *nm*, an increase in *l* decreases β / β_0, indicating poor field emission characteristics. The results show that as s increases, β / β_0 also increases, which substantiates our previous result. However, again it is observed that as *s* increases beyond *2l*, i.e., the array becomes sparse, CNTs start behaving as individual emitters. Hence, taking advantage of these results, one can design a CNT array by varying the plasma process parameters as reflected in this study to attain the best field emission characteristics.

The contour plots for field enhancement factor on the variation of inter CNT spacing and length (constant $d=40$ *nm*) is depicted in Figure 4.13 (i), and the average CNT diameter and length (constant $s=100$ *nm*) is depicted in Figures 4.13 (ii), respectively. The plots verify that an array with short and thin CNTs with large spacing shows the highest field enhancement. Hence, it is evident that short and sparse CNT arrays will be appropriate for producing the best field emitters. These results are in agreement with the field emission studies of CNT arrays by Bonard *et al.*[37], Jo *et al.*[55], Xu *et al.*[56] and Chhowalla *et al.*[57].

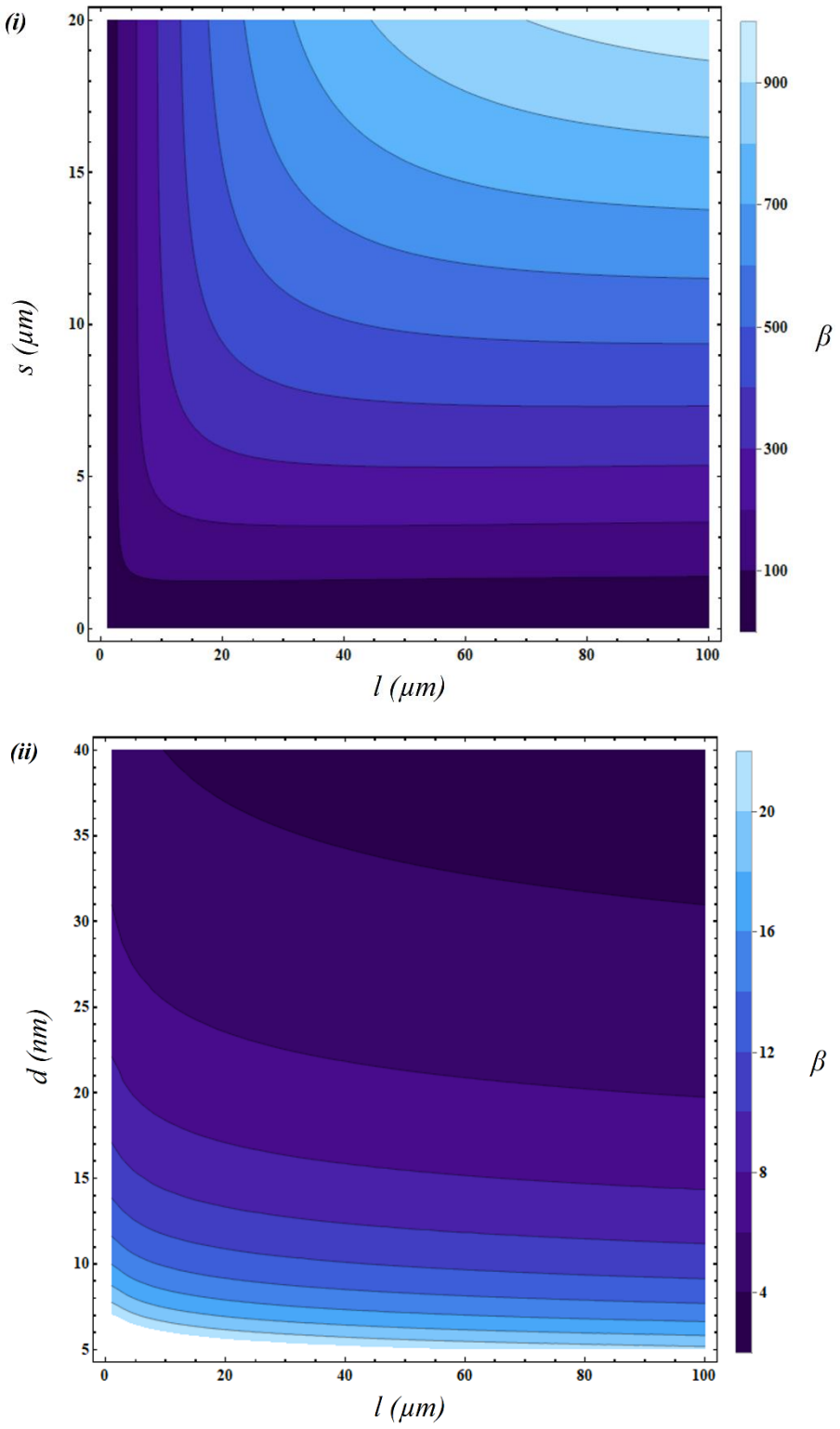

Figure 4.13 Contour plots for geometrical field enhancement factor of an array for (i) average CNT spacing and length, (ii) average CNT diameter and length.

4.5 CONCLUSIONS

The computational study is modelled to investigate the growth kinetics of a carbon nanotube array in a plasma. A pre-patterned film of catalyst nanoparticles was considered, and a model was developed that computes the influence of substrate temperature, plasma concentration, power and pressure on the aspects of the CNT array. From the outcomes, it is concluded that plasma processing conditions greatly influence the array's growth. The average CNT length increases with substrate temperature and decreases beyond an optimum value. Similarly, the plasma concentration can also be adjusted to accomplish appropriate CNT length. The effect of power and pressures on the carbon and hydrogen atom density that corresponds to deposition of carbon atoms and etching by hydrogen is also observed. The change in average length and diameter of CNTs of the array with power and pressures is revealed. The temporal change in average charge acquired by the nanotube and its length is also represented. The effect of gas ratio and substrate temperature on the width of a carbon film deposited on the substrate between CNTs is also presented. The field enhancement of the nanotube array is studied, and ways to improve the emission properties are discussed. The study can support optimizing various plasma parameters as discussed in the script for achieving a suitable CNT array that can be used as the best field emitters. This model can also be comprehensively used to design a study of the plasma-assisted growth of several nanostructured materials and optimization of their properties.

REFERENCES

[1] Y. Luo, X. Wang, M. He, X. Li, and H. Chen, J. Nanomater. **2012**, 542582 (2012).

[2] P.H. Lin, C.L. Sie, C.A. Chen, H.C. Chang, Y.T. Shih, H.Y. Chang, W.J. Su, and K.Y. Lee, Nanoscale Res. Lett. **10**, 1 (2015).

[3] X. Tang, H. Yue, L. Liu, J. Luo, X. Wu, R. Zheng, and G. Cheng, ACS Appl. Nano Mater. **3**, 7659 (2020).

[4] L. Nilsson, O. Groening, C. Emmenegger, O. Kuettel, E. Schaller, L. Schlapbach, H. Kind, J.M. Bonard, and K. Kern, Appl. Phys. Lett. **76**, 2071 (2000).

[5] U. Sharma and S.C. Sharma, IEEE Trans. Plasma Sci. **50**, 888 (2022).

[6] T. Kato, G.H. Jeong, T. Hirata, R. Hatakeyama, K. Tohji, and K. Motomiya, Chem. Phys. Lett. **381**, 422 (2003).

[7] S. Hofmann, C. Ducati, J. Robertson, and B. Kleinsorge, Appl. Phys. Lett. **83**, 135 (2003).

[8] S.K. Srivastava, V.D. Vankar, and V. Kumar, Thin Solid Films **515**, 1552 (2006).

[9] S.K. Srivastava, V.D. Vankar, D. V. Sridhar Rao, and V. Kumar, Thin Solid Films **515**, 1851 (2006).

[10] Y. Hayashi, T. Fukumura, K. Odani, T. Matsuba, and R. Utsunomiya, Thin Solid Films **518**, 3506 (2010).

[11] M.S. Bell, K.B.K. Teo, R.G. Lacerda, W.I. Milne, D.B. Hash, and M. Meyyappan, Pure Appl. Chem. **78**, 1117 (2006).

[12] M.S. Bell, R.G. Lacerda, K.B.K. Teo, N.L. Rupesinghe, G.A.J. Amaratunga, W.I. Milne, and M. Chhowalla, Appl. Phys. Lett. **85**, 1137 (2004).

[13] U. Sharma and S.C. Sharma, Phys. Plasmas **25**, 103509 (2018).

[14] H. Okuyama, N. Iwata, and H. Yamamoto, Mol. Cryst. Liq. Cryst. **472**, 209/[599] (2007).

[15] T. Ikuno, S. Takahashi, K. Kamada, S. Ohkura, S.I. Honda, M. Katayama, T. Hirao, and K. Oura, Surf. Rev. Lett. **10**, 611 (2003).

[16] J. Lee, E. Oh, T. Kim, J.H. Sa, S.H. Lee, J. Park, D. Moon, I.S. Kang, M.J. Kim, S.M. Kim, and K.H. Lee, Carbon N. Y. **93**, 217 (2015).

[17] O.A. Louchev, Y. Sato, and H. Kanda, Appl. Phys. Lett. **80**, 2752 (2002).

[18] G. Zhong, T. Iwasaki, J. Robertson, and H. Kawarada, J. Phys. Chem. B **111**, 1907 (2007).

[19] A. Thapa, K.L. Jungjohann, X. Wang, and W. Li, J. Mater. Sci. **55**, 2101 (2020).

[20] T. Campo, S. Pinilla, S. Gálvez, J.M. Sanz, F. Márquez, and C. Morant, Nanomaterials **9**, 571 (2019).

[21] M. Morassutto, R.M. Tiggelaar, M.A. Smithers, and J.G.E. Gardeniers, Mater. Today Commun. **7**, 89 (2016).

[22] H. Mehdipour, K. Ostrikov, A.E. Rider, and Z. Han, Plasma Process. Polym. **8**, 386 (2011).

[23] Z. Marvi, S. Xu, G. Foroutan, and K. Ostrikov, Phys. Plasmas **22**, 013504 (2015).

[24] I. Denysenko and K. Ostrikov, J. Phys. D. Appl. Phys. **42**, 015208 (2009).

[25] H. Mehdipour, K. Ostrikov, and A.E. Rider, Nanotechnology **21**, 455605 (2010).

[26] M. Mao and A. Bogaerts, J. Phys. D. Appl. Phys. **43**, 315203 (2010).

[27] I.B. Denysenko, S. Xu, J.D. Long, P.P. Rutkevych, N.A. Azarenkov, and K. Ostrikov, J. Appl. Phys. **95**, 2713 (2004).

[28] M.A. Lieberman and A.J. Lichtenberg, *Principles of Plasma Discharges and*

Materials Processing: Second Edition (John Wiley & Sons, 2005).

[29]UMIST Database Astrochem. (2012).

[30] M.S. Sodha, S. Misra, S.K. Mishra, and S. Srivastava, J. Appl. Phys. **107**, 103307 (2010).

[31] I. Denysenko and N.A. Azarenkov, J. Phys. D. Appl. Phys. **44**, 174031 (2011).

[32] N. V. Mantzaris, E. Gogolides, A.G. Boudouvis, A. Rhallabi, and G. Turban, J. Appl. Phys. **79**, 3718 (1996).

[33] O.A. Louchev, C. Dussarrat, and Y. Sato, J. Appl. Phys. **86**, 1736 (1999).

[34] I. Denysenko, K. Ostrikov, M.Y. Yu, and N.A. Azarenkov, J. Appl. Phys. **102**, 074308 (2007).

[35] K.B.K. Teo, M. Chhowalla, G.A.J. Amaratunga, W.I. Milne, G. Pirio, P. Legagneux, F. Wyczisk, D. Pribat, and D.G. Hasko, Appl. Phys. Lett. **80**, 2011 (2002).

[36] C.J. Edgcombe and U. Valdrè, J. Microsc. **203**, 188 (2001).

[37] J.M. Bonard, N. Weiss, H. Kind, T. Stöckli, L. Forró, K. Kern, and A. Châtelain, Adv. Mater. **13**, 184 (2001).

[38] J. Benedikt, J. Phys. D. Appl. Phys. **43**, 043001 (2010).

[39] C. Bower, W. Zhu, S. Jin, and O. Zhou, Appl. Phys. Lett. **77**, 830 (2000).

[40] M. Chhowalla, K.B.K. Teo, C. Ducati, N.L. Rupesinghe, G.A.J. Amaratunga, A.C. Ferrari, D. Roy, J. Robertson, and W.I. Milne, J. Appl. Phys. **90**, 5308 (2001).

[41] H. Cui, O. Zhou, and B.R. Stoner, J. Appl. Phys. **88**, 6072 (2000).

[42] S. V. Bulyarskiy, G.G. Gusarov, A. V. Lakalin, M.S. Molodenskiy, A.A. Pavlov, and R.M. Ryazanov, Diam. Relat. Mater. **103**, 107665 (2020).

[43] S. V. Bulyarskiy, A. V. Lakalin, M.S. Molodenskii, A.A. Pavlov, and R.M. Ryazanov, Inorg. Mater. **57**, 20 (2021).

[44] G.Y. Chen, C.H.P. Poa, V. Stolojan, S. Henley, and S.R.P. Silva, Mater. Res. Soc. Symp. Proc. **858**, 91 (2004).

[45] W.Z. Collison, T.Q. Ni, and M.S. Barnes, J. Vac. Sci. Technol. A Vacuum, Surfaces, Film. **16**, 100 (1998).

[46] T. Ikuno, M. Katayama, K. Kamada, S. Hiwatashi, S. Ohkura, S.I. Honda, and K. Oura, Japanese J. Appl. Physics, Part 1 Regul. Pap. Short Notes Rev. Pap. **42**, 6717 (2003).

[47] H.W. Wei, K.C. Leou, M.T. Wei, Y.Y. Lin, and C.H. Tsai, J. Appl. Phys. **98**, 044313 (2005).

[48] V.I. Merkulov, D.K. Hensley, A. V. Melechko, M.A. Guillorn, D.H. Lowndes, and M.L. Simpson, J. Phys. Chem. B **106**, 10570 (2002).

[49] S.C. Chang, T.C. Lin, and C.Y. Pai, Microelectronics J. **38**, 657 (2007).

[50] G. Shivkumar, S.S. Tholeti, M.A. Alrefae, T.S. Fisher, and A.A. Alexeenko, J. Appl. Phys. **119**, 113301 (2016).

[51] B.A. Cruden, A.M. Cassell, D.B. Hash, and M. Meyyappan, J. Appl. Phys. **96**, 5284 (2004).

[52] Z.L. Tsakadze, K. Ostrikov, C.H. Sow, S.G. Mhaisalkar, and Y.C. Boey, J. Nanosci. Nanotechnol. **10**, 6575 (2010).

[53] W.Z. Li, J.G. Wen, and Z.F. Ren, Appl. Phys. A Mater. Sci. Process. **73**, 259 (2001).

[54] M. Tanemura, K. Iwata, K. Takahashi, Y. Fujimoto, F. Okuyama, H. Sugie, and V. Filip, J. Appl. Phys. **90**, 1529 (2001).

[55] S.H. Jo, Y. Tu, Z.P. Huang, D.L. Carnahan, D.Z. Wang, and Z.F. Ren, Appl. Phys.

Lett. **82**, 3520 (2003).

[56] Z. Xu, X.D. Bai, and E.G. Wang, Appl. Phys. Lett. **88**, 133107 (2006).

[57] M. Chhowalla, C. Ducati, N.L. Rupesinghe, K.B.K. Teo, and G.A.J. Amaratunga, Appl. Phys. Lett. **79**, 2079 (2001).

Chapter - 5

EFFECT OF HYDROGEN PLASMA AND OTHER CARRIER GASES ON GROWTH OF CARBON NANOTUBES

PUBLICATION

- **Umang Sharma** and Suresh C. Sharma, "Investigating the effect of different carrier gases on plasma-assisted multiwalled carbon nanotube growth", *46th European Physical Society Conference on Plasma Physics*, ECA Volume **43C**: P2.3009 (2019).
- **Umang Sharma**, Suresh C. Sharma, Ravi Gupta and Neha Gupta, "Theoretical Investigations to Study the Effect of C_2H_2/H_2 gas ratio on the Multi-walled Carbon Nanotubes Growth", *44th European Physical Society Conference on Plasma Physics*, ECA Volume **41F**: P2.309 (2017).
- **Umang Sharma**, Neha Gupta, Ravi Gupta, and Suresh C. Sharma, "Analytical modelling to study the effect of hydrogen plasma on the growth of multi-walled carbon nanotubes", *IOP: Journal of Physics: Conference Series*, Volume **36**: 012017 (2017).

5

EFFECT OF HYDROGEN PLASMA AND OTHER CARRIER GASES ON GROWTH OF CARBON NANOTUBES

5.1 BRIEF OUTLINE OF THE CHAPTER

In this chapter, a theoretical model has been established to examine the hydrogen plasma and different gases effects on the multi-walled carbon nanotubes (MWCNTs) growth. The model includes the carbon nanotube (CNT) charging rate, the energy of all the plasma species, and the multi-walled carbon nanotube (MWCNT) growth rate due to the particle accumulation and surface and bulk diffusions on the surface of catalyst particle in the presence of three different plasma environments- I: CH_4 (methane) + H_2 (hydrogen); II: C_2H_2 (acetylene) + H_2 (hydrogen); III: C_2H_2 (acetylene) + NH_3 (ammonia) or N_2 (nitrogen), or Ar (argon), respectively. The analytical calculations helps to understand the influence of H_2 density on the MWCNT size for plasma glow-discharge parameters. The effect of H_2 on the density of hydrocarbons has also been studied. Our investigations also establish that on increasing C_2H_2/H_2 gas ratio, the growth rate of CNTs increases. We have also established the effect of different carrier gases on the CNT growth considering C_2H_2 as the hydrocarbon source. The work can be thought useful to serve to a better understanding of the growth of MWCNT in the plasma and to study their field emission applications.

5.2 INTRODUCTION

The carbon nanotube (CNT) is a novel carbon structure found since 1991[1]. CNTs due to their extraordinary mechanical properties, have been getting much attention for a wide variety of applications. Plasma enhanced chemical vapor deposition (PECVD) has garnered attention than other methods due to the advantages of a highly efficient and vertical growth of nanotubes at low-temperature[2–5]. The plasma-aided CNT fabrication via plasma-enhanced chemical vapor deposition (PECVD) has many advantages over other techniques namely low-temperature growth, vertical and uniformly aligned growth, single-walled CNT (SWCNT) or multi-walled CNT (MWCNT), etc.

Maruyama *et al.*[6] prospered in producing high-purity single-walled CNTs (SWCNTs) with a high number density.

Hata *et al.*[7] discovered a way to grow high-purity SWCNTs with a high growth rate by adding a small amount of H_2O vapour to the carbon source. They advocated that OH radicals worked as a weak oxidizer to eradicate impurities without damaging the CNT.

Zhang *et al.*[8] argued the effects of H radicals in the gas phase on SWCNT growth. They suggested that the balance of carbon and hydrogen radicals were vital for CNT growth.

Ostrikov *et al.*[9] examined $CH_4/H_2/Ar$ plasma for synthesis of carbon nanostructures. They noted that H atoms affected catalyst activity and that cations were provided as precursors for the carbon nanostructure.

Denysenko *et al.*[10] exhibited that C_xH_y ions increased with the supply of the carbon source and that H atoms also increased with the C_xH_y molecules formed in the $CH_4/H_2/Ar$ plasma. Hydrogen plays a dual role in the PECVD growth of CNT. It acts as an activator for the dissociation of hydrocarbon species into more active species and also as an etching reagent of CNT.

Srivastava *et al.*[11] investigated the effect of hydrogen plasma on the growth of multiwalled CNTs and observed that without hydrogen plasma or les treatment time, the synthesised CNTs had high quantity of amorphous carbon.

Zhi *et al.*[12] deliberated the effect of hydrogen treatment on the field emission properties of CNTs. They suggested that the presence of hydrogen plasma in CNTs growth is beneficial for improving their field emission (FE) properties.

Lee *et al.*[13] considered a plasma with H_2, Ar and CF_4 to study their effect on the CNT morphology and their FE characteristics. They observed CNTs with higher defect density and small diameters signifying the plasma etching effects. They also reported that the field emission is highest for CNTs treated with the H_2 plasma.

Feng *et al.*[14] observed the effects of H_2, N_2 and NH_3 plasma treatment on the microstructure and FE properties of CNT films. They found that on plasma treatment, the CNT films showed astonishing FE characteristics with emission site density (ESD) dramatically increasing from 10^3 to 10^6 cm^{-2}.

Several groups have experimentally observed the effect of various carrier gases such as ammonia (NH_3), nitrogen (N_2), and argon (Ar) on the growth of CNTs.

Yap *et al.*[15] suggested the influence of carrier gases on the growth, density and structure of CNTs. They synthesized CNTs under various plasma conditions (i) pure C_2H_2, (ii) C_2H_2 + Ar, (iii) C_2H_2 + H_2, and (iv) C_2H_2 + N_2 and revealed that argon dilutes acetylene and reduces the amount of acetylene molecules on the catalyst. Also, hydrogen and nitrogen diminishes the growth density of nanotubes. They proposed that an equilibrium between carbon supply rate and segregation rate is essential for high growth rate and high density of nanotubes.

Mi and Jia *et al.*[16] grew CNT arrays over macro porous substrate for NH_3 and N_2 carrier gases for varying time via floating catalyst method. Their results show that the VACNTs could possibly grow over a macro porous substrate. These carrier gases have significant effect on the CNT radius and growth rate. They also suggested that in keeping the CNTs vertically aligned, the aspects of the CNTs play a key role.

Toussi *et al.*[17] studied the change in flow rate of Ar (50 ml/min, 100 ml/min, and 150 ml/min) and its consequence on the CNT growth. They observed that the CNT yield increases with the increase in flow rate of Ar.

Jung *et al.*[18] explored the growth of CNT for different carrier gases such as N_2, H_2, Ar, NH_3, as well as their mixtures. They concluded that CNT growth was considerably enhanced for NH_3 compared to the mixture of N_2 and H_2.

Kayastha *et al.*[19] observed that carrier gases alter the CNT growth rate and growth density. Ar addition to C_2H_2 enhances whereas N_2 and H_2 reduces the growth rate of nanotubes.

Reynolds *et al.*[20] deliberated the H_2 flow rate effect on CNT growth and saw that at higher CH_4 rate and lower H_2 rate, the density of nanotubes decreases considerably.

In the next section, we have developed a theoretical model to study the carrier gas effects on the MWCNT growth. The model consists of the dynamics of all the species present in the reactive plasma, and the CNT growth equation to examine the effect of carrier gases have on the MWCNT growth.

5.3 MODEL DESCRIPTION

Following the detailed analysis of our previous work[21], an investigative model is considered to study three different plasma environments - **I:** CH_4 (methane) + H_2 (hydrogen); **II:** C_2H_2 (acetylene) + H_2 (hydrogen); **III:** C_2H_2 (acetylene) + NH_3 (ammonia) or N_2 (nitrogen), or Ar (argon), respectively. Throughout the chapter, the reactive plasma species (electrons, neutrals, and ions) of hydrocarbon (CH_4 or C_2H_2) are denoted as type A, and carrier gases (namely H_2, NH_3, N_2, or Ar) denoted as type B. All the terms have their usual notations[21].

5.3.1 Electron balance equation in bulk plasma

$$\partial_\tau(n_e) = \sum_j \beta_j n_j - \sum_j \alpha_j n_e n_{ij} - \gamma_e \frac{n_{CNT}}{\lambda_s}\begin{pmatrix} tip & cyl \\ \xi & \xi \\ e & e \end{pmatrix} - \mathrm{K}^{e}_{wall} n_e, \tag{5.1}$$

The first term of Eq. (5.1) represents the rise in electron density via ionization of neutrals, the second term denotes decrease due to recombination of electron and ions, the third term represents decrease owing to their accumulation at the MWCNT surface, and the discharge loss to the walls of the chamber is denoted lastly.

5.3.2 Positive ion balance equation in bulk plasma

$$\begin{aligned}\partial_\tau(n_{iA}) = {} & \beta_A n_A - \alpha_A n_e n_{iA} - \frac{n_{CNT}}{\lambda_s}\begin{pmatrix} tip & cyl \\ \xi & \xi \\ iA & iA \end{pmatrix} \\ & + \sum_{\ell AB} k_\ell n_A n_{iB} - \sum_{qBA} k_q n_B n_{iA} - \mathrm{K}^{iA}_{wall} n_{iA} + \left(\frac{P}{E^{diss}_{CH} V}\right),\end{aligned} \tag{5.2}$$

$$\begin{aligned}\partial_\tau(n_{iB}) = {} & \beta_B n_B - \alpha_B n_e n_{iB} - \frac{n_{CNT}}{\lambda_s}\begin{pmatrix} tip & cyl \\ \xi & \xi \\ iB & iB \end{pmatrix} \\ & + \sum_{qBA} k_q n_B n_{iA} - \sum_{\ell AB} k_\ell n_A n_{iB} - \mathrm{K}^{iB}_{wall} n_{iB} + \left(\frac{P}{E^{diss}_{H} V}\right),\end{aligned} \tag{5.3}$$

In Eqs. (5.2) and (5.3), first term denotes the elevates the ion density because of dissociation of neutrals, next term denotes the dissipation due to recombination of ions with electrons, third term represents the loss due to their accumulation at the MWCNT surface; the ion-neutral reactions are incorporated in the fourth and fifth terms, sixth terms denotes the discharge loss to the walls and the last term incorporates the dissociation by plasma power.

5.3.3 Neutral atom balance equation in bulk plasma

$$\partial_\tau(n_A) = \alpha_A n_e n_{iA} - \beta_A n_A + \frac{n_{CNT}}{\lambda_s}\left(1-\gamma_{iA}\right)\begin{pmatrix} tip & cyl \\ \xi & \xi \\ iA & iA \end{pmatrix} - \frac{n_{CNT}}{\lambda_s}\gamma_A\begin{pmatrix} tip & cyl \\ \xi & \xi \\ A & A \end{pmatrix} + Q_A^{IF} - Q_A^{OF} - \sum_{lBA} k_l n_A n_{iB} + \sum_{qAB} k_q n_B n_{iA} - J_A^{adsp} + J_A^{desp} - K_{wall}^{A} n_A, \quad (5.4)$$

$$\partial_\tau(n_B) = \alpha_B n_e n_{iB} - \beta_B n_B + \frac{n_{CNT}}{\lambda_s}\left(1-\gamma_{iB}\right)\begin{pmatrix} tip & cyl \\ \xi & \xi \\ iB & iB \end{pmatrix} - \frac{n_{CNT}}{\lambda_s}\gamma_B\begin{pmatrix} tip & cyl \\ \xi & \xi \\ iB & iB \end{pmatrix} + Q_B^{IF} - Q_B^{OF} - \sum_{qBA} k_q n_B n_{iA} + \sum_{\ell AB} k_\ell n_A n_{iB} - J_B^{adsp} + J_B^{desp} - K_{wall}^{B} n_B + J_{thd}, \quad (5.5)$$

In Eqs. (5.4) and (5.5), first term descibes the rise in neutral density due to the ion-electron recombination, next term denotes the dissipation due to dissociation of neutrals the rise in neutral atom density due to ion neutralizationis descibed in third term, the fourth term characterizes the dissipation due to neutral atom accumulation at the MWCNT surface, the neutral plasma species influx and outflux is denoted by the fifth and sixth terms, the neutral-ion reactions are incorporated in the seventh and eighth terms, ninth and tenth term represents the adsorption and desorption of neutrals onto/from the catalyst. The eleventh term of Eq. (5.5) indicates an increase in hydrogen species density due to the thermal de-hydrogenation process. The ending terms both equations signify the discharge loss.

5.3.4 Carbon and hydrogen generation over the catalyst

The decomposition outcomes of hydrocarbon and hydrogen precursors over the catalyst surface results in the generation of carbon species and hydrogen radicals crucial for the growth of CNT. The time evolution of the carbon and hydrogen species created per unit area over the surface of the catalyst are given by

$$\begin{aligned}\partial_\tau(n_C) = \Bigg[& \sum_A \left\{ J_A(1-\theta_t) + n_A^{surf}\upsilon \exp\left(-\frac{\delta E_{CH}^{diss}}{k_B T_S}\right) - n_A \upsilon \exp\left(-\frac{\delta E_{dCH}}{k_B T_S}\right)\right\} \\ & + \sum_{iA}\left\{\left(\sum_A \frac{n_A^{surf} y_d}{\upsilon_0}\right) J_{iA} + J_{iA}\right\} + J_C + \sum_{iB}\left(\sum_{iA}\frac{J_{iA}\sigma_{ads}}{\upsilon}\right) J_{iB} \\ & - \sum_B \left(\sum_A n_A^{surf}\sigma_{ads}\right) J_B - n_C \upsilon \exp\left(-\frac{\delta E_{ev}}{k_B T_S}\right) - n_C \sigma_{ads} \upsilon n_H \Bigg] \\ & \times d_\tau(\Omega_C),\end{aligned} \tag{5.6}$$

$$\begin{aligned}\partial_\tau(n_H) = \sum_B \Bigg\{ & J_B(1-\theta_t) + n_B^{surf}\upsilon \exp\left(-\frac{\delta E_H^{diss}}{k_B T_S}\right) - n_B^{surf}\upsilon \exp\left(-\frac{\delta E_{dH}}{k_B T_S}\right) \\ & - n_B^{surf}\sigma_{ads} J_B - n_B^{surf}\sigma_{ads} J_{iB}\Bigg\} + \sum_{iA}\left(\sum_A \frac{n_A^{surf} y_d}{\upsilon_0}\right) J_{iA} \\ & + \sum_{iB} J_{iB} - n_H \sigma_{ads} \upsilon n_C,\end{aligned} \tag{5.7}$$

where n_C and n_H are the number density of carbon and hydrogen species generated per unit area on the catalyst surface, respectively. The rate of generation of carbon species over the surface of the catalyst is represented by Eq. (5.6). The first and second term designates the increase in carbon number density due to the adsorption of neutral hydrocarbons over the surface of the catalyst and the hydrocarbon thermal dissociation, respectively. The third term denotes decrease in carbon number density owed to the desorption of hydrocarbon species from the surface of the catalyst, the fourth and fifth terms indicate increase in carbon density due to the hydrocarbon ion-induced

dissociation and positive ion decomposition, respectively. The sixth term represents the carbon influx directly towards the particle surface, the seventh term denotes increase due to the ion-ion interaction of hydrocarbon and hydrogen ions. The eighth term shows the decrease in carbon species owing to the hydrocarbon neutrals and hydrogen interaction. The ninth and tenth term incorporates the reduction due to evaporation of carbon species and interaction between the carbon and hydrogen species generated on the catalyst nanoparticle, respectively. The last term of Eq. (5.6) indicates the rate of poisoning of the catalyst which depends upon the carbon number density over the catalyst surface generated throughout the growth[22]. The creation of hydrogen species on the surface of the catalyst is represented by Eq. (5.7). The first and second term denotes the increase in hydrogen species due to adsorption of hydrogen neutral species on the surface of the catalyst and thermal dissociation of the hydrocarbons, respectively. The third term denotes the loss due to desorption of hydrogen from the surface of the catalyst. The fourth and fifth term represents the interaction between the hydrogen adsorbed on the surface with the incoming neutrals and ions of hydrogen, respectively. The sixth and seventh term denotes the increase due to the hydrocarbon ion-induced dissociation and hydrogen influx near the particle surface. The last term signifies the loss in hydrogen caused by interaction between the generated hydrogen and carbon species on the nanoparticle.

5.3.5 Graphitic shell formation rate

$$\partial_{\tau}\left(N_g\right)=\left[D_s+D_b+2\pi\kappa v r^2\right]\times n_C S-n_{cg}S, \tag{5.8}$$

The first term of Eq. (5.8) signifying the rate of cylindrical graphitic shell formation[23] denotes surface diffusion over catalyst surface, the second term denotes bulk diffusion through the catalyst, the third term incorporates the C-atom precipitation around the catalyst rear end forming cylindrical shells where n_C is the number density of carbon species on the catalyst nanoparticle[21] and, the last term denotes etching effects of the carrier gas species.

5.3.6 Growth equation of CNT

The growth of CNT in a reactive plasma is evaluated in Eq. (5.9) i.e., a volumetric change in the CNT (variation of radius and height) with the number densities of carbon and hydrogen species generated over the surface of the catalyst by considering various growth processes.

$$\partial_\tau\left(\pi r^2 l\right)=\left[\left\{D_S+D_b+2\kappa\upsilon r^2\right\}\times\frac{P\left(8\pi r\right)n_C}{\upsilon\rho_{CNT}\sum\limits_{A}\xi_{iA}}+\left\{\frac{D_m}{4\pi r^2}+n_H\left(4\pi r^2\right)\sum\limits_{B}\xi_{iB}\right\}\right]\times\frac{m_{ct}}{\rho_{ct}}, \tag{5.9}$$

The functional terms and parameters mentioned in Eq. (5.9) have their usual meaning as described before. The first term represents the carbon species diffusion over the surface of the catalyst. The diffusion over the catalyst surface is dominant for the growth of outer shells of the CNT. However, the second term denotes the carbon species bulk diffusion through the catalyst. The third term signifies the incorporation or precipitation of carbon species around the posterior of the catalyst particle and forms an inner cylindrical shell. The dominance of bulk diffusion over the surface diffusion leads to the formation of MWCNTs otherwise SWCNTs are formed and this generally depends on the substrate temperature and catalyst particle size[24,25]. The formation of graphitic shells develops the stress between the graphene sheet and catalyst rear interface. The fourth term denotes the metal catalyst particle self-diffusion along the growth direction of CNT and the last term represents the hydrogen etching of the growing CNT walls.

5.4 RESULTS AND DISCUSSION

The above mentioned equations are solved simultaneously with others mentioned in our previous work for the energy balance and kinetics of electrons, ions, neutrals with suitable boundary conditions, viz., at $\tau = 0$, $T_{e0} = 0.6eV$, $T_{i0} = 2400K$, $n_{ct} = 10^6 cm^{-3}$, $n_{A0} = n_{B0} = 5.1\times10^{11}\ cm^{-3}$, $n_{e0} = 1.1\times10^{12}\ cm^{-3}$, $n_{iA0} = 0.58 n_{e0}$, $n_{iB0} = 0.42 n_{e0}$, and $T_{n0} = T_{ct} = 2000K$.

For plasma environment **I:** CH_4 (methane) + H_2 (hydrogen), temporal variations of hydrocarbon density and CNT radius for changing hydrogen ion density is observed.

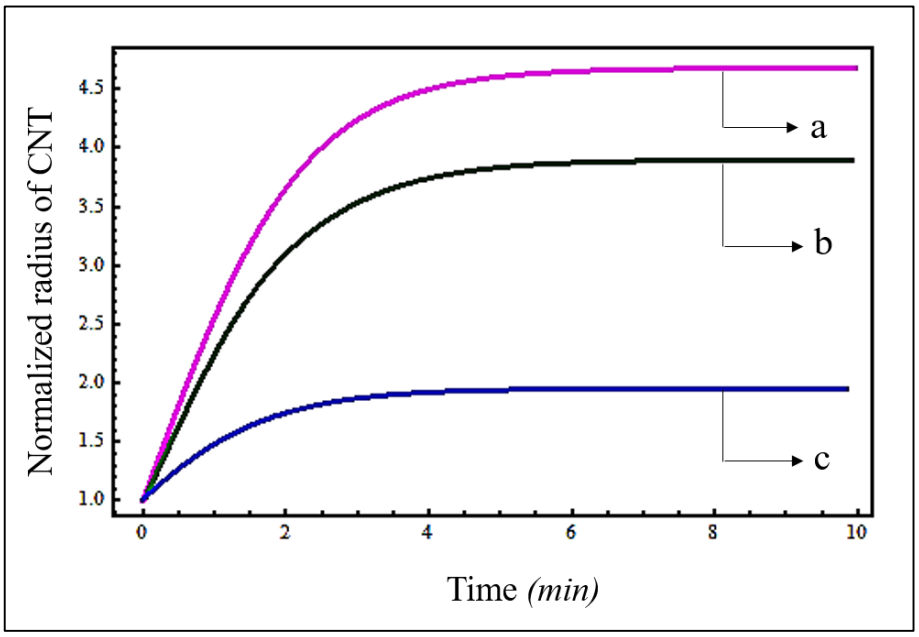

Figure 5.1 Time variation of hydrocarbon density on CNT (where a, b and c corresponds to 10^9, 10^{10} and $10^{11}\ cm^{-3}$ hydrogen ion density).

Figure 5.1 illustrates variation of the normalized radius of a CNT with time for different hydrogen ion number densities. The normalized CNT radius first increases with time and then attains a saturation value. Also, normalized radius decreases with the hydrogen ion density. This happens because for larger values of the hydrogen density

compared to hydrocarbon density, the etching rate of hydrogen dominates the deposition rate of carbon thereby decreasing the radius of nanotube.

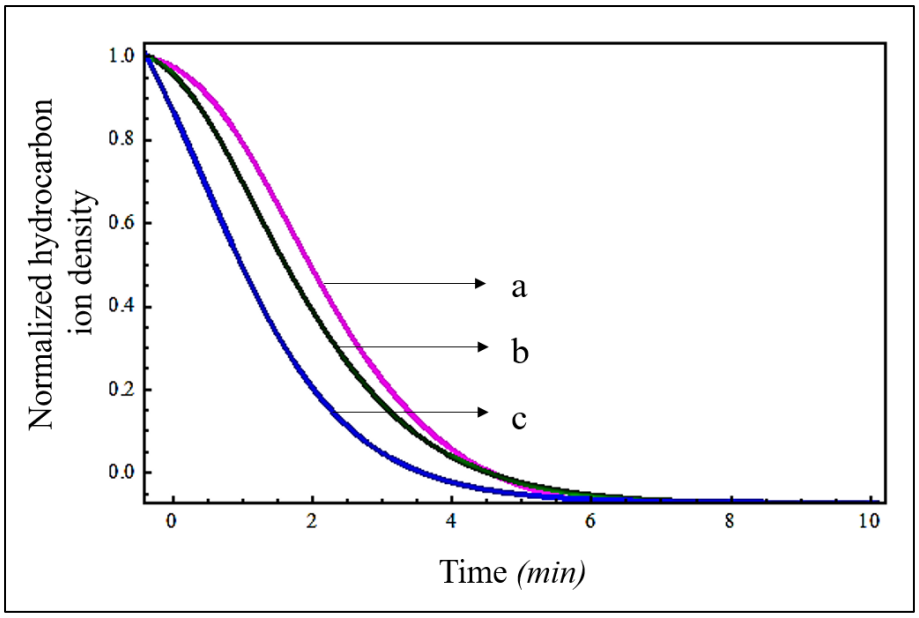

Figure 5.2 Time variation of normalized radius of CNT (where a, b and c corresponds to 10^9, 10^{10} and 10^{11} cm^{-3} hydrogen ion density).

Figure 5.2 illustrates variation of the hydrocarbon density with time for different hydrogen ion number densities. The normalized hydrocarbon ion density decreases with time. Also, with the increase in hydrogen ion densities, the hydrocarbon density decreases owing to the incessant reactions between hydrogen ions and hydrocarbon neutrals in plasma. This decreases the nanotube radius.

For plasma environment **II:** C_2H_2 (acetylene) + H_2 (hydrogen), temporal variations of CNT radius and height for changing C_2H_2/H_2 gas ratio is observed.

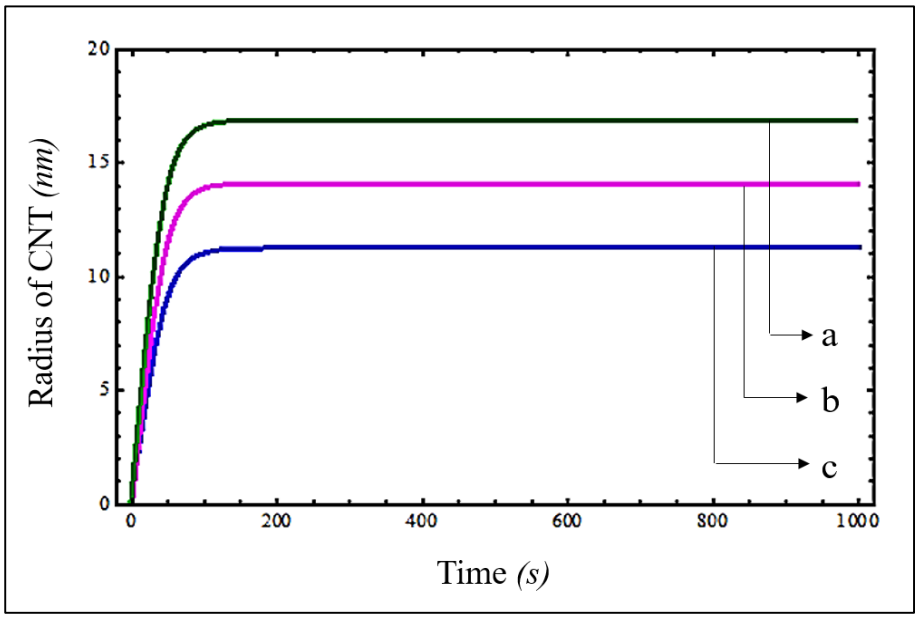

Figure 5.3 Temporal behaviour of radius of CNT (where a, b and c corresponds to 1/4, 1/2, 3/4 (C_2H_2/H_2) gas ratio).

Figure 5.3 illustrates the temporal behaviour of the average radius of MWCNTs for varying C_2H_2/H_2 gas ratio. With time, the average radius of the CNT initially increases and then acquires saturation. Also, decline in the CNT radius is observed with the increasing gas ratio. This is due to quick consumption of catalyst active surface by carbon atoms (as hydrocarbon concentration increases) thereby producing CNT with smaller radius.

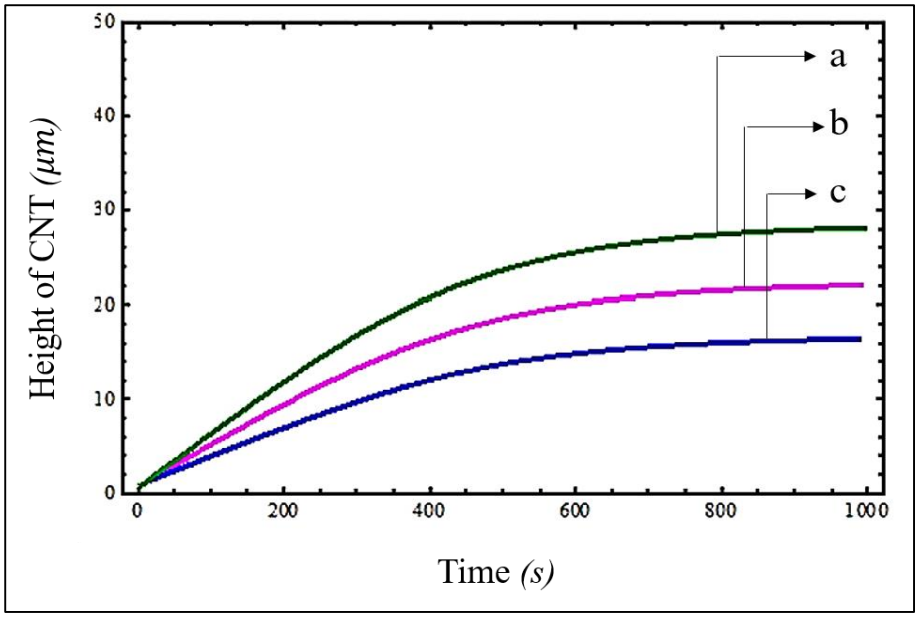

Figure 5.4 Temporal behaviour of height of CNT (where a, b and c corresponds to 1/4, 1/2, 3/4 (C_2H_2/H_2) gas ratio).

Figure 5.4 illustrates temporal behaviour of the height of MWCNTs for varying C_2H_2/H_2 gas ratio. The height of the CNT and thereby the growth rate decreases with the increasing gas ratio due to creation of amorphous carbon layer over the catalyst surface which diminishes the growth rate of CNT.

For plasma environment **III:** C_2H_2 (acetylene) + NH_3 (ammonia) or N_2 (nitrogen), or Ar (argon), time progressions of carbon number density on catalyst particle and number of graphitic shells of MWCNT for different carrier gas is observed.

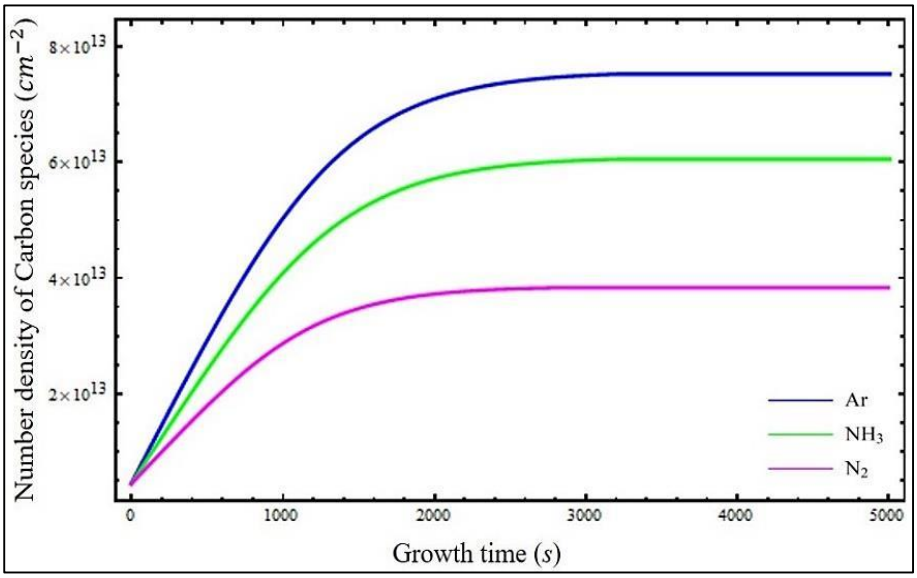

Figure 5.5 Time progression of carbon number density on catalyst particle for different carrier gas.

The dissociation of hydrocarbon species, increases the number density of carbon species on the catalyst nanoparticle. This carbon number density is higher for Ar compared to NH_3 and N_2, hence it would offer better MWCNT growth compared to others as shown in Figure 5.5.

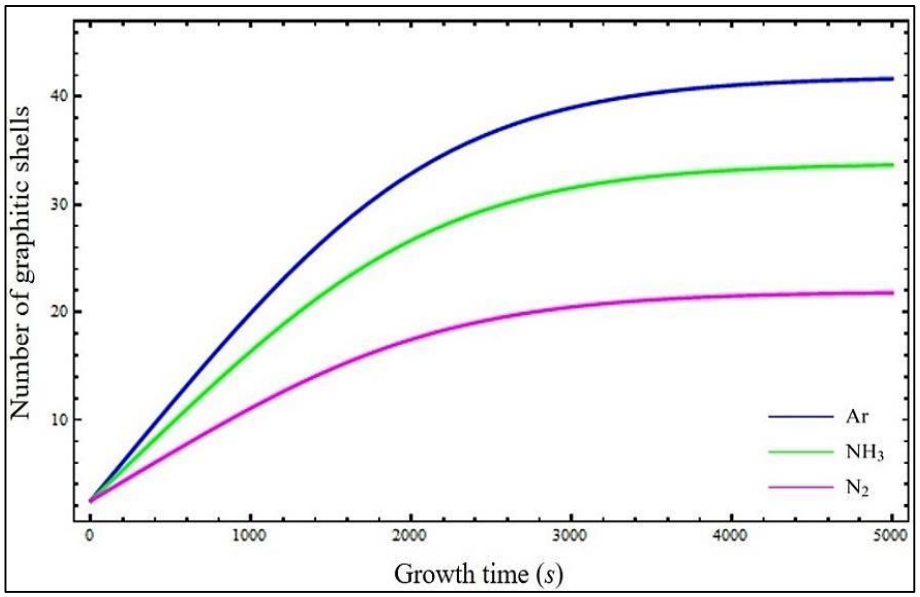

Figure 5.6 Time progression of number of graphitic shells of MWCNT for different carrier gas.

As in case of Ar, the carbon number density is higher, so the number of cylindrical graphitic shells formed in this case are more compared to NH_3 and N_2, as shown in Figure 5.6. This increase in number of shells increases the radius of MWCNT, consequently, Ar offers a better MWCNT growth than NH_3 and N_2.

The results obtained for the study comply with the experimental works of Zhang *et al.*[8], Ostrikov *et al.*[9], Denysenko *et al.*[10], Srivastava *et al.*[11], Yap *et al.*[15], Mi and Jia[16], Kayastha *et al.*[19], Jung *et al.*[18], and Reynolds *et al.*[20].

5.5 CONCLUSIONS

A model is established to comprehend the impact of hydrogen plasma and other carrier gases on CNT growth. It is analyzed from the studies that on increasing the hydrogen ion density, nanotube radius decreases due to decease in deposition rate. With the increase in H_2 ion densities, the hydrocarbon density decreases which endorses the decreases in CNT radius. The results indicate the decline in the CNT radius with increasing gas ratio. Also, the height of CNT decreases with the increasing gas ratio. With the increasing C_2H_2/H_2 ratio i.e., as the concentration of C_2H_2 increases in plasma, CNTs of smaller radius and height were produced as abundance of carbon atoms are produced compared to hydrogen atoms and the amorphous carbon layer which hinders the CNT growth generates rapidly. We have also established the effect of different carrier gases on the CNT growth considering C_2H_2 as the hydrocarbon source. The work can be thought useful to serve to a better understanding of the growth of MWCNT in the plasma and to study their field emission applications.

REFERENCES

[1] S. Iijima, Nature **354**, 56 (1991).

[2] C. Bower, W. Zhu, S. Jin, and O. Zhou, Appl. Phys. Lett. **77**, 830 (2000).

[3] V.I. Merkulov, D.H. Lowndes, Y.Y. Wei, G. Eres, and E. Voelkl, Appl. Phys. Lett. **76**, 3555 (2000).

[4] M. Chhowalla, K.B.K. Teo, C. Ducati, N.L. Rupesinghe, G.A.J. Amaratunga, A.C. Ferrari, D. Roy, J. Robertson, and W.I. Milne, J. Appl. Phys. **90**, 5308 (2001).

[5] L. Delzeit, I. McAninch, B.A. Cruden, D. Hash, B. Chen, J. Han, and M. Meyyappan, J. Appl. Phys. **91**, 6027 (2002).

[6] S. Maruyama, R. Kojima, Y. Miyauchi, S. Chiashi, and M. Kohno, Chem. Phys. Lett. **360**, 229 (2002).

[7] K. Hata, D.N. Futaba, K. Mizuno, T. Namai, M. Yumura, and S. Iijima, Science **306**, 1362 (2004).

[8] G. Zhang, D. Mann, L. Zhang, A. Javey, Y. Li, E. Yenilmez, Q. Wang, J.P. McVittie, Y. Nishi, J. Gibbons, and H. Dai, Proc. Natl. Acad. Sci. U. S. A. **102**, 16141 (2005).

[9] K. Ostrikov, Z. Tsakadze, P.P. Rutkevych, J.D. Long, S. Xu, and I. Denysenko, Contrib. to Plasma Phys. **45**, 514 (2005).

[10] I.B. Denysenko, S. Xu, J.D. Long, P.P. Rutkevych, N.A. Azarenkov, and K. Ostrikov, J. Appl. Phys. **95**, 2713 (2004).

[11] S.K. Srivastava, V.D. Vankar, and V. Kumar, Nano-Micro Lett. **2**, 42 (2010).

[12] C.Y. Zhi, X.D. Bai, and E.G. Wang, Appl. Phys. Lett. **81**, 1690 (2002).

[13] S.F. Lee, Y.P. Chang, and L.Y. Lee, J. Mater. Sci. Mater. Electron. **20**, 851 (2009).

[14] T. Feng, J. Zhang, Q. Li, X. Wang, K. Yu, and S. Zou, Phys. E Low-Dimensional

Syst. Nanostructures **36**, 28 (2007).

[15] Y.K. Yap, V. Kayastha, S. Hackney, S. Dimovski, and Y. Gogotsi, Mater. Res. Soc. Symp. Proc. **818**, 305 (2004).

[16] W. Mi and D. Jia, J. Chil. Chem. Soc. **55**, 153 (2010).

[17] S.M. Toussi, A. Fakhru'L-Razi, A.L. Chuah, and A.R. Suraya, Sains Malaysiana **40**, 197 (2011).

[18] M. Jung, Diam. Relat. Mater. **10**, 1235 (2001).

[19] V. Kayastha, Y.K. Yap, S. Dimovski, and Y. Gogotsi, Appl. Phys. Lett. **85**, 3265 (2004).

[20] C. Reynolds, B. Duong, and S. Seraphin, J. Undergrad. Res. Phys. **23**, 1 (2010).

[21] U. Sharma and S.C. Sharma, Phys. Plasmas **25**, 103509 (2018).

[22] R. Gupta and S.C. Sharma, Phys. Plasmas **24**, 073504 (2017).

[23] R. Gupta, N. Gupta, and S.C. Sharma, Phys. Plasmas **25**, 043504 (2018).

[24] I. Denysenko and K. Ostrikov, Appl. Phys. Lett. **90**, 10 (2007).

[25] S. Hofmann, G. Csányi, A.C. Ferrari, M.C. Payne, and J. Robertson, Phys. Rev. Lett. **95**, 036101 (2005).

Chapter - 6

SUMMARY AND FUTURE SCOPE OF THE WORK

6

SUMMARY AND FUTURE SCOPE OF WORK

6.1 SUMMARY

The work accomplished in this thesis aims toward a better understanding and knowledge of nucleation and growth of CNTs in a reactive plasma environment using a theoretical model. The different models deliberated in the research work consider various plasma gaseous mixtures, particle, energy and momentum balance of all the reactive plasma species, i.e., ions, electrons, neutrals atoms, dynamics of metal catalyst thin film, segregation of film to create catalyst nanoparticles, generation of carbon and hydrogen species, nucleation of CNT over these particles, charge balance over the nanotubes. Along with these kinetics processes, all the various chemical process required for nanotube growth are also incorporated, such as the direct influx of carbon and hydrogen species towards the catalyst and growing CNTs, dissociation of hydrocarbon and hydrogen species over the catalyst surface, surface diffusion and bulk diffusion of carbon atoms on the catalyst, carbon atom precipitation to form cylindrical graphitic tubules upon saturation of catalyst with carbon, and finally the vertical alignment of nanotube in the direction normal to the substrate due to the presence of plasma sheath induced electric field. Several issues raised regarding the effect of plasma parameters on the growth, structure and field enhancement factor have so far gone unexplored (experimentally as well as theoretically). The work has provided a deeper insight of the CNT synthesis in the presence of plasma environments and their technical feasibility. Our theoretical models and the results from numerical simulations would help comprehensively understand the experimental results from several leading experimental groups. This work would also pave the way for fabricating highly efficient CNTs-based field emitters.

— It is presented how carbon nanotubes align and grow with the help of a catalyst particle in plasma of methane and hydrogen. The plasma sheath electric field affects plasma parameters (density and temperature) and applied substrate bias potential. By considering the kinetics of the plasma sheath, the dynamics of charged species (ions, electrons, and others) and neutrals in the considered plasma environment, the kinetics of the catalyst particle, the generation of carbon and hydrogen species over the catalyst surface, as well as other processes required for nanotube growth, the effect of the plasma sheath electric field in establishing the necessary alignment force and its impact on the vertically aligned CNT growth in the plasma are studied. The outcomes of the model demonstrate how the force exerted by the plasma sheath electric field at the CNT tip, where the catalyst is positioned, affects the alignment of the CNTs. This force results from the plasma sheath electric field, which depends on several plasma variables and the substrate bias voltage. Moreover, this alignment force adjusts continuously as the CNT grows due to changes in the length and radius of the CNTs. The findings of the study are compared with the experimental data that are currently available, which supports the suggested mechanism.

— A theoretical model for the plasma pre-treatment of catalyst thin film was created and investigated. The impact of process variables, such as power, pressure, gas flow, and plasma temperature, were discussed. We have also deliberated on the effect of using different catalysts nanoparticles on the growth of nanotubes. The model accounts for the dynamics of catalyst thin film, segregation of film into nanoparticles, the kinetics of plasma sheath, and plasma species (ions, neutrals, and electrons), as well as the generation of atomic C and H species on the catalyst surface, while also taking several procedures crucial for plasma-assisted CNT growth into consideration. By analyzing their impact on CNT growth, the theoretical study seeks to advance our understanding of the use of diverse catalysts in many scientific areas. We carefully consider how pre-treatment will affect the catalyst thin film's ability to generate

nanoparticles. The impact of increasing catalyst nanofilm thickness on the catalyst size and density was discovered. Under the same plasma surroundings, the effects of using three different metal catalysts (Ni, Fe, and Co) on CNT development were investigated.

— A vertically aligned carbon nanotube (VACNT) array in plasma is investigated using a computational analysis that models its growth based on the variation of plasma operating conditions and process factors. We have considered how the characteristics of the VACNT array are affected by plasma concentration, power, pressure, and substrate temperature. Additionally, the deposition of amorphous carbon between the CNTs of the array is discussed. Since field emission is one of the VACNT array's most notable applications, the field enhancement factor for the array is carefully thought through and tuned. The study's results consider the balance of plasma species, plasma-CNT energy exchange, hydrocarbon and hydrogen generation over the catalyst surface, VACNT array growth, and amorphous carbon deposition over the substrate nanotubes of the array via PECVD. The model is solved by considering the initial conditions and plasma parameters cited in the experimental literature. The dimensions of an array, i.e., its length and average CNT diameter, can be optimized as convenient by altering the operating conditions and glow discharge parameters. The effects of array aspects on the field emission properties are also examined.

— The effect of three different plasma compositions on the CNT growth are considered I: CH_4 (methane) + H_2 (hydrogen); II: C_2H_2 (acetylene) + H_2 (hydrogen); III: C_2H_2 (acetylene) + NH_3 (ammonia) or N_2 (nitrogen), or Ar (argon), respectively. Case 1 considers plasma species of methane CH_4 and hydrogen H_2 and analyses the hydrogen ion density effect on the growth of CNTs. It was observed that the CNT radius decreases with increasing hydrogen ion density owing to a drop in deposition rate. Also, the hydrocarbon density decreases with increasing hydrogen ion densities, which advocates the decrease in CNT radius. Case 2 considers plasma species of acetylene C_2H_2 and

hydrogen H_2 and analyses the effect of changing gas ratio on the growth of carbon nanotubes. It was indicated that the CNT radius declines with an increasing gas ratio. Moreover, the height of CNT also decreases with the increasing gas ratio. As the concentration of C_2H_2 increases in plasma, nanotubes of lesser radius and height are produced as an abundance of carbon atoms are produced compared to hydrogen atoms and the amorphous carbon layer, which hinders the CNT growth generates rapidly. Case 3 analyses the consequence of different carrier gases on PECVD-CNT growth considering acetylene C_2H_2 + ammonia NH_3, nitrogen N_2, or argon Ar argon, respectively. The effect of these carrier gases on the CNT structure was compared. It was concluded that while Ar promotes the CNT growth, NH_3 and N_2 diminish the growth of carbon nanotubes in plasma.

6.2 FUTURE SCOPE OF WORK

The field of plasma-assisted carbon nanostructure growth is fascinating and progressive in nanoscience and technology. This research work done in the thesis can lead to the production of CNT in a reactive plasma environment in a controlled way for numerous potential applications by altering its synthesis conditions as mentioned in the preceding chapters, especially for field emitters as the field emission from carbon nanotubes is a consequence of their geometry instead of their crystalline structure.

Still, many issues regarding plasma-assisted CNT growth have gone unexplored experimentally and theoretically, which can expand the knowledge of this area. Some of the recommendations for future work that is required to be done are-

- Hydrocarbon precursors and carrier gases are known to synthesize CNTs in a plasma setup successfully. A few of the plasma mixtures for the growth of CNT were studied in this research work theoretically. However, many plasma compositions can still be studied, and their effect on the plasma-assisted CNT growth is still not appropriately tackled.

- Understanding the importance of catalyst-substrate interactions on the growth of CNT in a reactive plasma is crucial. As observed throughout the research work, the presence of a catalyst is a necessity for the growth of CNT. It could be seen at the tip of fully grown CNTs or the base of the CNT, anchored at the substrate which is a consequence of the interaction between catalyst and substrate. This catalyst-substrate interaction has not been studied thoroughly and needs to be investigated in detail.